THE EFFECTS OF MODEL RESOLUTION ON THE SOUTH ASIAN AND WEST AFRICAN MONSOONS IN THE PLIOCENE

A thesis submitted to the
School of Environmental Sciences
of the
University of East Anglia
in partial fulfilment of the requirements for the degree of
Doctor of Philosophy

By
Andrea Williamson
April 2022

Abstract

The Pliocene Epoch (5.33 – 2.58 Million years ago) is currently being used as a future climate change analogue due to CO_2 levels during this time which are close to those of the present day, similar continental configuration between the two and a wealth of paleoenvironmental proxy data available. However, most model simulations involving the Pliocene are run at coarse resolution and include many boundary condition changes from the present day.

This thesis examines the effects of increased model resolution on the Pliocene climate using an atmopshere-only, spectral global climate model (the IGCM4) with the sea surface temperature field as the only boundary condition change between Pliocene and present day. Using the present day as a control experiment, basic state differences between the Pliocene and present day are explored. Then, a step-change approach is utilised: first, the dynamical resolution of the model is increased while the topography field remains constant (at low resolution). A further step follows to additionally increase the resolution of topography (to high resolution), in order to separate these two effects of increased resolution.

Two monsoon systems are examined - the South Asian monsoon (SAM) and the West African monsoon (WAM). Dynamical differences are found between Pliocene and present day for the SAM region, affecting monsoonal circulation. A northward shift in climatic features is observed with increased dynamical resolution, while the effects of topographic resolution are confined to the immediate area surrounding certain topographic features. Resolution effects are found to have varying effects regionally, with dynamical resolution generally being more important than topography.

Acknowledgements

I would like to firstly thank my supervisors, Manoj Joshi and Adrian Matthews, for their guidance, encouragement, motivation and patience (over 7 long years!) in providing me this truly life-changing opportunity. I cannot imagine what life would have been like had I not had the privilege of coming to UEA and working alongside you.

Thank you to the School of Environmental Sciences at UEA for awarding me the Lord Zuckerman scholarship, without which achieving my dream of a PhD would not have been possible. I thoroughly enjoyed my time spent here and will miss it greatly.

Thank you to friends and family, near and far. For keeping me sane, not letting me give up and believing in me when I doubted myself. Special thanks to my girls, for teaching me what's important in life and changing me for the better. Above all, thank you to my husband Aidan who has been my rock through thick and thin: you have provided me with stability and everything I have ever needed to make this possible. Thank you for putting up with me rambling on about things you don't understand and the many weekends spent entertaining Emily and Lizzie so that I could get more done. I am very lucky to have you.

The research presented in this thesis was carried out on the High Performance Computing Cluster supported by the Research and Specialist Computing Support service at the University of East Anglia

LIST OF ACRONYMS

AEJ	African Easterly Jet
AEW	African Easterly Wave
CAS	Central American Seaway
CCA	Convective Cloud Amount
CMIP	Coupled Model Intercomparison Project
EAIS	East Antarctic Ice Sheet
EARS	East African Rift System
ECMWF	European Centre for Medium-Range Weather Forecasts
EPV	Ertel Potential Vorticity
ESS	Earth System Sensitivity
GCM	Global Circulation Model
GrIS	Greenland Ice Sheet
IGCM	Intermediate Global Circulation Model
IPCC	Intergovernmental Panel on Climate Change
ITCZ	Inter Tropical Convergence Zone
ITF	Indonesian Through flow / Inter-Tropical Front
JJAS	June, July, August, September
LCA	Low Cloud Amount
MCS	Mesoscale Convective System
MLCA	Mid-Level Cloud Amount
MPWP	Mid-Pliocene Warm Period
MSLP	Mean Sea Level Pressure
NASA	National Aeronautics and Space Administration
NCEP	National Centers for Environmental Prediction
PMIP	Paleoclimate Modelling Intercomparison Project
PRISM	Pliocene Research, Interpretation and Synoptic Mapping
PV	Potential Vorticity
PlioMIP	Pliocene Model Intercomparison Project
SAL	Saharan Air Layer
SAM	South Asian Monsoon
SST	Sea Surface Temperature
TPW	Total Precipitable Water
TRMM	Tropical Rainfall Measuring Mission
WAIS	West Antarctic Ice Sheet
WAM	West African Monsoon

Contents

List of Tables

List of Figures

Chapter 1

Introduction

This chapter will first present the Pliocene: in a wider geological context, alongside major environmental trends in Earth's recent geological history. Then, main tectonic processes which affected the Pliocene will be presented in detail. A section regarding environmental conditions in the Pliocene follows, discussing recent efforts to reconstruct the Pliocene, especially during the mid-Piacenzian warm period. Then, the global monsoon in the Pliocene is discussed in detail, with results from modelling studies which rely upon the environmental reconstructions introduced in the previous section. A thesis outline closes the chapter; presenting research questions and describing the aims and goals of the chapters that follow.

1.1 The Pliocene

1.1.1 General Setting

The Pliocene epoch, $\sim$5.33 – 2.58 Million years ago (Ma)(Cohen *et al.* (2014)), continues the long term cooling trend observed in the past $\sim$50 million years, since the Early Eocene Thermal Maximum, approximately 55 million years ago. Figure 1.1 describes major trends and events on Earth over the last 65 million years, using data obtained from ocean sediment cores. $\delta^{18}O$ and $\delta^{13}C$ trends are used as proxies for surface temperature and primary productivity (as an indicator of ocean circulation changes), respectively.

In the Pliocene, CO_2 levels were similar to those of the present day (discussed later in this chapter). Figure 1.2 shows CO_2 along $\delta^{18}O$ trends for the past 40 Ma. The long term exposure of the earth to these CO_2 levels (which are elevated compared with the pre-industrial period) alongside very similar continental configuration to the present day allow for the exploration of the Pliocene as a future climate

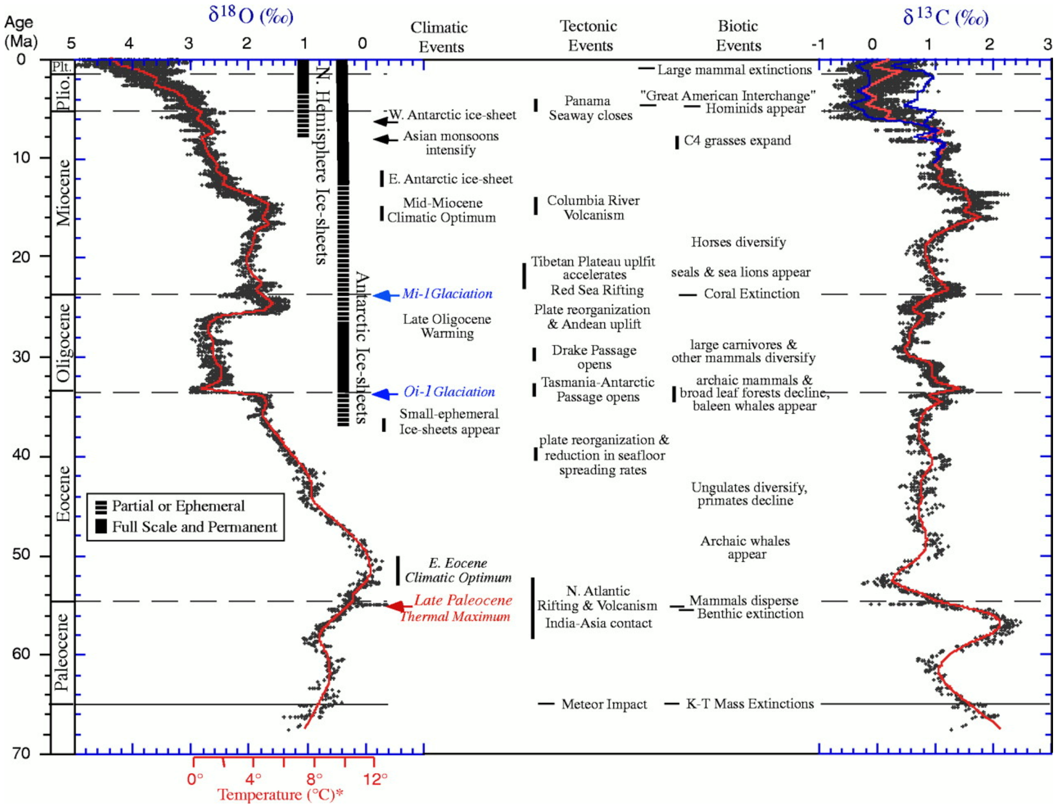

Figure 1.1: A summary of major trends and events in the last 65 million years, using data from ocean drilling and deep sea drilling projects. δ^{18}O fluctuations correspond to temperature changes at high latitudes up to ~35 Ma and ice cover changes since that time. δ^{13}C is used as a proxy for primary productivity; an indicator of ocean circulation changes. Blue lines represent the Atlantic and Pacific basins separately, to show the emerging divergent trend in recent times. Figure taken from Zachos *et al.* (2001), figure 4

change analogue - a look into the Earth at a possible state of CO_2 equilibrium.

The boundary between the Pliocene and Miocene which comes before it occurs at the end of the Messinian salinity crisis. During the Masinity salinity crisis, the Mediterranean endured a desiccation process (Hsu *et al.* (1973)). Water exchange between the Mediterranean and Atlantic was re-stablished with the Zanclean flood through what is today's Gibraltar straits (Blanc (2002),Garcia-Castellanos *et al.* (2009)). The name Pliocene, derived by Sir Charles Lyell in the 19th century, comes from two Greek words meaning "more" (pleion) and "new" (kainos). This is because the species of plant and animal life fossils found in the Pliocene soil strata are not extinct and exist in similar forms today and aids in gathering crucial proxy data from the Pliocene, as will be expanded upon later in this chapter.

Geographic changes to topography and ocean circulation occurred during the Pliocene, as a result of large scale tectonic dynamics. These will be described in detail in the next part of this chapter.

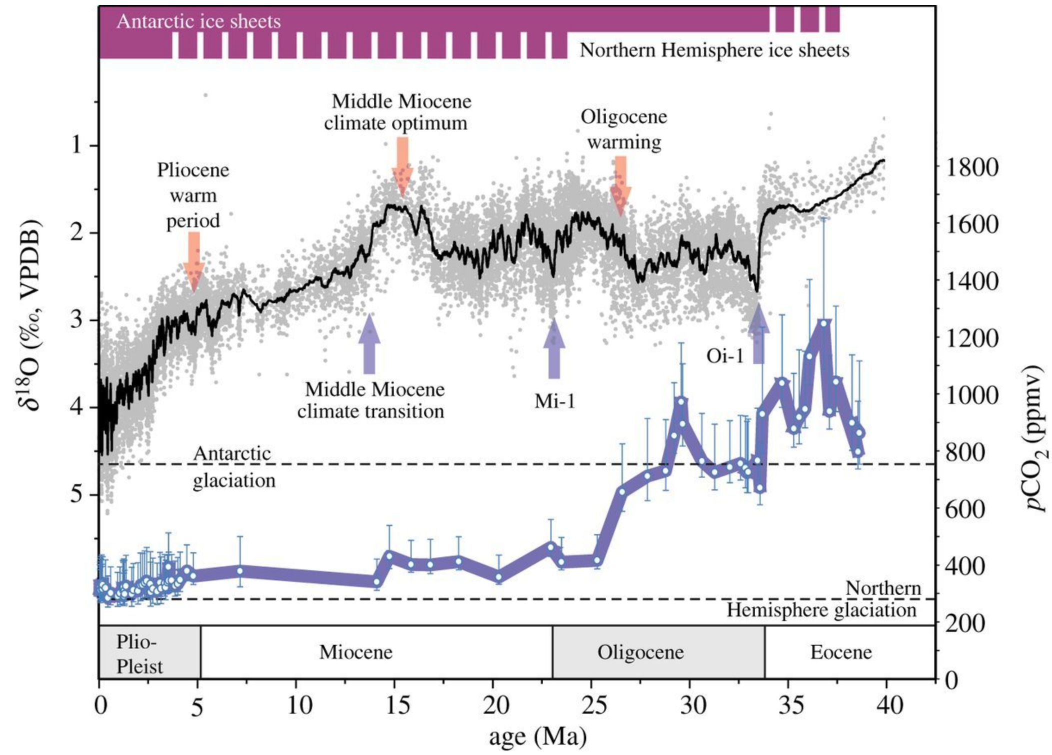

Figure 1.2: Climate and atmospheric CO_2 history for the past 40 Ma. Benthic $\delta^{18}O$ from Zachos *et al.* (2001). Major warming (red arrows) and cooling (blue arrows) events are labelled. Red bars indicate brief history of Antarctic and Northern Hemisphere ice sheets. Antarctic glaciation thresholds (approx. 750 ppm) and Northern Hemisphere glaciation threshold (approx. 280 ppm) deduced from climate models are marked by dashed lines. Figure taken from Zhang *et al.* (2013), figure 5

1.1.2 Geographic Changes

Several Geological processes ended, begun or underwent abrupt phases of change during the Pliocene, some with possible effects on the Pliocene climate. Figure 1.3 summarises the major processes identified in the Pliocene timeline. Figure 1.4 provides a topographic reconstruction of the Pliocene, with geological processes discussed in this section marked by red rectangles. In order of discussion: The Isthmus of Panama, Indonesian seaway, Tibetan Plateau and East African mountains.

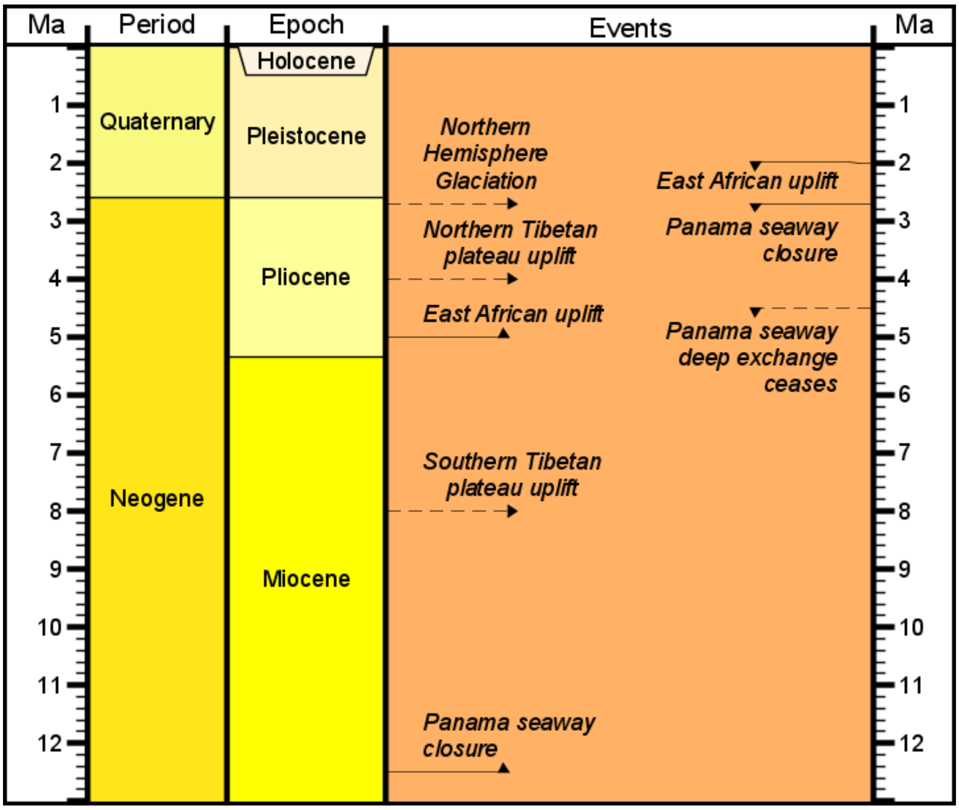

Figure 1.3: Geological timeline showing relevant events and their approximate time of occurrence. Up arrows show the beginning of a process while down arrows mark the ending of one. Horizontal arrows are used for abrupt events, rather than processes. Dashed lines show greater uncertainty regarding the timing of an event. Generated using timescalecreator.org

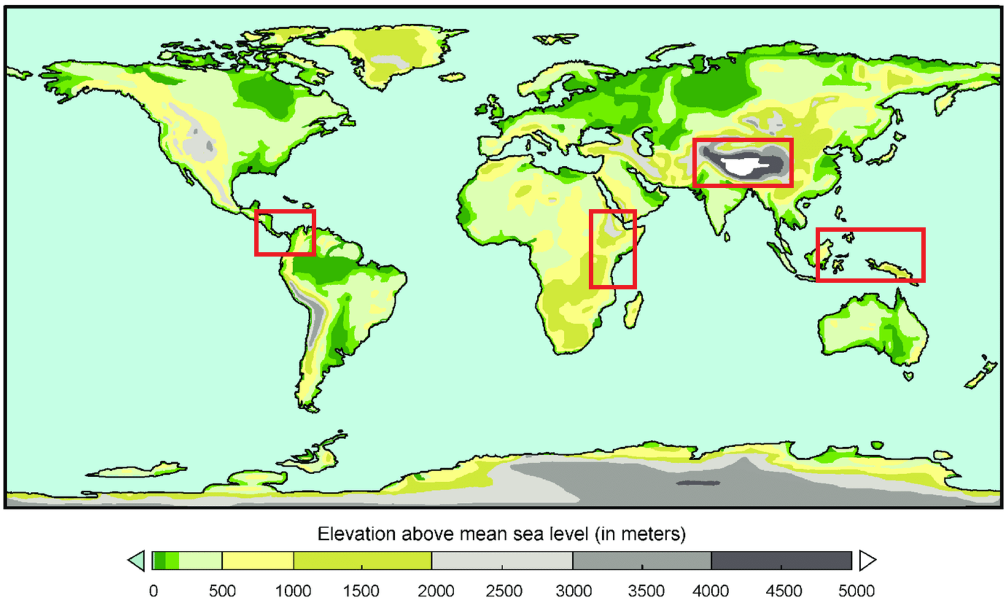

Figure 1.4: Mid-Pliocene topographic reconstruction, including a +25m coastline relative to modern. Notable differences from modern include the removal of Hudson Bay, the Great Lakes, and the West Antarctic Ice Sheet. Red rectangles indicate approximate locations of ongoing geological processes in the Pliocene. From West to East: Isthmus of Panama, the East African mountains, Tibetan plateau and the Indonesian Seaway. Modified from Dowsett *et al.* (2010), text figure 4.

Isthmus of Panama

In the Miocene/early Pliocene, the two Americas were not yet joined together which allowed for water exchange between the Pacific and Atlantic oceans through the Central American Seaway (CAS) or Panama seaway. Figure 1.5 shows an illustration of the three stages which make up the full closure of the seaway. As in Haug and Keigwin (2004), at its early stages and before ocean circulation was affected, water exchange between the Pacific and Atlantic existed which allowed for mixing between the two basins, roughly balancing their salinities. As the North American, South American and Caribbean plates converged, gradual shoaling of the seaway began and water exchange was restricted between the Atlantic and Pacific, causing their salinities to diverge. On the eastern side of the seaway, the Gulf Stream began to intensify while flow in the Pacific diverged to the south and north of the now narrow and shallow seaway. At present, with the seaway fully closed, trade winds carry fresh water vapour as a result of evaporation in the Tropical Atlantic and Caribbean over the isthmus, depositing fresh water into the Pacific Ocean through rainfall, strengthening the salinity differences between the Atlantic and Pacific and intensifying the Gulf Stream which carries more warm, salty waters to the high latitudes. In the Pacific, modern ocean currents are established; the North Equatorial, Equatorial and South Equatorial currents.

Figure 1.5: The closure of the Central American Seaway (CAS) and its effect on ocean circulation. Illustration by Jack Cook, Woods Hole Oceanographic Institute. Taken from Haug and Keigwin (2004)

The closure of the seaway began very early in the Miocene, at around 12.5 Ma (Duque-Caro (1990)). The seaway closed bottom to top, with interruptions to deep water exchange evident since about 4.6 Ma, inferred by an increase in thermohaline circulation and Gulf Stream flow since this time and an increase in surface water salinity at the Caribbean inferring a shoaling of the seaway to $<$100m at this time (Haug and Tiedemann (1998)). Modern Pacific-Atlantic salinity differences were established at 4.2 Ma, as reflect by δ^{18}O enrichment in the Caribbean Sea, interpreted as the result of restricted surface water exchange between the tropical Pacific and Atlantic basins in response to the shoaling of the seaway (Haug *et al.* (2001)). Evidence from benthic and planktonic foraminifera in the Caribbean and Pacific suggest modern circulation in the eastern Pacific was established $\sim$3 Ma (Keigwin (1982)).

Coates *et al.* (1992) find that the Panama seaway was effectively closed by 3.5 Ma while the closure was finalised by 2.7 Ma, marked by widespread mammal exchange between the Americas, through the Isthmus (Marshall *et al.* (1982)).

The oceanic reorganisation of circulation and the formation of the isthmus of Panama coincide with the intensification in glaciation of the northern hemisphere (iNHG) (e.g., Lisiecki and Raymo (2007)) and has been considered as a primary cause for the glaciation (e.g., Keigwin (1982), Bartoli *et al.* (2005)).

It has been suggested by Keigwin (1982) that the formation of the Isthmus of Panama through the closure of the seaway could have caused the intensification in glaciation, due to the reorganisation of ocean dynamics in such a way that caused an increase in heat and moisture transport poleward into the Arctic. This hypothesis, known as the "Panama Hypothesis", has been examined using a Global Circulation Model (GCM) with Pliocene boundary conditions by Lunt *et al.* (2007) and seems to hold true, though the magnitude of this effect is unclear. It is likely that it, like in many other cases, this is only one of several factors contributing to the glaciation. Haug and Tiedemann (1998) postulate that the formation of the Isthmus of Panama enabled iNHG through changes in ocean dynamics and atmospheric moisture supply, but peak orbital obliquity amplitude triggered the glaciation. Brierley (2015) use a coupled GCM (CESM) to investigate the effects of changes in inter-ocean gateways. They find that the closure of the CAS strengthens the Atlantic Meridional Overturning Circulation (AMOC) by around 2 Sv. Karas *et al.* (2017) find that between $\sim$4.8-3.8 Ma, reduced SST and δ^{18}O gradients between the North and South Atlantic support these hypotheses (Keigwin (1982), Haug and Tiedemann (1998), Lunt *et al.* (2007), Brierley (2015)) through a strengthening in the AMOC. Many other mechanisms have been suggested as important factors to iNHG (See Maslin *et al.* (1998), Lisiecki and Raymo (2007) and references therein).

Maritime Continent and Indonesian Throughflow

The northward shift of Australia and New Guinea and resulting geological processes caused land to emerge from below sea level and, in addition, a general increase in elevation across parts of the Maritime Continent (Molnar and Cronin (2015)) and references therein). This had potentially large effects on climate, both directly and remotely through changes in ocean circulation.

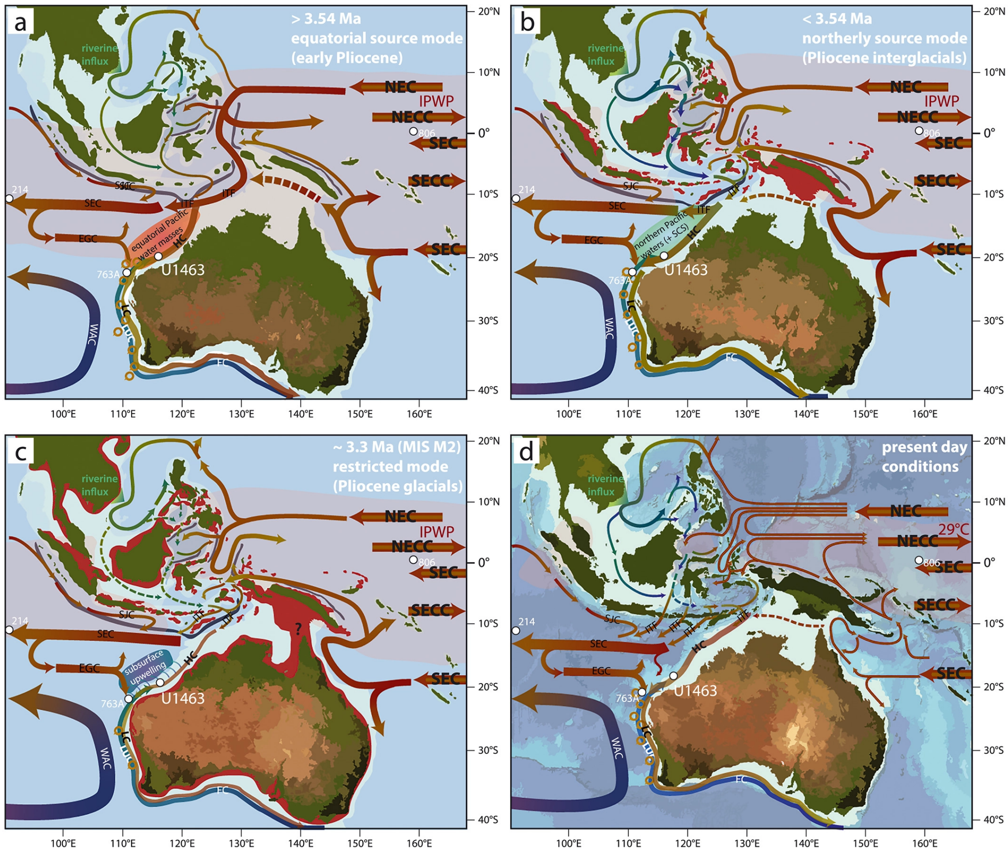

Figure 1.6: Tectonic and oceanographic change between 3.65 and 2.97 Ma. Red shaded ocean areas represent the theorized extend of the 29°C isotherm in the Indo-Pacific Warm Pool (IPWP). (a) Map showing the proposed open equatorial connection between the Pacific and the Indian Ocean; (b) configuration with landmasses potentially above sea level after 3.54 Ma (Molnar and Cronin (2015)) shown in red. Deep blue lines indicate active subduction zones during the Pliocene. Vegetation cover was reduced in this map to reflect lower riverine influx indicating reduced precipitation. Desertification remained weak; (c) throughflow geometry with the potentially maximum emergent land during marine isotope stage M2 (assuming a sea level lowstand of -30 m with modern-day shelf configuration of the Sunda and Sahul shelves). Aridification and reduced vegetation cover reflects our riverine influx and dust flux records; (d) modern configuration as a reference to compare the modern throughflow geometry to the proposed geometry changes between 3.65 and 2.97 Ma. NEC = North Equatorial Current; NECC = North Equatorial Counter Current; SEC = South Equatorial Current; SECC = South Equatorial Counter Current. Taken from Auer *et al.* (2019), Figure 5.

The Indonesian throughflow currently flows north and west of Sulawesi, crossing the Equator as it flows south into the Indian Ocean (Figure 1.6). This throughflow consists of cold, fresh North Pacific waters. Cane and Molnar (2001) postulated that in the Pliocene, 5-3 Ma, with many features of the Maritime Continent being farther south, the Indonesian throughflow transported warmer, more saline South Pacific waters into the eastern Indian Ocean, increasing its temperature and possibly affecting East African rainfall through observed and modelled relations between Indian Ocean sea surface temperatures and East African rainfall (e.g., Goddard and Graham (1999)). The idea of a warmer Indian Ocean with the northward movement of Australia and New Guinea has been supported by GCM simulations (e.g., Rodgers *et al.* (2000)).

Karas *et al.* (2009) tested the theory of Cane and Molnar (2001) and found compelling evidence through $\delta^{18}O$ and Mg/Ca measurements of deep-dwelling foraminifera (single cell, shelled organisms) of a $\sim$4°C cooling between 3.5 and 2.95 Ma which they attribute to a switch in Indonesian throughflow with possible dramatic effects for mid Pliocene climate. This evidence, however, was found in the subsurface layer of the eastern Indian Ocean and not at the surface, as predicted by Cane and Molnar (2001). East African rainfall could have still been impacted as the Somali jet, which brings rainfall inland, relies on moisture from coastal upwelling off Somalia, which is partly fed by waters originating from the Indonesian throughflow (Bruce *et al.* (1980)) and thus would have had less moisture supplied to it by the colder waters being upwelled in the area.

Dayem *et al.* (2007) found a correlation between rainfall over the Maritime Continent and the strength of the Walker cell. Molnar and Cronin (2015) used this relationship with an estimate of rainfall over the Maritime Continent during the early Pliocene, $\sim$5 Ma, taking into account the changes in island fraction (grown by $\sim$60% since 5Ma), concluding a rough decrease of 6% in the strength of the Walker cell during that time. In addition, the newly emerged land surface in the Maritime Continent exposed basaltic rock to a warm, moist environment. This caused an increase in CO_2 extraction from the atmosphere through greater weathering of silicate in these rocks - the Maritime Continent has one of the highest rates of chemical weathering and consequent CO_2 consumption per unit area in the world. This increase in CO_2 uptake was possibly enough to affect global temperatures and contribute to the overall cooling trend (Molnar and Cronin (2015)).

Using records from IODP Site U1463 combined with existing Indo-Pacific data, Auer *et al.* (2019) reconstruct the timing and pacing of tectonic ITF restriction during the Pliocene (3.66-2.96Ma). They find that the Indian Ocean was no longer connected to the Indo-Pacific Warm Pool by $\sim$ 3.54 Ma, with the switch to dominant northern Pacific ITF source for the first time. The MIS M2 glaciation (3.3Ma) caused sea level driven ITF restriction to lead to the irreversible cooling of the eastern Indian Ocean.

Tibetan Plateau

The Tibetan Plateau stretches across 2500km (Le Fort (1975)) and is up to 5km high (Fielding (1996). Its uplift has been ongoing for many millions of years, occurring in a south to north direction, as the Indian and Eurasian continental tectonic plates collided some ~70-50 million years ago (Fielding (1996)). Uplifting of the plateau continues today (Raymo and Ruddiman (1992)).

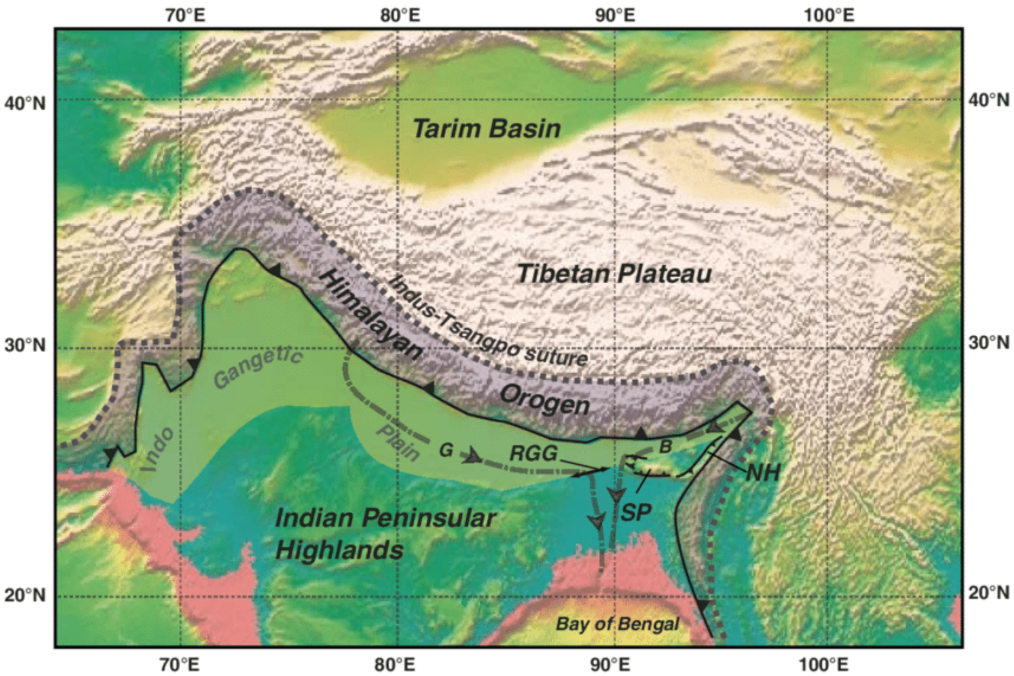

Figure 1.7: Orography around the Tibetan Plateau. G and B denote the Ganges and Brahmaputra rivers. Taken from Yin *et al.* (2010), Figure 1

Tracing timings of individual uplift stages during this slow, continuous uplift is a debatable matter: there are two main views on Tibetan uplift. The old uplift view supports the theory that most of the uplift occurred in the Miocene, with the plateau reaching its current height ~8 Ma and slowly losing elevation through faulting after that time (Fielding (1996)). Hsü *et al.* (1995) put forward an alternative view of a younger uplift theory in which uplift occurred in the late Pliocene and early Pleistocene. The debate regarding timings is mostly due to the different geological mechanisms identified. There is evidence to support the younger uplift theory in northern Tibet, with uplift identified as late as ~4.6-3.6 Ma and 1.6 Ma. (Zheng *et al.* (2000) and references therein)

The role of the Tibetan Plateau in the South Asian monsoon is two-fold. Hahn and Manabe (1975) find that, thermodynamically, the presence of the Tibetan Plateau is crucial in maintaining the monsoonal low pressure system at its present day location as high temperatures over Tibet produce the low pressure belt which extends southward over South Asia. In addition, mechanically, the presence of the mountains affects the evolution of the South Asian monsoon: the mountains act as a physical block to the subtropical jet which abruptly jumps from a latitude of about 25°N, to the south of Tibet, to 45°N in boreal summer. This draws in humid, southerly flow northwards from equatorial latitude to the low pressure belt.

Raymo and Ruddiman (1992) suggest that uplift of the Tibetan plateau caused the inception of the Asian monsoon and, through weathering due to intense rainfall on the Himalayan slope, cause a decrease in atmospheric CO_2 which assisted glaciation in the Northern Hemisphere. Zhisheng *et al.* (2001) examined the effects of different elevations in GCMs and found that an elevation increase consistent with uplift occurring ~8 and ~3 Ma causes crucial changes to Asian climate - initiating the Asian monsoon and intensifying the East Asian monsoon. Zheng *et al.* (2004) link between uplift phases and geological evidence for climate change, both in land and sea records. They find that a prominent monsoon system developed at ~8 Ma, with significant uplift to cause rain shadow over central Asia. At ~3.6 Ma, a further enhancement of the Indian and Asian monsoons occurred.

East African Mountains

The East African Mountains are located within the East African Rift System (EARS) (Figure 1.8). The EARS is divided into two main branches; eastern and western. The mountains are spread around the Great African Lakes, to the east (eastern branch) and to the west (western branch) of the region. The EARS was formed as a result of the divergent movement of the African and Somalian tectonic plates (Chorowicz (2005). Divergent movement of tectonic plates creates many rifts and mountains, leading to a very intricate orography.

Different stages of uplift exist for individual rift segments but as a whole the eastern branch developed earlier and is of higher elevation than that of the western branch. Rifting began north to south, starting in the Ethiopian region at ~30-35 Ma.

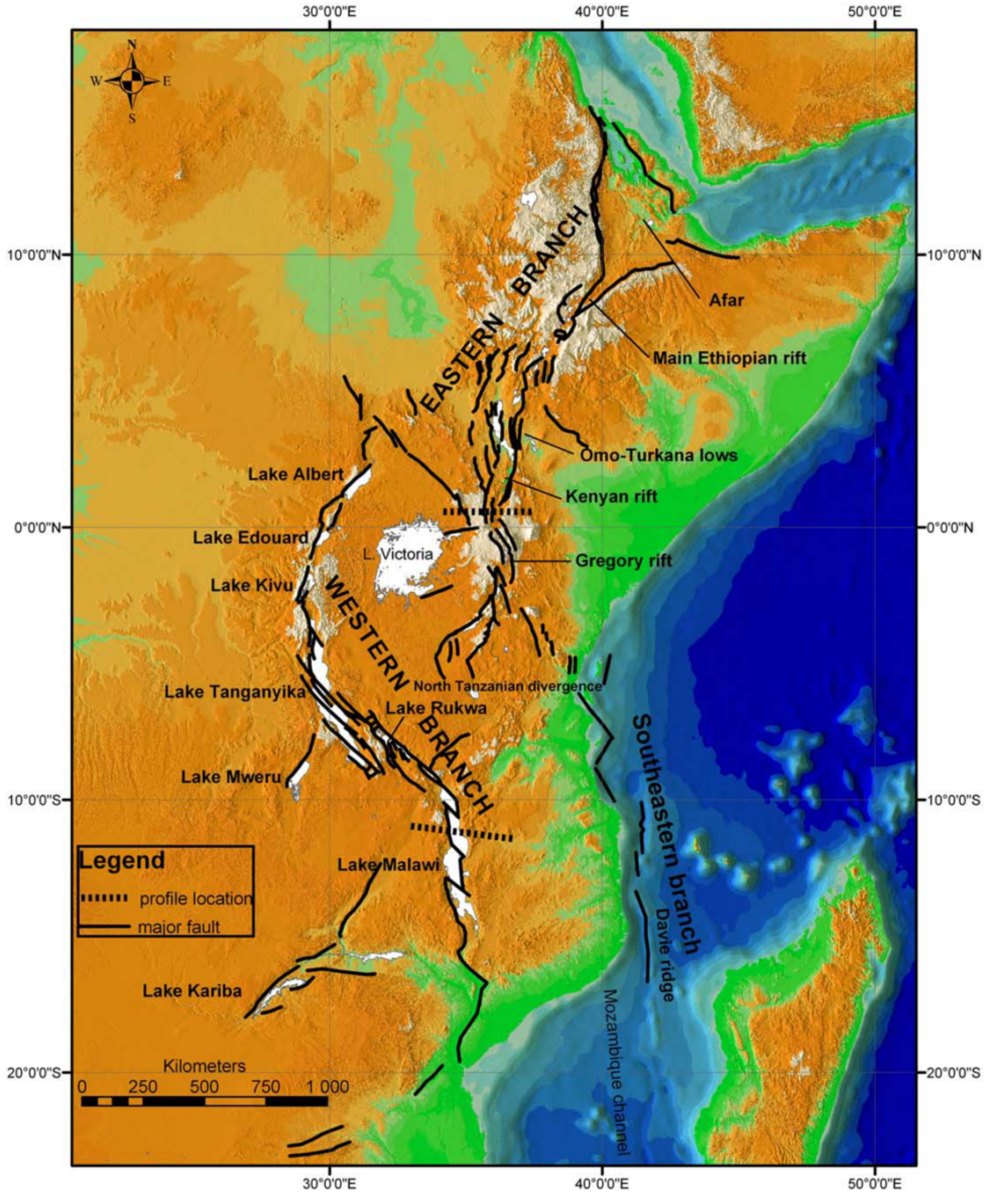

Figure 1.8: Hypsographic digital elevation map of the East African Rift System (EARS). Black lines mark main faults. White surfaces are lakes. The East African rift system is a series of several thousand kilometres long aligned successions of adjacent individual tectonic basins (rift valleys), separated from each other by relative shoals and generally bordered by uplifted shoulders. Taken from Chorowicz (2005)

Main features of the eastern branch were in place by $\sim$11 Ma, whereas the western branch started rifting between 12-8 Ma, with rift shoulders being climatically significant at 4 Ma in the Lake Albert region (Chorowicz (2005) and references within).

Uplift rates and maximum altitude of key tectonic features in the EARS are still unconstrained, despite much work which has been carried out (Maslin *et al.*

(2014) and references therein). Sepulchre *et al.* (2006) explored two extreme topographic conditions of African orography uplift using an atmosphere only GCM and found topography to have a clearly demonstrated effect on moisture transport through altering fluctuations in wind direction at lower levels and therefore affecting rainfall patterns and amounts: A simulation with the Ethiopian traps at 2000m saw an increase of 15% in rainfall compared with a present day control equivalent while a simulation with very low Ethiopian traps (400m) saw an increase in rainfall of 40%.

The aridification of Africa present in proxy data has been attributed to orographic changes through the EARS in the last 20 million years (Sommerfeld *et al.* (2014)) and has also been linked to human migration (Maslin *et al.* (2014)). A study of C_3 and C_4 vegetation - used to distinguish between more precipitation rich, wooded environments (C_3) and dry, open environments (C_4) in which water supply is more scarce, relies upon stable carbon isotope analysis tools and has been performed extensively for the East African region. Debates exist regarding the timing of this very important switch in vegetation. Ségalen *et al.* (2007) reviewed available data regarding vegetation type in soil, egg shells, tooth enamel and herbivore diet. It was concluded that C_4 vegetation appeared at $\sim$7-8 Ma at the earliest, C_3 vegetation was the dominant type until $\sim$3 Ma and from $\sim$3 to 1 Ma, a shift in vegetation type from C_3 to C_4 occurred, culminating with the dominance of the dry savannah and grassland C_4 vegetation. This coincides with the appearance of significant rift shoulders in the Lake Albert region, mentioned earlier.

1.2 Environmental Conditions and Modelling the Pliocene

The Mid-Piacenzian Warm Period (mPWP), formally known as the Mid-Pliocene Warm Period, 3.264 – 3.025 Ma (Dowsett *et al.* (2010)) is one of the most researched periods in Earth's geological history. Its popularity is gained by the possibility of using this period as an analogue for future climate change, which could provide insight regarding the coming future of the Earth.

Continental configuration during the mPWP was almost identical to the present day, as discussed in the previous section. One notable exception is the Maritime Continent. The closure of the Panama seaway had already concluded in an atmospheric and oceanic sense, by this point. Major changes to the Tibetan Plateau had also concluded, leaving topographic changes in East Africa as the main factor of uncertainty during this time, with significant changes appearing at $\sim$3 Ma.

The accuracy in timing this period links back to the fact that many of the fauna and flora species used as paleoproxies evolved to exist today. In addition to this, the abundance of such fossilised life forms is high, which provides very good coverage of the Earth in the mPWP. These proxies are relied upon not only for time dating purposes but also for determining many other environmental factors which existed during this time such as temperature, salinity, vegetation types and more.

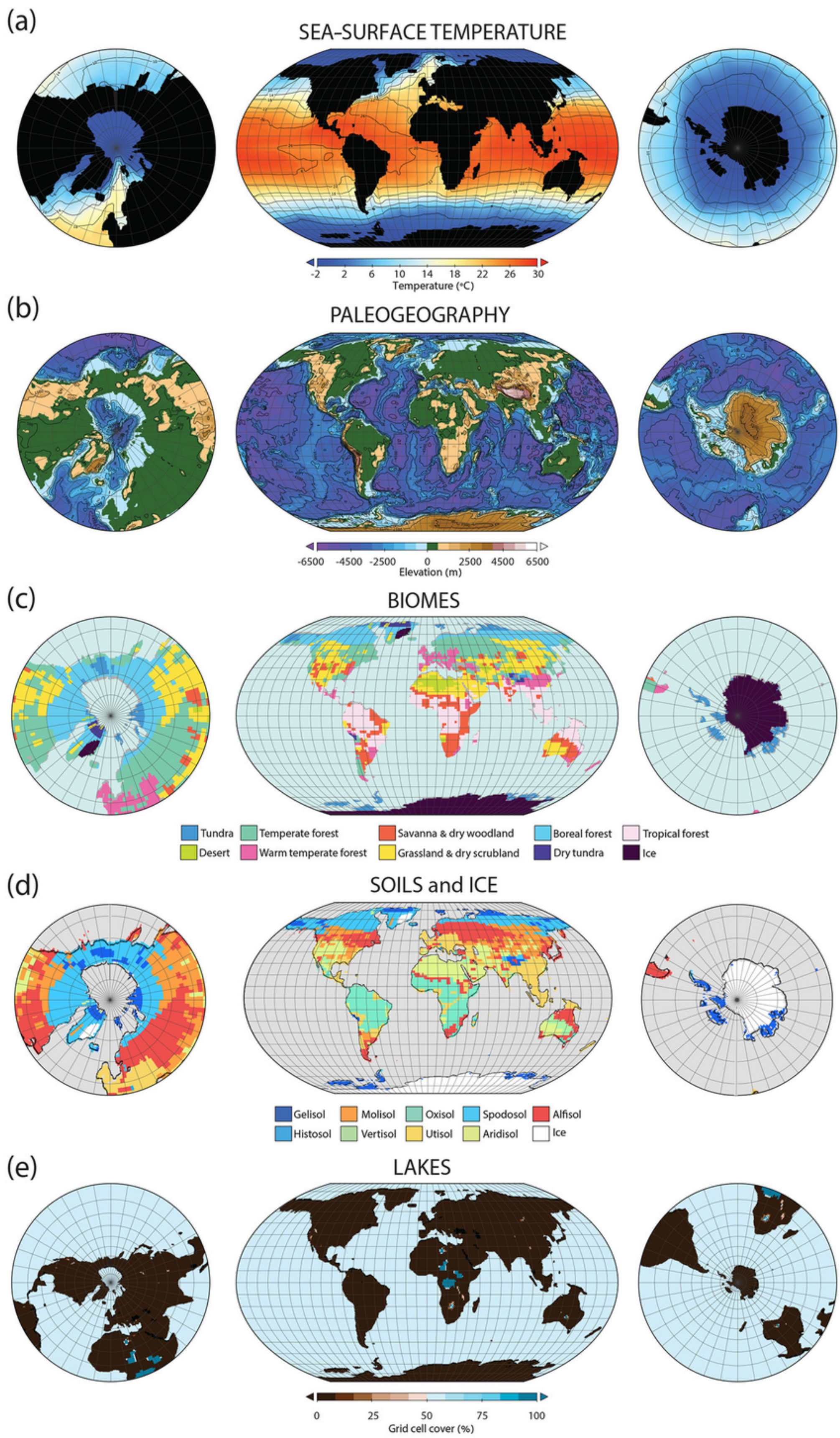

Figure 1.9: PRISM4 reconstruction. (a) Mean annual sea-surface temperature, (b) paleogeography, (c) biomes, (d) soils and land ice, and (e) large lakes. taken from Dowsett *et al.* (2016), figure 3.

CO2

CO_2 levels in the Pliocene are estimated using many different techniques and calibrations, depending on source material:
Estimates from the stomatal density of fossil leaves (e.g Kürschner *et al.* (1996)): 350-380 ppm;
Carbon isotope analyses (e.g., Raymo *et al.* (1996)): peak at 425 ppm, with levels around 400 ppm;
Alkenone based estimates (e.g., Pagani *et al.* (2010), Seki *et al.* (2010), Badger *et al.* (2013)): 365-415 ppm;
Boron isotope analyses (δ^{11}B) (e.g Seki *et al.* (2010), Bartoli *et al.* (2011)): 425 ppm peak early in the Pliocene, averaging 400 ppm for the mPWP and then decreasing to 350 ppm between 2.7 and 2Ma

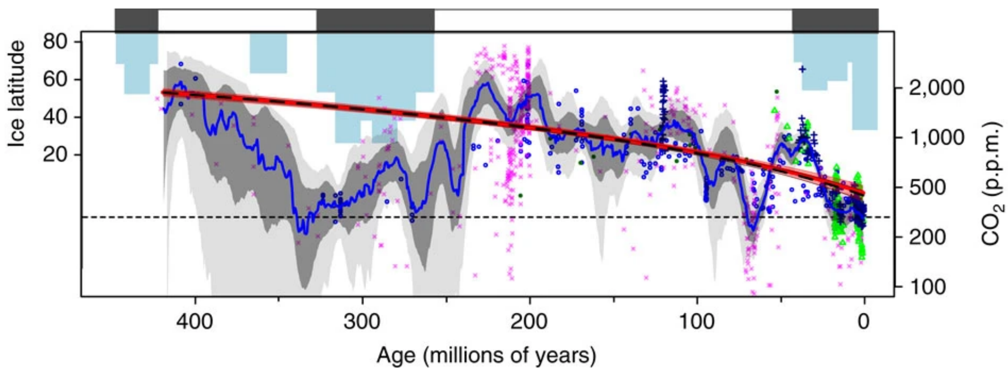

Figure 1.10: Temporal evolution of climate and atmospheric CO_2. Latitudinal extent of continental ice deposits (blue bars) and multi-proxy atmospheric CO_2 (in p.p.m.) compiled from the literature (data found in Supplementary Data 1; symbols). CO_2 from leaf stomata shown in blue circles, paedogenic carbonate δ^{13}C as pink crosses, boron isotopes in foraminifera as green triangles, liverwort δ^{13}C as dark blue filled circles and δ^{13}C of alkenones as dark blue crosses. The most likely LOESS fit through the data, taking into account X- and Y- uncertainty is shown as the blue line (data found in Supplementary Data 2). 68 and 95% confidence intervals are shown as dark and light grey bands. Red line is a linear best fit (curved due to log-scale for y axis) and 95% confidence interval for least squares regression through the CO_2 data. Black line is least squares fit through the LOESS best fit (blue line) resampled to original data density. Dashed line is pre-industrial CO_2 (278 p.p.m.). Icehouse time intervals are indicated by a black band and greenhouse intervals by a white band. Foster *et al.* (2017), figure 1

Foster *et al.* (2017) provide a comprehensive compilation of atmospheric CO_2 from ~1500 discrete estimates drawn from 112 published studies, using five independent techniques (CO_2 from leaf stomata, paedogenic carbonate δ^{13}C, boron isotopes in foraminifera, liverword δ^{13}C, alkenone δ^{13}C), covering the last 420 million years. Through a standardization process, better agreement between the different methods of CO_2 reconstruction is found. To address the existence of fewer observations and a reduced diversity in proxy type for the early parts of the record, a probabilistic approach using Monte Carlo re-sampling was used to eventually gain a locally estimated scatter-plot smoothing (LOESS) fit, providing insight into the multi-million-year evolution of CO_2. The resulting compilation is seen in Figure 1.10.

Badger *et al.* (2019) attempt to address the discrepancies during some time intervals between two of the main ocean-based proxy methods used to reconstruct atmospheric CO_2: the carbon isotope fractionation that occurs during photosynthesis as recorded by haptophyte biomarkers (alkenones) and the boron isotope composition (δ^{11}B) of foraminifer shells. They perform alkenone and δ^{11}B analysis on the same samples across a glacial-interglacial cycle at ODP site 999 and compare these to results from ice core analysis. The alkenone paleobarmoeter is found to be unable to reconstruct the low levels of atmospheric CO_2. Caution is suggested in the interoperation of alkenone-based records at periods of low CO_2 levels as it fails to capture the glacial-interglacial changes observed in ice cores. This is of particular importance in tropical waters, where CO_2(aq) is especially low. The δ^{11}B proxy was found to faithfully represent CO_2 changes found in ice cores, increasing the confidence in use of this proxy.

de la Vega *et al.* (2020) produced a new high resolution record of atmospheric CO_2 using the δ^{11}B-pH proxy from 3.35 to 3.15 Ma at a temporal resolution of 1 sample per 3-6 thousand years. They found that CO_2 during the KM5c interglacial had a mean value of 371 (with peak-to-trough values of 342 to 403), based on the five samples in this interval. Other CO_2 proxy systems such as stomata and palaesol δ^{13}C are lacking in this interval and marine-based alkenone δ^{13}C CO_2 proxy underestimates CO_2 levels in the Pliocene. The mPWP as a whole is of relatively high CO_2 with a mean of 360 ppm. Orbital cyclicity is seen, similarly to the Lisiecki and Raymo (2005) stack which also uses boron isotopes, but with reduced amplitude. Furthermore, CO_2 is seen to lag δ^{18}O by about 10kyr. Based on CO_2 alone, mPWP values were exceeded in the mid-1990s. Upper quartile range estimates (389 +38) suggest that CO_2 in the mPWP is very likely to have been under 427 ppm and thus by 2024-2025 CO_2 will surpass even the highest values.

CO_2 paleoproxy development has moved from a plethora of different proxies with differing CO_2 ranges to a current focus on the use of Boron isotopes which was found to best represent CO_2 levels in the Pliocene. The most recent mean estimates for the mPWP and KM5c are 371 and 360 ppm (de la Vega *et al.* (2020)), respectively.

Sea level

Sea level rise estimates during the mPWP vary greatly (Miller *et al.* (2005), Dowsett *et al.* (2010), Raymo *et al.* (2011) and references within, Miller *et al.* (2012), Rovere *et al.* (2014)). The most cited estimates relay on field mapping on palaeoshoreline deposits and range between 15-60 metres higher than present (Raymo *et al.* (2011)). Amongst a number of corrections that could be made to provide a more accurate estimate using this proxy, Raymo *et al.* (2011) suggested glacial isostatic adjustment (GIA) can have a big impact on the data provided by this method, mainly in high latitude regions once covered by ice sheets. Rovere *et al.* (2014) build upon the work on Raymo *et al.* (2011) and combined observations with GIA modelling to produce a palaeo-sea level elevation data set. This non global data set infers an estimate of $<$20 m of sea level rise. Using a range of different techniques, Miller *et al.* (2012) find that peak sea level during the mPWP was very likely to be 22 $\pm$ 5 m and extremely likely to be 22 $\pm$ 10 m higher than present. In global circulation models, the widely use value is 25m above present (Dowsett *et al.* (2010), Raymo *et al.* (2011)).

The growth and decay of continental ice sheets has the most dominant effect on water volume changes (Miller *et al.* (2005)). Negative peaks in δ^{18}O from benthic foraminifera during the mPWP suggest a reduction in global ice volume (Lisiecki and Raymo (2005)). The deglaciation of the West Antarctic Ice Sheet (WAIS) accounts for a sea level rise of 5m (Lythe and Vaughan (2001)), while the deglaciation of the Greenland Ice Sheet (GrIS) accounts for a rise of 7m (Bamber *et al.* (2001)). Hence, the deglaciation of both ice sheets accounts for a 12-14 m sea level rise (depending on bedrock topography assumptions, see Raymo *et al.* (2011)). In their work, Miller *et al.* (2012) use benthic δ^{18}O, along with Mg/Ca analysis (a proxy for temperature) to estimate that a sea level rise of 22 $\pm$ 10 m would imply loss of the equivalent of the Greenland (GrIS) and West Antarctic (WAIS) ice sheets, and some volume loss from the East Antarctic Ice Sheet (EAIS).

DeConto and Pollard (2016) discuss the inclusion of melting from above the ice sheet as well as below in ice sheet models, describing a process known as Marine Ice Cliff Instability (MICI), to accurately capture sea level changes in the past and the future. The Ross and Weddell seas in Antarctica and many buttressing glacier outlets are sensitive to atmospheric warming. With summer temperatures reaching and exceeding 0°C these low, flat surfaces which require little change to heating rates to enable meltwater to exist on the surface. Meltwater can weaken an ice shelf by increasing its hydrofracturing rates and thus speeding up its collapse compared with melting only occurring underneath, known as Marine Ice Shelf Instability (MISI). Pliocene summer air temperatures were capable of producing substantial surface meltwater, especially during warm austral summer orbits. Coupled nested RCM-Ice sheet modelling experiments show Pliocene Antarctica could have contributed 11.3m sea level rise with MISI included - ice shelf retreat is triggered by meltwater induced hydrofracturing of ice shelves, which relieves backstress and initiates both MISI and MICI retreat into the deepest sectors of WAIS and EAIS marine basins.

Edwards *et al.* (2019) employ statistical techniques of uncertainty quantification for computationally expensive computer models to re-examine and estimate probability distributions for the projections presented in DeConto and Pollard (2016). They find that MICI is not necessarily required to reproduce sea-level changes due to Antarctic ice loss in the mid-Pliocene epoch with use of this statistical approach.

Grant *et al.* (2019) use biological and sedimentological tracers from Whanganui Basin in New Zealand, which offers one of the highest resolution shallow-marine records of orbitally paced, Late Neogene global sea level change in the world. The sedimentary fill of the site is about 5 km thick, accumulated under relatively linear basin subsidence (due to plate boundary interactions) and has no erosion due to waves or sub-aerial exposure. A novel approach to estimating sea level change using the relationship between grain size and water depth relative to wave energy is used to provide a new constraint on Pliocene relative sea level which is independent of $\delta\ ^{18}O$ and does not rely on geochemical proxies. Using this technique, an upper boundary of 25m to mean sea level, with sea level changes of 13 $\pm$ 5 m between glacial and interglacial periods (on a 20kyr cycle) were found.

With consideration of processes such as Glacial Isostatic Adjustment (GIA, Raymo *et al.* (2011)) and Marine Ice Shelf Instability (MISI, DeConto and Pollard (2016)), alongside advancements in statistical modelling (Edwards *et al.* (2019)) and new $\delta\ ^{18}O$ independent limits (Grant *et al.* (2019)), mean sea level rise in the Pliocene is mostly estimated to have been no greater than 25m.

Sea Surface Temperatures (SSTs)

Pliocene SSTs differ from modern, especially in upwelling zones and higher latitudes (Figure 1.9). During the mPWP, the global mean temperature could have been between 2-3°C higher than present (Dowsett *et al.* (2010)), which is in the range of the current CO_2 increase scenarios set out by the Intergovernmental Panel on Climate Change (IPCC) (Masson-Delmotte *et al.* (2021)).

Meridional and zonal gradients were weaker in the Pliocene, though the magnitude of this reduction, especially in the tropical Pacific, is an issue very much up for debate. Fedorov *et al.* (2006) found that El Nino conditions may have been continual rather than an intermittent phenomenon up to $\sim$3Ma.

A study by Brierley *et al.* (2009) used a hypothetical SST profile to an estimated distribution of SST in the middle of the Pacific at $\sim$4 Ma and set this as a boundary condition for an atmospheric general circulation model in order to examine the atmospheric response to an expanded warm pool. In the Pacific, the temperature contrast between the Equator and 32°N increased by $\sim$5°C from 4 to 2 Ma, while at 3 Ma today's $\sim$6°C zonal SST gradient in the Equatorial Pacific was less than 2°C. Meridional temperature changes seemed to precondition zonal changes, which points at the expansion of the tropical warm pool in the Pliocene as a main contributing factor to the development of very weak meridional and zonal gradients and its implications for climate.

Brierley *et al.* (2009) also suggested that a uniform increase in vertical mixing (diffusion) rates in the upper layer of the ocean would improve the (then poor) ability of coupled atmosphere-ocean GCMs to replicate the reduction in zonal SST gradient observed in the Pliocene. Applying this, they were able to improve modelled simulation of a 'permanent El-Nino' captured in Pliocene records. Fedorov *et al.* (2010) included experiments of simply raising CO_2 levels (compared to pre-industrial) for a Pliocene SST scenario and raising CO_2 levels alongside increasing ocean diffusivity in the top 200m to show that increased CO_2 levels alone does not replicate the SST pattern seen in the Pliocene record (Figure 1.11).

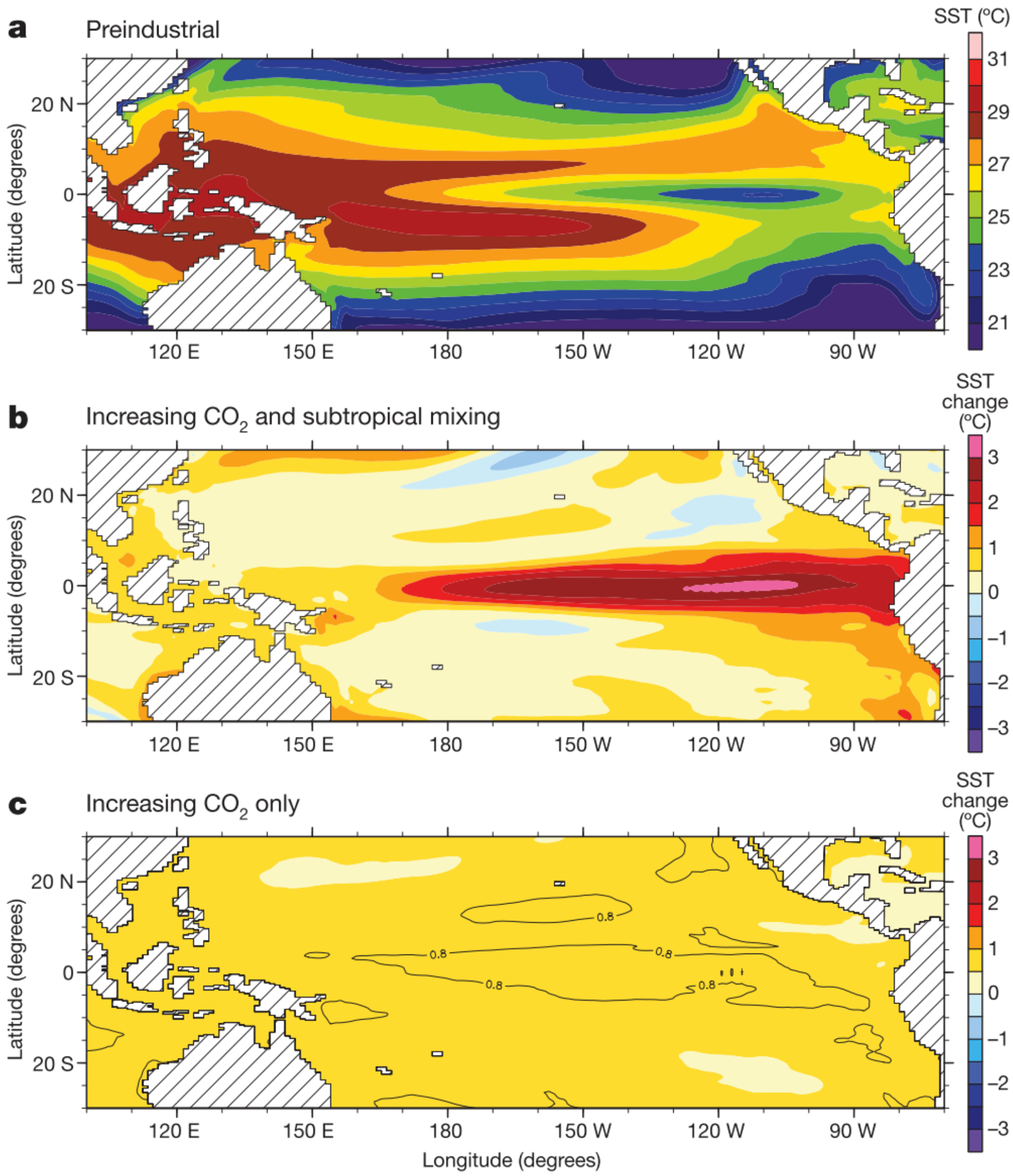

Figure 1.11: SST changes in the tropical Pacific simulated by the CCSM model. (a), SSTs for preindustrial climate conditions; (b), SST changes in response to increasing CO_2 concentration and vertical diffusivity in the upper ocean (top 200m) in the extra-tropical bands (8°- 40°north and south of the Equator) for the Pliocene scenario. (c) SST changes in response to increasing CO_2 concentration alone. Taken from Fedorov *et al.* (2010), Figure 4

Manucharyan and Fedorov (2014) use a fully coupled model (CESM) to explore the effect of thermocline warmth/depth and zonal SST gradient on ENSO. By increasing/decreasing extratropical ocean mixing, they induce changes to vertical and zonal temperature gradients in source regions for the equatorial thermocline - raising SSTs in the Eastern Equatorial Pacific (EEP) and lowering the zonal gradient.

This allows for the examination of these effecs separate from other Pliocene boundary conditions. The zonal gradient is reduced from 6°to 1°C and the amplitude of ENSO decreases only by 30%–40%, with its dominant period remaining close to 3–4 years (with the spectral peak staying above red noise). It is found that as a result of reorganization of the atmospheric Walker circulation in response to changes in the mean surface temperature gradient, the growth/decay rates of the ENSO mode stay nearly constant throughout different climates. These results explain the persistence of ENSO in the past and, in particular, reconcile the seemingly contradictory findings of ENSO occurrence and the small mean east–west temperature gradient during the Pliocene (Manucharyan and Fedorov (2014)).

White and Ravelo (2020) reconstruct changes in ENSO during the early and mid-Pliocene using foraminiferal Mg/Ca ratios and find that El Niño events were weaker between $\sim$5 and 3.5 Ma, compared to the late Holocene. by the mid-Pliocene, El Niño strength was variable on millenial timescales. This trend in ENSO amplitude mirrors the long term strengthening of zonal and vertical temperature gradients, verifying the results of Manucharyan and Fedorov (2014). A possible explanation to the change in El Niño strength between early and mid-Pliocene is given in the shoaling of the thermocline by the mid-Pliocene, so that precession-forced changes in depth affected SSTs in the Eastern Equatorial Pacific Ocean.

Cloud albedo has also been suggested to play a role through altering the amount of incoming solar radiation (Burls and Fedorov (2014), Burls and Fedorov (2017)), in addition to elevated levels of CO_2 and increased vertical mixing, in order to achieve a greatly reduced zonal gradient (and avoid other undocumented changes elsewhere in the Pliocene Earth). Lunt *et al.* (2012) look at different factors contributing to Pliocene warmth and polar amplification, give uncertainty intervals and discuss the varying importance of each factor tested locally; they find that CO_2 is the largest contributor to this, with orographic changes contributing significantly in the Northern hemisphere while changes to ice sheets contribute significantly in the Southern hemisphere.

Fedorov *et al.* (2015) highlight the connection between meridional and zonal gradients in the past 4 Ma, and the need to look outside of the tropics and the tropical ocean-atmosphere interactions to truly understand what determines the SSTs in the eastern Pacific and thus affects ENSO (since the West Pacific tropical warm pool has been shown to have only been about 1°C higher than present). The observational estimates and modelling results from this study suggest that the zonal SST gradient across the equatorial Pacific is tightly linked to the meridional SST gradient via the wind-driven circulation and upper-ocean stratification. Consequently, a reduced meridional SST gradient, as during the Pliocene, implies a weaker zonal SST gradient.

Tierney *et al.* (2019) followed Fedorov *et al.* (2015), recalculating Pacific SSTs during the mPWP based on existing estimates from $U_{37}^{K'}$ alkenone proxies (avoiding discrepancies around Mg/Ca and TEX_{86}, see Brierley *et al.* (2015)), utilising the BAYSPLINE calibration method (Tierney and Tingley (2018)) which improves predictions of SSTs near the saturation point (30°C) for this choice of proxy. Following the reduced space methodology of Gill *et al.* (2016), a spatial field of Pacific SSTs was created by subjecting Pacific SST anomalies from the ERSSTv5 product (Huang *et al.* (2017)) to singular value decomposition, using only locations where there are Pliocene proxy data. The leading principal components (PC) of the resulting field are then used to predict the PCs of the full field using Bayesian linear regression. The Pliocene proxy SST anomalies are then converted to PC space as well, and the regressions are used to predict full field PCs from which the Pliocene field is computed, using eigenvalue expansion. The resulting SSTs were diagnostic of a weaker Walker circulation, with temperature difference across the tropical Pacific which is smaller than today's but only by 1°C – a temperature gradient which does not meet the current threshold for El Nino, defined as a zonal gradient of less than 1.2°C (the average during the strongest historically observed El Nino events). This result supports other studies based on the TEX_{86} paleothermometer which conclude that the Pliocene Pacific zonal gradient was moderately lower than pre-industrial and disagrees with other studies (e.g., Fedorov *et al.* (2015)) which have argued a -3 to -4°C change, using different proxy methods/calibrations. The proxy model analysis presented in this study suggests that drastic changes in clouds or ocean mixing are not needed to explain Pliocene warmth, but does not exclude these factors.

Using Principal Component Analysis (PCA) on a compilation of previously published multiproxy (Mg/Ca, TEX_{86}, $U_{37}^{K'}$ and foraminifer assemblages) Pliocene SST records, Wycech *et al.* (2020) produces a reconstruction of spatial and temporal snapshots of SST anomalies in the equatorial Pacific and a time series of Niño indices from 5 to 1 Ma spanning 5-1 Ma. SSTs were found to be warmer than modern everywhere, with largest anomalies in the eastern equatorial Pacific (up to 4.8°C) and a mean El Niño-like state, characterized by a reduced zonal sea surface temperature differences existed in the Pliocene equatorial Pacific.

McClymont *et al.* (2020) provide a multi-proxy synthesis of SST data during one precession cycle within MIS KM5c (3.215-3.195 Ma) with data from 32 sites (23 using alkenone analysis and 12 using Mg/Ca). By comparing different calibrations (Muller/Prahl/BAYSPLINE) and two different proxy systems ($U^{K'}_{37}$ and Mg/Ca in planktonic foraminifera). several robust, proxy-independent signals were identified: global mean surface temperatures were warmer than pre industrial values by ~2.3°C for the combined proxy data or by 3.2-3.4°C based on alkenones only; meridional gradients are reduced and enhanced warming in the North Atlantic is also seen (2.6°C reduction in meridional SST gradient).

Through dust and export productivity reconstructions, mid-latitude westerly winds were found to be weaker and more poleward during Pliocene warmth, primarily driven by variations in Plio-Pleistocene thermal gradients and ice volume. (Abell *et al.* (2021)).

Overall, the mechanisms behind the reduced zonal and meridional gradients in the Pliocene are still very much up for debate, as is the magnitude of temperature change across the pacific and ENSO strength. As with recent developments into mean sea level in the Pliocene, recent research turns to statistical modelling to help constrain SST change in the Pliocene.

The Pliocene Model Intercomparison Project (PlioMIP)

PlioMIP is a network of paleoclimate modellers and geoscientists who, through the study of the mPWP seek to understand the sensitivity of the climate system to forcings and examine how well models reproduce past climate change (Haywood *et al.* (2021)).

Phase 1 of PlioMIP saw 15 coupled and atmosphere only GCMs run experiments initialised by Pliocene boundary conditions, detailed in Haywood *et al.* (2010).

The large scale results of this combined effort were reported in Haywood *et al.* (2013b). In the tropics, they include a complicated precipitation pattern: rainfall mainly increased over Africa and the Indian subcontinent and decreased over the Indian Ocean, while in the Pacific both increase and decrease in rainfall were noted, depending on the region. Surface air temperature was found to have increased by 1-2°C over the oceans and 1-5°C over land, with a zonal mean of 2°C.

These changes were thought to be a combined response to the weakened meridional SST gradient mainly, with added effect of the weakened zonal SST gradient in the Pacific. There could have also been a general broadening of the Hadley cell, as a result of the weaker meridional SST gradient. The reduced zonal SST gradient in the Pacific seems to have, in addition, generated a remote response over north America, where a dipole pattern of wet/dry conditions was observed. Generally, an enhanced hydrological cycle was observed, with increased rainfall over land.

The similar continental configuration alongside the increase in CO_2 levels and global temperature of the mPWP compared with modern (pre-industrial) climate inspire the use of the Pliocene as a possible analogue for future climate change, when the current climate may reach equilibrium with elevated CO_2 levels. Another point of interest in the mPWP due to these conditions concerns climate sensitivity, which is the equilibrium warming in response to the doubling of CO_2 concentrations in the atmosphere. The mPWP is useful for investigating climate sensitivity because it represents a world in quasi-equillibirium with high CO_2 for a sufficient period that long term feedbacks are close to equilibrium (Haywood *et al.* (2013b)) and so the effects of these feedbacks can be investigated.

Lunt *et al.* (2009) used different global circulation model simulations using Pliocene data from the PRISM project as boundary conditions to try and identify the correct forcing to be included when considering climate sensitivity (which traditionally only includes immediate, short-term radiative feedbacks), focusing on the importance of two often neglected long-term feedbacks for which records for the Pliocene are available - ice sheet and vegetation. Earth System Sensitivity (ESS), which includes forcing directly due to an increase in CO_2 and changes to orography in the Pliocene which affect the distribution of vegetation and ice sheet cover was found to be 30-50% stronger than the widely used Charney sensitivity (Charney *et al.* (1979)) which does not consider the long term climate feedbacks of vegetation and ice sheet. ESS was further explored using the PlioMIP (Pliocene Model Intercomparison Project) ensemble, where it was found to be 1.5 times as strong as Charney sensitivity, on average.

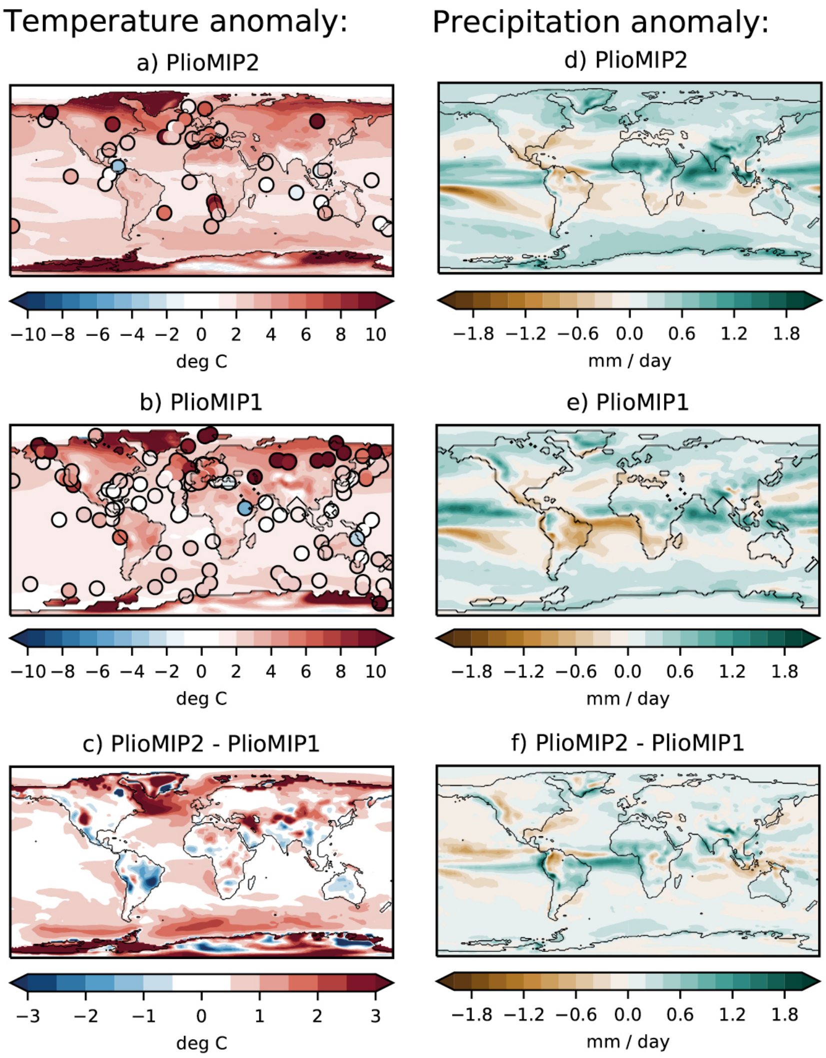

Figure 1.12: (A) PlioMIP2 and (B) PlioMIP1 multi-model annual mean surface air temperature (SAT) differences (over land) and sea surface temperature (SST) differences (over oceans) in °C, compared to the pre-industrial era. (C) Difference between PlioMIP2 and PlioMIP1 multi-modal means (°C). (D) PlioMIP2 and (E) PlioMIP1 multi-model annual mean total precipitation rate (mm/day) differences (compared to the pre-industrial era). (F) Difference between PlioMIP2 and PlioMIP1 multi-modal means (mm/day). Circles represent proxy-derived SST and SAT anomalies in (A) from McClymont *et al.* (2020) and Salzmann *et al.* (2013) respectively. Proxy-derived SST and SAT anomalies in (B) from Dowsett *et al.* (2010) and Salzmann *et al.* (2013) respectively. Taken from Haywood *et al.* (2021), Figure 1.

Data-model comparisons indicate models underestimate polar amplification (Dowsett *et al.* (2013), Salzmann *et al.* (2013)), with poor model-data agreement of sea surface temperatures in the North Atlantic and Pacific Oceans (Dowsett *et al.* (2013), Haywood *et al.* (2016a)). Additionally, although consistency in surface temperature change in the tropics is seen between data and model comparison, there is no consistency in total precipitation rates in the tropics (Haywood *et al.* (2013b)). Upwelling regions are additional primary areas of discord between simulated and estimated paleoclimate conditions due to the need for changes to thermocline depth as well as cloud-surface temperature feedbacks to properly simulate these (Haywood *et al.* (2016b)). Phase 1 of PlioMIP has highlighted temporal uncertainty as an important constraint on more robust methodologies for data–model comparison, although certainty surrounding any proxy data set is limited by analytical, spatial and temporal uncertainty (Haywood *et al.* (2016b) and references therein).

Currently, the PlioMIP project has entered its second phase (PlioMIP2, (Haywood *et al.* (2016b))). Most changes to boundary conditions in PlioMIP2 (which come from the PRISM4 reconstruction, Dowsett *et al.* (2016)) were performed in order to improve data-model comparison issues arising from the first phase of PlioMIP with and include new 1x1°palaeogeography, bathymetry, land-ice surface topography (which includes glacial isostatic response (GIS, Raymo *et al.* (2011))) and new soils and lakes (Pound *et al.* (2014)).

Most importantly, the PlioMIP2 experiment focuses on a very narrow time slice – Marine Isotope Stage KM5c (MIS KM5c, Figure 1.13), moving away from the mid-Piacenzian warm period (approximately 3.3 – 3.0 Ma). MIS KM5c (3.205 Ma) was chosen as a time slice that has near-modern orbital forcing and yet retains many of the characteristics of Pliocene warmth (Haywood *et al.* (2016b)). Minor changes to orbital forcing during MIS KM5c enables a wider target zone of ± 20kyr for data collection because the potential for orbitally forced regional and time-transgressive climate signals is minimised (Haywood *et al.* (2013a))

The solar constant in the PlioMIP2 experiments remains the same as pre-industrial, but with the new focus on the MIS KM5c time slice provides a better estimate of the solar constant during this time in the Pliocene as a narrow time slice includes within it less averaging of orbital cyclicity. CO_2 was set to 400 ppmv in the default model integration (down from 405 ppmv in PlioMIP1), with all other trace gases and aerosols as pre-industrial due to lack of proxy data. As a global data set of vegetation for the KM5c time slice is not available, vegetation from the PRISM3D dataset (Dowsett *et al.* (2010)) or dynamic vegetation is used by participating model groups.

Changes to paleogeography in PlioMIP2 include the Bering Strait and Canadian Arctic Archipelago ocean gateways which are closed compared with PlioMIP1 because of the inclusion of GIS in the topography dataset, effectively shutting off

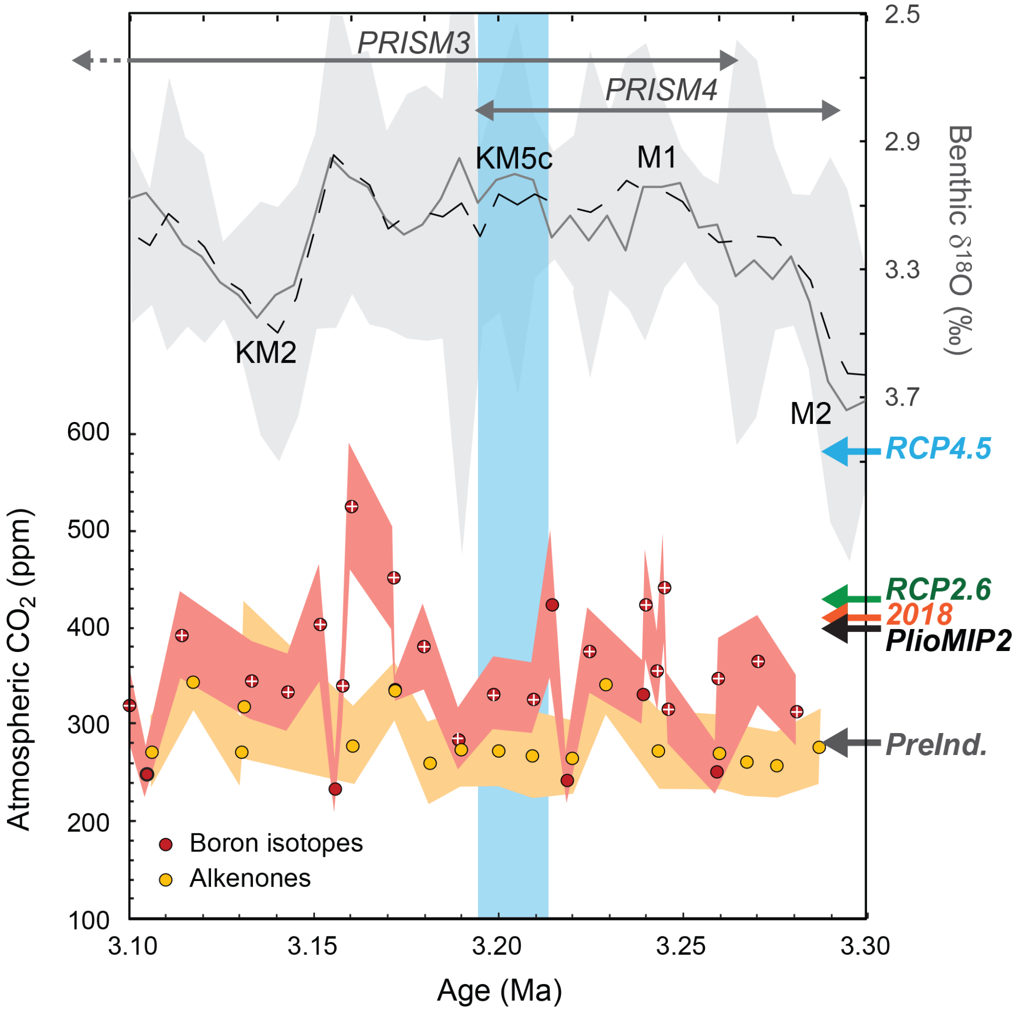

Figure 1.13: The KM5c interglacial during the late Pliocene (3.195 - 3.215 Ma. Upper part of graph: benthic oxygen isotope stack (Following Lisiecki and Raymo (2005)). Selected Marine Isotope Stages (KM2 through to M2) are highlighted. The KM5c interval of focus here is indicated by the shaded blue bar. Previous Pliocene synthesis intervals are also shown: PRISM3 (3.025–3.264 Ma) and PRISM4 (isotope stages KM5c–M2; Dowsett *et al.* (2016)). Lower part of graph: reconstructed atmospheric CO_2 concentrations; shading shows reported upper and lower estimates. Past and projected atmospheric CO_2 concentrations highlighted by arrows: PlioMIP2 simulations are run with CO_2 at 400 ppmv, close to the annual mean in 2018 (NOAA). Pre-industrial values from ice cores and projected representative concentration pathways (RCP) for 2100CE (Collins *et al.* (2013)). taken from McClymont *et al.* (2020), figure 1

the Atlantic connection to the Arctic through the Labrador Sea and Baffin Bay. (Otto-Bliesner *et al.* (2016) conducted sensitivity experiments based on PlioMIP1 and found that the closure of the Canadian Archipelago and Bering Strait ocean gateways strengthened the Atlantic Meridional Overturning Circulation (MOC) by inhibiting transport of less saline waters from the Pacific to the Arctic, leading to the warming of North Atlantic SSTs. The closure of the Bering Strait was done following PRISM4's own paleogeographic calculations, even though there is evidence of it being open during parts of the Pliocene (Dowsett *et al.* (2016). Ice over the Greenland Ice Sheet in PlioMIP2 is limited to high elevations in the East Greenland Mountains using the PRISM4 dataset compared with PRISM3D, a reduction of 25% which equates to a sea level rise of less than $\sim$24m. This relies on estimates from the PLISMIP project. The Indonesian region is elevated compared to present – shoaling in this region would have created a more restricted seaway between the Pacific and Indian oceans with potential effects on circulation and heat exchange with the atmosphere, supporting changes to the Indonesian Throughflow (ITF).

PlioMIP2 is comprised of 16 coupled climate models (up from 8 for phase 1) with atmospheric resolutions ranging from 1 to 3.75°. The minimum integration length is set to 500 years, in accordance with CMIP guidelines for equilibrated coupled model experiments (though all but 2 model groups achieved in excess of 1000 years)(Haywood *et al.* (2020)). The final 100 years of each integration was used for analysis, regridded on to a 1x1°grid, with means and standard deviations calculated for the final 50 years. PlioMIP2 includes two agendas – Pliocene4Future, which focuses on Climate and Earth System sensitivity and Pliocene4Pliocene, which focuses on CO_2 uncertainty and boundary condition contribution to total warmth. A two-tier of system of sensitivity experiments is used in the Pliocene4Pliocene agenda, with Tier 1 using CO_2 values of 350 and 450 ppmv to address uncertainty around CO_2 concentrations in the Pliocene and tier 2 addressing the contribution of individual boundary condition changes (namely CO_2, topography and ice sheets) to the climate response.

Large scale climatic features of the Pliocene resulting from PlioMIP2 were reported in Haywood *et al.* (2020). A robustness measure comprised of two parts: model agreement of 80% on sign of anomaly and a signal-to-noise ratio greater or equal to 1 was used. PlioMIP2 includes several sensitive climate models which were not included in PlioMIP1 which acts as a primary cause for most of the increased range of ensemble results. A correlation between sensitivity and resolution was also found, suggesting that low resolution models may not be able to capture the full extent of climate change.

RECONSTRUCTION	FEATURES		MODEL EXPERIMENTS
PRISM0 Dowsett et al. (1994)	Northern Hemisphere 8x10 SST (Feb, Aug) Topography Vegetation	Time slab Ice (global)	**Goddard Institute for Space Studies (GISS) GCM** Chandler et al. (1994)
PRISM1 Dowsett et al. (1996)	Global 2x2 SST (monthly) Topography Vegetation	Time slab Sea Ice Land Ice	**National Center for Atmospheric Research (NCAR) GENESIS** Sloan et al. (1996)
PRISM2 Dowsett et al. (1999)	Global 2x2 SST (monthly) Topography Vegetation	Time slab Sea Ice Land Ice (revised)	**UK Meteorological Office (UKMO) GCM** Haywood et al. (2000)
PRISM3D Dowsett et al. (2010)	Global 2x2 SST (monthly) Topography (revised) Vegetation (revised) Verification data	Time slab DOT (mean annual, 4x5) SST (MAX - MIN) Sea Ice (revised) Land Ice (revised)	**PlioMIP1** 8 AGCMs and 8 AOGCMs Haywood et al. (2013a)
PRISM4 Dowsett et al. (2016)	Global 1x1 SST (mean annual) Paleogeography (revised) Vegetation Verification data (revised)	Time slice Lakes Soils Sea Ice Land Ice (revised)	**PlioMIP2** 17 AOGCMs/ESMs Haywood et al. (2020)

Figure 1.14: Evolution of PRISM boundary conditions and their integration into climate models and PlioMIP. Taken from Haywood *et al.* (2021), Table 1.

Key features include: Multi model mean surface air temperature of 3.2°C relative to pre-industrial levels (4.3°C over land and 2.8°C over ocean); a 7% increase in precipitation (less than to be expected through the Clausius-Clapeyron relationship); a clear pattern of polar amplification (polewards of 60°S/N) with a value of 2.3 times the global mean warming and a reduction in the Atlantic and Pacific meridional temperature gradients, while tropical zonal gradients remain largely unchanged. The reconstructed SST anomaly for KM5c by McClymont *et al.* (2020) mentioned previously, is warmer than all but three of the PlioMIP2 model outputs.

Earth System Sensitivity (ESS), which includes ice sheet feedback, was found to be 67% greater than Equilibrium climate sensitivity (ECS) – up from 47% in PlioMIP1. A poleward shift in higher latitude precipitation marked by enhanced precipitation around latitudes associated with the westerly wind belt is also seen, consistent with the findings of Xiangyu *et al.* (2015). The Pliocene atmosphere is a warmer one which retains more moisture and has increased evaporation and precipitation rates, leading to an enhanced hydrological cycle. A land amplification factor was found with land warming more than the ocean due to differential lapse rates linked to moisture availability on land (Byrne and O'Gorman (2013)). More specifically, no relationship was found between a model's climate sensitivity and land amplification.

Polar amplification was found to be lower over land than the ocean, with

PlioMIP2 showing no significant differences between SH and NH warming. The lack of differences between hemisphere is likely due to the substantial changes to the albedo feedback in the Southern Hemisphere following the removal of large areas of the Antarctic ice sheet in the mid Pliocene.

In the tropics (20°N – 20°S), surface air temperature in the Pliocene was 2°C higher than pre-industrial levels. The Tropical zonal mean SSTs in the Atlantic and Pacific were found to be 1.5-2.5°C higher in the Pliocene, with the Pacific lacking the greater response at higher latitude. The tropical Atlantic MMM zonal mean SST increases by 1.9°C, with the zonal gradient remaining flat across the tropical Atlantic. In the Tropical Pacific, no evidence of a 'permanent El Nino' is found – supporting proxy derived reconstruction by Tierney *et al.* (2019) which found Pliocene ocean temperatures increased in both the eastern and western tropical Pacific. Tropical Pliocene temperature anomaly is more strongly related to ECS than other latitudes, suggesting that the SST data from the Pliocene have the potential to constrain model estimates of ECS.

Increased atmospheric moisture content within the PlioMIP2 ensemble was found to result in wetter conditions over the deep tropics (the Pacific intertropical convergence zone (ITCZ) and the Maritime Continent) and drier conditions over the subtropics (Han *et al.* (2021)).

1.2.1 Monsoons in the Pliocene

Using a hypothetical early Pliocene SST profile, Brierley *et al.* (2009) find a weakened Hadley circulation; eliminated Walker circulation; widened Intertropical Convergence Zone (ITCZ); and a vastly changed precipitation pattern suggestive of weak air uplift over the ocean (due to weak SST gradients and hence a lack of localized wind convergence, giving greater importance to air uplift due to orographic features and ocean-land temperature contrasts).

The largest precipitation rate differences in PlioMIP2 were found in monsoon regions (Haywood *et al.* (2020)) with enhancement in precipitation over northern Africa, consistent with weakening in Hadley circulation linked to a reduction in pole-to-Equator temperature gradient; an increase in precipitation over the modern Sahara Desert; and an increase in precipitation in the Asian monsoon region.

Li *et al.* (2018) provide insight into the global monsoon using the PlioMIP1 ensemble. They define three variables: (1) Global Land Monsoon Area (GLMA), which is identified by two criteria: summer minus winter mean precipitation rate goes beyond 2mm day-1 and the ratio of local summer precipitation to annual total precipitation exceeds 55% (most precipitation occurs during the summer); (2) Global Land Monsoon Precipitation, which is the sum of total summer precipitation in the GLMA; and (3) Global Land Monsoon Precipitation Intensity (GLMPI), which is measured by the area-weighted summer precipitation in the GLMA.

They find that relative to the pre-industrial period, both the GLMA and GLMP increase in the mPWP by an average of 7.3% and 5.8%, respectively. The increase in GLMP comes mainly from northern Africa, Asia, and northern Australia, roughly consistent with observations and is caused by the increase in monsoon area and not precipitation intensity. Inland water vapor transportation due to the reduced large-scale meridional thermal contrast in the mid to upper troposphere, together with the variation of vertical moisture advection and evaporation, explains most of the global land monsoon changes. On the regional scale, the land monsoon domains increase in northern Africa (15.1%), Asia (10.5%), and northern Australia (48.3%), decrease in North America (-27.1%), and vary slightly in southern Africa (-2.3%) and South America (2.5%).

Zhang *et al.* (2019) uses the National Centre for Atmospheric Research (NCAR)'s Community Earth System Model (CESM) with PRISM4 boundary conditions and breaks down the monsoon response to individual boundary conditions. The boundary conditions tested were: (1) topography, vegetation, and lakes (TVL); (2) ice sheets; and (3) orbital parameters. Their model results indicate that the late Pliocene monsoon domain expands, particularly in North Africa, Asia, and Australia, with changes in TVL contributing most to these expanded monsoon domains. Moreover, the changes in orbital parameters significantly affect these monsoon climates and cause significant fluctuations in the monsoon on the orbital scale.

On a regional level, Changes to TVL contributed most to changes in North Africa, with orbital parameters showing to have a greater effect than CO_2 concentration in this region. In the South Asian monsoon region, a weakened cross equatorial current (the Somali jet) is seen. Due to anomalous ascending motion, the precipitation increases in North Africa, the Arabian Peninsula, the Arabian sea and the north western Indian Peninsula. Anomalous descending motion causes a decrease in precipitation in Central Africa, the Bay of Bengal, and southern East Asia. For South Asia, the simulated wet climate in northern India is consistent with the existing geological evidence, and the simulated weakened South Asian summer monsoon winds are consistent with the existing weathering records. For North Africa, the simulated wet climate with a northward expansion of the monsoon domain agrees with available geological evidence from various sources (Zhang *et al.* (2019) and references therein).

Examining PlioMIP1 data for the East Asian summer monsoon specifically, Sun *et al.* (2015) found an enhanced East Asian Summer monsoon precipitation due to surface warming over East Asia. Increased moisture content seemed to be the cause of enhanced precipitation - both in coupled and atmosphere only simulation.

Through the relation between present day ENSO and Indian summer monsoon rainfall, Wycech *et al.* (2020) estimate Pliocene rainfall in this region to have been $\sim$ 20-40% weaker than modern, using their reduced-dimension reconstruction.

Analysing results from the first PlioMIP project, Zhang *et al.* (2016) found that the WAM strengthened and precipitation increased over North Africa in the mid-Piacenzian, compared to the pre-industrial. The strengthened monsoon activity was caused by increased net energy in the atmospheric column over North Africa. Furthermore, CAM4 simulations indicated that the combined changes of atmospheric CO_2 concentration and SST, as well as the vegetation change, were able to increase the net energy in the atmospheric column over North Africa, which promoted the strengthened WAM and increased the precipitation in the region.

Reviewing the WAM as simulated in the PlioMIP2 ensemble, Berntell *et al.* (2021) find that all models show a rainfall increase over the Sahel reaching up into the Sahara and negative anomalies over the Equatorial Atlantic, indicating an intensification and northward shift as well as expansion of the WAM. A warming over

Sahara, most likely driven by the changes in the atmospheric CO_2 concentration, topography, and related vegetation changes over West Africa, is also seen.

Direct evidence for monsoonal precipitation in the Pliocene is sparse and most of the work done on this subject leans upon direct links to tectonic changes, as discussed in section 1.1.2. A recent effort by the International Ocean Discovery Program in 2015, spanning across several expeditions (expedition numbers 353-356), hopes to shed additional light on the conditions, timing, and causes of the monsoon. Expedition 355 (Clemens *et al.* (2015)), in particular, set about to retrieve sediment cores recording Indian monsoon rainfall in the Bay of Bengal in hopes of obtaining more direct rainfall evidence for the epoch.

The cores have recently been processed and, using the revised magnetobiostratigraphic chronology of Routledge *et al.* (2020), Sarathchandraprasad *et al.* (2021) use a variety of geochemical proxies to explore changes in terrigenous input, clasticity, chemical weathering and productivity variability of the monsoon during 3.3-2.6 Ma collected during expedition 355. They find that a strengthening of the monsoon around 2.95Ma is most probably attributed to the reorganization of the Indonesian Throughflow (ITF). Mg/Ca surface and subsurface temperature reconstructions show that the major phase of reorganization, resulting in a sub-surface cooling of 4°C of the eastern Indian Ocean, occurred during $\sim$ 3.5-2.95Ma. This cooling also influences surface temperatures in the western Indian Ocean through upwelling (Schott *et al.* (2002)). Before 2.95Ma, it was found that monsoon rains follow the global pattern of temperature (glacial-interglacial cycles) in close correspondence. After 2.95Ma, orbital modulation, mainly by eccentricity cycles, was found. Also, after that time, the main trend for the SAM is of gradual weakening.

Wang *et al.* (2019) explore the history of C_4 grasses and quantitatively reconstruct the Asian monsoon climate since the late Miocene, based on modern environmental niches of grasses in China. C_4 grasses have been a dominant grassland component since $\sim$11 Ma, with a subsequent marked decrease in warm and humid adapted C_4 grasses and an increase in cool and dry adapted C_3 grasses at $\sim$4 Ma. The phytolith-based quantitative reconstruction of mean annual precipitation marked a decrease from 800-1673 mm to 443-900 mm, indicating a reduction in Asian monsoon rainfall in the Pliocene. These records conflict with the hypothesis that the growth of the Tibetan Plateau strengthened the Asian monsoon rainfall.

While the global monsoon strengthened in the Pliocene with increased net energy in the atmosphere, the response of each individual monsoon system is complex. The mechanisms behind those responses are still being investigated, with many factors possibly contributing to the overall response.

1.3 Research Questions and Thesis Outline

This thesis aims to answer the following overarching question:

Is increased resolution beneficial in simulating Pliocene-like conditions?

The subject of increase model resolution alone, without adding complexity or updated boundary conditions, has not been explored for the Pliocene. This thesis will investigate the effects of increased resolution on the early Pliocene climate using a step change approach, separating the effects of dynamical and topographic resolution. For the four-fold increase in resolution trialled here (detailed in chapter 2), higher resolution is expected to better resolve physical processes affecting the tropical region such as tropical waves, the African Easterly Jet (AEJ), and African Easterly Waves (AEWs). Topographically, the increase in resolution should induce elevation changes of a few hundred meters in very steep environments - such as the Himalayas and Tibetan Plateau mentioned in subsection 1.1.2.

Additionally, section 1.2 dealt with the many paleoproxies and different calibration/statistical methods used to obtain data about the Pliocene; conflicting reconstructions; the increased efforts to narrow the Pliocene time slab to a time slice and introducing increased complexity and more boundary conditions in the Pliocene model ensembles. All of these make it difficult to attribute a difference seen in a Pliocene simulation to a particular boundary condition/model attribute (e.g., Berntell *et al.* (2021)) .

Here, we induce just one boundary condition change - the prescribed SST field - to explore the effect of increased resolution on a Pliocene-like atmosphere. The SST field chosen (Brierley *et al.* (2009)) is particularly zonal in nature - isolating the role of SSTs and specifically meridional gradients of SSTs on the Pliocene climate, which are suggested to have a profound impact on features of the Pliocene by Haywood *et al.* (2013b), as mentioned earlier.

The focus here is on the tropical region, to steer clear of extreme temperature changes and ice/albedo changes near the poles as the goal is to make as little model changes as possible. In addition, most of the geographic changes mentioned in subsection 1.1.2 occurred in the tropics and the changes in the hydrological cycle in this region is of paramount importance in light of future climate change (drought/flooding).

This question breaks down into several smaller questions:

- **Is increased resolution beneficial for the present day?**

Each research chapter starts with a verification of model output versus observations for the present day, to have confidence in the use of higher resolution with Pliocene SSTs

- **What part of increased resolution affects the simulated climate more?**
  We break down the effects of increased resolution into two separate components using a step change approach - dynamical and topographical resolution. Since Pliocene topography is an important aspect of reconstructing the Pliocene, it is interesting to see if the scale of elevation change purely due to increase resolution has a dramatic effect on the simulated climate, or if it is the dynamical resolution increase that dominates, or both. The work by Brierley *et al.* (2009) suggests orographic features might be of higher importance in the Pliocene due to weaker air uplift over the ocean and the need of orography in triggering tropical convection - examining the role of topography and the effects of changes to the representation of topography will further clarify if it has an enhanced role in Pliocene precipitation.

- **Do the effects of increased resolution differ for the present day and the Pliocene?**
  Most model results report on difference between Pliocene and pre industrial climate; does increased resolution have the same effect on both or does the difference field between Pliocene and present also change with increased resolution?

- **How do resolution effects differ between different monsoon regions?**
  Since the step change approach utilised in this thesis differentiates between dynamic and topographic resolutions, two monsoon systems have been chosen to best match these characteristics: the South Asian monsoon has topographic elements confining the monsoon area and being an important part of its mechanisms (Tibet, Himalayas, Western Ghats, East African mountains) while the west African monsoon has many different processes on varying dynamical scales which together interact to produce the monsoon system.

Details of model description, experimental setup and methodology are outlined in chapter 2. A detailed analysis of the South Asian monsoon in the Pliocene and how increased resolution affects the monsoon is presented in chapter 3 and chapter 4, while chapter 5 deals with the effects of resolution on the West African monsoon. Finally, chapter 6 discusses the overall results of the thesis, highlighting new findings and addressing the research questions presented here.

Appendix A presents a wavenumber-frequency analysis of Convectively Coupled Equatorial Waves (CCEW) in the IGCM4 as an additional way of assessing the model's performance in the tropics while Appendix B includes supplementary figures for chapter 3.

Chapter 2

Experimental Design

2.1 Model Description

The climate model used for the purpose of this research is the Intermediate Global Circulation Model 4 (IGCM4), described in Joshi *et al.* (2015) and Forster *et al.* (2000). Part of the wider IGCM family of models based at the University of Reading and stemming from the spectral model of Hoskins and Simmons (1975), the IGCM4 is currently an atmosphere only model, employing a 50m slab ocean prescribed with a monthly mean seasonal cycle of sea surface temperatures. It includes simple parametrisations of surface processes and stratiform precipitation and schemes for dry and moist convection as well as radiation and clouds.

Following Hoskins and Simmons (1975), the IGCM4 solves the non dimensionalised horizontal equations of motion in their vorticity and divergence form, for an inviscid, adiabatic, hydrostatic perfect gas using spherical coordinates on a rotating planet. These are:
Horizontal momentum equations:

$$\frac{\partial \zeta}{\partial t} = \frac{1}{1-\mu^2}\frac{\partial}{\partial \lambda}F_V - \frac{\partial}{\partial \mu}F_U \tag{2.1.1}$$

$$\frac{\partial D}{\partial t} = \frac{1}{1-\mu^2}\frac{\partial}{\partial \lambda}F_U + \frac{\partial}{\partial \mu}F_V - \nabla^2\left(\frac{U^2+V^2}{2(1-\mu^2)} + \phi + \overline{T}\ln p_*\right) \tag{2.1.2}$$

Hydrostatic approximation:

$$\frac{\partial \phi}{\partial \ln \sigma} = -T \tag{2.1.3}$$

And the continuity equation:

$$\frac{\partial \ln p_*}{\partial t} = -V \cdot \nabla \ln p_* - D - \frac{\partial \dot{\sigma}}{\partial \sigma} \tag{2.1.4}$$

Where $F_U = V\zeta - \dot{\sigma}\frac{\partial U}{\partial \sigma} - T'\frac{\partial \ln p_*}{\partial \lambda}$, $F_V = -U\zeta - \dot{\sigma}\frac{\partial V}{\partial \sigma} - T'\left(1-\mu^2\right)\frac{\partial \ln p_*}{\partial \mu}$

ζ is the absolute vorticity, D is the divergence. temperature is represented as a deviation from mean profile, $T = \overline{T}(\sigma) + T'$, P_* the surface pressure and ϕ the geopotential. λ is the longitude, $\mu = \sin\theta$ where θ is the latitude. The model uses σ levels as a vertical coordinate, where $\sigma = \frac{pressure}{p_*}$. V and U are meridional and zonal velocities multiplied by $\cos\theta$

The equations are solved using the spectral method in the horizontal and finite differences method in the vertical. The variables for vorticity, divergence, deviation of temperature and geopotential are represented by a triangularly truncated series of spherical harmonics:

$$X = \sum X_n^m P_n^m(\mu) e^{im\lambda} \tag{2.1.5}$$

and are calculated at each σ layer.

The model uses the semi-implicit time scheme and employs a split time step approach which produces 'interim' fields of adiabatic processes which are used, through a semi-implicit adiabatic time step to determine the diabatic tendencies which are then added separately.

Sensible and latent heat transfer between the surface and atmosphere are calculated using differences in static energy and humidity, using potential temperature differences to describe an effective wind speed which includes the effect of atmospheric stability. A two level soil model, consisting of an upper layer of 6cm and a lower layer of 2.3m, is used to obtain the surface land temperature. Diffusive heat transfer exists between the two soil layers and the land surface temperature is taken as the temperature of the upper soil level. Soil moisture is represented by a simple bucket model. Available moisture at the surface is a function of bucket capacity, this being 0% below 1/3 capacity and linearly increasing to 100% at 2/3 capacity. The total bucket capacity has an equivalent depth of 0.5m

The convection scheme of the model includes dry and moist convection. Dry convection is a "hard adjustment" which occurs in a single time step, while moist convection (a simplified version of that described by Betts (1986)) is a "soft adjustment" which occurs over a period of time rather than a single time step. The entire atmospheric column is checked for dry unstable layers which are adjusted in a single time step to a well-mixed, neutral state. Then, based on cloud top height (under or over 700mb, 780mb in Betts (1986)), moist convection is diagnosed between shallow and deep convection. Reference profiles are constructed separately for precipitating and non-precipitating convection.

The reference thermodynamic profiles are used against the thermodynamic structure of temperature and atmospheric moisture in the convective adjustment procedure as follows:

$$\frac{\partial \overline{T}}{\partial t} = \frac{T_R - \overline{T}}{\tau} \tag{2.1.6}$$

$$\frac{\partial \overline{q}}{\partial t} = \frac{q_R - \overline{q}}{\tau} \tag{2.1.7}$$

Where $\overline{T}$ and $\overline{q}$ are the convective temperature and moisture profiles, respectively and T_R and q_R are the calculated reference profiles for temperature and moisture, respectively. τ, the relaxation time-scale for adjustment (rainout timescale), is pre-determined in the model for deep convection (and is set to 3 hours in the default model configuration) while for shallow convection it is determined interactively and relies on surface heat fluxes, with a maximum time scale of 6 hours in the default model configuration.

for non-precipitating convection, reference profile satisfies two constraints: that the condensation and precipitation rates are zero within the cloud - it simply redistributes heat and moisture within the vertical. For precipitating convection, the reference profile satisfies an enthalpy preservation constraint:

$$\int_{\rho_B}^{\rho_T} \left(H_R - \overline{H}\right) dp = 0 \tag{2.1.8}$$

Where $H = C_p T + Lq$ and ρB, ρT are a cloud base and top level, respectively.

after which a precipitation rate is calculated:

$$PR = \int_{\rho_B}^{\rho_T} \left(\frac{q_R - \overline{q}}{\tau}\right) \frac{dp}{g} = -\frac{c_p}{L} \int_{\rho_B}^{\rho_T} \left(\frac{T_R - \overline{T}}{\tau}\right) \frac{dp}{g} \tag{2.1.9}$$

No liquid water is stored in the scheme and so all excess moisture is rained out at the precipitation rate calculated.

The cloud base fraction for deep convective cloud is 4 times the fraction at all other levels, which is consistent with observed convective cloud profiles (Slingo (1987)), while for shallow convection the cloud fraction remains constant through all cloud levels, at 0.3. In the IGCM, if $PR < 0.15\frac{mm}{day}$, the cloud fraction is set to 0. if $PR > 0.15\frac{mm}{day}$, cloud fraction is directly calculated from the precipitation rate, following a variation of Slingo (1987), Table 1 and Equation 1:

$$cfraction = 0.25 * (0.245 + 0.125 * LOG(PR)) \tag{2.1.10}$$

Deep layers drier in depth than (approximately) the relative humidity of the convective reference state fail to generate precipitation in the deep scheme and shallow convective adjustment is performed instead if the cloud-base is at low-levels.

The IGCM4 uses a modified Morcrette radiation scheme (Zhong and Haigh (1995)). The scheme has a representation of O_3 absorption of ultra-violet radiation (0.12-0.25 μM), two radiation bands in the visible part of the spectrum and five bands in the infra-red part. H_2O is advected self-consistently in the model while a zonally averaged climatology of O_3 is prescribed. Aerosols are not in the standard IGCM4 - to compensate for this, their effect on surface temperatures has been parameterised by raising the albedo of land and ocean by 0.05 (Joshi *et al.* (2015)). Cloud cover in the model is calculated by employing a simplified version of the diagnostic cloud scheme of Slingo (1987), which has been tuned to better match observed profiles of convective clouds. Marine stratocumulus clouds in the model are parameterised by a version of the Kawai and Inoue (2006) parameterisation scheme.

The resolution of a spectral model is determined by the maximum zonal wavenumber *k*, which is responsible for the number of Gaussian longitudes in grid space. The resolution is increased by choosing a larger value for *k*, which provides a smaller wavelength in the spherical harmonic series which represents the prognostic variables in the model. Spectral models provide a more accurate approximation to derivatives, as the error is smaller than in grid point models. This improvement in accuracy comes with a cost; computational needs of a spectral model are greater than that of its grid point counterpart - it is therefore more expensive and takes longer to run. Another limitation arises with regards to boundary conditions - since spherical harmonics are periodic functions, a non-global model poses difficult challenges; not all calculations can be done in spectral space - some may only be calculated while in real space, namely local processes and their parametrizations.

The IGCM 4 is a valuable tool for understanding main processes of key scientific questions in climate science; it's intermediate complexity and global extent mean it is physically advanced enough to simulate a wide range of climate processes yet its simplicity is convenient for idealised experiments as it provides fast, cost-effective run-time compared with state of the art models (van der Wiel *et al.* (2016), Joshi and Brierley (2013)).

2.2 Experimental Setup

This research made use of 6 total model configurations: two scenarios under three different spatial resolutions. All six integrations were run for 20 model years with the first year discarded as spin up, leaving 19 model years for analysis. Each year consists of 360 days (to avoid leap years and similar complications), where the temporal resolution for data output was set to once daily. The two scenarios include:

Present Day: A run continuously forced by monthly present day global Sea Surface Temperature (SST) field. (Joshi *et al.* (2015), Forster *et al.* (2000)) And present day topography (Forster *et al.* (2000)).

Pliocene: A run continuously forced by a Pliocene SST field (Brierley *et al.* (2009)) and present day topography.

Pliocene Meridional: An idealised, low resolution only run continuously forced by a modified Pliocene SST field (Brierley *et al.* (2009)), consisting of a meridional only SST change in the Indian Ocean and present day topography. Further details can be found in chapter 3.

A summary of all model integrations can be found in Table 2.1 below.

Resolution / Scenario	T42	Hybrid	T170
Present Day	Pres42	Pres170H	Pres170
Pliocene	Plio42	Plio170H	Plio170
Pliocene Meridional	PlioMSST		

Table 2.1: Different model configurations and their shorthand names

Two different spatial resolutions were used, at wavenumber 42 and 170 triangular truncation. Both of these consist of 20 vertical layers above the surface (up to 50 hPa) based on σ coordinates (relative to surface pressure), and do not represent the stratosphere very well. T42 resolution provides a horizontal grid of 128x64 (approximately 2.7° in the tropics) while T170 provides a horizontal grid four times finer - 512x256 (approximately 0.75° in the tropics). A third, 'hybrid' resolution, using T170 spatial resolution with the spectral topography field smoothed down to T42 resolution, using T42 spectral coefficients, was also deployed in an attempt to attribute changes between low and high resolution to either dynamical or topographic changes - the dynamical core operates at the same resolution as the T170 configuration, yet with T42 equivalent topography. Differences between this and a full, high resolution dynamics and topography T170 run would show the effects of high resolution topography, while differences between hybrid and a T42 run would instead highlight resolution effects in the dynamical sense alone. Figure 2.1 shows present day topography under each different resolution case.

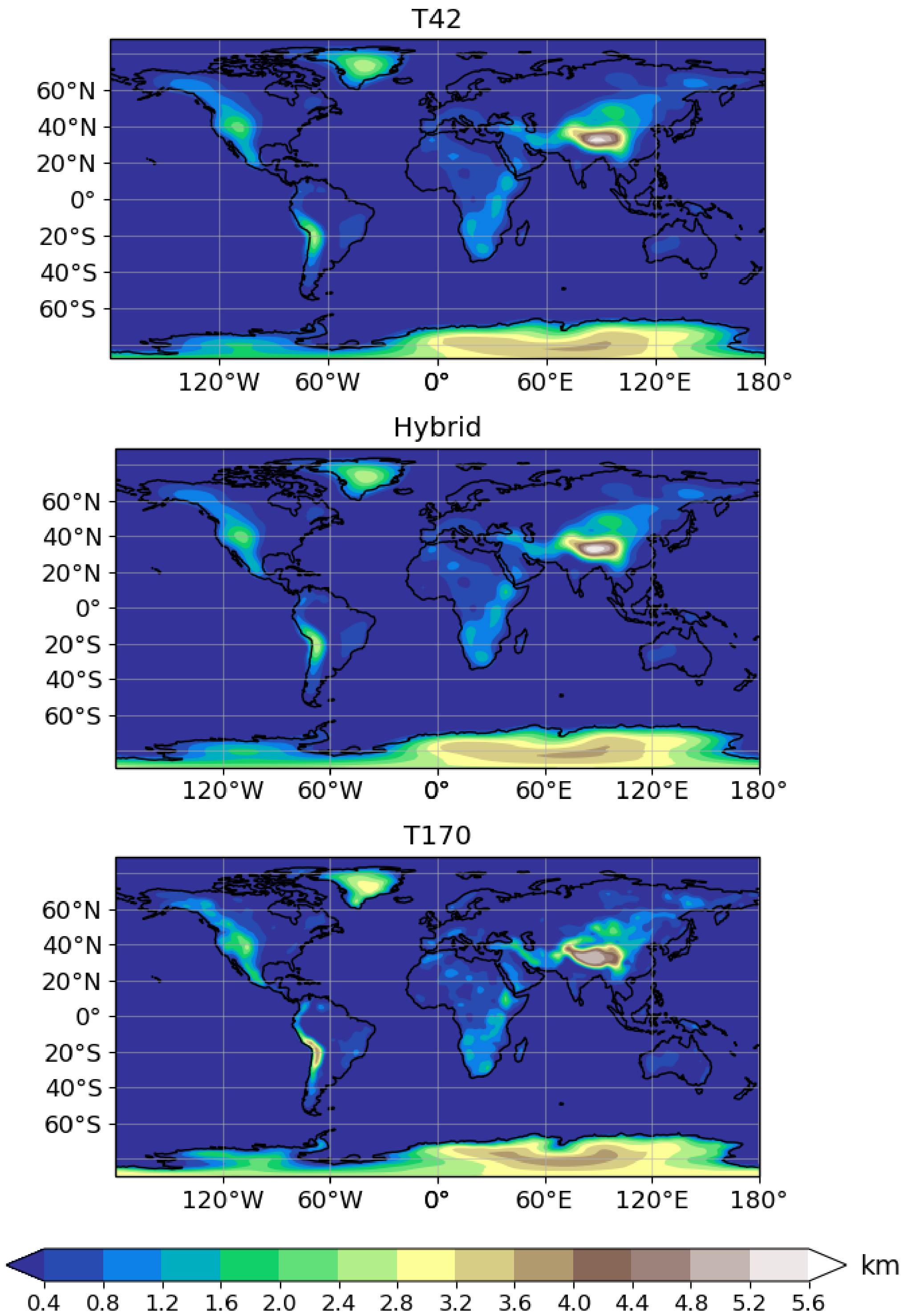

Figure 2.1: IGCM4 topography field for low resolution (top); Hybrid (middle); and high (bottom). The hybrid topography field is the same as low resolution but displayed on a horizontal grid with four times the resolution.

2.2.1 Sea Surface Temperature Data

The Pliocene SST field of choice used as the only boundary condition change between present day and Pliocene model integration is the reconstruction produced by Brierley *et al.* (2009).

The motivation behind the Brierley SST is to simulate the hypothesised expansion of the tropical warm pool. To achieve this, data from several studies in the Pacific, Indian and Atlantic Ocean (Figure 2.4) were utilised and a generic exponential equation was used with parameters chosen to fit these data:

$$T(\theta) = (T_{max} - T_{min})exp\left[\frac{1}{a}\left(\frac{|\theta|}{45}\right)^{N}\right] + T_{min} \tag{2.2.1}$$

where θ is the latitude in degrees, T_{min} is the temperature of freezing for sea water (set to 1.8°C). T_{max} is the maximum temperature in the tropics (set to 28.5°C). N is set to 4.5; while constant a is determined by a least-squares fit to the temperature estimates in the study. The value of a differs in the Atlantic from the rest of globe to allow for warmer temperatures in the North Atlantic, and a cold temperature anomaly is added to simulate the effect of the Peru Current along the coast of South America (see Brierley *et al.* (2009) for additional information).

This was applied to the whole globe, tapering off at 45°S/N. To replicate the annual cycle, the SST profile is shifted along the meridian seasonally to match the progression of the modern annual cycle. The SST fields used to force each model run are presented in Figure 2.2 and Figure 2.3.

The Brierley reconstruction uses alkenone and Mg/Ca paleoproxies. As mentioned in section 1.2, There are large uncertainties regarding the use of Mg/Ca as a paleothermometer. Although there is uncertainty and ongoing debates regarding the sampling methods employed to obtain Pliocene SST data in general and specifically the data used in this reconstruction, the main purpose in the creation of this hypothetical SST profile - exploring substantially suppressed colder SST temperatures in upwelling regions (the Somali current, especially for the purpose of this research), leading to a zonal distribution of temperatures and the expansion of the tropical warm pool, is well served. As commonly used in other Pliocene studies, there is only one data point in the entire Indian Ocean - supporting the use of this hypothetical SST reconstruction to explore the effects of fundamental, large scale changes in the Earth's SST gradient.

This reconstruction is quite different to the more widely used PRISM reconstruction (Figure 2.5) - both reconstructions include warmer upwelling regions

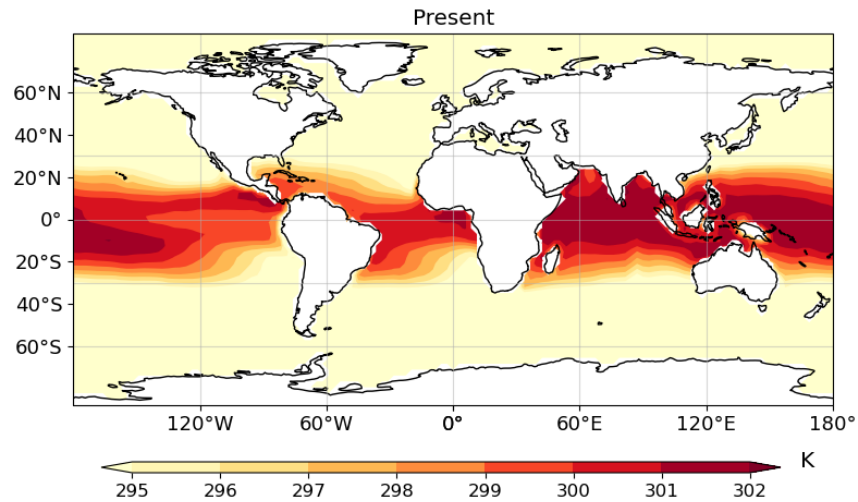

(a)

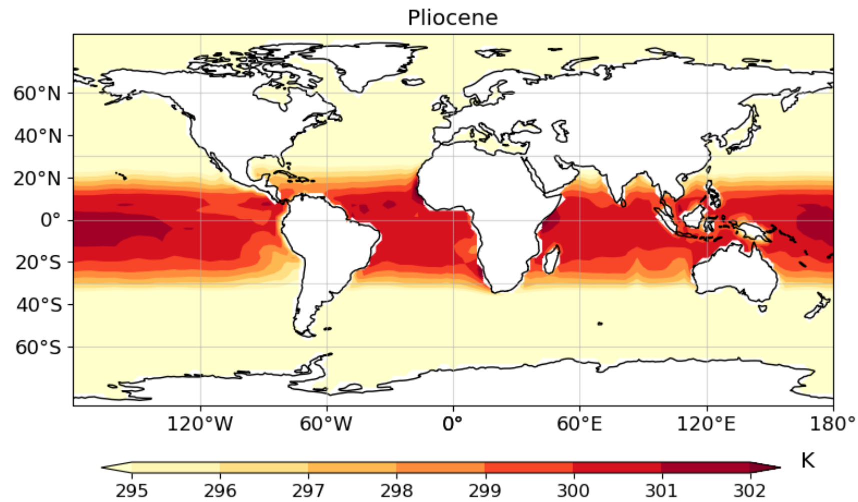

(b)

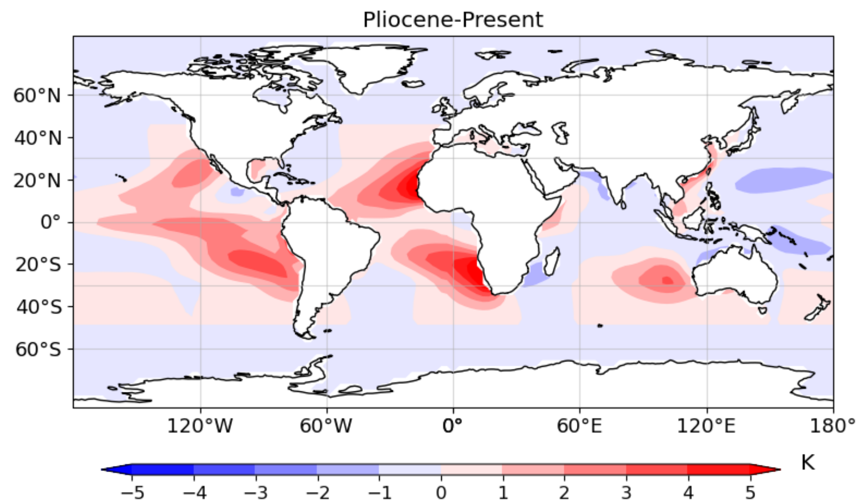

(c)

Figure 2.2: Global SST fields used in each model simulation for the month of February. Top: Present, middle: Pliocene, bottom: the difference between Pliocene and Present

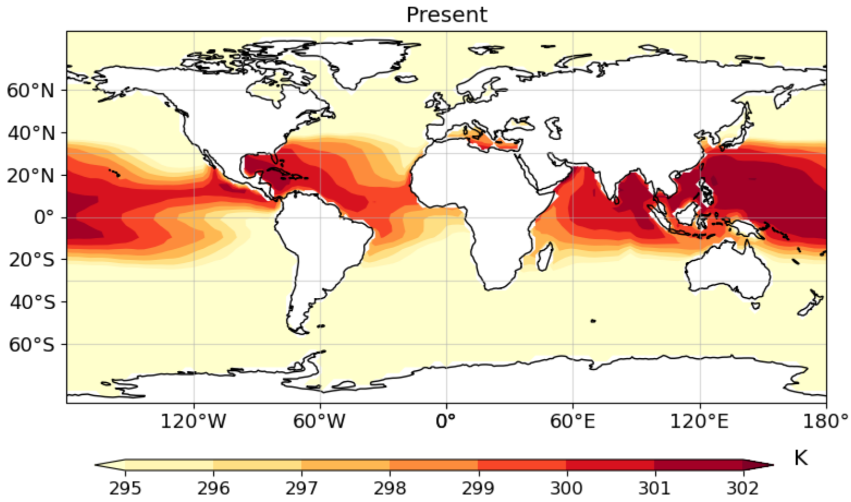

(a)

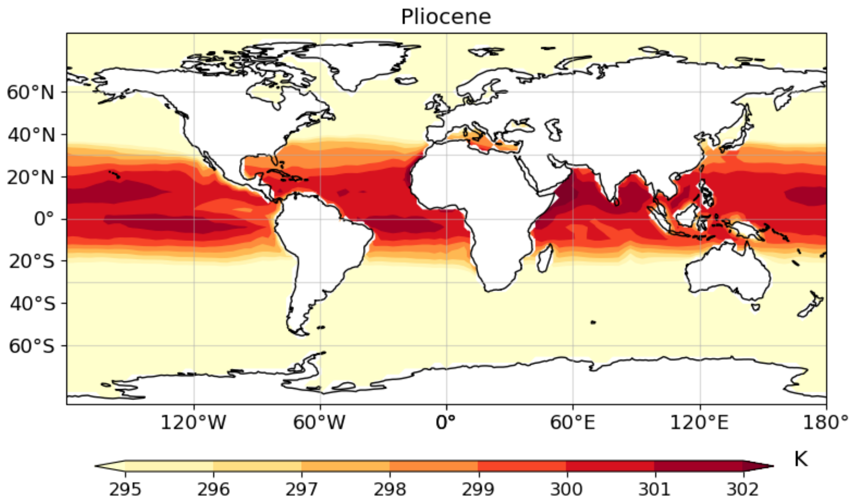

(b)

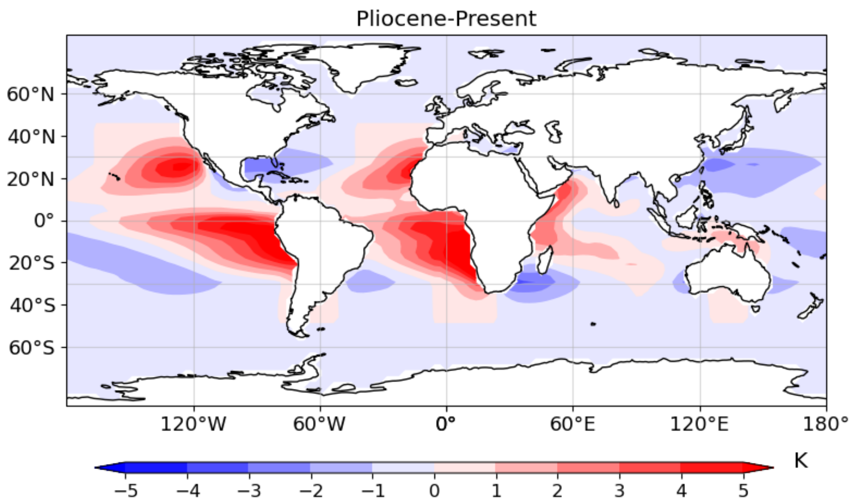

(c)

Figure 2.3: Global SST fields used in each model simulation for the month of August. Top: Present, middle: Pliocene, bottom: the difference between Pliocene and Present

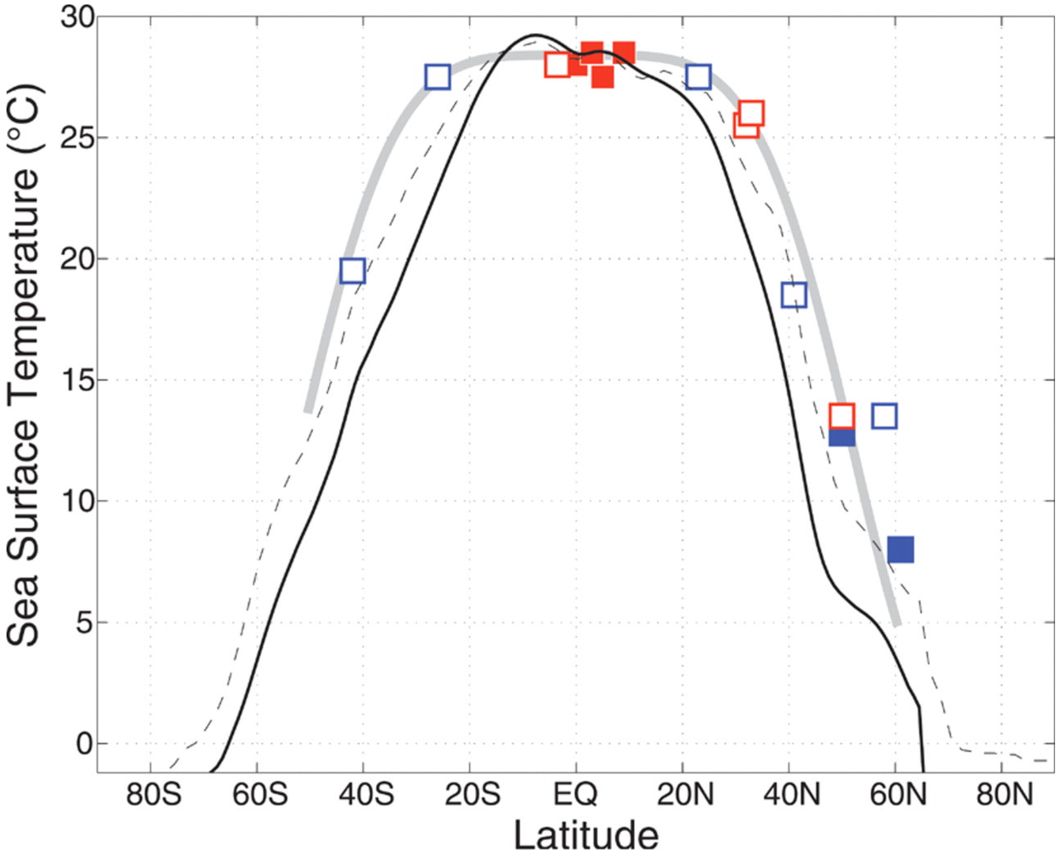

Figure 2.4: Estimated distribution of SST with latitude in the middle of the Pacific (roughly along the dateline) at ∼4 Ma. This temperature reconstruction uses data from the Pacific and Indian oceans (red boxes) and adjusted data from the Atlantic (blue boxes). Open boxes indicate alkenone-based data; solid boxes indicate Mg/Ca-based data. Thin solid line: SST from the dateline for the modern climate. Dashed line: estimates of the mid-Pliocene temperatures (3 Ma) along the dateline from the PRISM3 project (Dowsett and Robinson (2009)). Thick gray line: a portion of the hypothetical SST profile used as a boundary condition for numerical simulations. The original data and the temperature adjustments are given in Brierley *et al.* (2009), table S1. Taken from Brierley *et al.* (2009), Figure 2

(mainly to the west of Africa) compared to modern conditions but the Brierley reconstruction displays even warmer sea surface temperatures in upwelling regions than the PRISM equivalent, owing to reduced temperature gradients in the early Pliocene. In the Indian Ocean, the Brierley reconstruction shows lower than modern SSTs through the months while PRISM only does so for a period of three months. Additionally, in the western Indian Ocean, the Somali upwelling region is once again warmer in the Brierley reconstruction in the summer months (June-July) while SSTs in this region under the PRISM reconstructions do not see much change compared with modern.

The Brierley reconstruction can be seen as a more idealised, approximate approach to assess the importance of large scale changes to the Earth's SST field. It represents the Earth in a different climate regime, around a million years before the PRISM dataset (4Mya versus 3Mya); prior to the formation of the Greenland ice sheet and the recorded impact of changes to the Indonesian through flow (ITF) caused by the northward migration of Australia, which changed the ITF's source water masses - from delivering warm water into the Indian Ocean to transporting cold, fresh waters instead - with effects on East African rainfall and the South Asian monsoon through changes to the Somali jet (discussed in chapter 1).

The early Pliocene data gives hints of an alternate stable state of the tropical oceans - one where upwelling regions are much warmer than in the mid Pliocene (Dekens *et al.* (2007)) or the present day, leading to a very zonal distribution of temperature and highlighting the importance of the meridional temperature gradient.

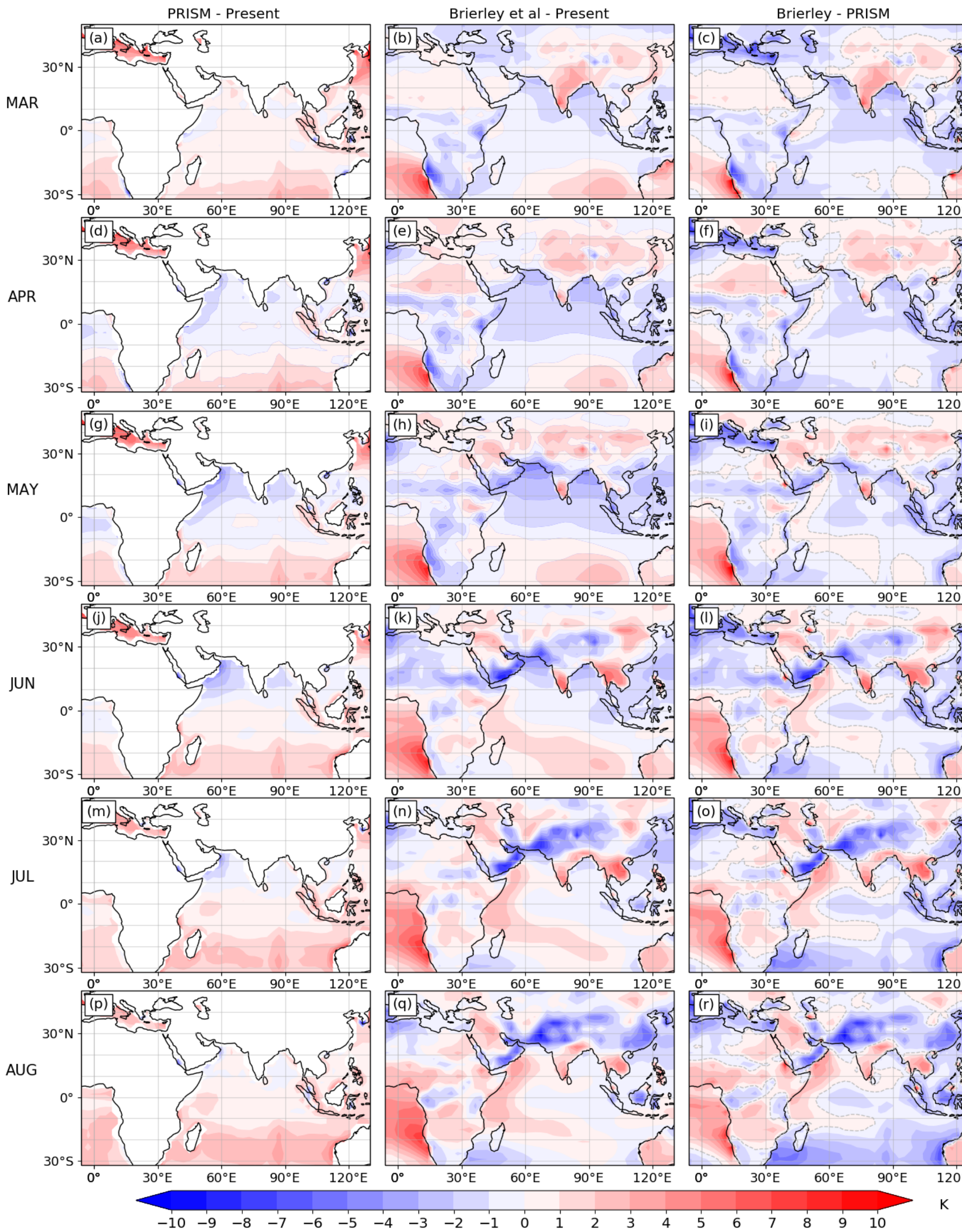

Figure 2.5: Sea surface temperatures in the Pliocene, March to August (rows). Differences between Present and PRISM reconstruction (left), Present and the Brierley reconstruction (middle) and between the Brierley and PRISM reconstructions themselves (right).

2.2.2 Convection Parameter Changes

Several parameters relating to convection in the model have been changed from the default T42 resolution set-up. This was done to allow the same set of parameters to be used in both the T42 and T170 (and hybrid) model integrations, which minimises differences relating to model set-up, improves comparability between the two different resolutions and improves the ability to attribute differences between model results to either dynamical resolution or that of topography. The parameters chosen provide more realistic rainfall under high resolution, which suffered from over representation of large-scale rainfall coupled with under representation of convective rainfall under default T42 parameters.

Changes were made to the relaxation time-scale of deep convection adjustment (90 minutes, down from 180); the time scale in which shallow convection is allowed to rain out (increased from 6 hours to 12) and the critical relative humidity above which the shallow convection scheme is allowed to rain out (increased from 80% to 90%). Some cloud tuning was also performed to slightly reduce the optical thickness of convective clouds by reducing the cloud water concentration from 5.0E-5 down to 10.0E-5. For all T170 integrations, the only standalone change which did not take place for the T42 equivalent was to the diffusion timescale on the shortest resolved scale which was set to 0.166 days (0.02 for T42 integrations). For more details about the convection scheme used, see Forster *et al.* (2000), appendix 1.3 and Betts (1986).

2.3 Methodology

Two study areas were selected - the South Asian monsoon (SAM) and the West African monsoon (WAM). The SAM was chosen as it represents an area of significant topographic features (the Tibetan Plateau, see section 1.1.2), allowing the exploration of topographic resolution and its effects on the local climate. The WAM on the other hand was selected for its dependence on scale-interaction, as it consists of processes of different spatial scales (Hall and Peyrille (2006)), as a test of the importance of dynamical resolution. Both areas border ocean regions with drastic sea surface temperature differences in the Pliocene, which is the only boundary condition change in the Pliocene model integrations. It is no coincidence that these two areas are both in the tropical region; most of the topographic changes that occurred in the Pliocene were in the Tropics (subsection 1.1.2) and thus this area is of particular significance to the Pliocene. Additionally, focusing on the tropics rather than the extra-tropics helps increase confidence in model results as it is free of ice and large areas of low, flat coastlines; avoiding inaccuracies relating to decreased ice cover and sea level rise in the Pliocene.

For each study area, an analysis into the basic state differences between present day and Pliocene is performed. Then, through a step-change approach, differences between the low (T42) resolution and the hybrid (T170 dynamical resolution with T42 equivalent topography) are examined for each scenario (present day and Pliocene) and the differences between the two scenarios, showing the effect of dynamical resolution increase. Finally, differences between hybrid and high (full T170) resolution are examined for each scenario and their differences, showing the effect of topographic resolution on the monsoon system.

Chapter 3

South Asian Monsoon: In the Pliocene

3.1 Introduction

This chapter assesses only the low resolution (T42, see chapter 2) model configuration in the South Asian monsoon (SAM) region. An overview of the SAM is provided, followed by information about available Pliocene evidence and modelling efforts in this region. Then, the representation of the present day SAM precipitation in the IGCM under low resolution is addressed, followed by a month-by-month analysis of the SAM system in the present day versus Pliocene, as seen in the IGCM.

3.1.1 Overview

The South Asian monsoon (SAM) is an integral part of agriculture, industry and basic human needs for over one billion people who rely on the monsoon's intense rainfall, which accounts for 80% of annual rainfall in South Asia (Turner and Annamalai (2012). Changes to the monsoon can be crucial to many aspects of life in the region, from destructive floods to life-threatening heat waves.

The SAM system is driven by moisture supply through the Somali jet which flows on the western boundary of the Indian Ocean. The Somali jet is a result of the pressure differences between the Mascarene high, off the coast of Madagascar in the southern Indian Ocean, and Indian heat low in northern India, creating a negative south-north meridional pressure gradient which the jet flows against. South of the Equator, the Somali jet flows in a north-westerly direction. Upon crossing the Equator, the jet flows in a north-easterly direction.

The Indian heat low is formed as a result of increased solar insolation over the

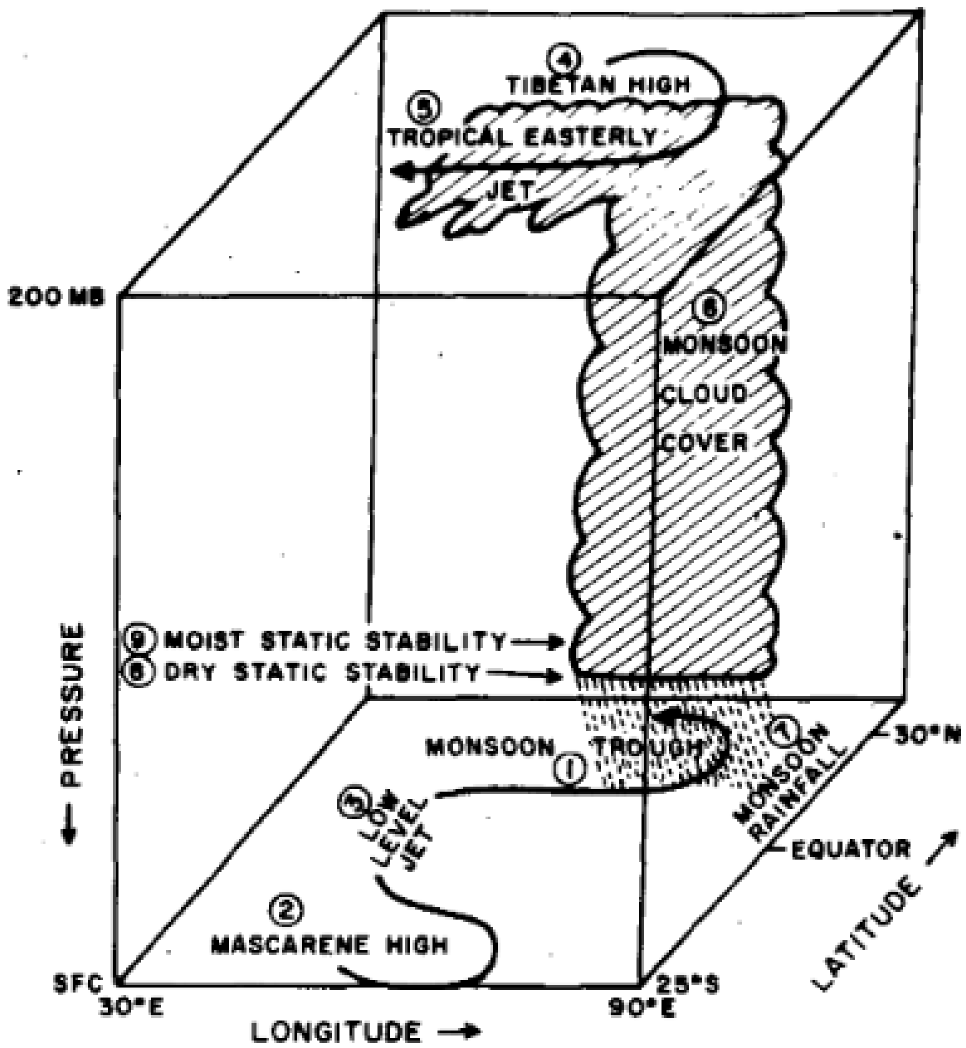

Figure 3.1: .
Vertical schematic of the monsoon system. Taken from Krishnamurti and Bhalme (1976)

Tibetan Plateau during the summer months, causing increased heating over land areas compared with the ocean due to differences in heat capacity between land and ocean (Li and Yanai (1996)). Assisted by orographic blocking caused due to the existence of the East African Highlands, the Somali jet is a strong, cross equatorial jet which peak at about 850hPa and lasts from June to September. It has a strong zonal component upon reaching the Indian sub-continent (Ruchith *et al.* (2014)).

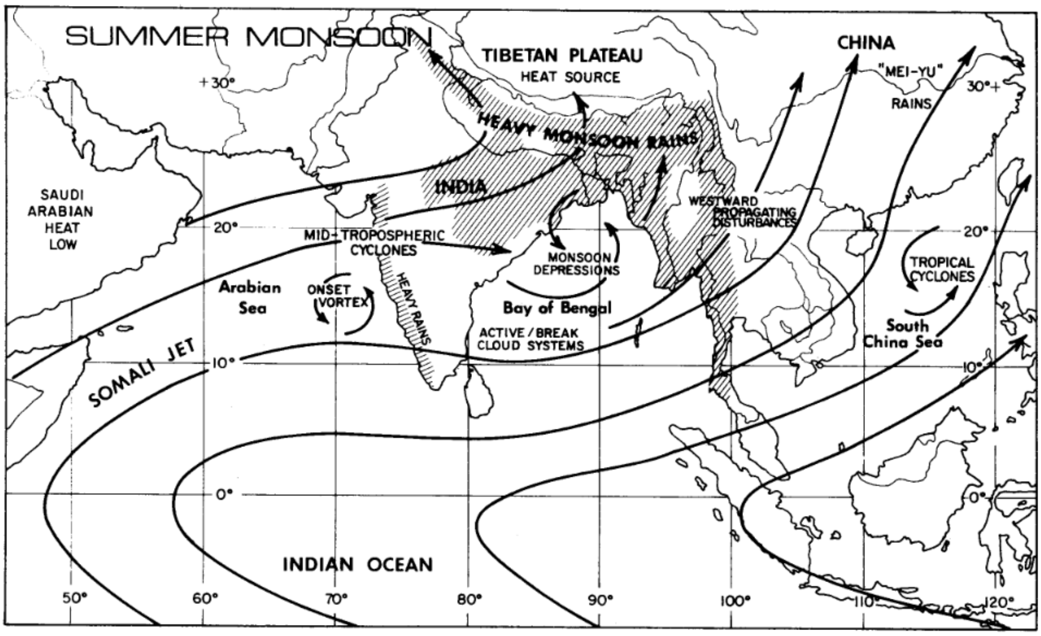

Figure 3.2: Primary synoptic and smaller scale circulation features that affect cloudiness and precipitation in the region of the summer monsoon. Locations of June to September rainfall exceeding 100cm over the land west of 100°E associated with the monsoon are indicated. Taken from Johnson and Houze (1987)

Upon reaching the southern tip of India, the Somali jet splits into two branches: the Arabian Sea branch and the Bay of Bengal branch. In the Arabian Sea branch, monsoon rainfall is orographic and occurs mainly on the western side of the Western Ghats mountain range as the air drains of moisture upon approaching the steep increase in elevation, leaving little rain to be precipitated past the mountain range. North of the Ghats, moist air from the Arabian Sea penetrates India in an eastward to north-eastward direction and precipitation occurs when these strong winds are faced with the barrier of the Himalayan mountain range.

The Bay of Bengal branch of the SAM deflects south of the Ghats and thus retains its high moisture. Upon reaching the Bay of Bengal, the already moist air picks up even more moisture before travelling in-land towards Bangladesh and North East India. The moist air soon meets with the Himalayas mountain range once again, curving in a westward direction along the ridge and causing intense rainfall along its path.

The steep pressure gradient which induces the monsoon through the creation of the Somali jet penetrates high into the troposphere, owing to sensible heating occurring high up on the Tibetan Plateau. This also causes a return flow aloft (Turner and Annamalai (2012)), which creates the monsoon anti-cyclone and tropical easterly jet at about 200 hPa.

3.2 Results

3.2.1 Representation in IGCM

To examine, qualitatively, how well the IGCM simulates the present day monsoon, comparisons of present day model integrations were made to present day observations and reanalysis data of precipitation and meridional, zonal winds respectively. For precipitation, 6-hourly satellite data spanning over 17 years (1997-2015) from NASA's Tropical Rainfall Measuring Mission (TRMM) (Kummerow *et al.* (1998)) was used. For wind products, 6-hourly reanalysis data from ECMWF's ERA-INTERIM analysis (1979-2012) (Dee *et al.* (2011) at the 850mb level was used. Both datasets were averaged monthly and re-gridded to match the low (T42) and high (T170) resolution model simulations used, described in chapter 2. Difference plots were then produced showing monthly (March - August) differences in wind speed and direction overlaid on precipitation differences for low resolution, high resolution with topography smoothed to low resolution (dubbed 'hybrid') and high resolution model simulations.

The large scale features seen in Figure 3.3 include a noticeable dryness over the Maritime Continent and equatorial Indian Ocean areas persisting throughout March to August (rightmost column). These areas stay completely dry in the IGCM from May (panel h) onwards; the Maritime continent area is dry in March and April as well (panels b,e): the main wet area in the region is misplaced in the IGCM and rainfall occurs in the middle of the Indian Ocean. It does not reach far enough east to cover the Maritime Continent.

Differences over the Tibetan Plateau area start to rise in April (e), with the IGCM seeing some rainfall while in observations the area stays dry in April (d) and throughout the season. In the Himalayan region (around 20°N, 90°E), starting April, differences around the topography are noticeable with a negative rainfall bias on the Himalayan band followed by a positive bias on the Tibetan Plateau (f). These differences intensify throughout the monsoon season (i onwards), with the IGCM seeing too much rainfall on the Tibetan Plateau and too little rainfall on the footsteps of the Himalayas. The Western Ghats mountains in India (15°N, 75°E) start to see intense rainfall in the IGCM in May (h), causing a positive rainfall bias which lasts throughout the monsoon season (i onwards). The Bay of Bengal (20°N, 90°E) sees a significant increase in rainfall amounts in the IGCM between May and June (panels h,k) which causes a strong positive bias (panel l). These exaggerated rainfall amounts continue throughout the season. The same is seen in the South China

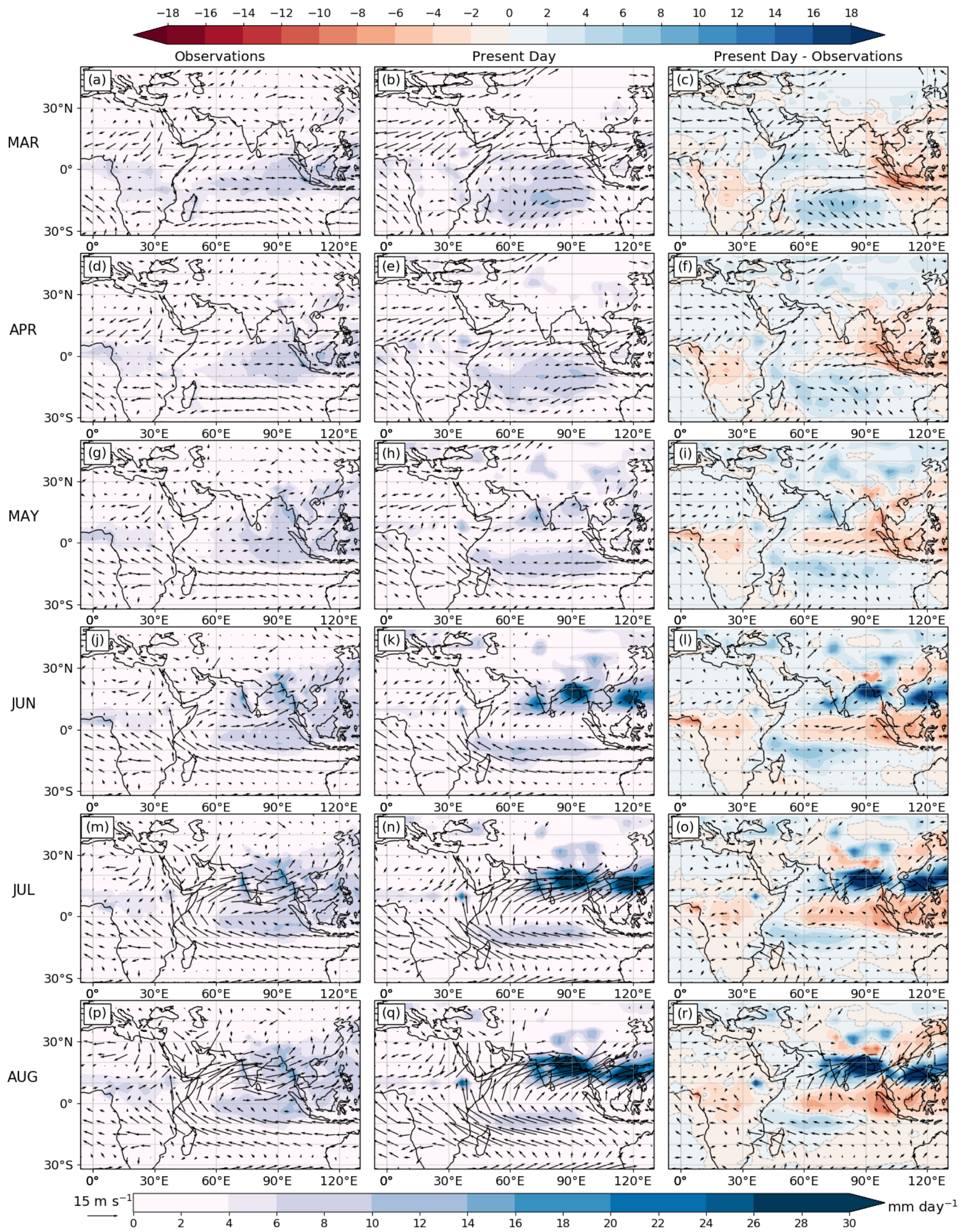

Figure 3.3: Monthly differences in precipitation (mm day^{-1}) between model and observations for present day conditions. rows show months, from March to August. Leftmost column shows observational data; Middle shows the low resolution, present day IGCM simulation and right shows differences between present day and observations. Contour intervals of 2 mm day $^{-1}$ for both absolute fields (bottom) and differences (top).

Sea and further into the Pacific Ocean. Africa is generally too dry in the Pliocene, with the exception of the Ethiopian Plateau, around 20°N, 40°E.

Wind speeds in the eastern Indian Ocean are too strong in the IGCM, in the area of reduced rainfall compared with observations. In the height of the monsoon seasons: July and August, flow across the Equator in the IGCM is established (panels n,q) and the bias in wind in the area diminishes. Wind speeds around the origin of the Somali jet (approximately 10°N, 60°E) are well represented in the IGCM. In the northerly portion of the jet in July and August, over India and the Bay of Bengal, wind speeds in the IGCM (o,r) are too strong compared with observations. In addition, the month of August sees increased wind bias around 10°N, as the meridional component of the Somali jet in the IGCM is too strong compared with observations.

3.2.2 Monsoonal Onset: Present day versus Pliocene

The effects of Pliocene sea surface temperatures (SSTs) on the onset of the SAM were explored using the IGCM4 (model and experiments described in chapter 2).

Surface temperature differences are shown in Figure 3.4. The prescribed Pliocene SST field imposes a weaker, more zonal meridional gradient particularly in the western Indian Ocean (panels h,k,n,q). This weaker Pliocene gradient compared with present day shows differences from the earliest month of the onset period (c), which intensify throughout the onset period (panels f,i) and peak in June - resulting in cooling of 4°K in the northern Arabian Sea and warming of 2°K around the Mascarene high region in the southern Indian Ocean compared with present day conditions (l). As the monsoon season progresses, the warm anomaly originating from the Mascarene high area spreads north, taking over the cold anomaly to the north. By August (r), the Indian Ocean in the Pliocene is almost wholly warmer than the present day equivalent.

Over land, temperatures are generally warmer in the Pliocene (especially over India) than the present day for the months of March and April (c,f). However, from May onwards, north western India and the Arabian Peninsula sees temperatures rise progressively for the present day (panel g onwards) while in the Pliocene temperatures in these regions see a much smaller increase through the season (h onwards). The differences between the two scenarios (i onwards) diverges progressively throughout the monsoon season with the Pliocene being much cooler than present day in the Indian heat low area as a result. For the southern tip of India, the Pliocene is warmer than present day throughout the season as it does not cool down as much in this scenario compared with the present day scenario. The Indian

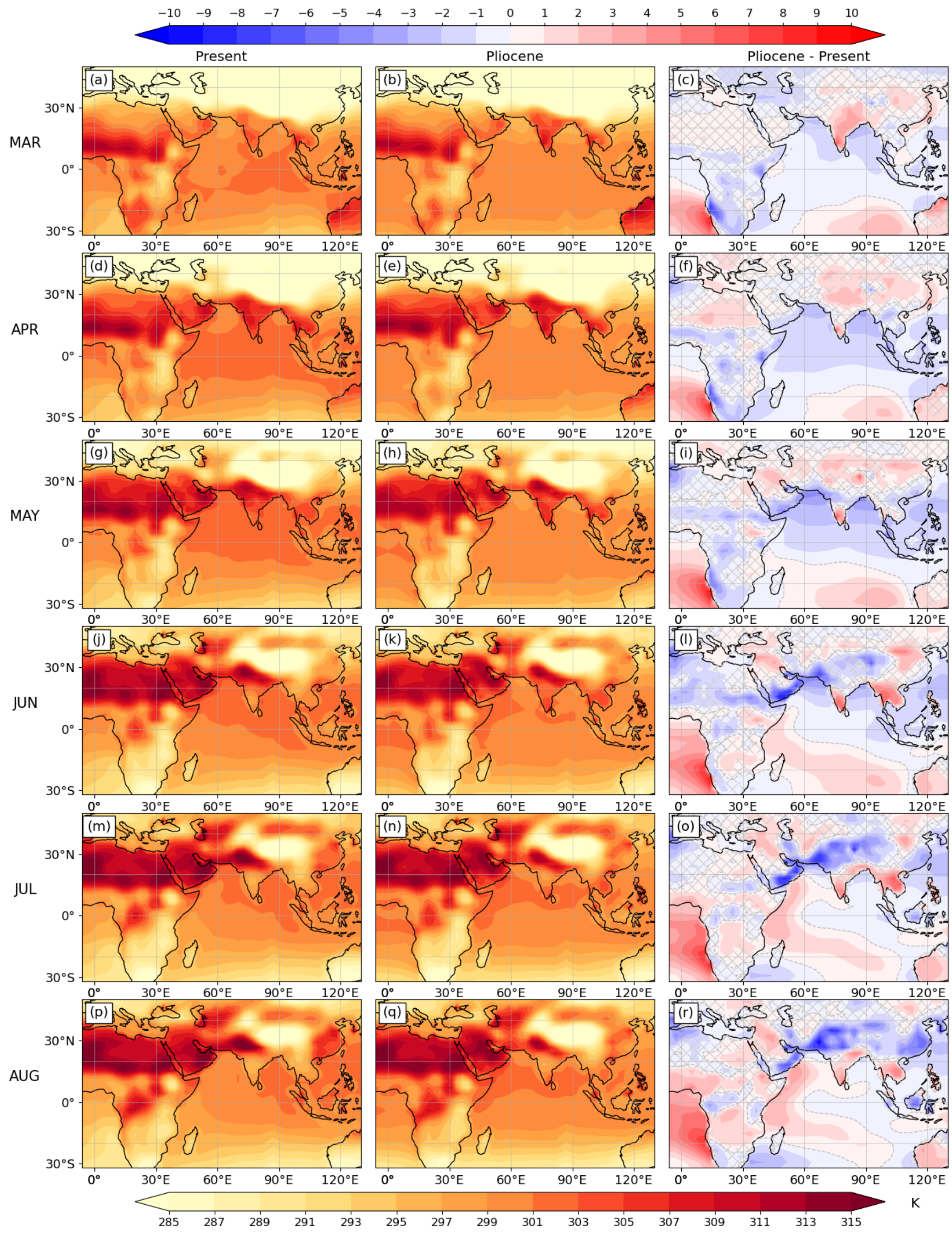

Figure 3.4: Monthly surface temperatures for Africa/Asia under low resolution, March to August (rows). Full fields for present (left) and Pliocene (middle) with contour intervals of 2°K (bottom). Difference between Pliocene and present day (right) with contour intervals of 1°K (top). Grey hatching indicates areas below the 95% significance threshold using a student's T-test.

heat low area and southern Arabian Peninsula region in the Pliocene are both 10°K cooler than the present day by July (panel o).

Changes to Mean Sea Level Pressure (MSLP)(Figure 3.5) follow these SST changes and the meridional pressure gradient across the Indian Ocean weakens in the Pliocene compared with present day, affecting features of monsoonal onset. A decrease in pressure in the Mascarene high area (60-90°E, 25°S) and an increase further north into the Arabian Sea begin to manifest in May (i), with the positive north-south gradient decreasing and reaching its lowest point in July (o). This leads to the weakening of the Indian heat low which is marked by an increase in pressure in the Pliocene compared with present day amounting to 9-11 hPa in June-August (panels l,o,r), implying a weakened monsoon. This pressure difference increases to 11-13 hPa in the Bay of Bengal.

A difference in the Indian heat low area in the Pliocene is also seen in Convective Cloud Amount (CCA)(Figure 3.6). In March and April, both the Pliocene (b,e) and present day (a,d) see little to no convective cloud present. Starting May, convective cloud amount in the Pliocene (panel h onwards) begins to increase in the heat low area throughout the season while the present day sees little to no convective cloud in the area (g,j,m,p). This increase in convective cloud in the Indian heat low area in the Pliocene compared with present day is seen in the differences between the two (panel i onwards) which, when combined with the increase in convective cloud amount in the present day compared with Pliocene further south (over the Arabian and Bengal seas), marks a northward shift of convective cloud pattern.

These differences in convective cloud amount between Pliocene and present day have a knock on effect on incoming solar radiation, seen in Figure 3.7. An increase (decrease) in tall, thick cloud reduces (increases) the amount of solar radiation travelling through the atmosphere, restricting (raising) the amount of heating absorbed by the surface. For the Pliocene compared with present day, lesser amounts of solar heating reach the ground around the heat low in northern India and further north as a result of the increase in convective cloud. This starts to show from May onwards (panel i), following the changes to CCA. Peaking in June (l) with values of -100 W m^{-2} or more compared with the present day, the reduction in incoming solar radiation is still pronounced in August (panel r) with the most obscure area remaining in the western Arabian Sea. An additional, small increase in mid-level cloud amount in the Pliocene slightly exacerbates this effect (see Appendix B). The increase in solar heating reaching the ground in the Pliocene compared with present day in these panels is also due to the northward shift in convective cloud in the Pliocene, which leaves this area bare of rain-heavy clouds in the Pliocene, allowing

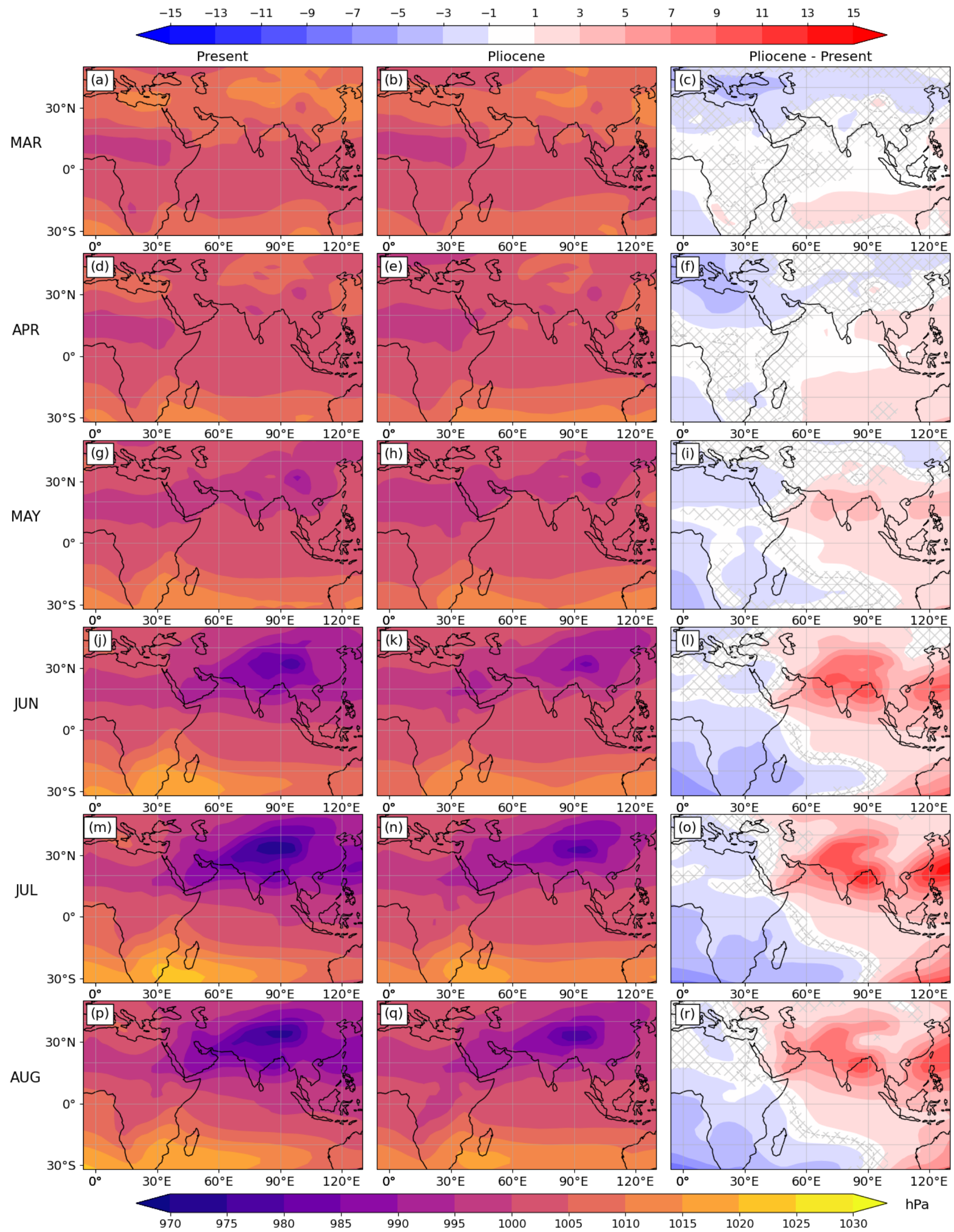

Figure 3.5: Monthly mean sea level pressure for Africa/Asia under low resolution, March to August (rows). Full fields for present (left) and Pliocene (middle) with contour intervals of 5 hPa (bottom). Difference between Pliocene and present day (right) with contour intervals of 2 hPa (top). Grey hatching indicates areas below the 95% significance threshold using a student's T-test.

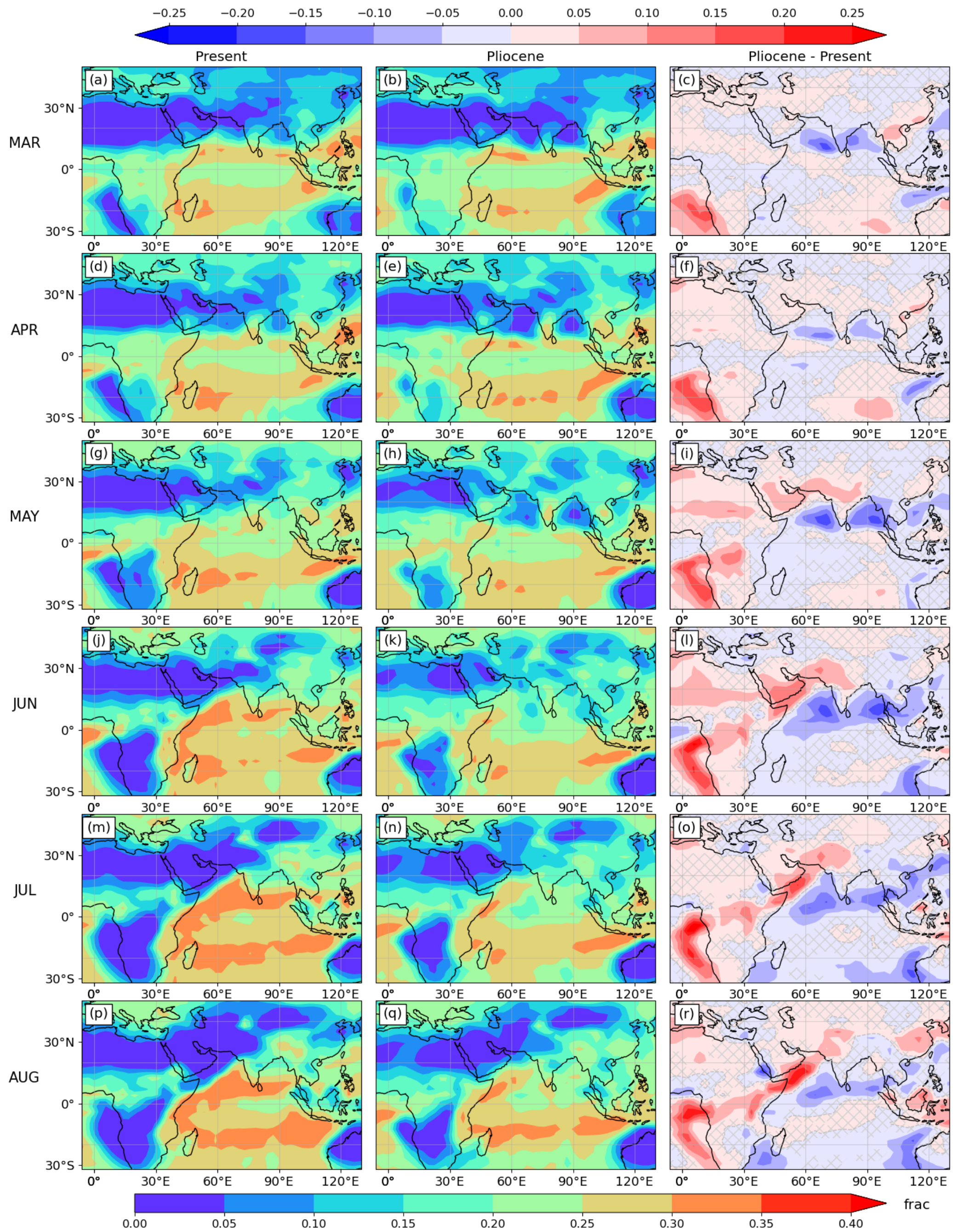

Figure 3.6: Monthly convective cloud amount under low resolution for Africa/Asia, March to August (rows). Full fields for present (left) and Pliocene (middle) with contour intervals of 0.05 (bottom). Difference between Pliocene and present day (right) with contour intervals of 0.05 (top). Units are in fraction. Grey hatching indicates areas below the 95% significance threshold using a student's T-test.

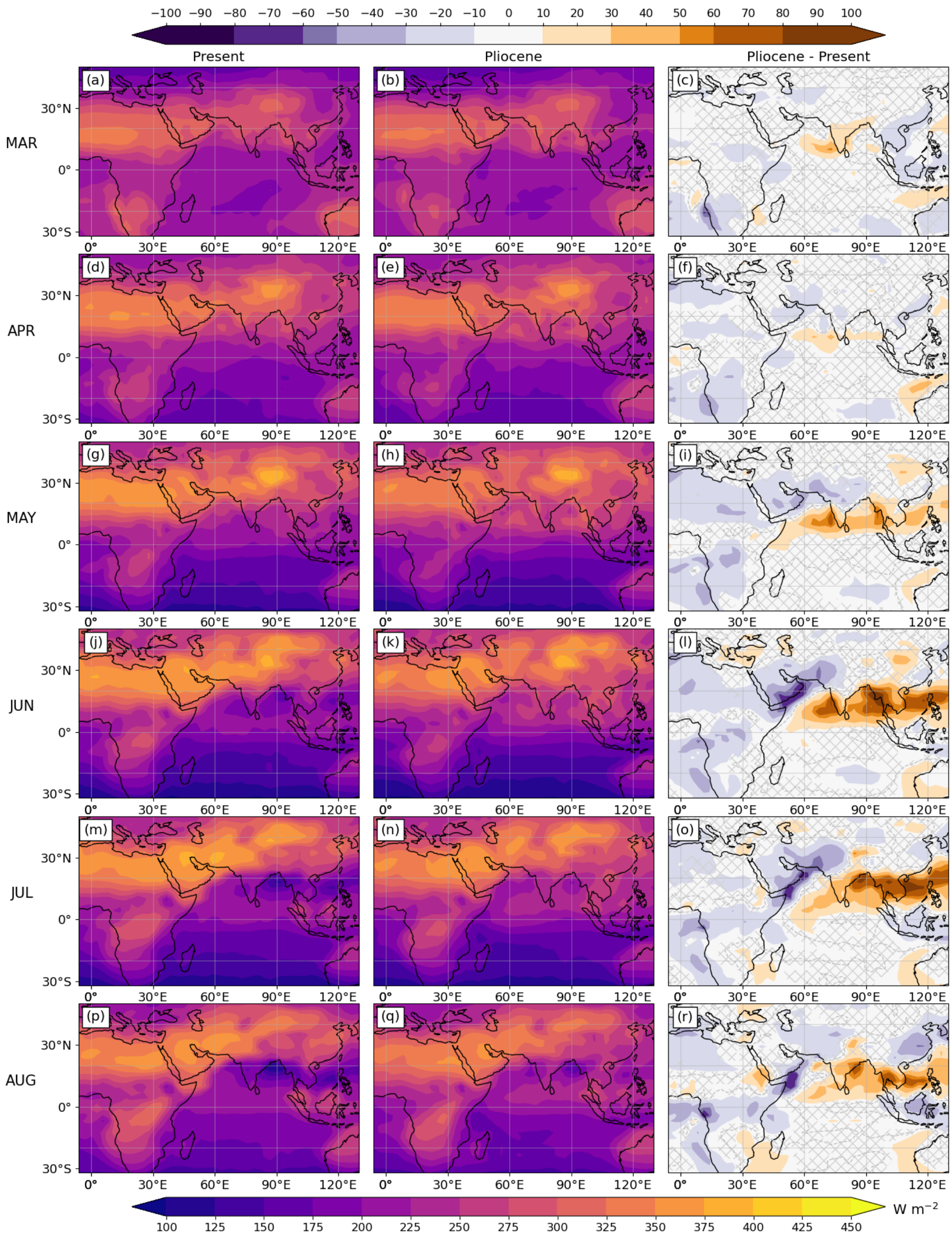

Figure 3.7: Monthly incoming shortwave radiation for Africa/Asia under low resolution, March to August (rows). Full fields for present (left) and Pliocene (middle) with contour intervals of 25 W m^{-2} (bottom). Difference between Pliocene and present day (right) with contour intervals of 10-30 W m^{-2}. Grey hatching indicates areas below the 95% significance threshold using a student's T-test.

solar heating to heat the ground much more than in the present day.

Following the changes to meridional temperature and pressure gradients, resulting from a decrease in solar heating reaching the Indian heat low area, wind flow and rainfall patterns are also changed in the Pliocene (Figure 3.8). Starting April, wind speeds of the emerging Somali jet are weaker in the Pliocene (e) than present day (d). Further north in the Arabian Sea, the Pliocene sees an increase in the northerly component of wind compared with present day (f), which is still affected by northerly winds in this region in April (d). In May, as the Somali jet strengthens in both scenarios (g,h), the reduction in wind speeds in the Pliocene compared with present day (i) intensifies and continues to do so throughout the monsoon season.

Flow across the Equator is much weaker in the Pliocene compared with present day, as easterly winds dominate the area (h). In the Arabian Sea area, the increase in the meridional wind component in the Pliocene also persists, allowing the Somali jet to extend further north than its present day counterpart. Cross-equatorial flow in the Pliocene remains weak and mostly easterly until July (panel n). This occurs at the same time as a large increase to rainfall amounts in the Bay of Bengal, which has been essentially deprived of rainfall until this point. This clockwise, northerly shifted flow in the Pliocene circulates moist, cold ocean air inland causing rainfall through convective clouds mentioned earlier, affecting the Indian heat low area starting June (panel k onwards).

On the western flank of the Somali jet in the Pliocene, which is much more to the north, rainfall occurs in the western Arabian Sea and over the eastern tip of the Arabian Peninsula in the Pliocene starting May (panel h) while the area is dry under present day conditions (g). Another increase of rainfall under the Pliocene scenario is found near the origin of the jet, north of Madagascar, starting June (panel o). A major decrease in rainfall over the main rain band across South Asia is seen as flow shifts northwards, depriving these areas of moisture.

Core Somali jet wind speeds are shown in Figure 3.9. A significant decrease in top meridional speed is seen in the Pliocene scenario, starting April (panel f). As the jet builds up through the monsoon season, wind speeds in the jet's core are 4 to 6 m s^{-1} slower in the Pliocene compared with present day (panels l,o,r) combined with a narrowing of the jet - corresponding to the weaker cross-equatorial flow seen in the previous figure (Figure 3.8). In July and August, the Somali jet in the Pliocene sees a 50% reduction in core wind speeds (o,r) with present day values reaching 16 m s^{-1} (m,p) while Pliocene values do not exceed 8 m s^{-1} (n,q).

Ertel Potential Vorticity (EPV) is a conserved quality over constant potential temperature (θ) surfaces (isentropic surfaces), in the absence of diabatic processes

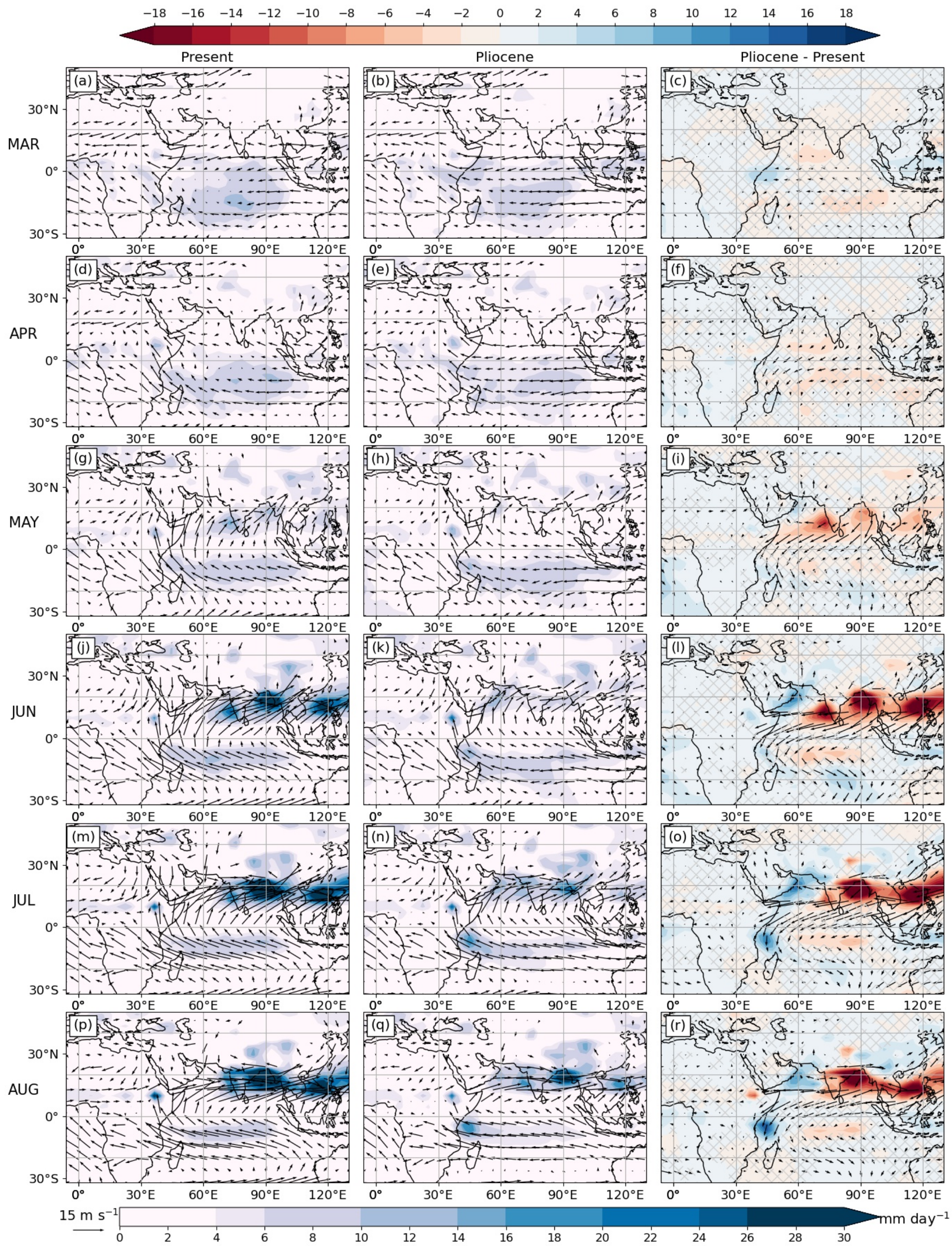

Figure 3.8: Monthly winds and precipitation at 880mb for Africa/Asia under low resolution, March to August (rows). Full fields for present (left) and Pliocene (middle) with contour intervals of 2 mm day^{-1} (bottom). Difference between Pliocene and present day (right) with same contour intervals (top). Grey hatching indicates areas below the 95% significance threshold using a student's T-test.

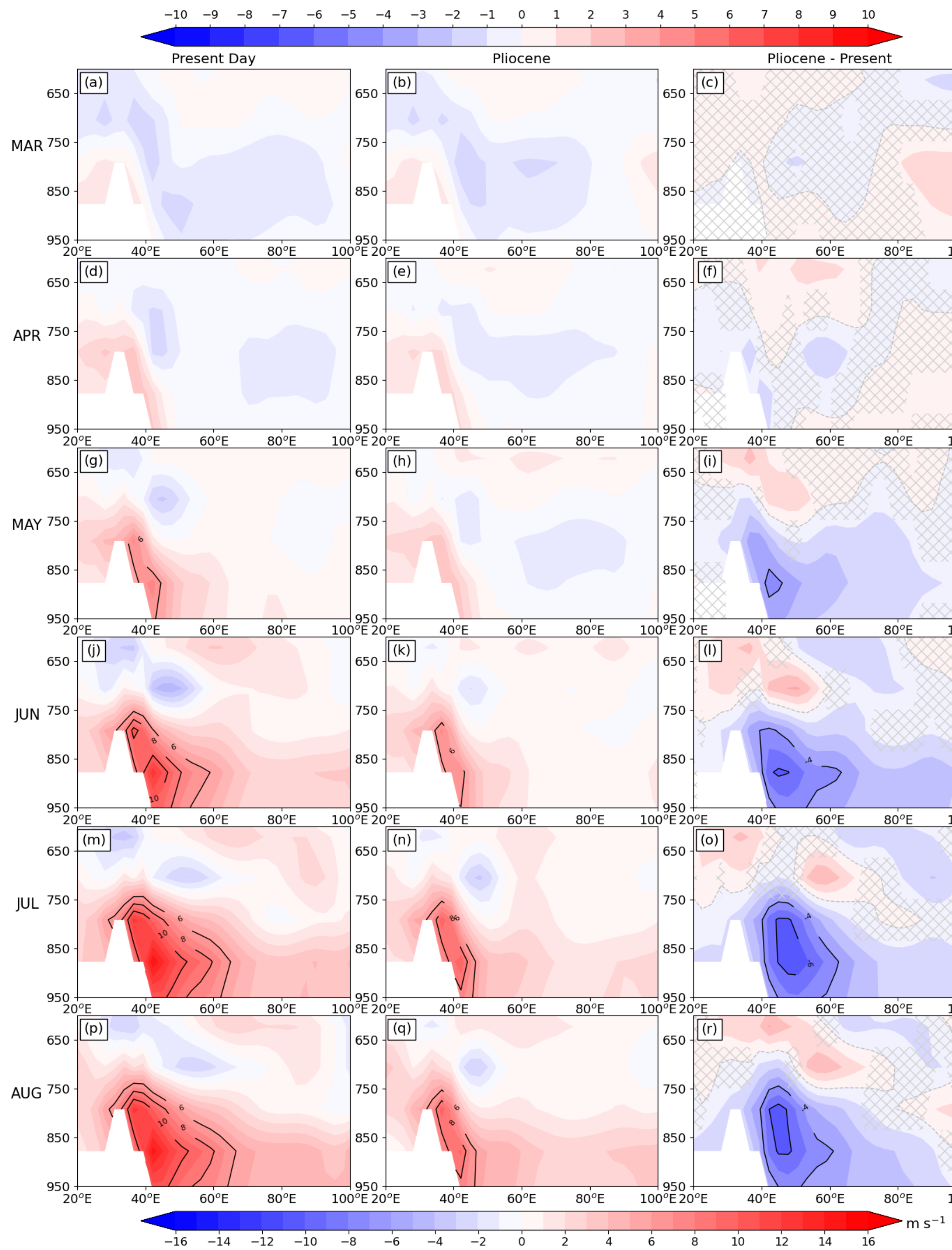

Figure 3.9: Monthly meridional wind speeds averaged over -1°S to 1°N under low resolution, March to August (rows). Full fields for present (left) and Pliocene (middle) with contour intervals of 1 m s^{-1} (bottom). 6,8 and 10 m s^{-1} contours in bold. Difference between Pliocene and present day (right) with same intervals (top), -4 and -6 m s^{-1} contours in bold. Grey hatching indicates areas below the 95% significance threshold using a student's T-test.

or friction. Thus, changes to EPV values are a direct result of changes to either diabatic heating, mainly, or the effects of friction. In the atmospheric column, away from the surface, the main source of diabatic heating is through changes to latent heat. A precipitating, convective cloud, releases latent heat into the atmosphere through condensation of rain droplets; this affects potential vorticity through altering absolute vorticity and static stability by changing the thickness of air levels in the atmospheric column. Below the level of maximum heating in the atmospheric column, latent heat release hydrostatically lowers the heights of constant θ surfaces, which increases absolute vorticity and thus increases potential vorticity.

Figure 3.10 shows Ertel Potential Vorticity (EPV) on the 305 θ surface, corresponding to a height of about 850 hPa along 15-20°N during the month of July (see Appendix B).

The negative anomalies between the Pliocene and present day in the eastern Arabian Sea seen in May and April (panels i,l) are associated with decreased convective rainfall under Pliocene conditions (seen in Figure 3.8) and thus a reduction in latent heat being emitted into the atmosphere, causing a reduction in EPV. The same goes for the positive anomaly in the northern Arabian Sea, where in the Pliocene an increase in convective rainfall is seen and thus an increase in latent heat release, contributing to an increase in EPV.

However, south of this anomaly in the month of July (o), lies a negative anomaly inhabiting the same convective rainfall area, working against the increase in latent heat release. This negative anomaly seems to be the signature of the jet's axis moving more to the norther and reaching further west, carrying negative potential vorticity (PV) from the southern hemisphere across the equator into areas previously unaffected by this jet under present conditions. In the Mascarene high area, in all potential temperature surfaces tested, an increase in potential vorticity is shown from May onwards. This is associated with the warmer superimposed SSTs in the Pliocene scenario, providing shallow heating from below (following Hoskins and Rodwell (1995)). This suggests that the Somali jet in the Pliocene was not only slower to carry negative PV across the equator due to decreased wind speeds shown earlier, but that the air that is being transported is already of less negative PV nature. The reduced PV qualities of the Somali jet in the Pliocene are suggestive of reduced vorticity and thus less of a curvature of the jet, allowing its west and north expansion.

These changes to the jet's attributes - its strength and potential vorticity, play a crucial role in its geographic extent and shape, altering its path and affecting South Asian monsoon rainfall in the Pliocene through the availability of low level moisture

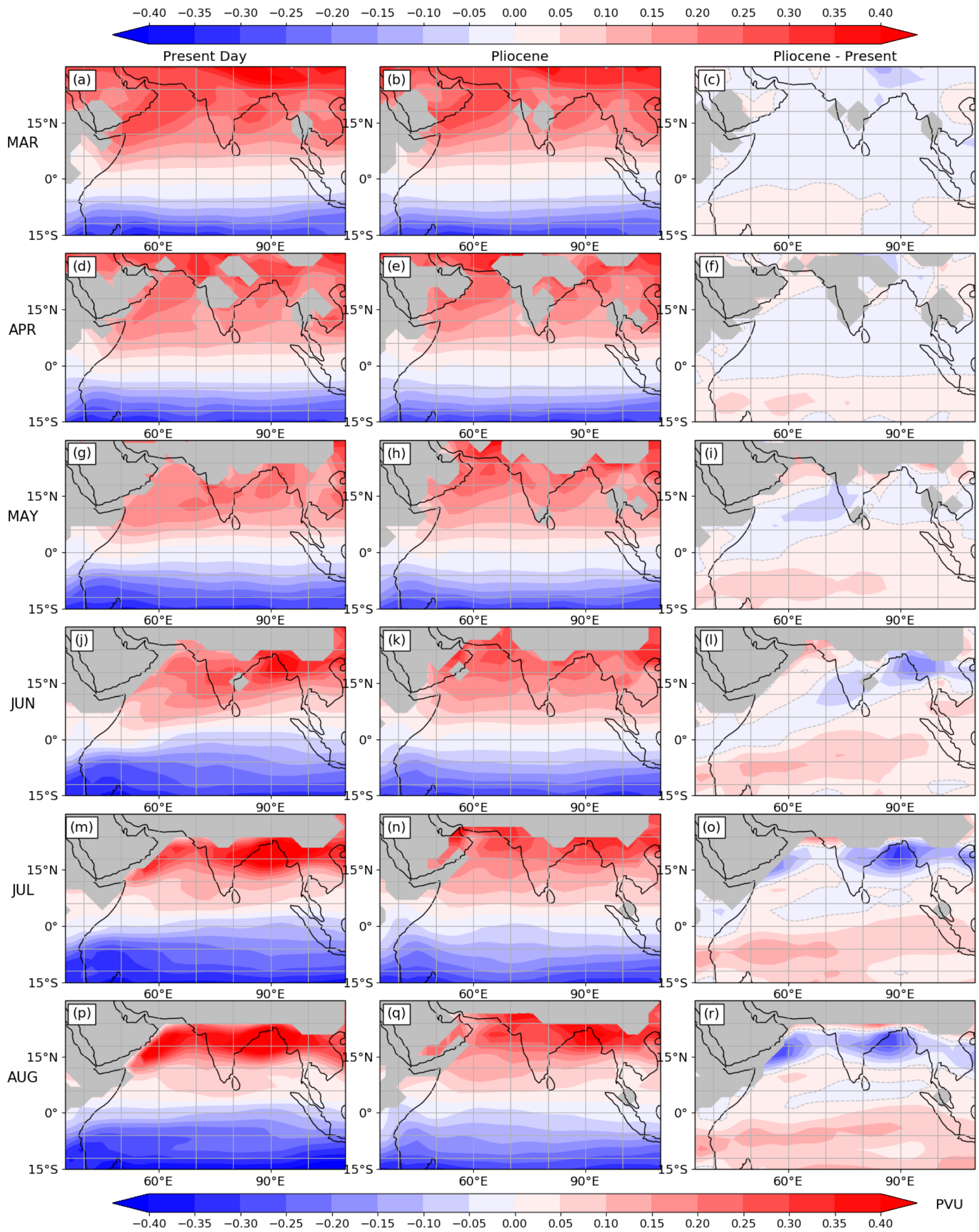

Figure 3.10: Monthly Ertel potential vorticity at the 305°θ surface for Africa/Asia under low resolution, March to August (rows). Full fields for present (left) and Pliocene (middle) with contour intervals of 0.05 PVU (bottom). Days where surface θ exceeded 305°K are discarded. Masked areas indicate 50% of days in the given month had surface θ exceeding 305°K. Difference between Pliocene and present day (right) with same intervals (top).

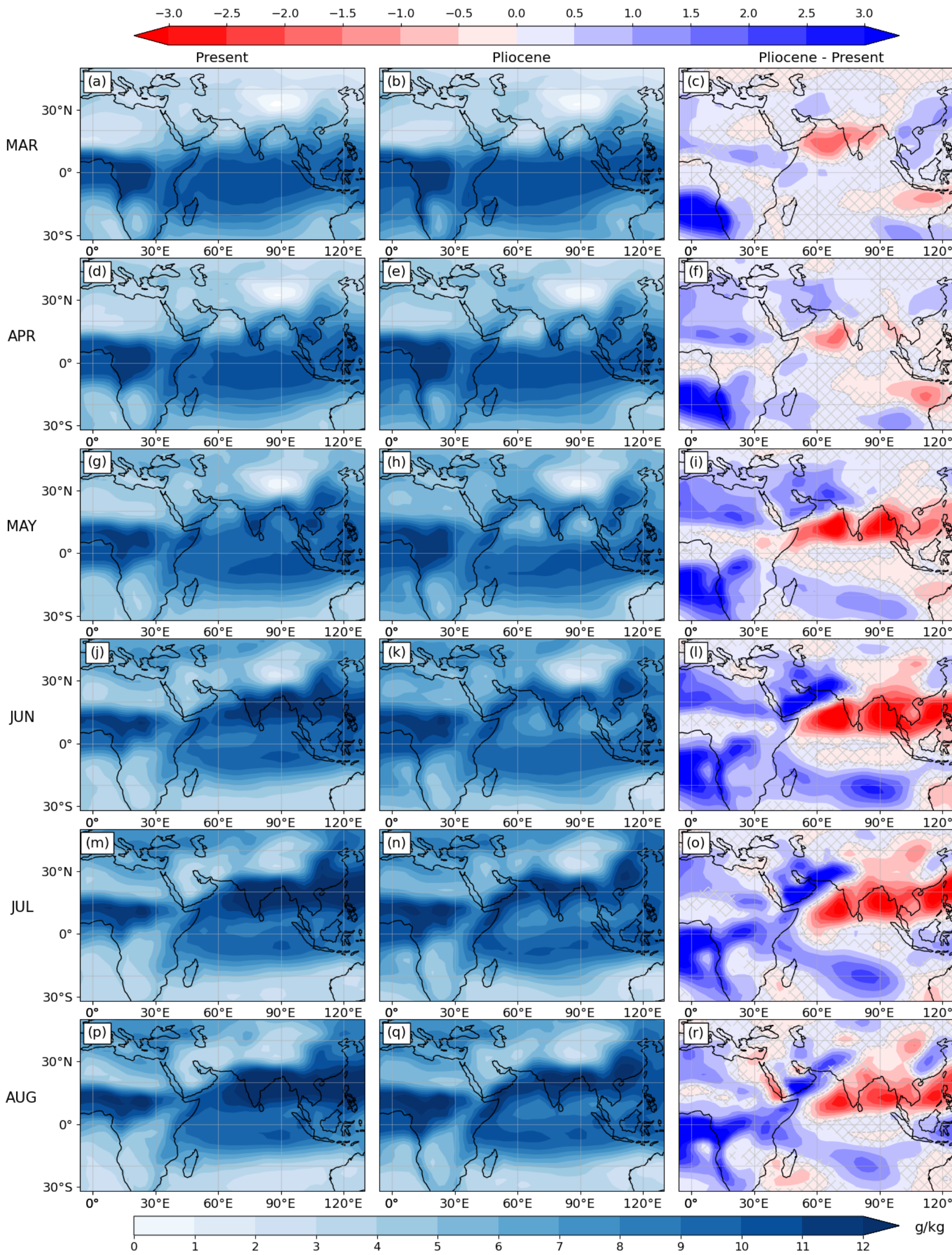

Figure 3.11: Monthly specific humidity at 880mb for Africa/Asia under low resolution, March to August (rows). Full fields for present (left) and Pliocene (middle) with contour intervals of 1 g/kg (bottom). Difference between Pliocene and present day (right) with contour intervals of 0.5 g/kg (top). Grey hatching indicates areas below the 95% significance threshold using a student's T-test.

(Figure 3.11). Starting May (g-i), higher levels of moisture are available over the Mascarene high area in the Pliocene, as a result of warmer SSTs in the region. This affects the area immediately north of Madagascar in May, progressing through to the north western Arabian Sea in June (l) and July (o). Due to the different position of the Somali jet in the Pliocene, moisture is deprived of the main monsoon area and is diverted to the north-western portion of the Arabian Sea and inland over the Indian heat low area, facilitating the aforementioned effects on temperatures in the area through convective rainfall.

Somali Jet development is slow in the Pliocene compared with present day (Figure 3.12). During the peak of the monsoon season, the jet in the Pliocene (q) has not yet reached the strength of the present day equivalent in June (j). Wind speeds are slower in the Pliocene throughout the season across the Indian Ocean. In the Pliocene, the jet axis is much more to the north than the present day (by 7-10°) for the months of June and July (l,o), reaching its southernmost position by August (r), remaining 3° north of the present day jet. Changes to the overall jet width, seen in Figure 3.9, are also visible. The jet in the Pliocene, being narrower owing to its decreased strength combined with a change in geographic position (more to the north), struggles to reach the southern tip of the Indian Peninsula. In the present day, high wind speeds are seen south of the peninsula throughout the monsoon season.

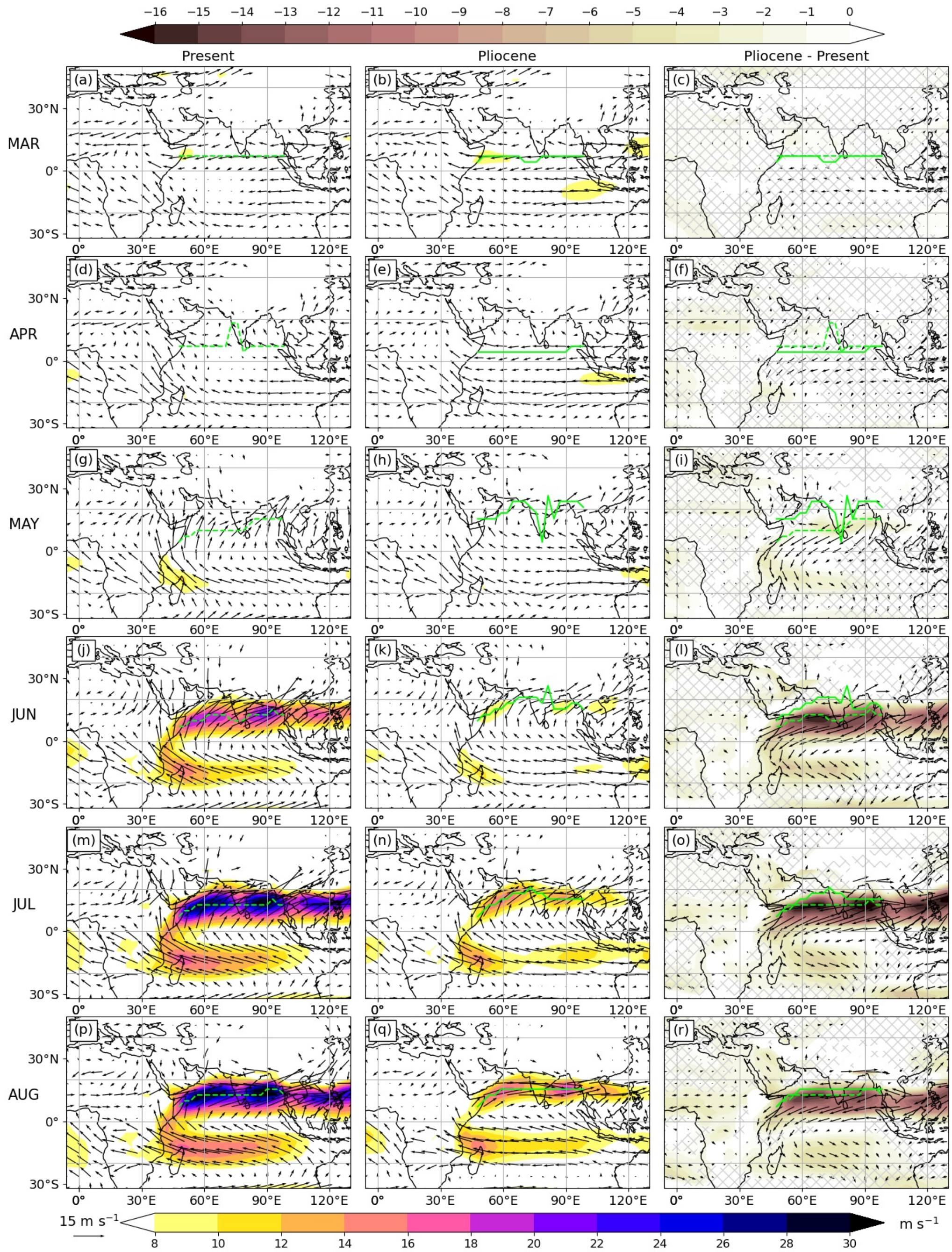

Figure 3.12: Monthly wind speed and direction at 880mb for Africa/Asia under low resolution, March to August (rows). Full fields for present (left) and Pliocene (middle) with contour intervals of 2 m s^{-1} (bottom). Difference between Pliocene and present day (right) with contour intervals of 1 m s^{-1} (top). Green lines indicate jet axes (dashed - present, solid - Pliocene). Grey hatching indicates areas below the 95% significance threshold using a student's T-test.

To further ascertain that the role of the meridional gradient is very important in the changes seen to the Somali Jet under Pliocene conditions, an additional sensitivity experiment was carried out, implementing a strictly meridional SST change to the present day achieved by zonally averaging the differences between present day and Pliocene SSTs in the Indian Ocean (between 30° - 120°E, 35°S - 32°N) and adding the averaged difference to Present day SSTs as follows:

$$SST_{PlioMSST_{(\phi,\lambda)}} = \begin{cases} SST_{Pres_{(\phi,\lambda)}} + \overline{\Delta SST}_{(\phi)} & -35° < \phi < 32°, 30° < \lambda < 120° \\ SST_{Plio_{(\phi,\lambda)}} & \text{elsewhere} \end{cases} \tag{3.2.1}$$

where ϕ is latitude, λ is longitude and:

$$\overline{\Delta SST}_{(\phi)} = \frac{1}{n} \sum_{\lambda=30°}^{\lambda=120°} (SST_{Plio_{(\phi,\lambda)}} - SST_{Pres_{(\phi,\lambda)}}) \tag{3.2.2}$$

Is the zonally averaged difference in SSTs between Pliocene and Present per latitude (ϕ), with n representing the total number of ocean grid boxes per given latitude, confined between 30° - 120° E.

This achieves similar changes to meridional gradients across the Indian Ocean with no zonal change from the present day. Figure 3.13 shows global figures for the month of August, comparing present day with PlioMSST, while fig Figure 3.14 shows the same for Pliocene and PlioMSST

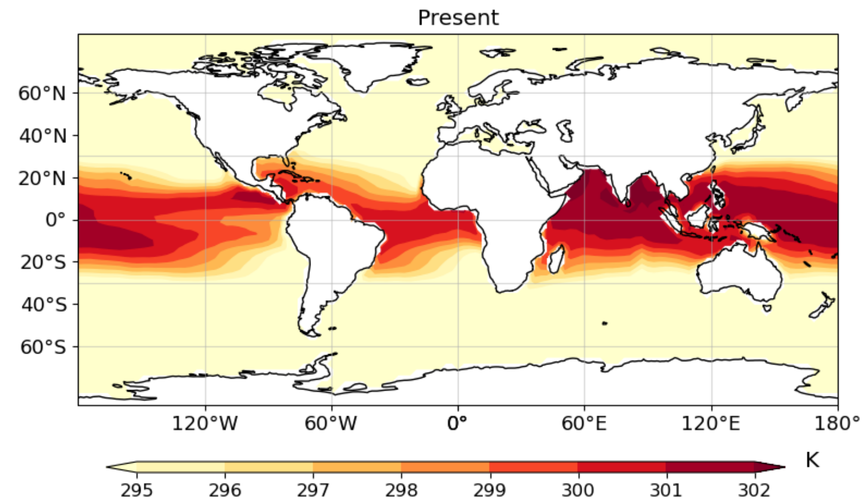

(a)

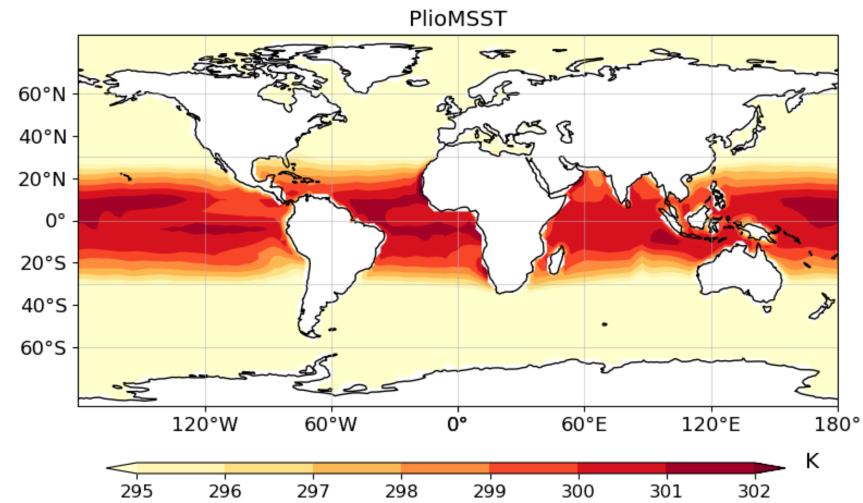

(b)

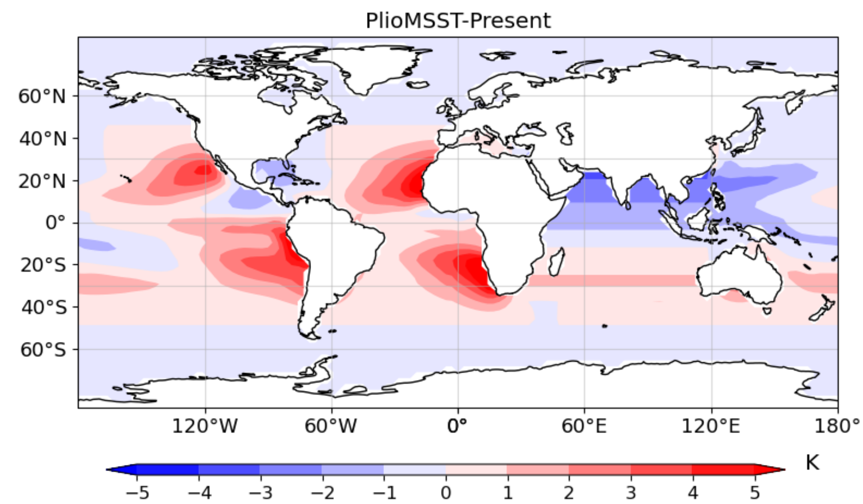

(c)

Figure 3.13: Global SST fields used in each model simulation for the month of May. Top: Present, middle: PlioMSST, bottom: the difference between PlioMSST and Present

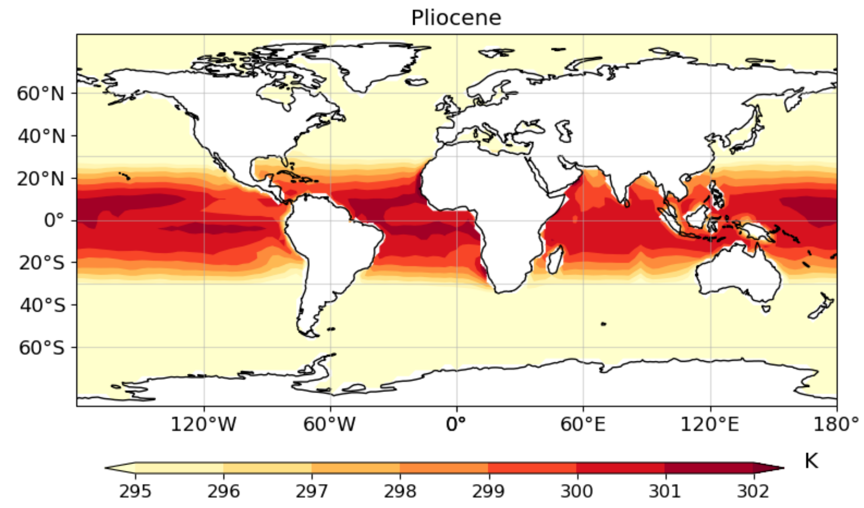

(a)

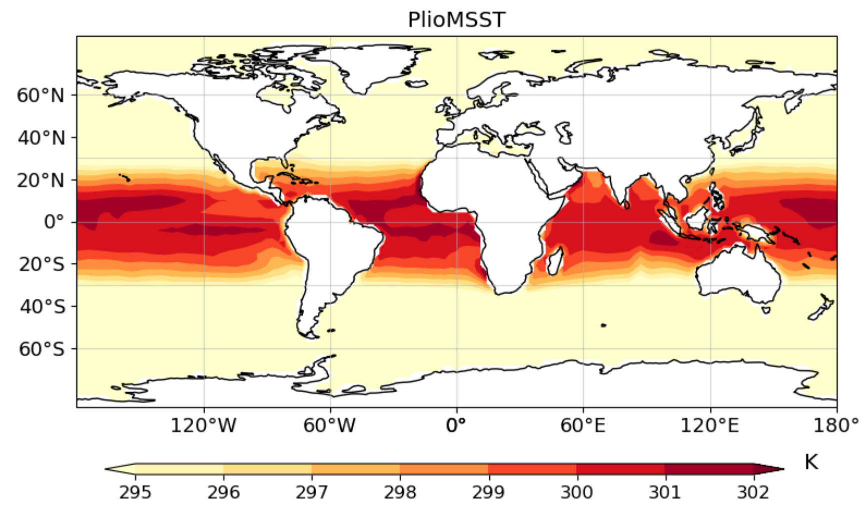

(b)

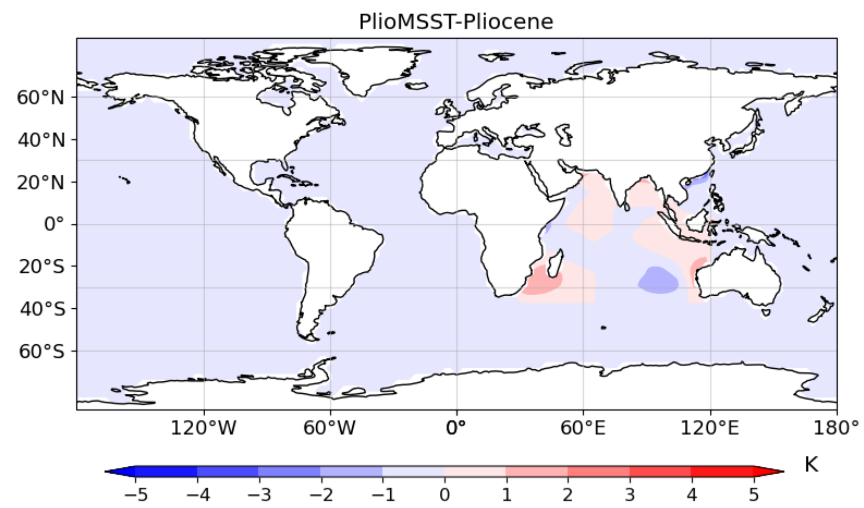

(c)

Figure 3.14: Global SST fields used in each model simulation for the month of May. Top: Pliocene, middle: PlioMSST, bottom: the difference between PlioMSST and Pliocene

Largest differences in SSTs (Figure 3.15) are seen during monsoonal onset in May (g-i) and June (j-l), with the northern Arabian Sea being up to 4°C cooler than present. Over land, the seasonal progression of cold temperatures in land over the heat low area and the northern Indian peninsula is significant and similar to that of the Pliocene experiment (Figure 3.4).

Figures discussed in this analysis will mainly refer to the differences between Pliocene and PlioMSST to highlight their similarities; a repeat analysis showing differences between present and PlioMSST are included in (section B.3) for a broader overview.

The main feature while comparing SSTs in PlioMSST to Pliocene (Figure 3.16) is the cooling of the western portion of the Arabian Sea (l,o,r), where PlioMSST is 2-3°C cooler than the Pliocene, on average. In dynamical terms, this effectively preserves present day upwelling rates in the Somali current area which is thought to have been reduced in the early Pliocene, thus leading to warmer SSTs (Sarathchandraprasad *et al.* (2021)). Over land, there are no significant differences in surface temperatures in the monsoon area, despite a slight warming of the Indian heat low area compared to the Pliocene.

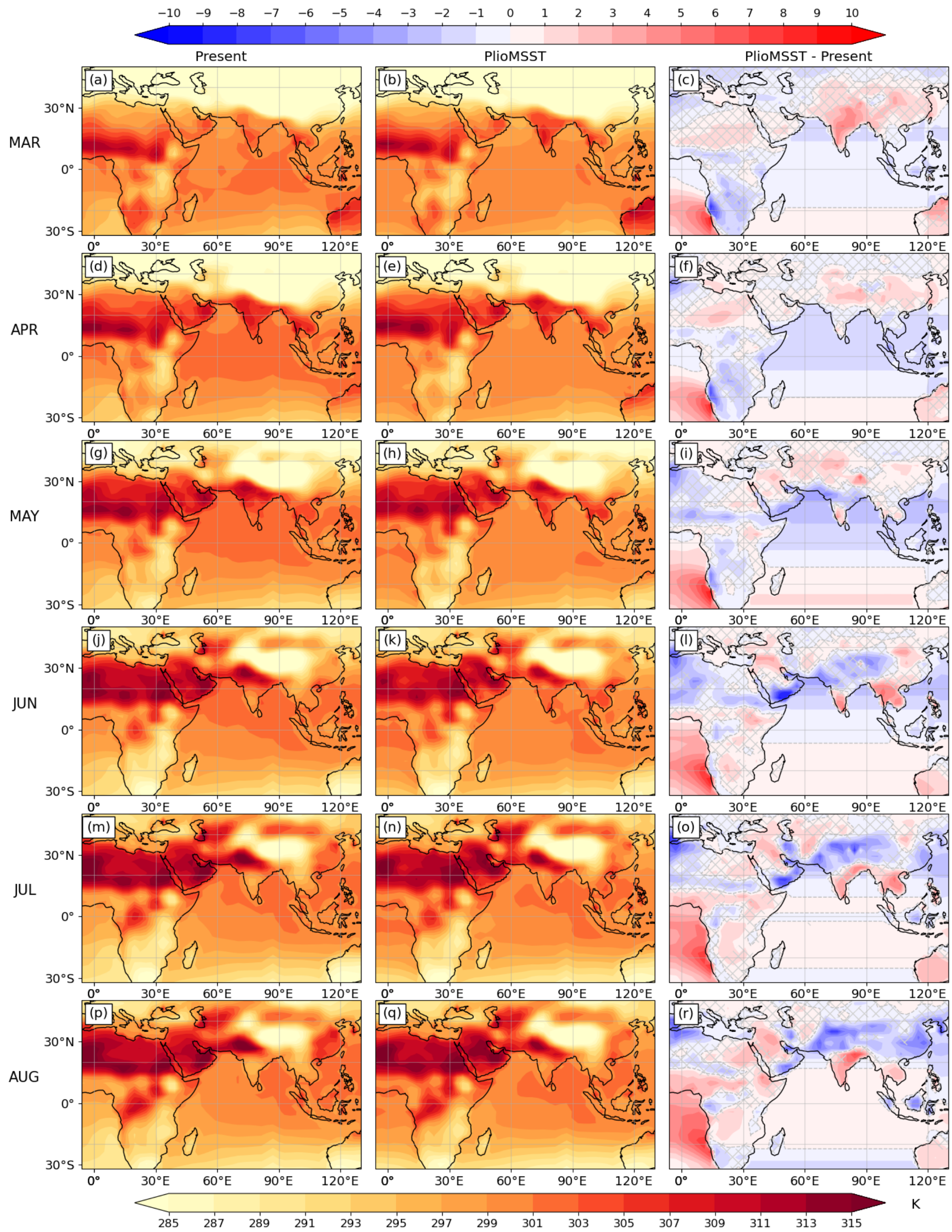

Figure 3.15: Monthly surface temperatures for Africa/Asia under low resolution, March to August (rows). Full fields for present (left) and PlioMSST (middle) with contour intervals of 2°K (bottom). Difference between PlioMSST and present day (right) with contour intervals of 1°K (top). Grey hatching indicates areas below the 95% significance threshold using a student's T-test.

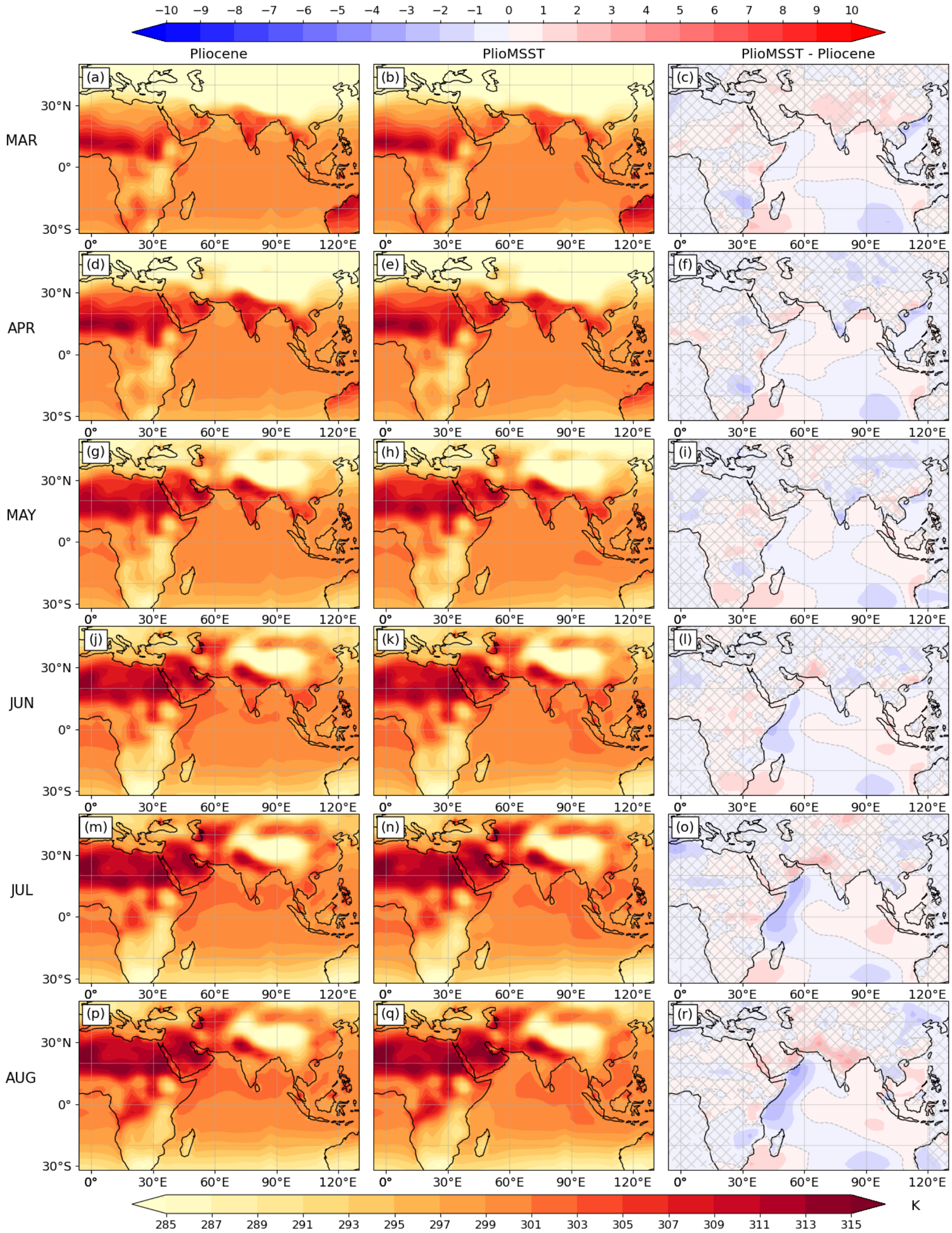

Figure 3.16: Monthly surface temperatures for Africa/Asia under low resolution, March to August (rows). Full fields for Pliocene (left) and PlioMSST (middle) with contour intervals of 2°K (bottom). Difference between PlioMSST and Pliocene (right) with contour intervals of 1°K (top). Grey hatching indicates areas below the 95% significance threshold using a student's T-test.

Major Significant rainfall differences between PlioMSST and Pliocene (Figure 3.17 lie in precipitation rates across the Arabian Sea, with rainfall heavily reduced north of Madagascar in PlioMSST, remaining at a constant 4-6 mm day^{-1} throughout the monsoon season (k,n,q) and weaker to no rainfall in the western Arabian Sea. This reduction in precipitation in the western Indian Ocean also penetrates inland into Eastern Africa, with drying of the Horn of Africa in PlioMSST becoming most significant in July (o). The Mascarene high area sees increased, zonally uniform rainfall in PlioMSST during the months of July and August (n,q) compared with the Pliocene (m,p), where the eastern region of the Mascarene high sees 5-6 mm day^{-1} more rainfall than the Pliocene.

Available low level moisture is significantly impacted in the PlioMSST experiment compared with the Pliocene (Figure 3.18). These specific humidity differences explain the aforementioned rainfall differences: the lack of zonal SST changes in PlioMSST means that the aforementioned cooler SSTs in the western portion of the Indian Ocean, peaking in July and August, impact on low level atmospheric moisture as less moisture is evaporated from the cooler sea surface (o,r), resulting in less rainfall in the western Indian Ocean, similarly to the present day (Figure B.4). Over land, there is a significantly less available moisture over the northern Indian peninsula during August (r) in PlioMSST, as the drier jet advances inland.

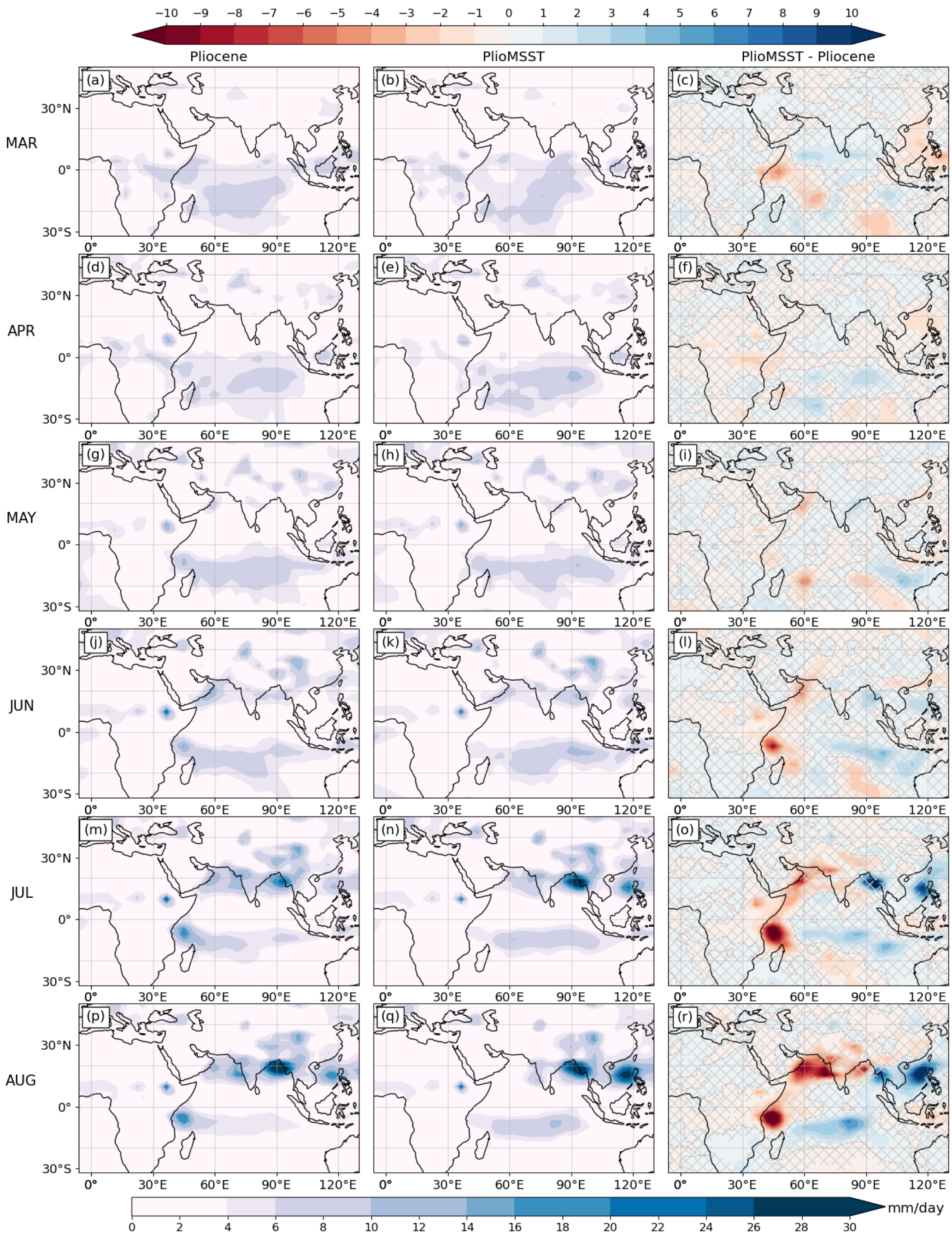

Figure 3.17: Monthly precipitation rates for Africa/Asia under low resolution, March to August (rows). Full fields for Pliocene (left) and PlioMSST (middle) with contour intervals of 2 mm day^{-1} (bottom). Difference between PlioMSST and Pliocene (right) with contour intervals of 1 mm day^{-1} (top). Grey hatching indicates areas below the 95% significance threshold using a student's T-test.

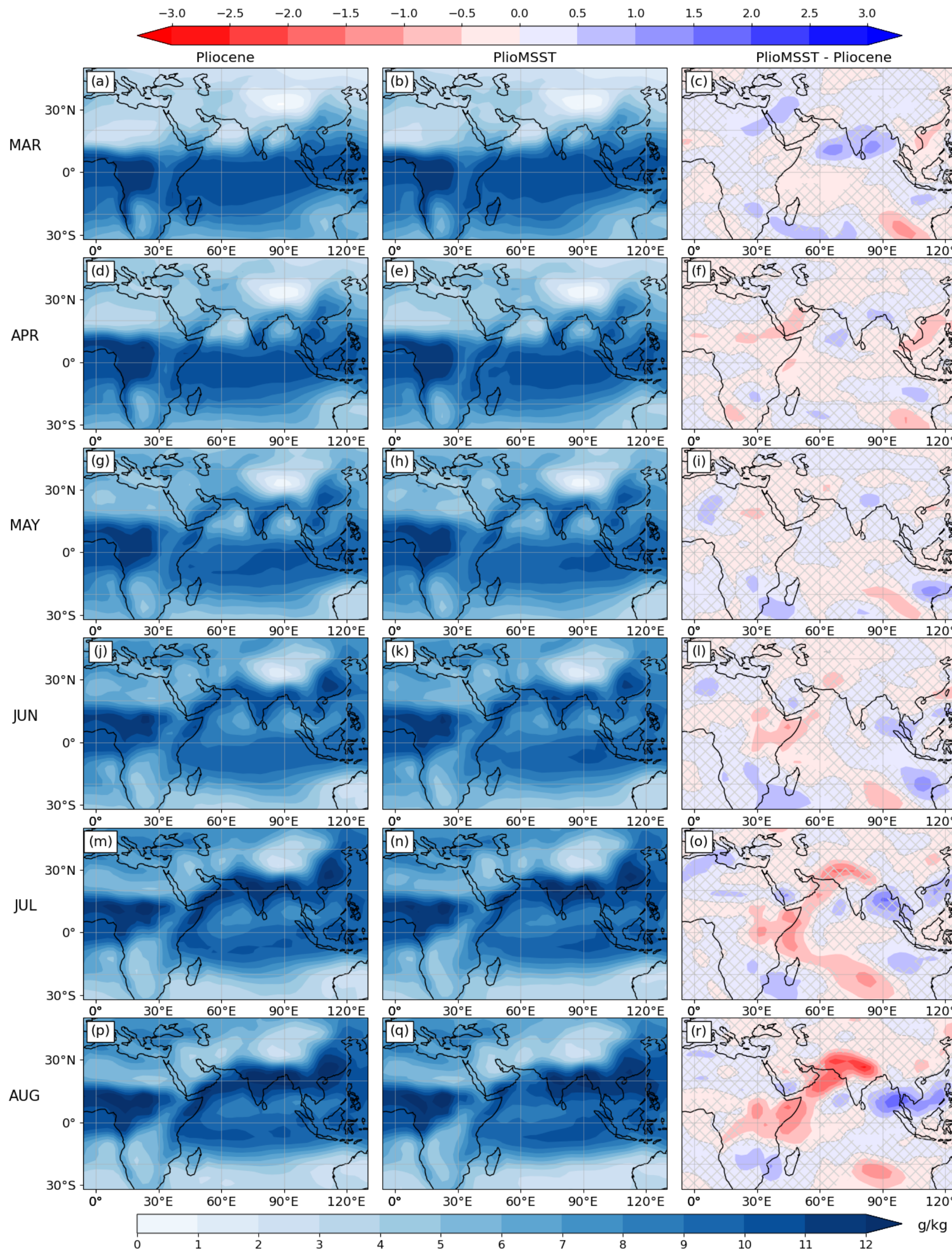

Figure 3.18: Monthly Specific Humidity at 880mb for Africa/Asia under low resolution, March to August (rows). Full fields for Pliocene (left) and PlioMSST (middle) with contour intervals of 1 g/kg (bottom). Difference between PlioMSST and Pliocene (right) with contour intervals of 0.5 g/kg (top). Grey hatching indicates areas below the 95% significance threshold using a student's T-test.

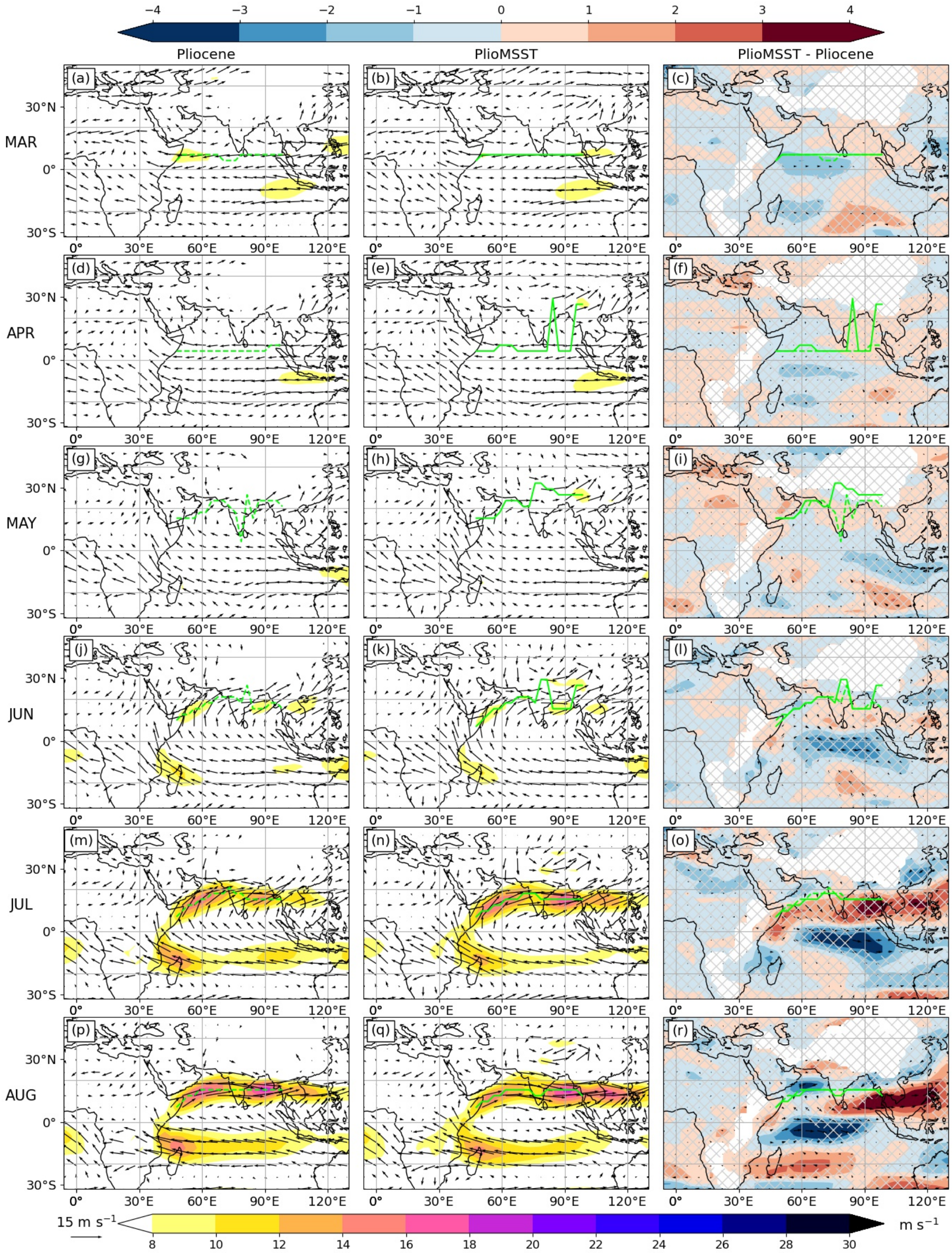

Figure 3.19: Monthly wind speed and direction at 880mb for Africa/Asia under low resolution, March to August (rows). Full fields for Pliocene (left) and PlioMSST (middle) with contour intervals of 2 m s^{-1} (bottom). Difference between PlioMSST and Pliocene (right) with 1 m s^{-1} contour intervals (top). Green lines indicate jet axes (dashed - Pliocene, solid - PlioceneMSST). Grey hatching indicates areas below the 95% significance threshold using a student's T-test.

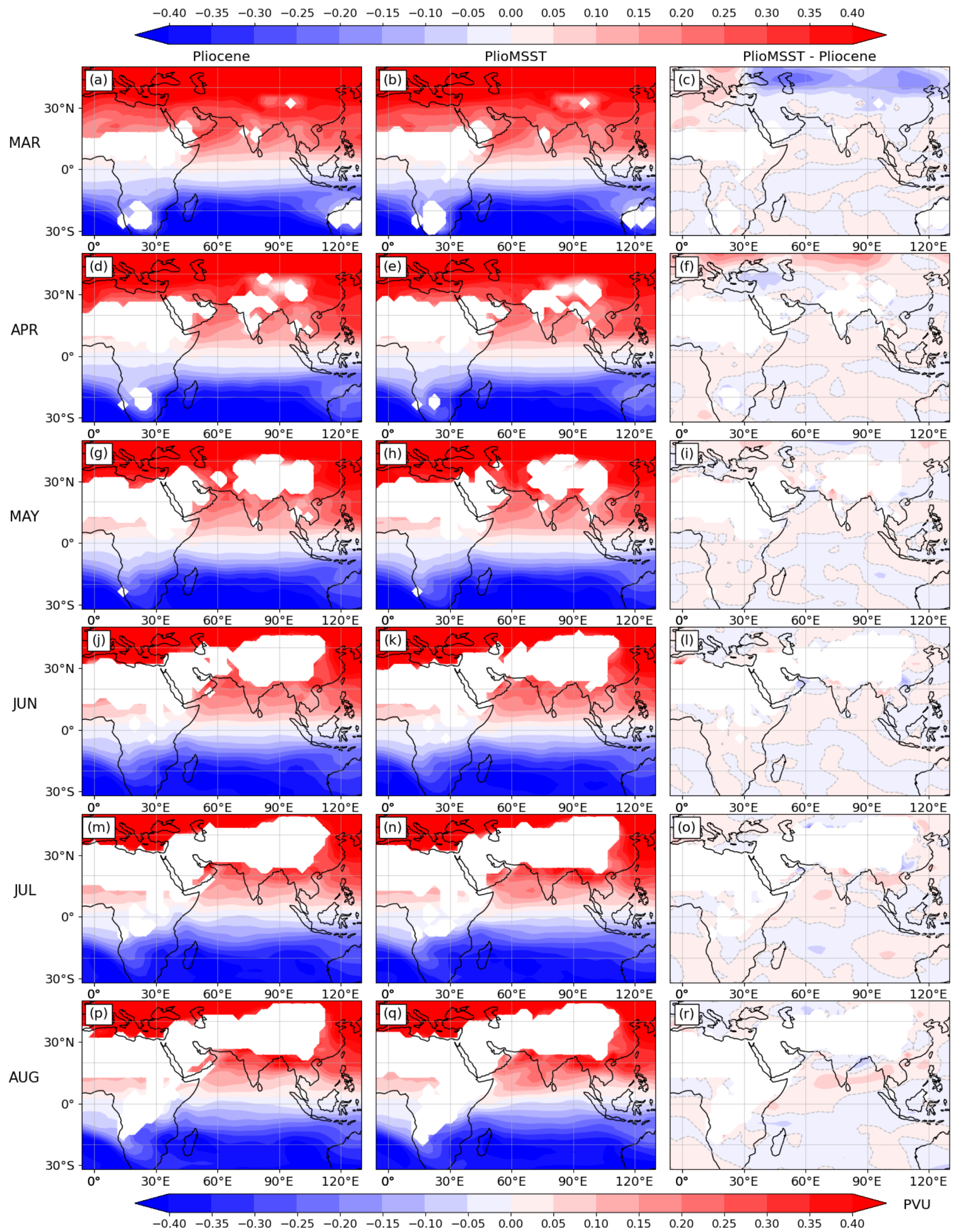

Figure 3.20: Monthly Ertel potential vorticity at the 305°θ surface for Africa/Asia under low resolution, March to August (rows). Full fields for Pliocene (left) and PlioMSST (middle) with contour intervals of 0.05 PVU (bottom). Days where surface θ exceeded 305°K are discarded. Masked areas indicate 50% of days in the given month had surface θ exceeding 305°K. Difference between PlioMSST and Pliocene (right) with same intervals (top).

The strictly meridional SST change induces similar, albeit slightly weaker, changes to potential vorticity (Figure 3.20) which are responsible for the same northward shift in the jet's position from June onwards (l), as seen by position of the jet's axis in both experiments (Figure 3.19) compared with the present day jet. No significant differences in wind speed were found between Pliocene and PlioMSST during onset. Flow across the equator is widespread in the Pliocene from June (l) onwards, while in PlioMSST it is restricted to the western Indian Ocean. Small north-south changes to the jet are seen in July (o) and August (r), at the jet's peak activity, where advection of potential vorticity is strongest.

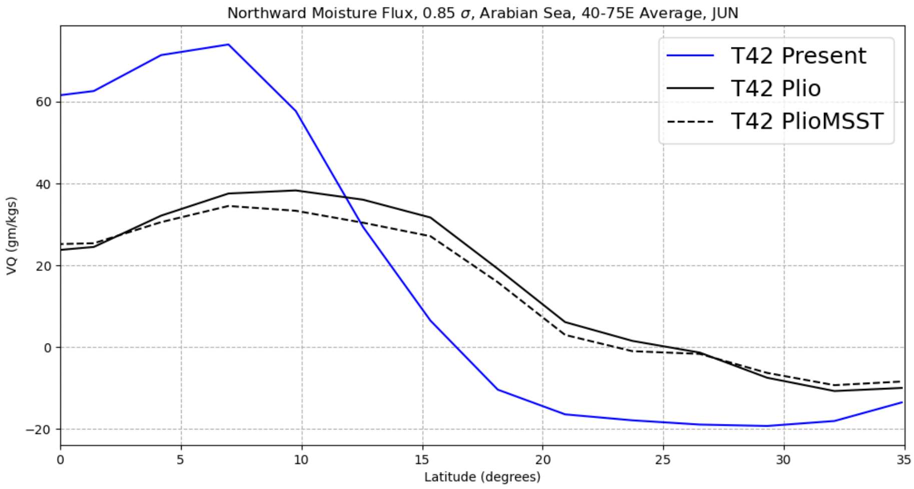

(a) June

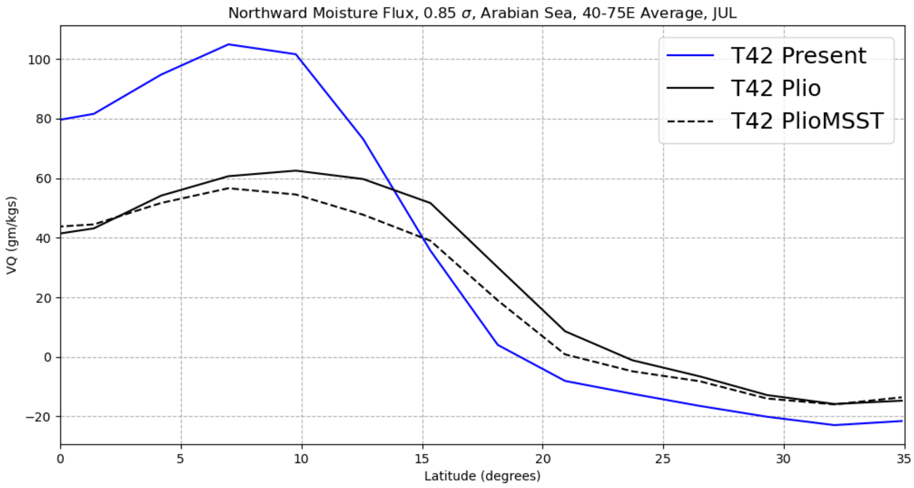

(b) July

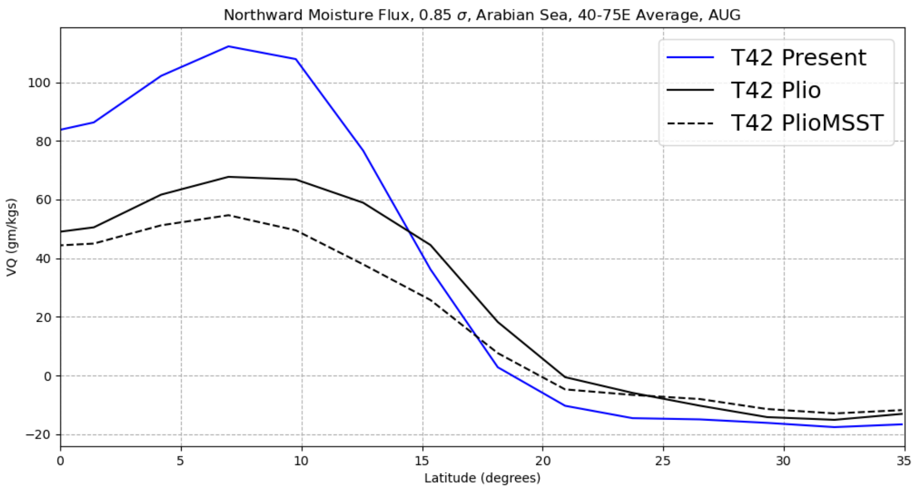

(c) August

Figure 3.21: Northward moisture flux at the 0.85σ model level (approximately 880mb) for the Arabian Sea (40-75°E cross-section). Top: June, middle: July, bottom: August.

In June in the Arabian Sea, while the monsoon is still establishing, both Pliocene runs transport more moisture (about 20 gm/kgs more) than present day past 12°N (Figure 3.21, a). Flux turns negative for present day at 16°N, well away from the northern Arabian coast, while for both Pliocene runs it remains positive past 20°N - nearly all the way to the Gulf of Oman. In July (panel b), the latitude at which the Pliocene transports more moisture than the present day shifts northward slightly to 14°N (Plio) and 15°N (PlioMSST); Plio has slightly more noticeable higher levels of moisture which are carried further north than PlioMSST. The present day moisture flux remains positive until 18°N, while the Pliocene experiments retain their northerly extent. Flux rates increase by $\sim$20 gm/kgs for all experiments. August (panel c) sees similar maximum flux rates as in July for all experiments. For the present day, the northward flux behaves in a very similar way to July. However, for the Pliocene runs, flux rates drop at a lower latitude than in July, with Plio transporting only $\sim$5 gm/kgs more than the present day past 14°N and PlioMSST barely transporting more moisture than the present day past 17°N.

In the Bay of Bengal (Figure 3.22), Both Plio and PlioMSST are very dry compared to the present day in June (a), with moisture barely changing meridionally - values of 15 gm/kgs on average upon approaching the Bay of Bengal. The present day moisture flux, however, more than doubles from equator to its maximum value of 70 gm/kgs at about 12.5°N, at the southern edge of the bay. Moisture supply increases for all scenarios in July (b) by about 20 gm/kgs, while maintaining very similar flux gradients. The present day maximum now peaks at 100 gm/kgs (up from 80 gm/kgs in June) while both the Pliocene experiments reach highs of 40 gm/kgs (up from 15 gm/kgs). Even by August (c), peak moisture flux rates for the Pliocene do not reach levels seen in June by the present day. During peak monsoon activity, in July (b) and August (c), the northward moisture flux depletes for the present day at about 24°N (the northern edge of the bay). For the Pliocene, PlioMSST reaches values approaching 0 gm/kgs in August at the same latitude.

The eastward moisture flux (Figure 3.23) provides higher rates of moisture to the Bay of Bengal than the northward flux - 150-250 (50-10) gm/kgs for the present day (Pliocene) compared with 70-120 (18-40) gm/kgs for present day (Pliocene) from the south. for July (b), the present day gets a third (100 gm/kgs) of the moisture supplied to the Bay of Bengal from the south and two-thirds (240 gm/kgs) from the west. Plio/PlioMSST receive less than a quarter (40 gm/kgs) from the south, while the rest of the moisture is being supplied from the west(110/130 gm/kgs for Plio/PlioMSST). Also notable is the reduction in eastward moisture flux for the present day over the BoB, where intense rainfall occurs; for both Pliocene runs

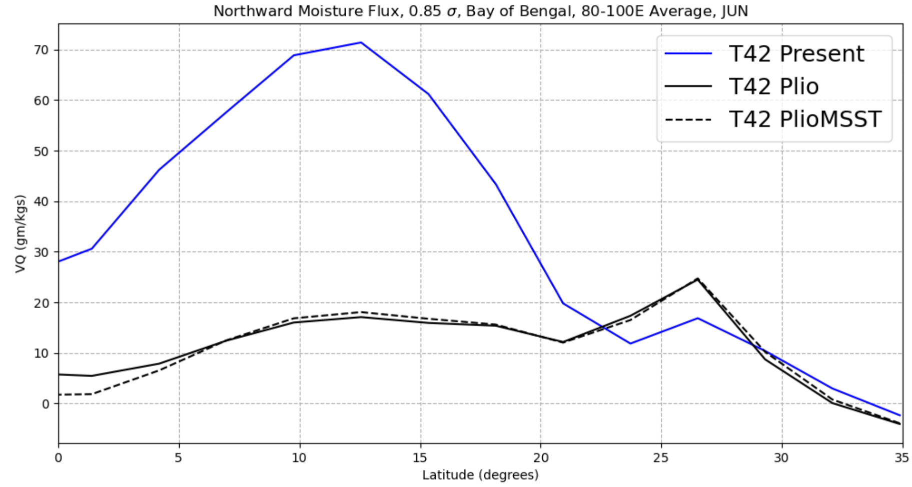

(a) June

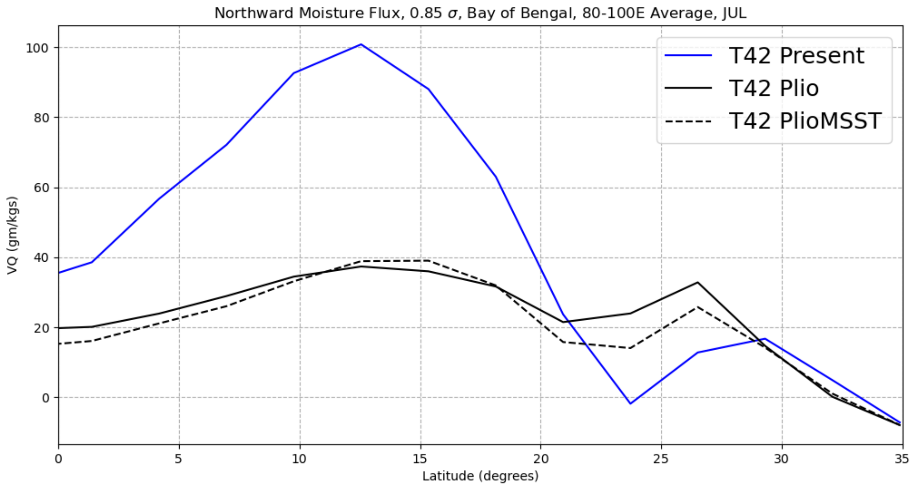

(b) July

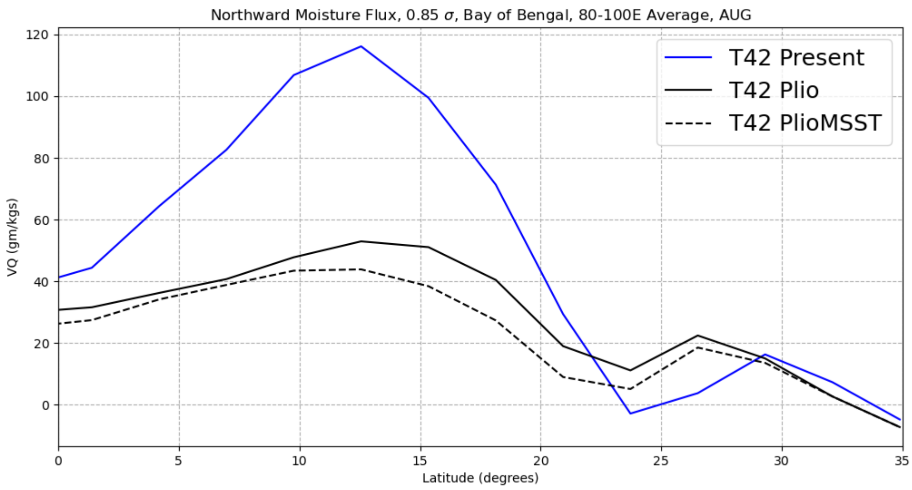

(c) August

Figure 3.22: Northward moisture flux at the 0.85σ model level (approximately 880mb) for the Bay of Bengal (80-100°E cross-section). Top: June, middle: July, bottom: August.

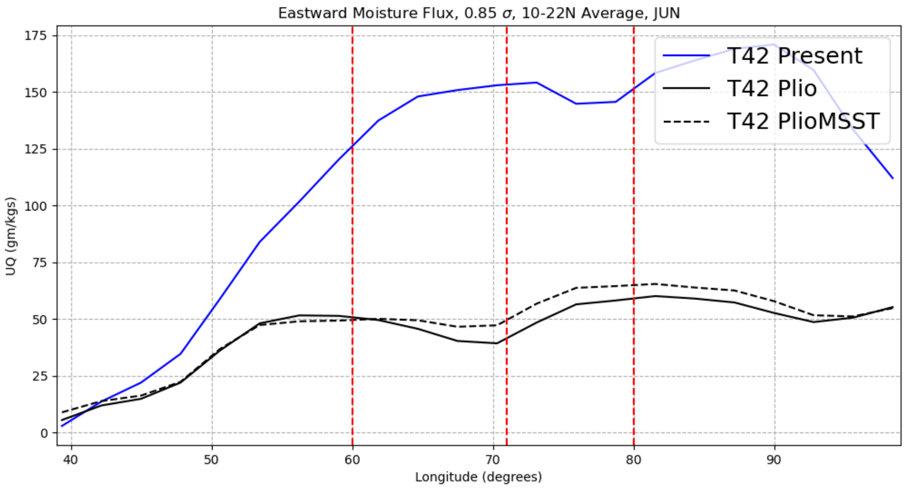

(a) June

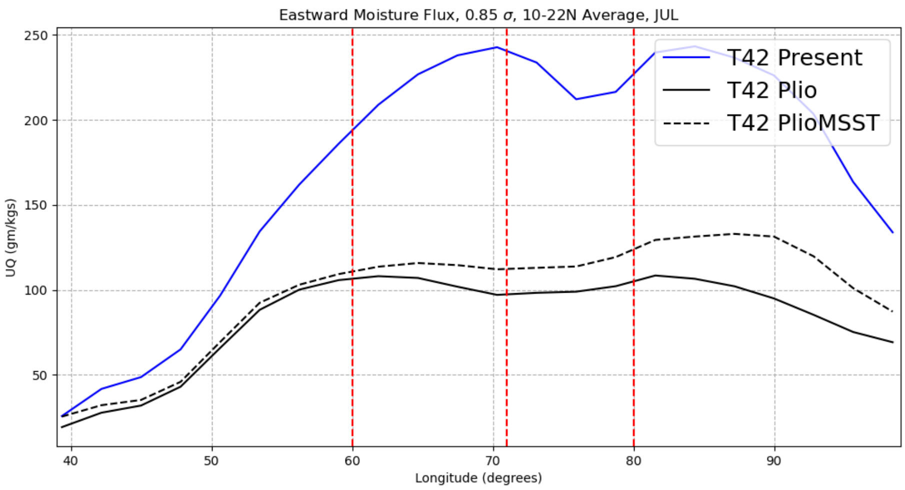

(b) July

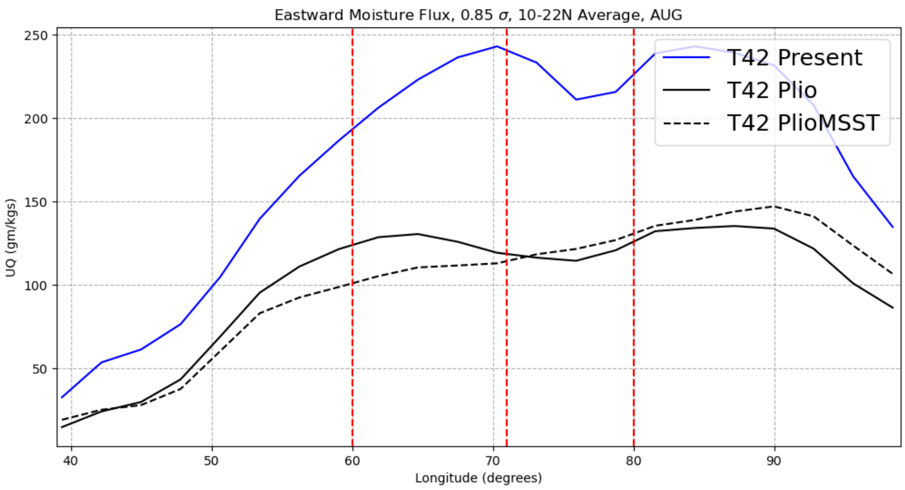

(c) August

Figure 3.23: Eastward moisture flux at the 0.85σ model level (approximately 880mb) for the Arabian Sea and Bay of Bengal (10-22°N cross-section). Dashed red vertical lines indicate the approximate locations of the western Arabian Sea, eastern Arabian Sea and western Bay of Bengal (left to right). Top: June, middle: July, bottom: August.

the moisture flux increases over the area and does not reduce, with the exception of Plio in August (c, black line) which sees a small reduction. Overall, moisture flux entering the BoB area in the Pliocene is about half that of the present day, with Northward flux playing a less significant role than in the present day. Two to two and a half times the moisture is supplied into the Indian Peninsula from a western direction in the present day compared with both Pliocene runs across the monsoon season, with even more moisture gained before reaching the western boundary of the BoB. The Pliocene scenarios, on the other hand, sees similar values upon entering/leaving the Indian Peninsula (eastern Arabian Sea/western BoB).

3.3 Discussion

3.3.1 Model Bias

While there clearly are some substantial biases in rainfall within the IGCM, these fall within the envelope of the Coupled Model Intercomparison Project (CMIP) phase 5 ensemble (Joshi *et al.* (2015)), indicating that the performance of the IGCM is not far from state of the art GCMs and highlighting the difficulty in capturing monsoonal features in climate models. Even within the CMIP project, improvements in representation of the monsoon between CMIP3 and CMIP5 still have not corrected systematic, pattern biases in the region (Sperber *et al.* (2013)). Regional climate models provide significantly increased resolution compared with global models and aim to represent local features more successfully, but even those have difficulty simulating the monsoon with rainfall biases relating to local processes (Lucas-Picher *et al.* (2011)).

Lucas-Picher *et al.* (2011) also mention the spareness and elevation of observational stations as a possible source of bias, stating that precipitation amounts are not well observed and probably underestimated in the Himalayas and Ghats in India for example, due to stations probably being situated in the valleys as that is where cities are located. Matthews *et al.* (2013) explored biases in observations using the TRMM dataset in Papua New Guinea, attributed to different phases of the Madden-Julian Oscillation, and found that TRMM data underestimates rainfall rates significantly in a number of key locations in the research area.

Overall, the climatologies of the low resolution IGCM and the observational data presented are similar (Joshi *et al.* (2015)) and the averaged error between model resolutions is negligible.

3.3.2 In the Pliocene

A change in wind patterns in the Arabian Sea is seen in the Pliocene, starting April (Figure 3.8, panel e). This increase in meridional wind component of the Somali jet strengthens in May (h) with the addition of an easterly flow around 10°N extending down to the equator. Under present conditions the flow in this region, though very weak, has no easterly component and is almost purely southerly. The easterly flow seen in the Pliocene continues into the monsoon season and is visible into June (k), with a near pure easterly flow just north of the equator.

A second, high-impact effect on monsoon dynamics in the Pliocene occurs from this northward displacement of Somali jet flow: it causes moist ocean air to flow over land north of the Arabian Sea; into the Arabian Peninsula and eastwards over northern India. This flow transforms low level clouds over the Arabian Sea seen in April (Figure B.2) into convective clouds of increasing strength throughout the Monsoon season (Figure 3.6). These convective systems cause cooling over the land surface through a reduction in incoming solar radiation in one important key area: the monsoon heat low over northern India. This cooling, compared with present conditions, weakens the north-south pressure gradient essential to monsoon development: the weakened meridional pressure gradient in turn would have an effect on the Somali jet, weakening it further and reducing upwelling off the coast of Somalia. The slower Somali jet then transports air of already less negative PV into the northern hemisphere (Figure 3.10), resulting in its northward and westward expansion.

Rai *et al.* (2018) examine the role of potential vorticity anomalies in the Somali Jet during active(wet) and break(dry) events using reanalysis data. Analysis of these anomalies shows a mechanism whereby SST anomalies propagate north/north-westwards through the Arabian Sea, caused by a positive feedback loop joining anomalies in SST, convection, modification of PV by diabatic heating and mixing in the atmospheric boundary layer, wind-stress curl, and ocean upwelling processes. Positive SST anomalies in the southern Arabian Sea precede a break event and cause increase mixing of PV, leading to a negative PV anomaly in the northern Arabian Sea and induced anticyclonic anomaly. Next, the negative anomaly causes downwelling wind stress curl which leads to surface warming. This depends on the depth of the ocean mixed layer and requires a coupled GCM to simulate. However, the atmospheric portion of the process bears resemblance to the anomalies shown between the Pliocene/PlioceneMSST simulations and the present day - the meridional SST gradient, especially in the Arabian Sea, is negative. Similarly to Rai *et al.* (2018), a negative PV anomaly develops in the northern Arabia sea, and the monsoon region is significantly drier compared to the present.

The convective clouds seen in the Pliocene might feedback further onto the northward-shifted flow seen in the Pliocene compared with the zonal flow over the Arabian Sea and Indian subcontinent seen under present conditions. Through means of potential vorticity conservation, Hoskins and Rodwell (1995) show that deep convection may cause enough friction in the atmosphere to lead to a reduction in vorticity, which in the northerly part of this cross-equatorial flow implies a less zonal flow with a northerly tilt.

The PlioMSST experiment reveals two main features - (1) the meridional gradient is the main factor responsible for the position and strength of the Somali jet through potential vorticity advection while (b) SSTs in the western Arabian Sea affect the resulting rainfall pattern by controlling available moisture to the jet. For the present day, with higher meridional moisture flux rates, this leads to an increase in available moisture for the main monsoon region.

Chung and Ramanathan (2006) examine observational data and use model simulations to show that the summertime weakening in SST gradient weakens the monsoon circulation, resulting in less monsoon rainfall over India and excess rainfall in sub-Saharan Africa.

Moisture flux analysis (Figure 3.21, Figure 3.22, Figure 3.23) shows major differences between Pliocene and present day during late onset (June): for the present, there is no northward flux inland into the heat low area during monsoonal onset; in both Pliocene runs (and a little more so in the Plio scenario), the northward flux provides available moisture. During peak monsoon season, the much lower levels of moisture supply in both Pliocene show shed light on the cause of reduced rainfall in the BoB.

The Indian Ocean Dipole (Webster *et al.* (1999),Saji *et al.* (1999)) is a relatively recent discovery, affecting weather patterns across the Indian Ocean (Jain *et al.* (2021), Ratna *et al.* (2021)). However, its relationship with the El-Niño Southern Oscillation (ENSO) (Ratna *et al.* (2021) and references therein, Hameed *et al.* (2018),Stuecker *et al.* (2017),Izumo *et al.* (2010)) remains unclear. Yu *et al.* (2021) suggest a link between ENSO and SAM rainfall which can be identified by correlation of Tropical Indian Ocean SSTs as a whole, rather than the west-east SST difference that is the IOD.

Although previous studies have shown that SST changes in the Indian, Pacific and Atlantic oceans influence the SASM rainfall, the combined and independent contributions of these three regions are unclear (MA *et al.* (2019)), further highlighting the complexity of this monsoon region.

3.4 Conclusions

A month-by-month analysis of the SAM is presented, showing differences in monsoonal onset between the present day and Pliocene scenarios. Fundamental differences between the basic states of present day and Pliocene South Asian monsoon were found. The northerly shift of the Somali jet further into the Arabian Sea and inland in the Pliocene compared to present day causes a change to moisture supply and convective rainfall in both branches of the monsoon. A mechanism to explain the northward shift in wind circulation and the resulting anticyclonic flow in the

Arabian Sea is proposed through means of potential vorticity conservation and its advection from the southern hemisphere. An idealised SST experiment consisting of a meridional-only SST change in the Indian Ocean, further separating the effect of SST change on the SAM, is used to determine the significant impact of meridional gradient changes. Although the idealised experiment (PlioMSST) is very similar to the Pliocene in the main monsoon area, there are some differences in moisture transport and rainfall over the Arabian Sea.

Since the model used in this analysis is an atmosphere only GCM, it is difficult to determine whether this change of flow emerges as a result of the already weakened monsoon system, as preserved in paleo-proxies and expressed by different sea surface temperatures controlling the model, or if it is part of the forcing on the monsoon system, helping to create the weaker monsoon in the Pliocene instead of acting as a positive feedback mechanism to the weakening of the monsoon. Further investigations using a coupled GCM may aid this, to examine whether or not this flow can be maintained and what its effects will be on the sea surface temperature field, when allowed to adapt to the climate.

Chapter 4

South Asian Monsoon: Effects of Increased Resolution

4.1 Introduction

Building on the previous South Asian monsoon chapter (chapter 3), this chapter will provide an analysis into the effects of increased resolution - both dynamical and topographic, on the South Asian monsoon (SAM) in the Pliocene and under present day conditions, as depicted in the IGCM.

The geographical region includes several distinct orographic features: the Himalayan mountains/Tibetan plateau, the East African mountains, and the western Ghats in India. Thus, this makes for an interesting area in which to explore the effects of increased resolution on climate: past and present. The difference in model topography between the three model resolutions in the Indian Ocean region is displayed in Figure 4.1.

First, a validation of high resolution and hybrid (high resolution dynamics with low resolution topography, see section 2.2) model configurations will be shown, building upon the previous low resolution equivalent in subsection 3.2.1. In section 4.2, results of increasing dynamical model resolution alone: from low, T42 integrations to hybrid which includes high resolution dynamics with the same low resolution topography will be shown. Following this, results of increasing the topographic resolution in addition to the dynamical resolution: from hybrid (high resolution dynamics combined with low resolution topography) to a full high resolution, T170 configuration dynamic and topographic resolution will be presented - in terms of the Pliocene scenario itself and the differences between Pliocene and present day for each resolution case. It is thought to be the first analysis of its kind - separating

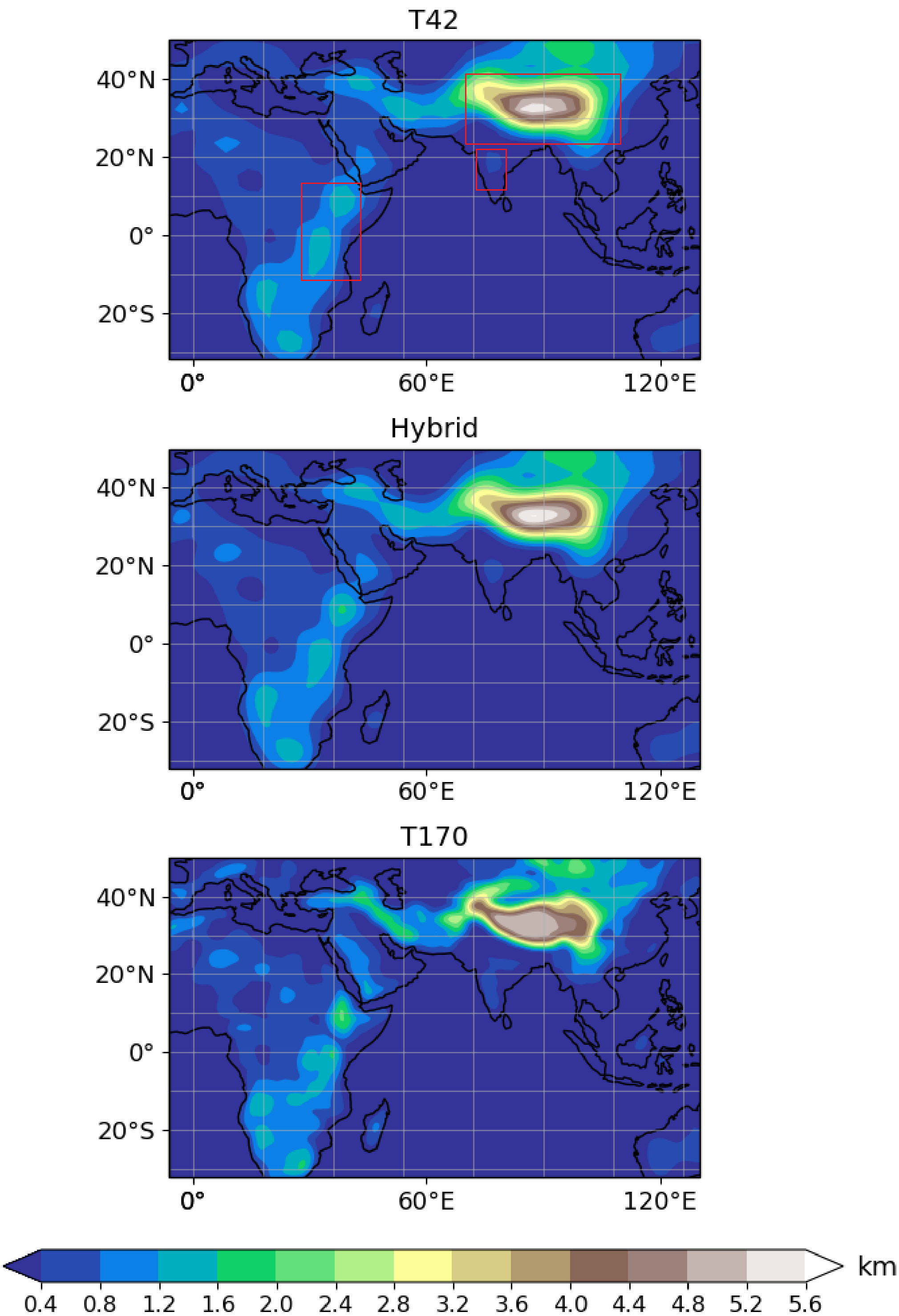

Figure 4.1: Model topography for each of the three model resolutions for the South Asian monsoon region. Low resolution (top); hybrid (middle); and high (bottom). The hybrid topography field is the same as low resolution but displayed on a horizontal grid with four times the resolution. Major topographical features marked with a thin rectangle; west to east: East African mountains, Western Ghats, Tibetan Plateau.

the dynamic and topographic effects of resolution for the Pliocene climate. in section 4.3, discussion of changes to model bias and the overall effects of resolution on Pliocene climate and in general follows, and finally section 4.4 conclusions are drawn upon this investigation into resolution for the South Asian monsoon area.

4.2 Results

Figures in this section all follow the same layout matrix (unless otherwise stated). Top row shows the two scenarios - Present day and Pliocene (panels a,b) and the difference between them (c) for a given model resolution. Middle row displays the same for a different resolution (d,e and f) while the bottom row deals with differences between the two resolutions for a given scenario (g,h) and a final difference-of-differences panel (i, panel f-c or h-g), describing the effect of model configuration change on the Pliocene response compared to present day. All plots are a June, July, August, September (JJAS) average.

4.2.1 Representation in IGCM

In order to have more confidence of the effects of resolution on the Pliocene climate, we first examine the change to present day conditions with increasing resolution compared with observations. This builds upon the analysis in subsection 3.2.1, with fields now shown as an average of June, July, August and September (JJAS) as opposed to the month-by-month analysis in the previous chapter.

An improvement to the JJAS averaged rainfall difference with increasing resolution from low to hybrid is seen in Figure 4.2. The over-representation of rainfall in the Bay of Bengal in the IGCM is reduced by about 10 mm day^{-1} under hybrid model configuration (panel h/i) and the under-representation of rainfall further north is nearly completely gone (panel f), with rainfall amounts in this area increasing by 10-12 mm day^{-1}. In northern India, there is slightly too much rainfall under hybrid resolution (f), with a further increase in rainfall of 6 mm day^{-1} west of the Indian Peninsula (h/i).

Improvement is also seen on top of the Tibetan Plateau, where two positive rainfall bias peaks have been transformed and are now uniformly spread over the area (panels c,f). In eastern Africa, the very high (18-20 mm day^{-1}), centred bias around the western Afar region (10°N, 40°E) is all but removed under hybrid resolution (panels c,f). Another improvement is noted over the South China Sea, where rainfall amounts are an average of 6 mm day^{-1} lower west of the Philippines. The

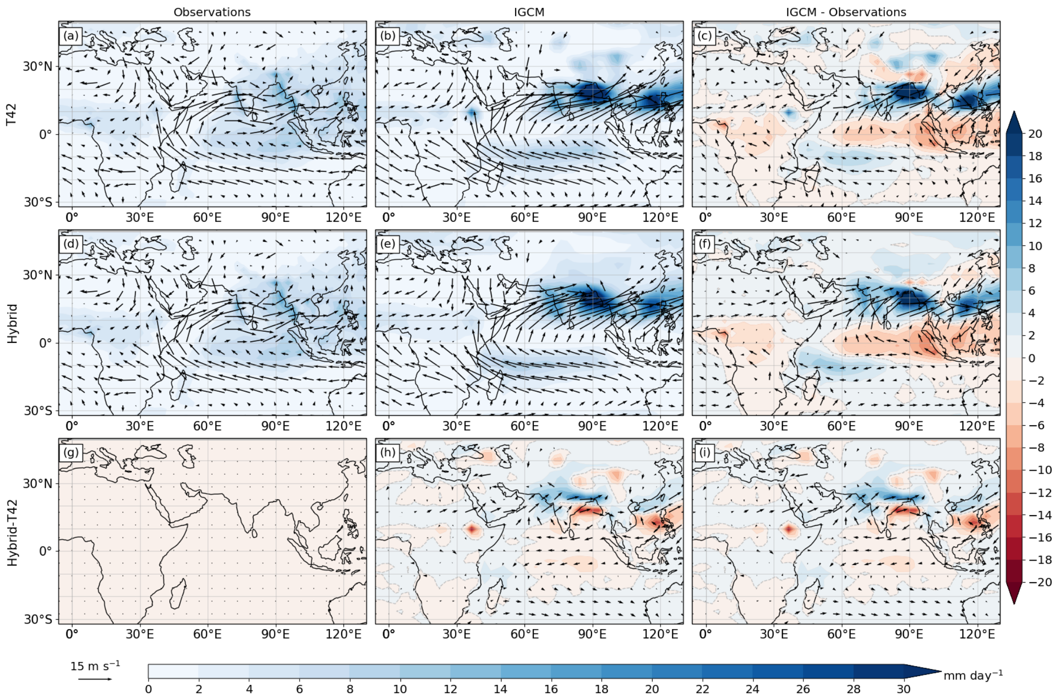

Figure 4.2: JJAS averaged rainfall and wind vectors under low (top row) and hybrid (middle row) resolutions for the Indian Ocean region. Panels a,b,d,e show full fields for observations (left) and IGCM in the present day (middle) with contour intervals of 2 mm day^{-1} (bottom). Differences between fields are shown on the bottom row and right column with same contour intervals.

winds of the Somali jet are already too strong in the lower resolution of the model, and seem to be even stronger (by about 10 m s^{-1}) in its northern section under hybrid resolution (f). In addition, the northern extent of the jet seems to shift slightly northwards, in accordance with the aforementioned changes to rainfall in northern India (h/i).

Progressing to high resolution (Figure 4.3) sees a notable Himalayan rain band appear (6 mm day^{-1} to 14 mm day^{-1}, panel e), though it is misplaced compared with observations and appears slightly too far north (f). The Bay of Bengal sees another decrease in rainfall of an average of 6 mm day^{-1} which helps correct the bias in this area (panel h/i). off the western Indian coast, an improvement is seen in the over-representation of rainfall over the eastern Arabian Sea, displaying a narrower rain band, and the rain shadow effect to the east of the Western Ghats (15°N, 82°E) is better captured (e,f). Winds are almost unchanged from its hybrid equivalent, with a very slight reduction in wind speeds in the Arabian Sea under high resolution.

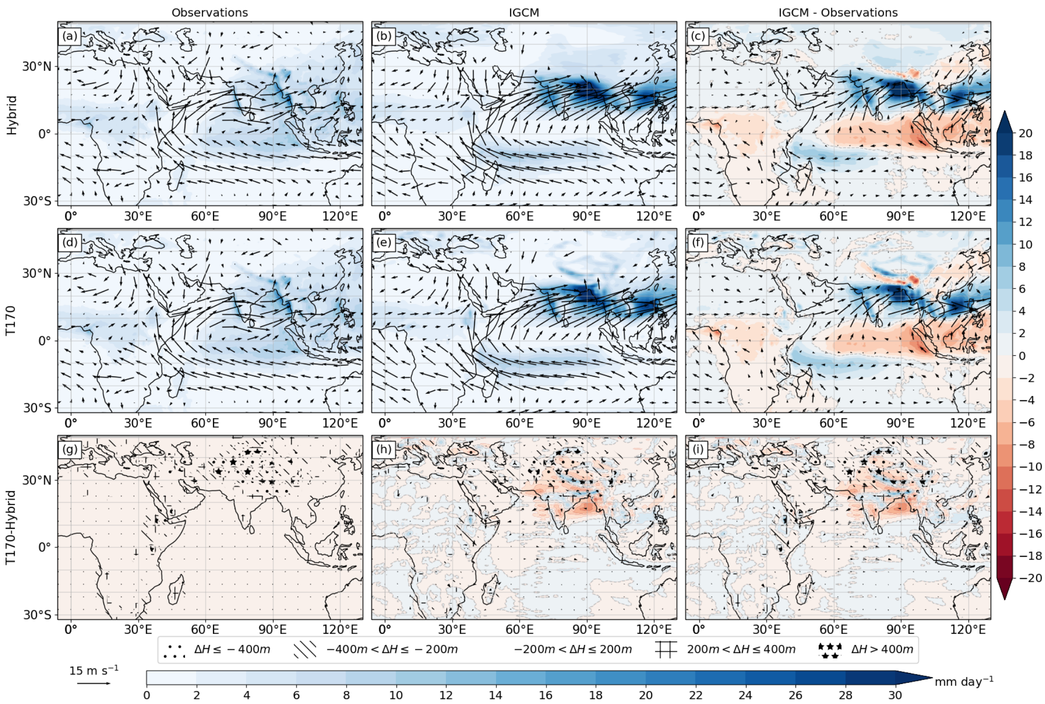

Figure 4.3: Same as Figure 4.2 but for hybrid (top) and high (middle) resolution.

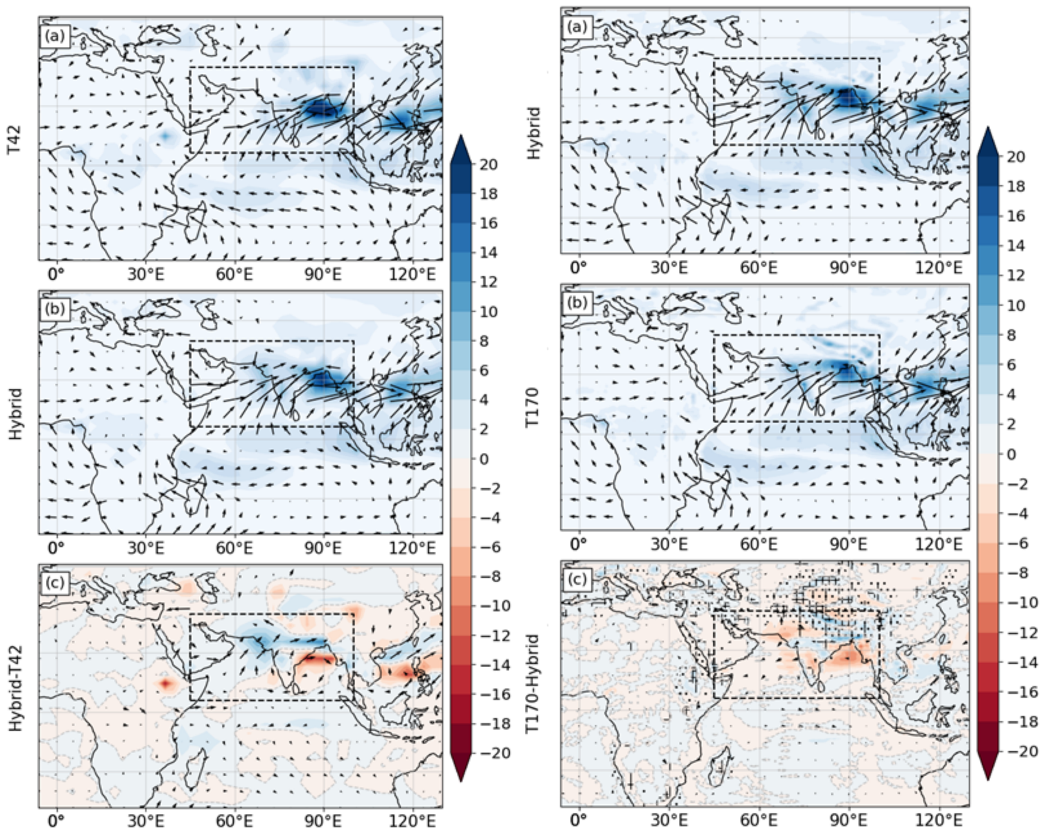

(a) Low and Hybrid

(b) Hybrid and High

Figure 4.4: Absolute error of different model resolutions and the change in absolute error with increasing resolution. Left: low and hybrid resolutions, right: hybrid and high resolutions. Dashed rectangle indicates the area over which the averaged absolute error was calculated.

Figure 4.4 shows model absolute error between all different resolutions utilised. An area average was performed on the main monsoon domain in order to quantitatively assess changes to how the IGCM captures rainfall amounts across resolutions. Absolute error increases by approximately 15% between low (4 mm/day) and hybrid (4.6 mm/day) resolutions - the improvement in the Bay of Bengal area seen under hybrid resolution is overshadowed by the introduction of a larger, area-averaged error in the northern portion of the peninsula. Increasing model resolution further to full high resolution reduces the absolute error down to 3.8 mm/day, a 5% improvement on the area-averaged error under low resolution. Areas of increased error are almost exclusively in areas of topographic change, while the error improves further in the Bay of Bengal and to the west/north-west of the Indian peninsula.

Overall, the high resolution IGCM model integration provides the most realistic rainfall pattern of the three resolutions, albeit winds in the northern portion of the Somali jet being too strong. Model error remains stable for the domain compared with low resolution, with only a 5% change. The high resolution integration combines the benefits of high resolution dynamics introduced under hybrid resolution, which allow for smaller phenomena to be resolved by the model, alongside a more accurate representation of topography - without compromising model accuracy.

4.2.2 Dynamical Resolution

Increasing the model's dynamical resolution (low versus hybrid) leads to some large differences in surface temperatures between Pliocene and present day (Figure 4.5, panel f). The Pliocene is now 2°K warmer to the north of the Arabian Sea instead of 6-8°K colder, the eastern Arabian Peninsula is only 4°K colder (down from 8°K) and the warm anomaly to the north of the Bay of Bengal has nearly disappeared. The maximum temperature difference between present day and Pliocene is now just 3°K on land. This decrease in temperature differences between low and hybrid resolutions is due to the resolution effects on the present day (panel g) being more severe than for the Pliocene (panel h): though both scenarios seem to mainly experience cooling with increase in resolution, the cooling in northern India (10°K and over) spreads further west under present day.

West of the Arabian Sea, the present day cools by 3-4°K on average while the Pliocene experiences no significant change. The Pliocene exhibits stronger cooling in the Himalayan band only, but the magnitude of this cooling is small in comparison to that seen under present day conditions and amounts to 3°K over the area (panel i).

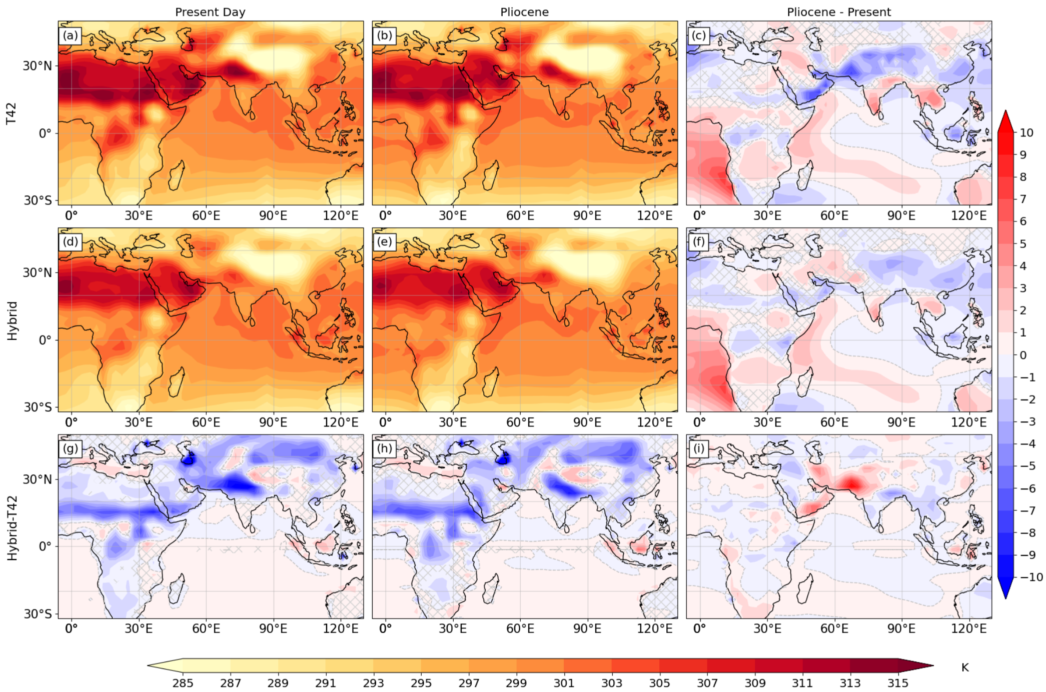

Figure 4.5: JJAS averaged surface temperatures under low (top row) and hybrid (middle row) for the Indian Ocean region. Panels a,b,d,e show full fields for present (left) and Pliocene (middle) with contour intervals of 2°K (bottom). Differences between fields are shown on the last row and right column with contour intervals of 1°K. Grey hatching indicates areas below the 95% significance threshold using a student's T-test.

Total precipitable water (TPW) (Figure 4.6), calculated as a vertical sum of absolute humidity for a given grid-point, shows a change in availability of precipitable water in the northern Arabian Sea and further north inland (panel i). Under hybrid model configuration, the Pliocene has less precipitable water across Asia (panel f). This is not the case for low resolution configuration where the Pliocene has more precipitable water in the Pakistan region (around 25°N, 70°E) (panel c). Considering the effect of resolution on each scenario (panels g,h) reveals that under hybrid resolution the Pliocene only gains precipitable water in northern India, essentially expanding the area of already high TPW levels slightly northwards, while the present day scenario sees an increase in precipitable water amounts within existing areas in the Arabian Sea and Northern India alongside a northward expansion similar to that seen in the Pliocene. These changes occur in the same areas as the changes to surface temperatures, shown in Figure 4.5. There is also a slight change in structure seen for the present day between resolutions (a,d) with a clearer hemispheric separation of TPW while the Pliocene scenario remains very similar under increased dynamical resolution.

The changes in total precipitable water levels subsequently follow on to respec-

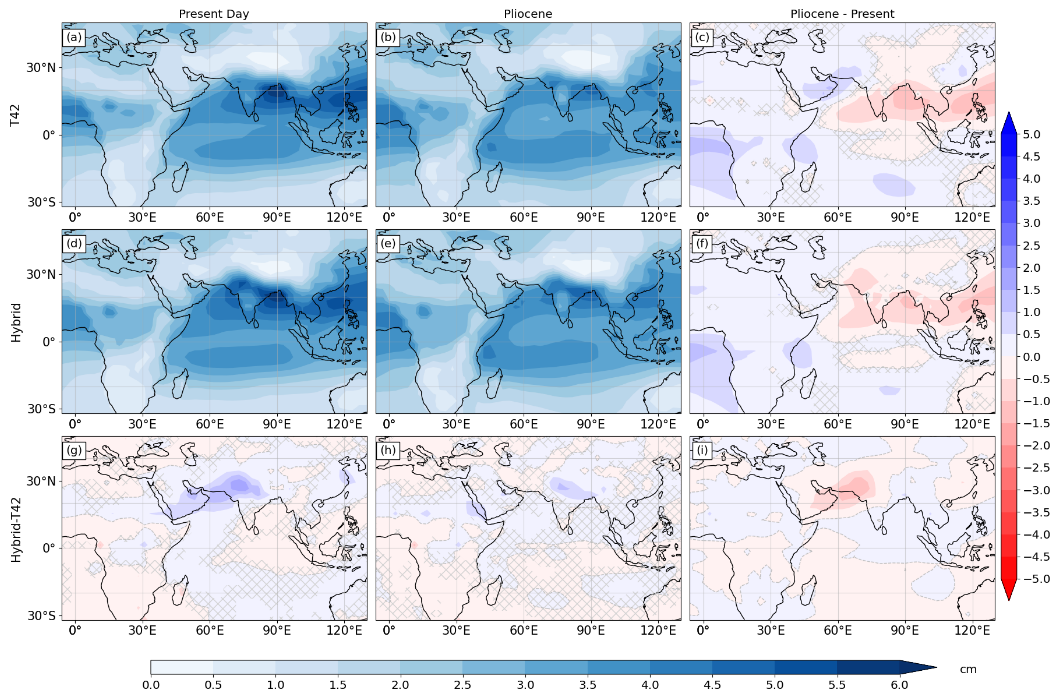

Figure 4.6: JJAS averaged total precipitable water under low (top row) and hybrid (middle row) resolutions for the Indian Ocean region. Panels a,b,d,e show full fields for present (left) and Pliocene (middle) with contour intervals of 0.5 cm (bottom). Differences between fields are shown on the last row and right column with same contour intervals. Grey hatching indicates areas below the 95% significance threshold using a student's T-test.

tive changes in convective cloud amount (CCA) (Figure 4.7). The diagonal divide of convective cloud differences over the Arabian Sea persists through resolutions, with the Pliocene having increased convective cloud over the north-western portion of the Arabian Sea and present day dominating over the south-eastern portion, continuing on to the Bay of Bengal (panels c,f). However, further inland over northern India, where changes in TPW were seen with increased resolution, there is a shift in the difference field - present day now has more convective cloud than the Pliocene (f). In addition, the trail of convection in the Pliocene hybrid case compared with present day is not so pronounced, owing to a general increase in convective cloud under hybrid resolution for the present day in northern India (panels g,i). Resolution increase seems to increase convective activity overall north of 10°N, particularly over the Tibetan Plateau and northern India (g,h). CCA over the Pakistan region increases for the present day only, causing the aforementioned shift in the difference field.

The increase in optically thick convective cloud for the present day with increasing resolution translates to a decrease in incoming solar radiation of 60-80 W m^{-2} (Figure 4.8, panel i). The pattern of changes seen in incoming solar radiation are very closely related to those changes in convective cloud. Together, these two fields explain the most major differences in surface temperature discussed earlier - ultimately leading to a colder surface temperature under present day in the hybrid model configuration in this area.

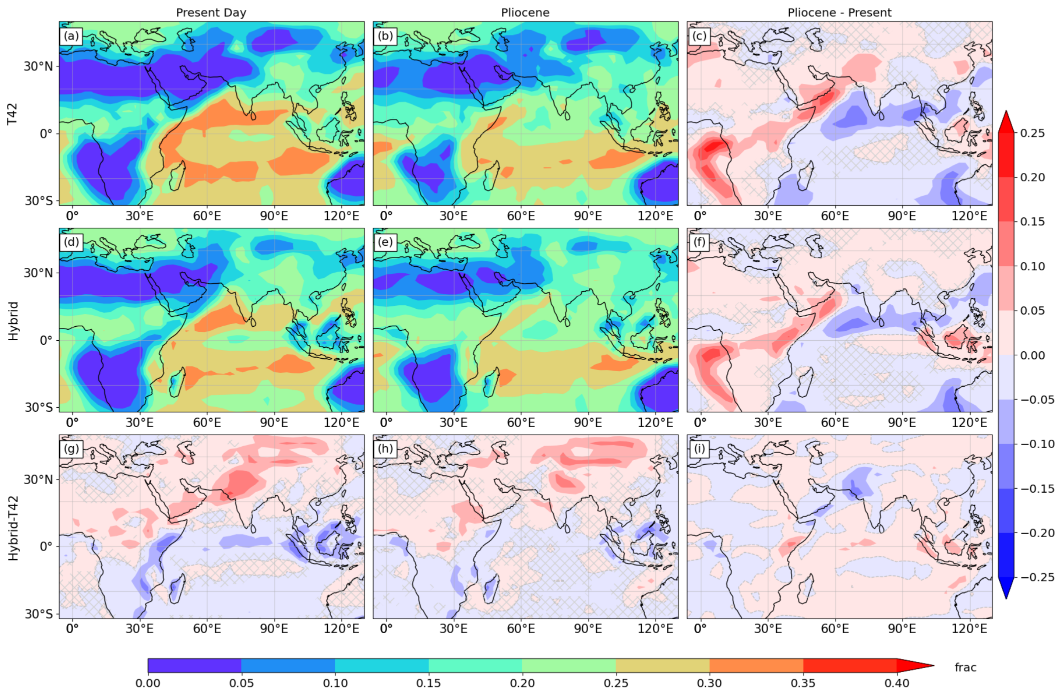

Figure 4.7: JJAS averaged convective cloud amount under low (top row) and hybrid (middle row) resolutions for the Indian Ocean region. Panels a,b,d,e show full fields for present (left) and Pliocene (middle) with contour intervals of 0.5 (fraction)(bottom). Differences between fields are shown on the bottom row and right column with same contour intervals. Grey hatching indicates areas below the 95% significance threshold using a student's T-test.

The Pliocene is still much drier overall than the present day under hybrid resolution (Figure 4.9, panel f), though less so than in low resolution (panel c). In the western Arabian Sea, rainfall as a result of convective activity in the Pliocene still dominates. However, further inland in the Pakistan region (25°N, 28 °E), the negative anomaly becomes positive under hybrid resolution (panels c to f), with the present day now wetter than Pliocene (total change of 6 mm day^{-1} on average, panel i). Early rainout near the origin of the Somali jet (off the eastern African coast) in the Pliocene is enhanced under hybrid resolution (by 2 mm day^{-1}, panel h). Increasing model resolution has a tendency to shift existing rainfall northwards (g,h). This effect seems to greatly dry out the Bay of Bengal for the present day (6-8 mm day^{-1} less) but not the Pliocene - most probably due to rainfall amounts being already reduced in the Pliocene compared with present day.

Wind changes are confined to 20°N for the Pliocene (h) and consist mainly of

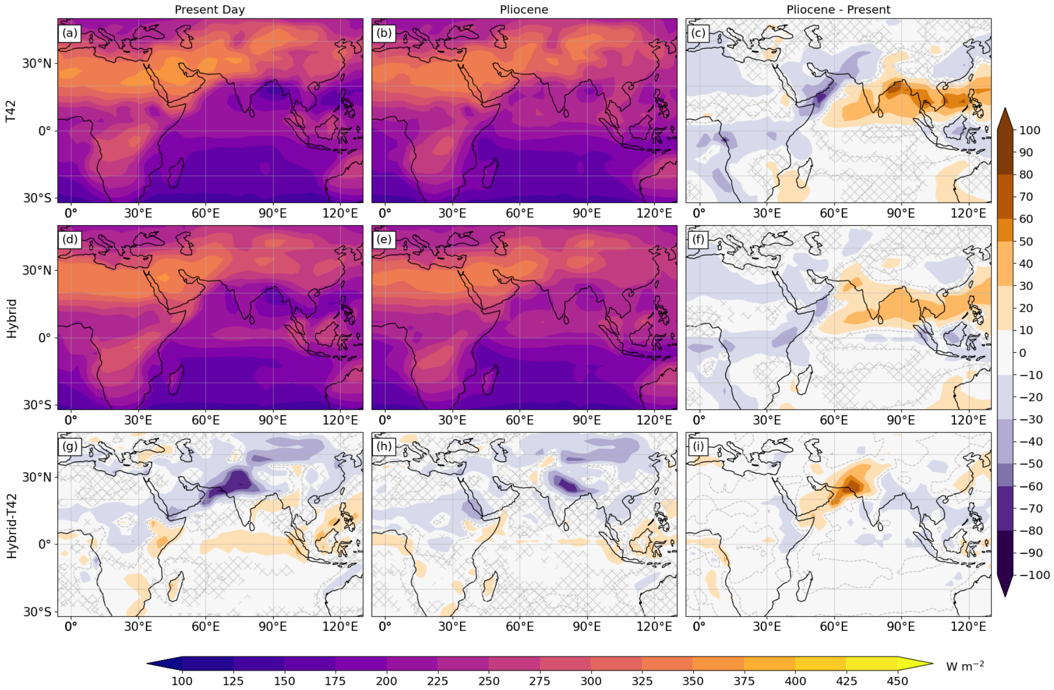

Figure 4.8: JJAS averaged incoming solar radiation under low (top row) and hybrid (middle row) resolutions for the Indian Ocean region. Panels a,b,d,e show full fields for present (left) and Pliocene (middle) with contour intervals of 25 W m^{-2} (bottom). Differences between fields are shown on the last row and right column with contour intervals of 10-30 W m^{-2}. Grey hatching indicates areas below the 95% significance threshold using a student's T-test.

a weak zonal increase in speed. For the present day, changes in the same area are greater and include a meridional as well as zonal component, bringing the flow deeper in-land than under low resolution (g). Also notable is the anti-cyclonic anomaly around the Indian Peninsula.

Circulation changes are also visible in the upper atmosphere (Figure 4.10). The difference in strength of the Tibetan high under low resolution between Pliocene and present day intensifies with increased resolution, with the biggest differences now surpassing 100m in height, spreading to the west and bordering the Arabian Peninsula (panel c,f,i). Differences in anti-cyclonic winds around the Tibetan high are also much stronger under hybrid resolution, in the area of 15 m s^{-1}. Here, increased resolution boosts the strength of the Tibetan high and its associated circulation for both scenarios (panels g,h), but causes significant westward expansion of the high only for the present day. The core of the Tibetan high stretches a remarkable 20° westwards and the Tropical Easterly Jet (TEJ) is also stronger in both the hybrid model integrations - and more so for the present day.

Ertel Potential Vorticity (Figure 4.11) shows very little change between resolutions. The jet's signature signal (discussed in chapter 3) is slightly clearer un-

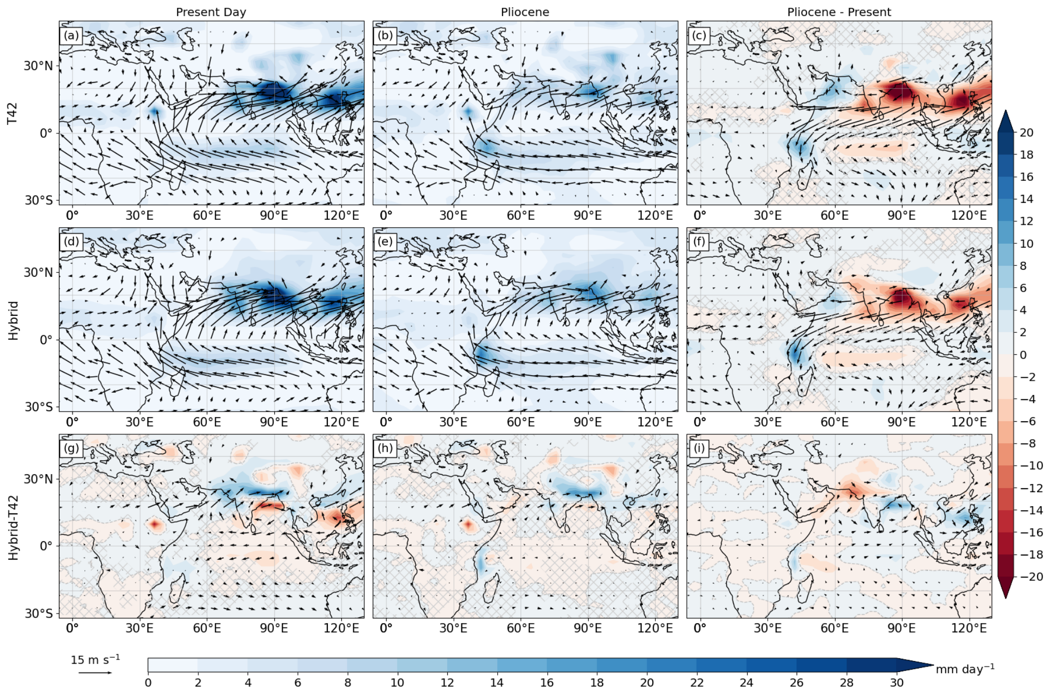

Figure 4.9: JJAS averaged rainfall and 880mb winds under low (top row) and hybrid (middle row) resolutions for the Indian Ocean region. Panels a,b,d,e show full fields for present (left) and Pliocene (middle) with contour intervals of 2 mm day^{-1} (bottom). Differences between fields are shown on the last row and right column with same contour intervals. Grey hatching indicates areas below the 95% significance threshold using a student's T-test.

der hybrid configuration (f) with any additional changes to potential vorticity to be expected as a consequence of increase/decrease of rainfall and the attributed increase/decrease in latent heat release, as discussed in chapter 3.

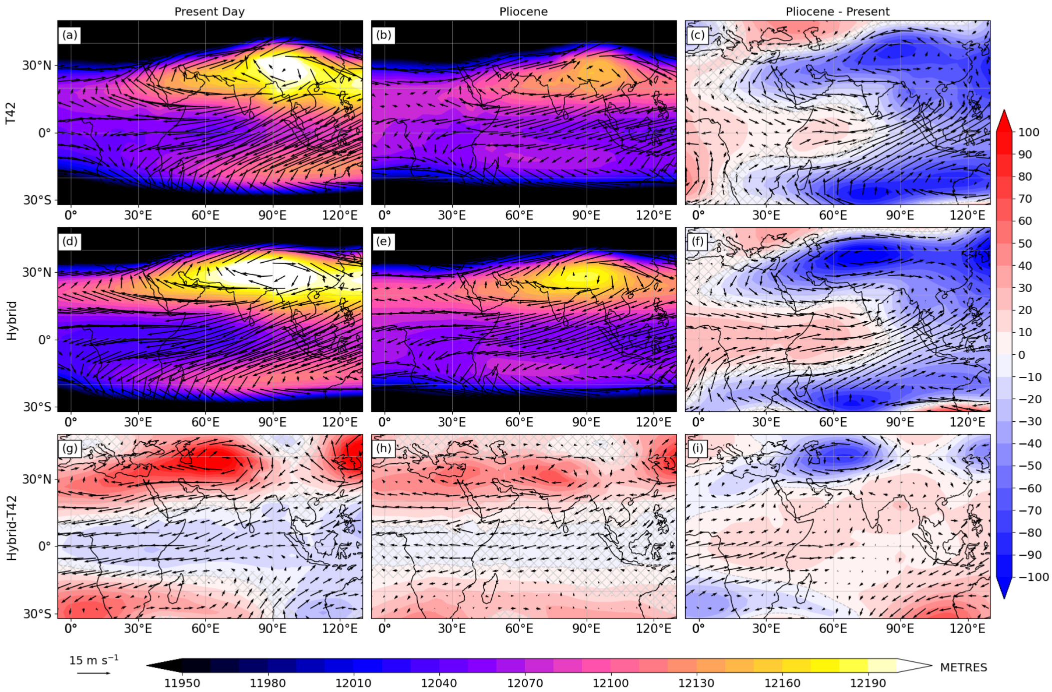

Figure 4.10: JJAS averaged geopotential height and 200mb winds under low (top row) and hybrid (middle row) model resolutions for the Indian Ocean region. Panels a,b,d,e show full fields for present (left) and Pliocene (middle) with contour intervals of 10 metres (bottom). Differences between fields are shown on the last row and right column with same contour intervals. Grey hatching indicates areas below the 95% significance threshold using a student's T-test.

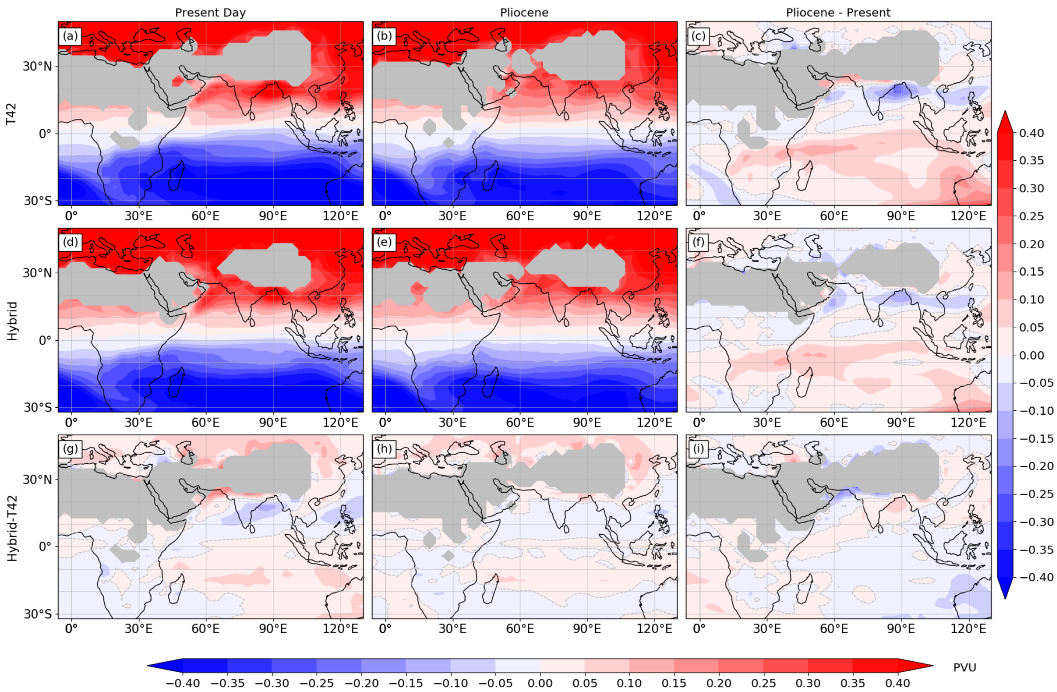

Figure 4.11: JJAS averaged Ertel potential vorticity for low (top row) and hybrid (middle row) resolutions on the 305 °K θ surface for the Indian Ocean region. Panels a,b,d,e show full fields for present (left) and Pliocene (middle) with contour intervals of 0.05 PVU (bottom). Differences between fields are shown on the last row and right column with same contour intervals.

4.2.3 Topographic Resolution

In this subsection, the usual figure layout will be complimented by hatched areas indicating differences in elevation between hybrid and high model resolution.

Figure 4.12 shows surface temperature differences between hybrid and high resolutions. As evident by hatching, nearly all differences are directly related to changes in topography and subsequent surface pressure (not shown here). As the main difference not directly related to topography seen is around the Pakistan area, and to better appreciate the changes in topography, the remaining figures in this analysis will deal with a more focused area around the South Asian monsoon, seen in Figure 4.13.

Increasing topographic resolution reverses the heating anomaly in the Pakistan area; from a Pliocene that is 3°K warmer than present day to one that is 3°K cooler (panels c,f,i). This cooling brings the Pliocene and present day surface temperature difference field closer to the original pattern seen under low resolution (Figure 4.5), though differences are now lower. The cause for change in differences between hybrid and high scenarios is seen in the present day, with the Pakistan area under high resolution being 5°K warmer than under hybrid resolution, on average, in the present day than its Pliocene counterpart (panels g,i).

Incoming solar radiation (Figure 4.14), shows increasing topographic resolution slightly increases the amount of solar radiation received at the surface for both scenarios (panels g,h). The effect is stronger in areas of higher increase in topographic height under high resolution, such as the Himalayan mountain range where an increase of 30-50 W m^{-2} is seen. This is once again supported by a decrease in convective cloud amounts in the same regions (Figure 4.15), bar the change around Pakistan which sees a decrease in convective cloud under the present day (g) without an associated change in elevation. This shows the orographic nature of rainfall in this region of the monsoon. With the slopes better defined under high resolution, convection is better constrained and occurs in a narrower band than with smoothed, low resolution topography.

Rainfall differences (Figure 4.16) also show distinctive features around topography changes, with the Himalayan rain band better defined due to the decrease in convective cloud amount to the north and south of it, narrowing the rainfall band (panels d,e). A further northward shift in rainfall is seen for the monsoon region as resolution increases (g,h), drying out the Bay of Bengal by a further 6-8 mm day^{-1} for the present day and reducing the differences between Pliocene and present day

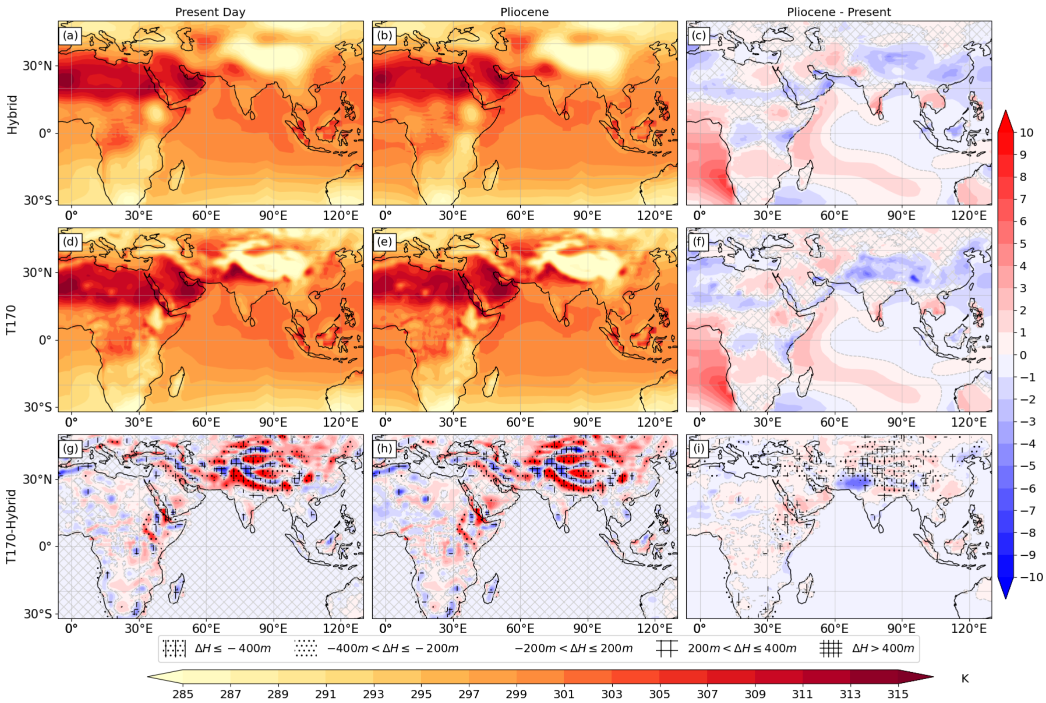

Figure 4.12: JJAS averaged surface temperatures under hybrid (top row) and high (middle row) resolutions for the Indian Ocean region. Panels a,b,d,e show full fields for present (left) and Pliocene (middle) with contour intervals of 2°(bottom). Differences between fields are shown on the last row and right column with contour intervals of 1°K. Grey hatching indicates areas below the 95% significance threshold using a student's T-test.

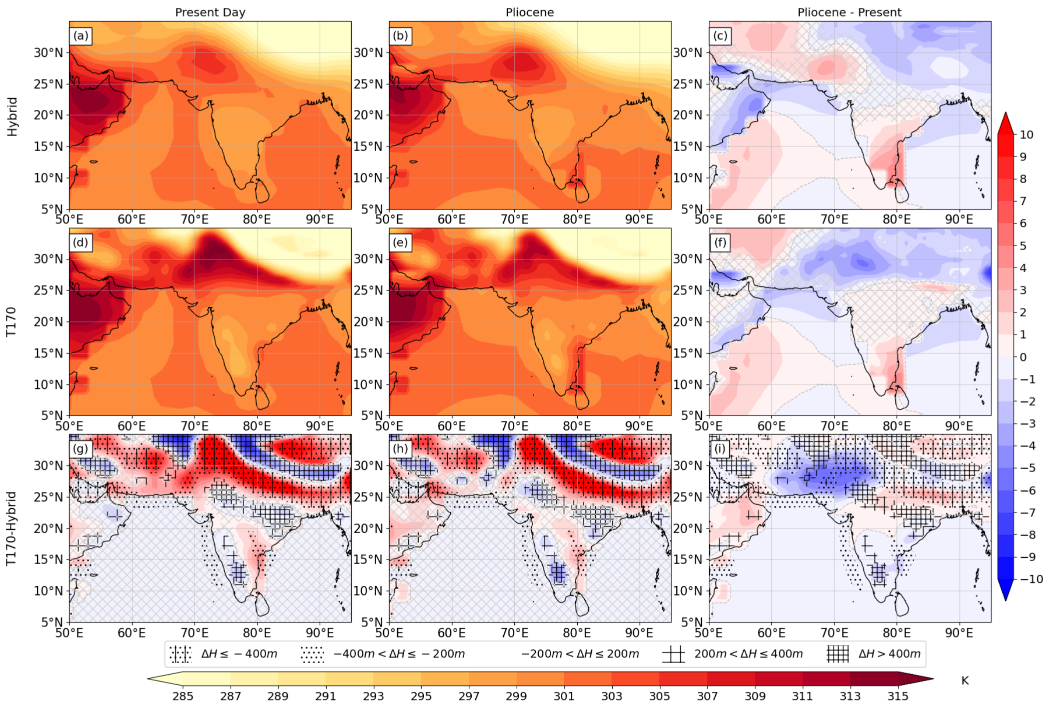

Figure 4.13: Same as Figure 4.12 but for the South Asian monsoon region.

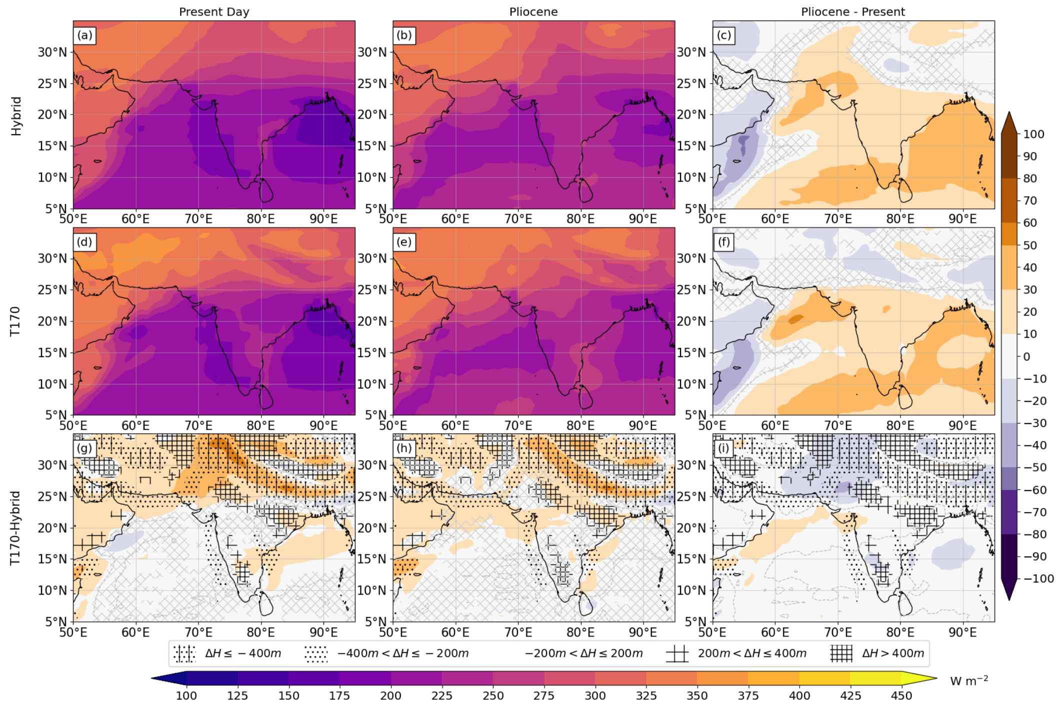

Figure 4.14: JJAS averaged incoming solar radiation under hybrid (top row) and high (middle row) resolutions for the South Asian Monsoon region. Panels a,b,d,e show full fields for present (left) and Pliocene (middle) with contour intervals of 25 W m^{-2} (bottom). Differences between fields are shown on the last row and right column with contour intervals of 10-30 W m^{-2}. Grey hatching indicates areas below the 95% significance threshold using a student's T-test.

in the bay under high resolution (f,i). An improvement is seen in the noisy nature of rainfall west of the Indian Peninsula (a,b,d,e) and, combined with the 4 mm day^{-1} decrease in rainfall in the Pakistan area under present day (panel g) means differences between present day and Pliocene under hybrid resolution are now insignificant for most of the Pakistan region (panel f). Winds, both at lower and higher levels are not substantially different and as such are not shown in this analysis.

Both dynamical and topographic resolution increases have an effect on the onset of the monsoon and its severity (Figure 4.17). Onset times vary greatly between resolutions for a given scenario with latest onset occurring under low resolution around the start of July for the present day and about three weeks later for the Pliocene. The monsoon season is also much shorter in the Pliocene, ending in early September and lasting for a month and a half while in the present day the monsoon lingers nearly until October and lasts over twice as long at three and a half months. Peak rainfall amounts are higher in the present day compared with Pliocene, with 11 and 7 mm day^{-1}, respectively.

Hybrid resolution sees a 4mm day^{-1} increase in peak rainfall amounts for both

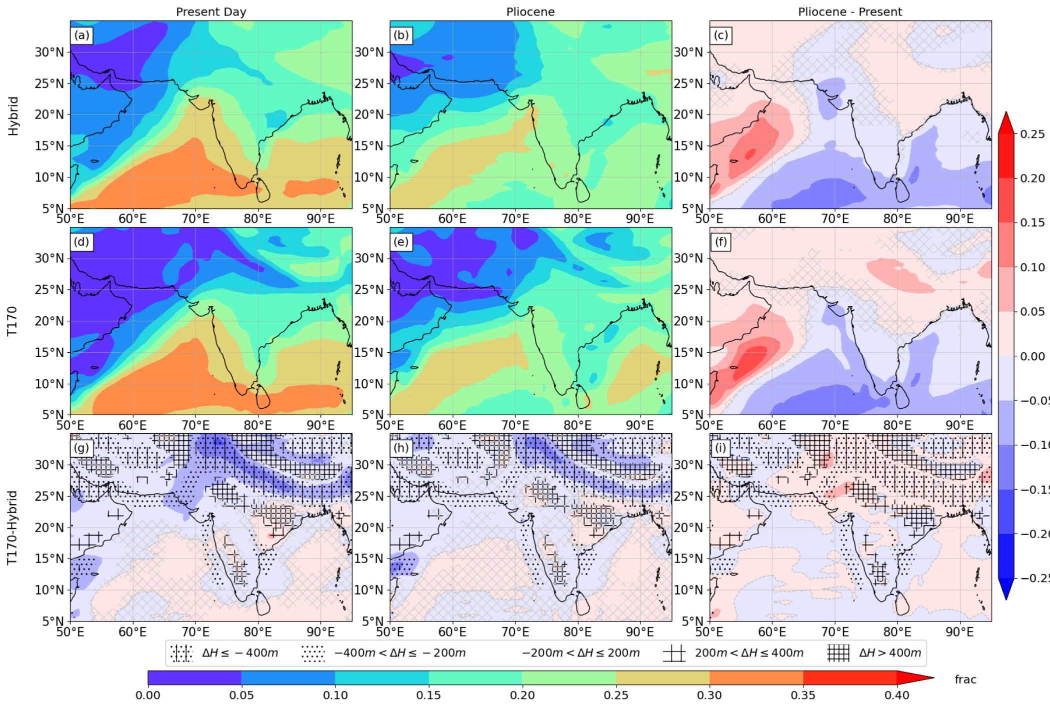

Figure 4.15: JJAS averaged convective cloud amount under hybrid (top row) and high (middle row) resolutions for the South Asian monsoon region. Panels a,b,d,e show full fields for present (left) and Pliocene (middle) with contour intervals of 0.5 (fraction)(bottom). Differences between fields are shown on the last row and right column with same contour intervals. Grey hatching indicates areas below the 95% significance threshold using a student's T-test.

scenarios compared with low resolution, with onset now occurring at the start of June for both. The monsoon season ends in early September in the Pliocene while for the present day it persists through to mid October, maintaining the gap in durations seen under low resolution. High resolution sees different effects on the Pliocene and present day: for the present day, it slightly increases peak rainfall amounts with monsoon onset occurring about a week earlier. For the Pliocene, it sees a considerable decrease in peak rainfall amounts and a shorter monsoon season lasting just over two months.

The effect of increasing topographic resolution is probably so different for the Pliocene due to the re-positioning of the Himalayan rain band outside of the area chosen for the calculation of all India rainfall (Figure 4.16), which is of the same magnitude for both scenarios and thus has a larger effect on the Pliocene with smaller rainfall amounts to begin with. This, combined with the northward drift in rainfall from the Bay of Bengal creating a secondary rain band in the present day but not in the Pliocene, negatively impacts on the monsoon in the Pliocene under high resolution.

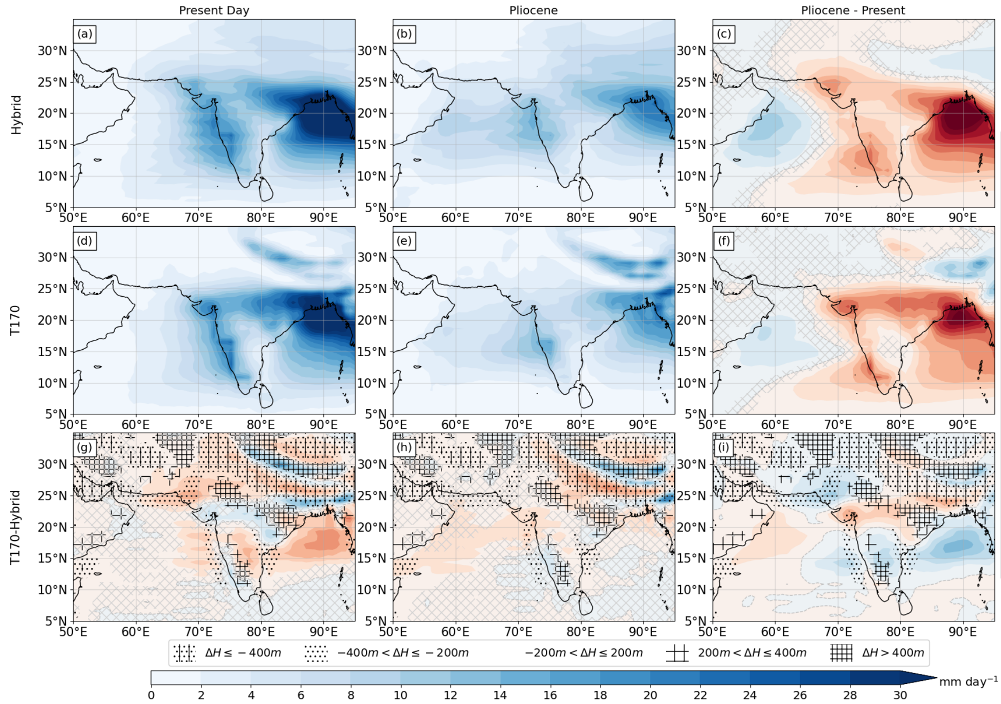

Figure 4.16: JJAS averaged rainfall under hybrid (top row) and high (middle row) resolutions for the South Asian monsoon region. Panels a,b,d,e show full fields for present (left) and Pliocene (middle) with contour intervals of 2 mm day^{-1}. Differences between fields are shown on the last row and right column with same contour intervals. Grey hatching indicates areas below the 95% significance threshold using a student's T-test.

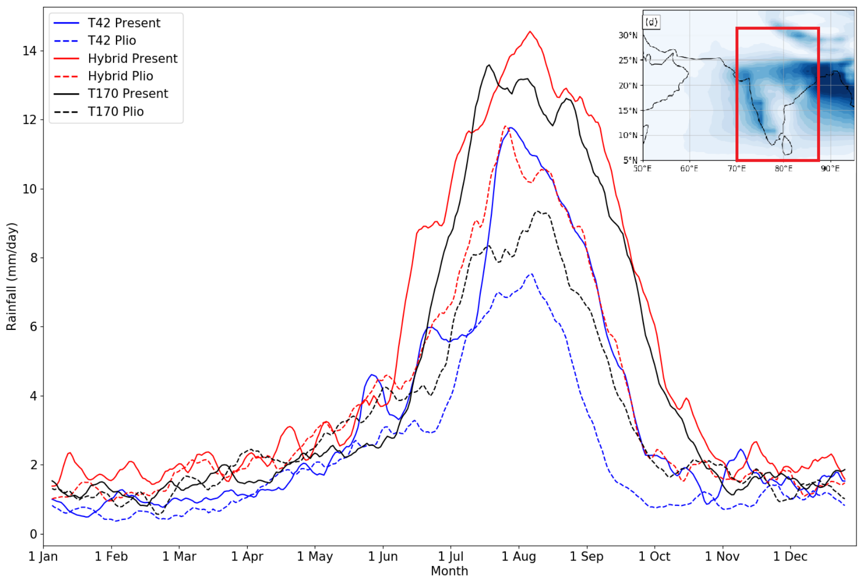

Figure 4.17: All India rainfall (rainfall on land between 4-32°N and 70-88°E) for all resolutions. Solid lines represent present day resolutions while dashed lines represent Pliocene. Colours indicate the different resolutions. Data was smoothed using a 10-day running average.

4.3 Discussion

4.3.1 Model Bias

The performance of the model in its low (T42) resolution set-up, which was explored in subsection 3.2.1 and in Joshi *et al.* (2015), showed its biases fall within the envelope of the Coupled Model Intercomparison Project (CMIP) phase 5 ensemble. While these biases persist through resolution, they are improved - with the full high resolution model integration providing rainfall fields which are most similar to present day. This improvement upon present day rainfall provides confidence in the meaning of the increase in resolution for the Pliocene boundary condition and its implications.

4.3.2 Resolution Effects

Increasing dynamical model resolution also inherently reduces diffusion in the model for a given wavenumber through the relationship of dissipation timescale and highest wavenumber in the model. For wavenumber 42, which is the highest wavenumber for the low resolution model configuration, the dissipation timescale would be just four hours while under high resolution, for that same wavenumber, it would take over five days for dissipation to complete. Dissipation works to weaken flow - the reduction of dissipation in the high resolution model hence leads to a notably stronger (less weakened) Somali jet upwind (as the jet increases in strength), seen in Figure 4.9. This additional boost to the jet's strength causes it to reach further north before curving eastwards. Figure 4.11 shows that for increasing resolution, unlike the analysis of present day versus Pliocene under low resolution, changes in the nature of the Somali jet are not related to the advection of potential vorticity across the hemispheres.

Following (Jablonowski and Williamson (2011)), an "amplification factor" between time steps in transform models can be represented by:

$$E_n = \frac{\Psi_n^{t+\Delta t}}{\Psi_n^t} \tag{4.3.1}$$

Which is a damping mechanism for any $E_n < 1$.

$$\Psi_n^{t+\Delta t} = E_n \Psi_n^t \tag{4.3.2}$$

The response function to the diffusion coefficient in spectral transform models, equivalent to the amplification factor, is:

$$E_n \approx \left\{1 + \Delta t \left[\frac{1}{\tau_{n_0}} \left(\frac{n(n+1)}{n_0(n_0+1)}\right)^{\frac{N}{2}}\right]\right\}^{-1} \tag{4.3.3}$$

Where Δt is the length of time step in the model, τ_{n_0} is the e-folding time scale for the diffusion at the smallest wavelength, n_0 symbolizes the maximum wavenumber corresponding to the smallest wavelength (specified by a triangular truncation limit), N is the order of diffusion and n is the wavenumber. The response function is scale-dependant.

The variables for the low (T42) and high/hybrid (T170) model resolutions are as follows:

Variable \ Resolution	T42 (Low)	T170 (Hybrid/High)
Time Steps Per Day	72	288
Order of Diffusion (N)	6	4
Dissipation Timescale (τ)	4 Hours	0.5 Hours
Max Wavenumber (n_0)	42	170

Table 4.1: Variables for Hyperdiffusion Scale Analysis

The choice of effective wavenumber (n) should reflect the length of the Somali jet; an approximation of the length scale of the jet is 1500km. This leads to n = $\frac{a}{1500km} \approx 27$ (where a is the Earth's circumference - 40,075km)

For the low, T42 resolution, the response function yields:

$$E_{27,\,T42} \approx \left\{1 + 1200 \left[\frac{1}{14400} \left(\frac{27(28)}{42(43)}\right)^{3}\right]\right\}^{-1} \approx 0.99392 \tag{4.3.4}$$

For the high/hybrid, T170 dynamical resolution:

$$E_{27,\,T170} \approx \left\{1 + 300 \left[\frac{1}{1800} \left(\frac{27(28)}{170(171)}\right)^{2}\right]\right\}^{-1} \approx 0.99989 \tag{4.3.5}$$

The time to decay by 50% for T42 and T170 could then be found by first calculating the dissipation timescale for n=27:

$$E_n = e^{-\frac{t_{(n+1)}-t_n}{\tau}} = e^{-\frac{\Delta t}{\tau}} \rightarrow \tau_n = -\frac{\Delta t}{\ln E_n} \tag{4.3.6}$$

the half-life is related to τ through:

$$t_{\frac{1}{2}} = \tau \ln 2 = -\frac{\Delta t}{\ln E_n} \ln 2 \tag{4.3.7}$$

$$\rightarrow t_{\frac{1}{2}(27,\,T42)} \approx 1.6 \text{ days } t_{\frac{1}{2},(27,\,T170)} \approx 21.9 \text{ days} \tag{4.3.8}$$

Since the Somali jet varies on a timescale of a few days, hyperdiffusion in the T42 model configuration is a significant damping term on these wavelengths (Rodwell and Hoskins (1995)). With T170 model parameters, the diffusion timescale for a wave the length of the Somali jet is much longer than its variability timescale and thus would have a negligible effect on wind speeds seen.

For the present day, with a jet that is already stronger than its Pliocene counterpart, this resulting strengthening of Somali jet due to model-inherited diffusion, alongside a northward shift in the jet, lead to the presence of convective rainfall inland in an area where convective activity was absent in the low resolution case (Figure 4.7). For the Pliocene, the same mechanism causes a smaller increase in already existing convective cloud and rain. The associated effects on incoming shortwave solar radiation and ultimately surface temperatures are amplified in the present day against Pliocene for this reason. The significant increase in convective rainfall for the present day has another slightly less direct, far reaching effect; It releases latent heat which, through a Matsuno-Gill (Matsuno (1966), Gill (1980)) type response, causes an upper level anti-cyclone which acts to strengthen the Tibetan high (Figure 4.10).

The northward shift in rainfall amounts (Figure 4.9) is explained by the increase in number of grid-boxes between the two model configurations: whereas one low resolution grid box covers about 2.5°, four grid boxes would be required to cover the same area under high resolution. This means that the grid box adjacent to a topographic slope, such as the Himalayas, would be nearly 2° larger under low resolution, with rainfall occurring over the whole grid box. The steeper the slope, the greater the consequences for rainfall position - especially for areas with intense rainfall.

Progressing to increasing the topographic resolution (same high resolution dynamical resolution, less smoothed, high resolution topography) seems to have more defined, small-scale effects in similar areas, with mostly local effects induced by topography (Figure 4.13). The biggest of which occur in the area of greater topographic changes - the footsteps of the Himalayas and Bay of Bengal. The only other, notable difference has to do with decrease in convective rainfall around the Pakistan area. It is uncertain whether this decrease in convective cloud is due to the very defined reduction in topographic height in this area, affecting orographic rainfall, or if perhaps it is a symptom of the general northward migration of rain in this region, aided by the reduction in noisy rainfall in the area.

4.4 Conclusions

The differences between Pliocene and present day South Asian monsoon rainfall decrease with increased dynamical resolution, due to a stronger resolution effect on the presence of convective cloud (and rain) in the present day climate than its Pliocene counterpart: convective cloud amounts increase more in the present day than in the Pliocene, minimising differences in rainfall. Through investigation of model bias in this chapter, these changes to the present day in the hybrid model set-up are consistent and realistic. Dynamical resolution has a bigger effect than topographic resolution through changes to grid-box sizes and reduced dampening due to hyper-diffusivity, with the latter only providing local improvements. However, these targeted improvements which lead to better defined rain bands and large changes over small areas could become crucial when considering the Pliocene as a future climate change analogue and its implication on the society that depends on the rains of the monsoon.

Increased resolution is assumed to more accurately describe the overall climate in question, whether the present day, Pliocene, or any other, based on its representation in the IGCM. However, these improvements are dependent upon the magnitude of the existing field. As the circulation, rainfall and associated variables in the Pliocene are all weaker due to the weakening of sea surface temperature gradients, it is the comparison of the Pliocene climate to present day conditions that improves most with increased resolution, rather than the representation of the Pliocene climate itself.

Chapter 5

The West African Monsoon

5.1 Introduction

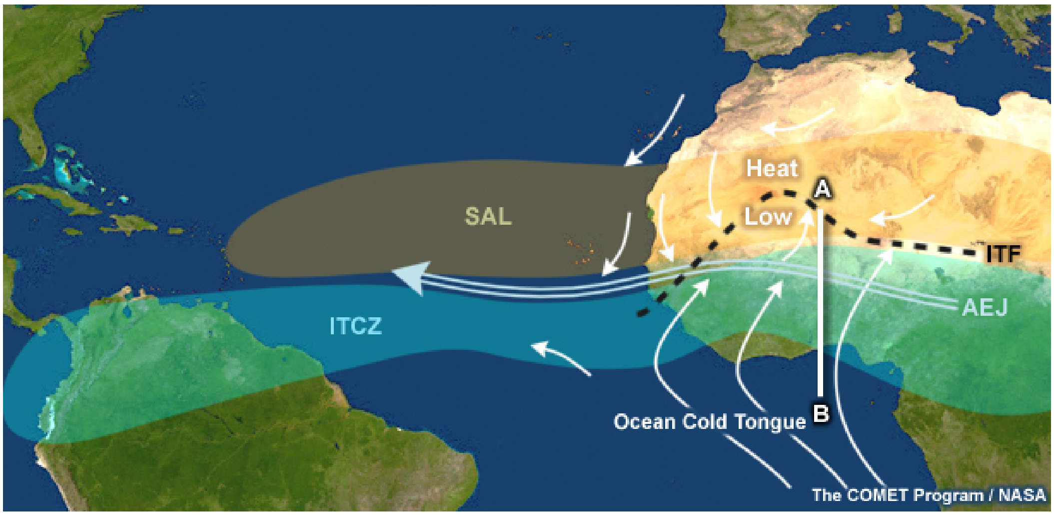

Figure 5.1: Schematic of the West African monsoon. ITF: Intertropical Front; AEJ: African Easterly Jet; SAL: Saharan Air Layer; ITCZ: Intertropical Convergence Zone. A-B line marks the meridional cross-section for Figure 5.2. Image taken from the COMET program / NASA.

The West African Monsoon (WAM) occurs south of the zonally oriented Intertropical Front (ITF), which separates the dry and hot Saharan air layer (SAL) from relatively cool, moist monsoon flow from the Atlantic (Issa Lélé and Lamb (2010)). The front tilts southwards, causing an inversion layer to form immediately to the south with hot Saharan air overlaying cooler Atlantic air, preventing convection. In Boreal summer, with the northward shift in maximum solar insolation, the Intertropical Convergence Zone (ITCZ) shifts northwards and the meridional gradient of temperature and soil moisture is exacerbated across western Africa.

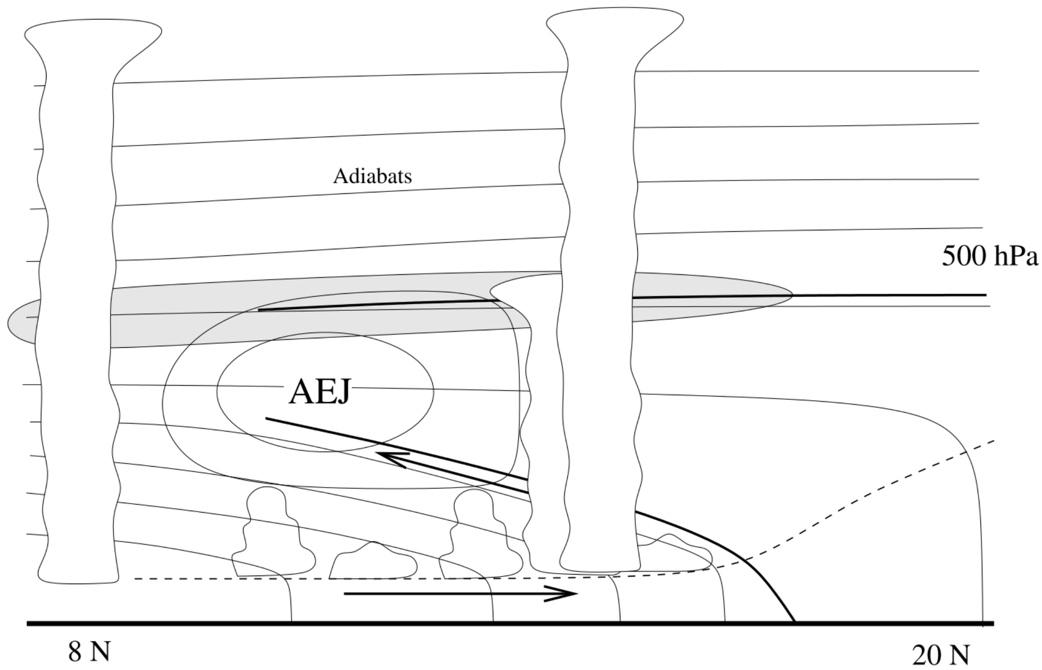

Figure 5.2: A schematic diagram of the thermodynamic structure on a latitude–height section through the African easterly jet system. Adiabatic 'Saharan Air Layer' (SAL) boundaries are denoted by bold lines and the top of the monsoon layer by a dashed line. A shallow layer of intermittent altocumulus and stratocumulus (grey shading) occurs at the top of the SAL, with increasing amounts and depth towards the south. The meridional circulation marked is that of the 28 August 2000 observations, and is expected to vary diurnally and synoptically. Taken from Parker *et al.* (2005), Figure 10.

These gradients contribute to the creation of the African Easterly Jet (AEJ), which exists at a height of about 600mb, corresponding with the balance of two different vertical heat profiles: one fuelled by latent heat advection over moist, cooler temperatures to the south - removing heat from lower levels and depositing heat back again in the middle and upper troposphere up via condensation, and one powered by sensible and thermal heat transfer over the dry and hot Sahara though the SAL to the north, giving a steady vertical heat profile (Cook (1999)). These differences in vertical cooling result in a strong north-south meridional temperature gradient closer to the surface which weakens with height until flattening out at about 600mb - the level of the jet (Figure 5.3). The largest gradients in these surface heat fluxes coincide with the largest soil moisture gradient, and are all centred on the latitude of the AEJ (Cook (1999)).

The AEJ then plays a role in triggering African Easterly Waves (AEWs). These westward-propagating waves occur at a height of about 700mb - slightly lower than the level of the jet (Céron and Guérémy (1999)), with wavelengths of around 4000km and a period of 3-5 days (Hall and Peyrille (2006)). The AEWs then cause

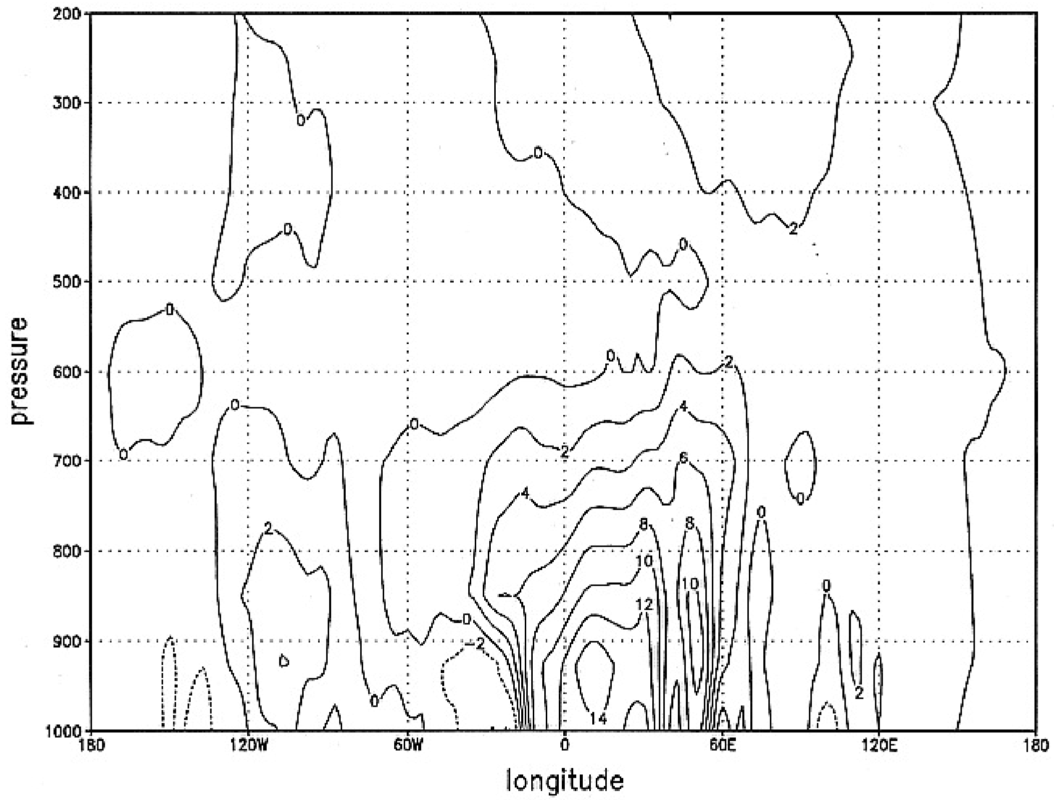

Figure 5.3: Longitude-height cross section of meridional temperature gradient at 12.5°N in July from National Center's for Environmental Prediction (NCEP) reanalysis. Contour interval of $2x10^{-6}Km^{-1}$. Taken from Cook (1999), figure 5.

a string of mesoscale convective systems (MCS) and squall lines, which account for a significant proportion of summer monsoon rainfall over western Africa (Mathon *et al.* (2002)). Figure 5.4 shows a schematic for AEW and associated convection.

The WAM system includes within it processes of different scales - ranging from planetary to cumulus (Hall and Peyrille (2006)). This chapter explores changes to these processes and particularly to the African Easterly Waves under varying horizontal resolutions in the present day and under Pliocene SST conditions. First, A comparison of WAM precipitation in the IGCM versus observations is shown to assess the model's ability of reproducing realistic results. Then, an analysis of dynamical resolution (low versus hybrid) is followed by an equivalent analysis of topographic resolution (hybrid versus high). A discussion into the general representation of the monsoon system in the IGCM and the effects of both resolutions is later presented. The chapter finishes with overall conclusions about the WAM under present and Pliocene SST conditions.

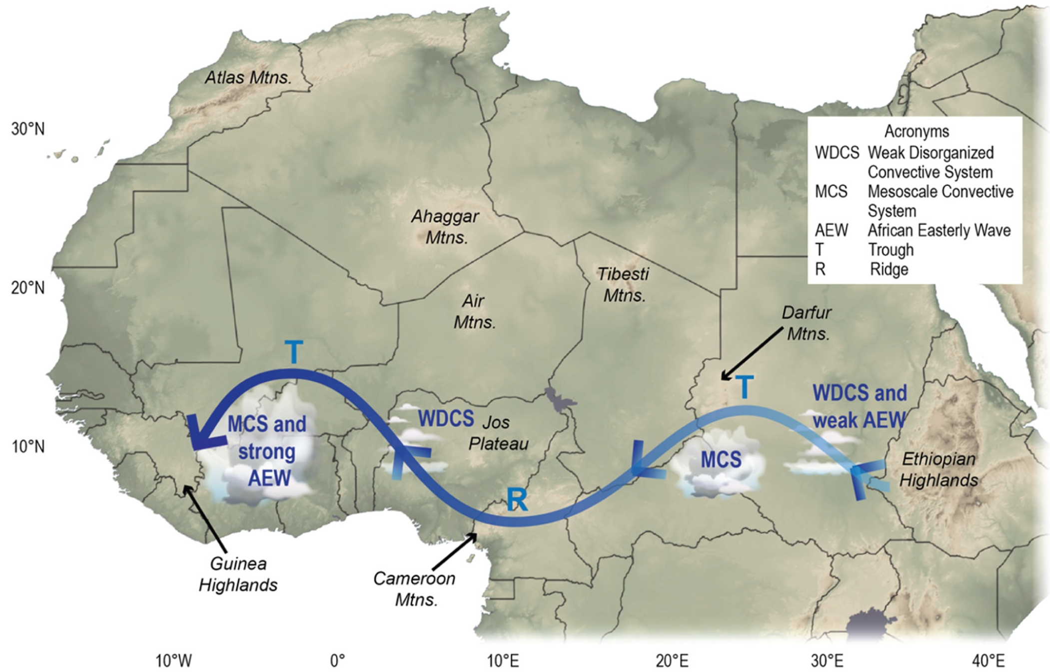

Figure 5.4: Schematic of African Easterly Waves (AEWs) and associated convective systems over a topographical map of northern Africa with topographical features labelled. Taken from Semunegus *et al.* (2017).

5.2 Results

Figures in this section all follow the same layout matrix (unless otherwise stated). Top row shows the two scenarios - present day and Pliocene (panels a,b) and the difference between them (c) for a given model resolution. Middle row displays the same for a different resolution (d,e and f) while the bottom row deals with differences between the two resolutions for a given scenario (g,h) and a final difference-of-differences panel (i, panel f-c or h-g), describing the effect of model configuration change on the Pliocene response compared to present day. All plots are a June, July, August, September (JJAS) average.

5.2.1 Representation in IGCM

Using the same datasets in previous chapters (6-hourly satellite precipitation data spanning over 17 years (1997-2015) from NASA's Tropical Rainfall Measuring Mission (TRMM) (Kummerow *et al.* (1998)) and 6-hourly wind products reanalysis data from ECMWF's ERA-INTERIM analysis (1979-2012) (Dee *et al.* (2011) at the 850mb level), the ability of the IGCM to correctly simulate precipitation and wind fields in the African region was assessed. Both datasets were averaged monthly and

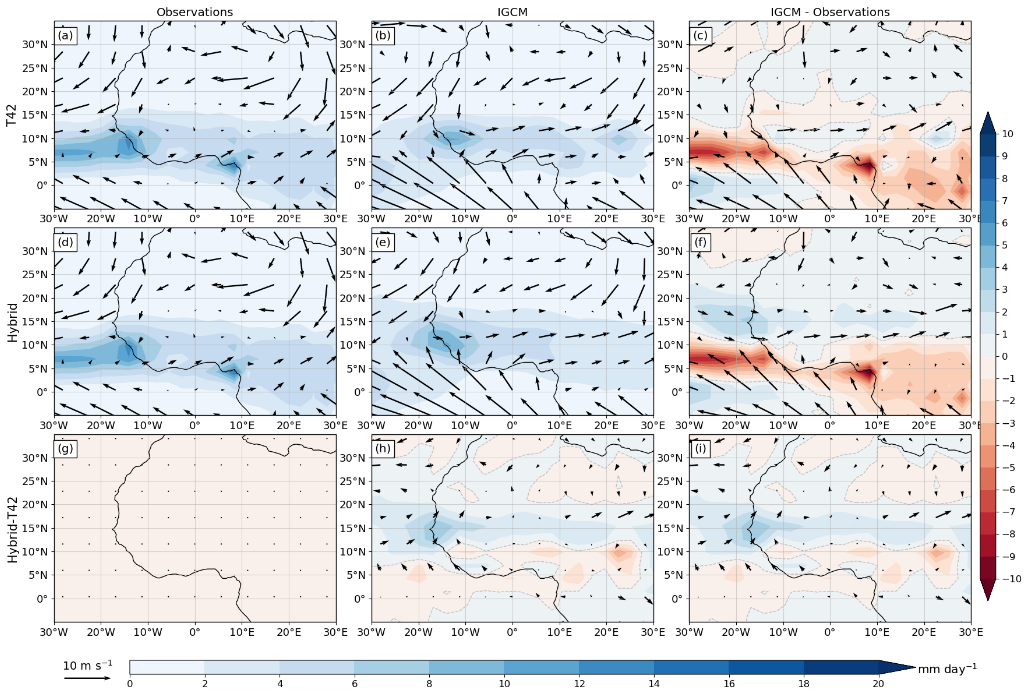

Figure 5.5: JJAS averaged rainfall and wind vectors under low and hybrid resolutions for the West Africa region. Panels a,b,d,e show full fields for observations (left) and IGCM present day (middle) with contour intervals of 2 mm day^{-1} (bottom). Differences between fields are shown on the last row and right column with contour intervals of 1 mm day^{-1}.

re-gridded to match the low and high resolution model simulations used. Difference plots were then produced showing seasonal (June, July, August and September averaged) differences in wind speed and direction overlaid on precipitation differences for low (T42) resolution, high resolution with topography smoothed to low resolution (dubbed 'hybrid') and high (T170) resolution model simulations.

Figure 5.5 shows rainfall and wind differences between low (T42) and hybrid (T42 topography with T170 dynamics) resolutions versus observations. In the low (T42) resolution model set-up (a-c), the IGCM captures the main rain band in its correct position, including the precipitation maximum on the West African shoreline. This precipitation maximum, however, occurs more inland in the IGCM rather than slightly offshore in TRMM observations. A second maximum at around 4°N, in the eastern Gulf of Guinea (5°N, 8°E) is all but missed in the IGCM. In addition, there is an area of excess rainfall in the western edge of the rain band in the model, at around 15°N. Rainfall amounts in the IGCM are lower than observations, with equatorial Africa being especially dry. Over the ocean, precipitation in the IGCM is spread out meridionally while it is concentrated around 5-10°N in observations and confined to a narrower zonal band.

The IGCM correctly simulates wind directions over land, with the exception of the divide between Saharan flow and Monsoon flow - in the IGCM, there is no area of low to no wind at 12°N. This is replaced by moderately strong westerly flow, similar to that of the monsoon to the south. Wind speeds are slightly lower in the IGCM than in observations for the Saharan region, mostly away from the coast. Over the ocean, the easterly flow that borders the northern edge of high precipitation in observations at around 12°N, is missing in the IGCM. South of this, wind speeds in the IGCM are much higher than observations. In the Gulf of Guinea area in observations there is little to no wind while in the IGCM an extension of the strong winds to the west exists.

Under hybrid resolution (d-f), with low (T42) topography and high (T170) model dynamics, a slight widening in the width of the main rain band is evident, which now stretches to 18°N over western Africa and the adjacent ocean and reaches down to the equator in equatorial Africa. The position of peak rainfall on the western African coast is better represented as it moves to the west onto the coast rather than to the east of it in low resolution. The excess rainfall seen to the east under low resolution has been corrected in the hybrid set-up. Wind directions between low and hybrid resolutions see no real change, with wind speeds being generally higher in hybrid.

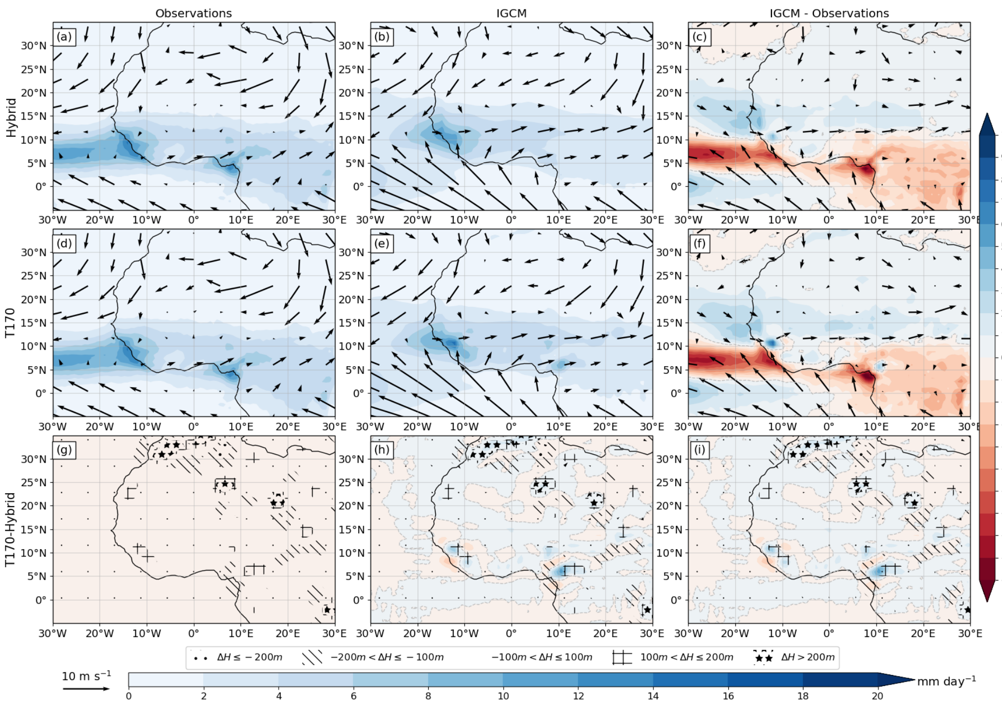

Figure 5.6: JJAS averaged rainfall and wind vectors under hybrid and high resolutions for the West Africa region. Panels a,b,d,e show full fields for observations (left) and IGCM present day (middle) with contour intervals of 2 mm day^{-1} (bottom). Differences between fields are shown on the last row and right column with contour intervals of 1 mm day^{-1}.

Increasing topographic resolution and moving on to a full high resolution (T170) set-up (Figure 5.6) introduces slight improvements in rainfall patterns: the peak on the western African coast now has higher rainfall to match observations, though this is misplaced and exists over land rather than just off the shore; rainfall amounts inland north of the Gulf of Guinea are higher and more defined; and the pattern of rainfall to the eastern edge of the main band is more detailed. There is no visible change to the wind field under this resolution.

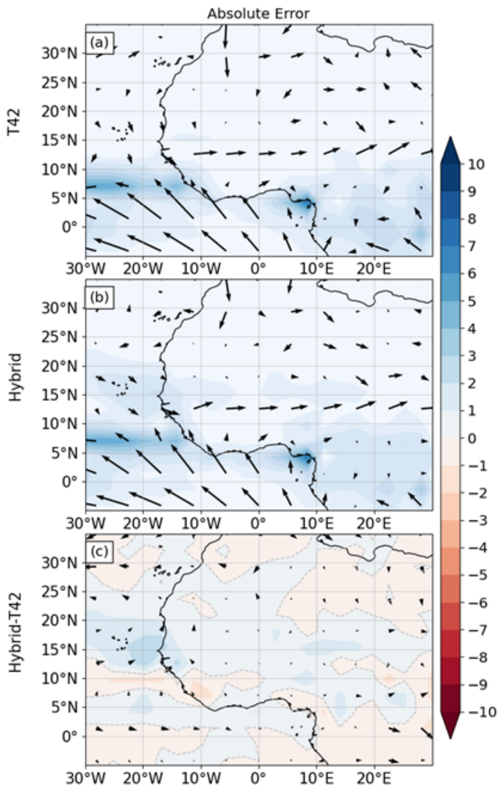

(a) Low and Hybrid

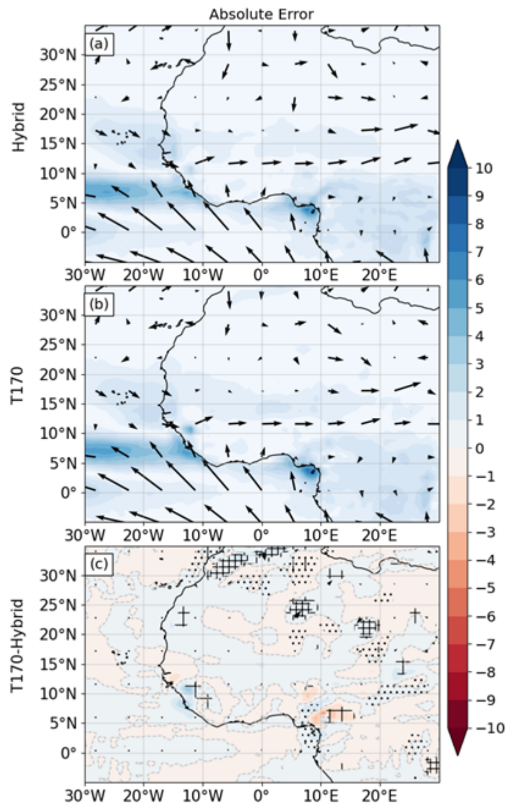

(b) Hybrid and High

Figure 5.7: Absolute error of different model resolutions and the change in absolute error with increasing resolution. Left: low and hybrid resolutions, right: hybrid and high resolutions.

Figure 5.7 shows model absolute error between all different resolutions utilised. Here, the area average was performed on the entire domain in order to quantitatively assess changes to how the IGCM captures rainfall amounts across resolutions. Absolute error remains steady throughout resolution change, with errors of 2.0 mm/day for low resolution, 1.93 mm/day for hybrid and 1.95 mm/day for the full, high resolution model integration.

5.2.2 Dynamical Resolution Increase

In this subsection, the effects of increasing the dynamical resolution alone - keeping low (T42) resolution topography with high (T170) model dynamics (see chapter 2) are explored for the West African monsoon region.

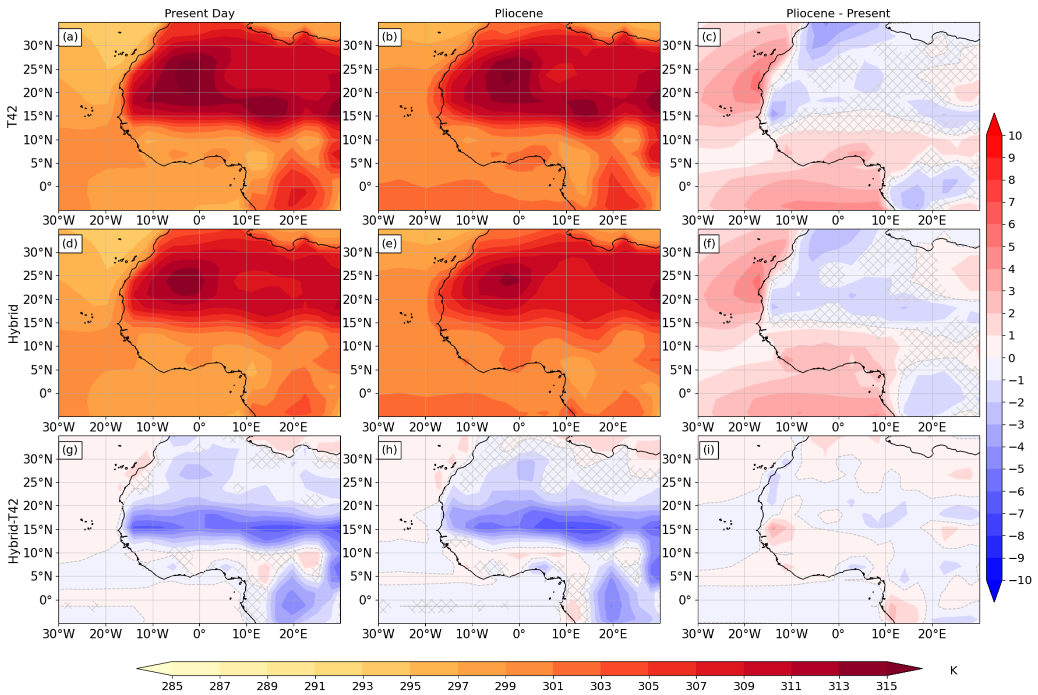

Figure 5.8: JJAS averaged surface temperatures under low and hybrid resolutions for the WAM region. Panels a,b,d,e show full fields for present (left) and Pliocene (middle) with contour intervals of 2°K (bottom). Differences between fields are shown on the last row and right column with contour intervals of 1°K. Grey hatching indicates areas below the 95% significance threshold using a student's T-test.

Surface temperatures (Figure 5.8) show the differences in prescribed Sea Surface Temperature (SST) fields between present day and Pliocene for this region. SSTs are much more zonal off the West African coast, indicative of a reduction of upwelling in the Pliocene. This manifests as areas of warming in the Pliocene compared with present day, of 3-4°K on average (panels a-c). The warmer region south of the Equator extends inland in the Pliocene under both resolutions, causing a warming of 1-2°K (panels c,f), though it is more confined under the hybrid resolution set-up. Elsewhere over land, the Sahara is cooler in the Pliocene, especially to the north west. Equatorial Africa sees cooling of 1-2°K in both resolutions. The distinct, near-zonal meridional temperature gradient seen around 13°N in both scenarios under low resolution (panels a,b) sees a temperature change of 14-16°K over 1-2° of latitude, consistent with the increase in dynamical resolution. For the hybrid equivalent (panels d,e), the gradient is less steep and totals a change of 10-12°K for both scenarios (stronger to the west). The gradient also stretches further north by 2-3°, highlighted in panels g and h. Panel i shows a difference around an area of topography: The Guinea Highlands on the western coast experiences more cooling in the present day compared with Pliocene under hybrid resolution (panels g,h).

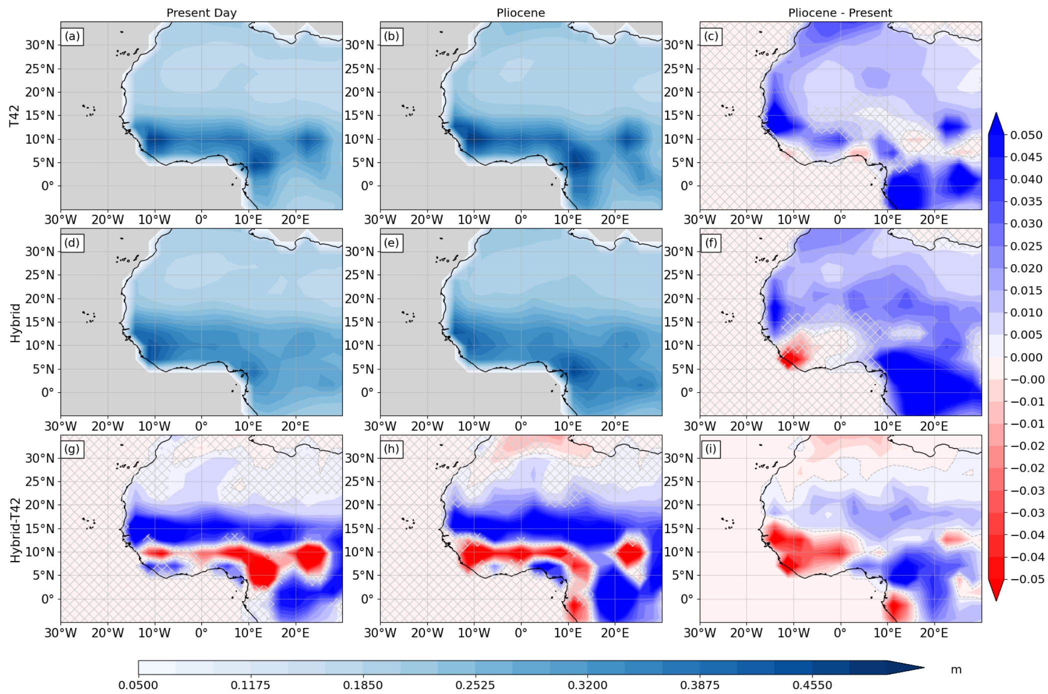

Figure 5.9: JJAS averaged soil moisture under low and hybrid resolutions for the WAM region. Panels a,b,d,e show full fields for present (left) and Pliocene (middle) with contour intervals of 0.0225 m (bottom). Differences between fields are shown on the last row and right column with contour intervals of 0.05 m. Grey hatching indicates areas below the 95% significance threshold using a student's T-test.

A strong meridional gradient of soil moisture (Figure 5.9) accompanies that of surface temperature, centred around the same latitude (13°N) for low model resolution (panels a,b). With an increase in dynamical resolution, the gradient shifts north and is now centred around 15°N (panels d,e) - shown by a decrease of soil moisture to the south and increase to the north of the gradient (panels g,h). There is also a notable drying of soil moisture to the east in the Darfur mountains area (10°N, 25°E). Outside of gradient changes, the Pliocene sees a more moist Sahara (especially to the west), and much higher soil moisture levels in equatorial Africa (panels c,f). Increasing the dynamical resolution sees the south western tip of West Africa drying considerably in the Pliocene compared with present day (panels c,f,i).

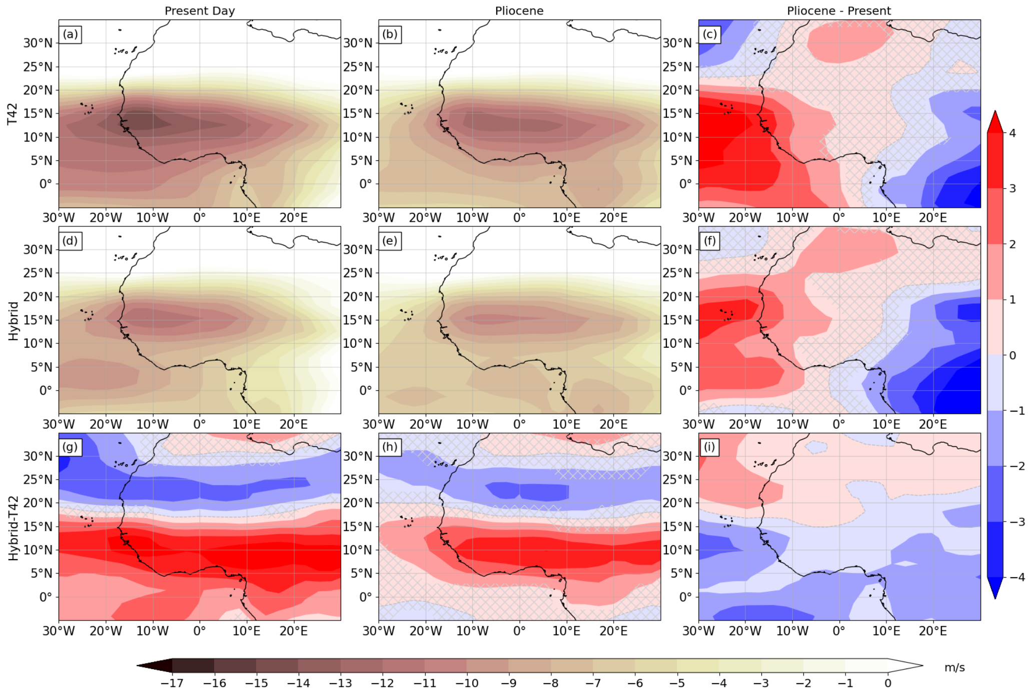

Figure 5.10: JJAS averaged zonal wind at 620mb under low and hybrid resolutions for the WAM region. Panels a,b,d,e show full fields for present (left) and Pliocene (middle) with contour intervals of 1 m/s (bottom). Differences between fields are shown on the last row and right column with same contour intervals. Grey hatching indicates areas below the 95% significance threshold using a student's T-test. Note that only negative (westward) winds are shown.

The resulting flow of the African Easterly Jet as response to these meridional gradients is seen in Figure 5.10. The jet's core reaches higher speeds in low resolution and under present day conditions (panels a,b,d,e) compared with Pliocene and hybrid configurations. For both resolution cases, the AEJ is positioned slightly to the east in the Pliocene, with wind speeds higher to the east and lower to the west of the jet's core (panels c,f). Increasing dynamical resolution has a similar effect on both scenarios, slowing zonal wind speeds around the jet's core and to its south.

Figure 5.11 presents a zonal cross-section of the jet and shows changes to its average meridional position and strength during the course of the year. Resolution increase affects both scenarios similarly, with the jet reaching slightly further north under hybrid resolution (panels g,h) and weakening to the south. Additionally, for

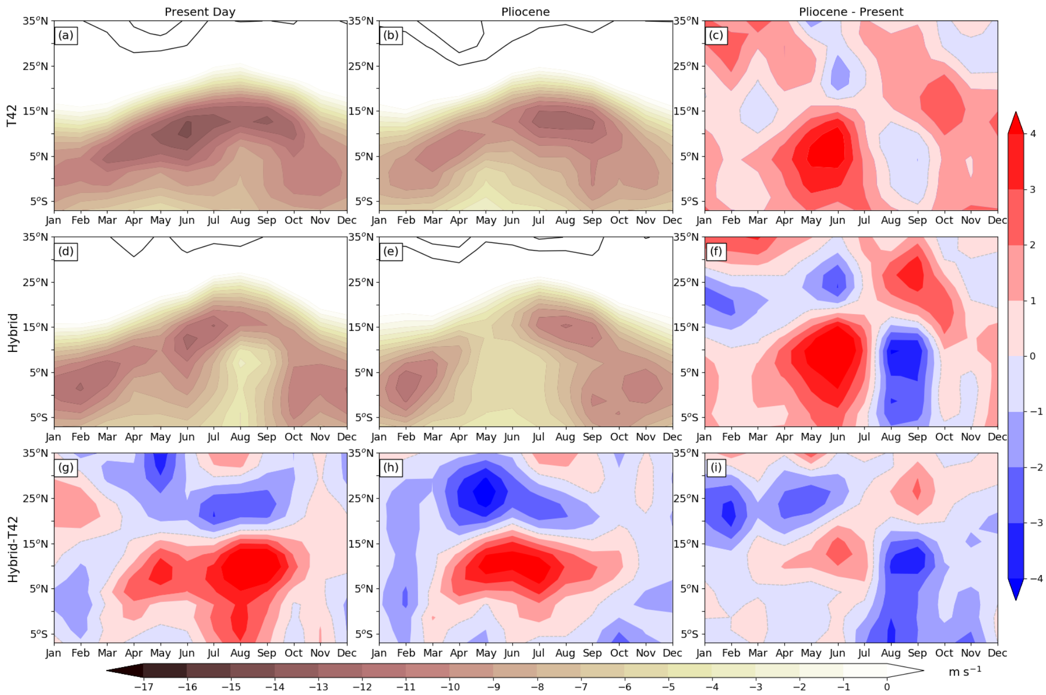

Figure 5.11: JJAS averaged zonal wind at 620mb under low and hybrid resolutions for the WAM region, averaged over 16°W - 16°E. Panels a,b,d,e show full fields for present (left) and Pliocene (middle) with contour intervals of 1 m s^{-1} (bottom). Differences between fields are shown on the last row and right column with same contour intervals. Note that only negative (westward) winds are shown.

both scenarios, a break in zonal wind speeds is evident around May-June (panels d,e) before the jet strengthens for the monsoon season. Present day sees highest wind speeds at the start of the season,in June, which then become more confined meridionally and weaken from September onwards. For the Pliocene, Wind speeds strengthen throughout the monsoon season, peaking around August and weakening with the southward retreat of the AEJ in October.

The steep meridional gradient of specific humidity and the area of high humidity at low levels (Figure 5.12) in southern West Africa is preserved between present day and Pliocene model configurations in both low and hybrid resolutions (panels a-c, d-f). The Pliocene has higher specific humidity across the Sahara and Equatorial Africa, alongside areas of strongly increased humidity over the ocean, corresponding to areas of higher sea surface temperatures in the Pliocene. Increasing resolution has similar effects on both scenarios inland, increasing specific humidity north of the steep meridional gradient (panels g,h) and thus causing a very slight northward shift (by 1-2°) of the gradient in both resolutions (panels d,e).

Eastern Equatorial Africa also sees an increasing in specific humidity in both scenarios, equally. For the present day, increasing the dynamical resolution also

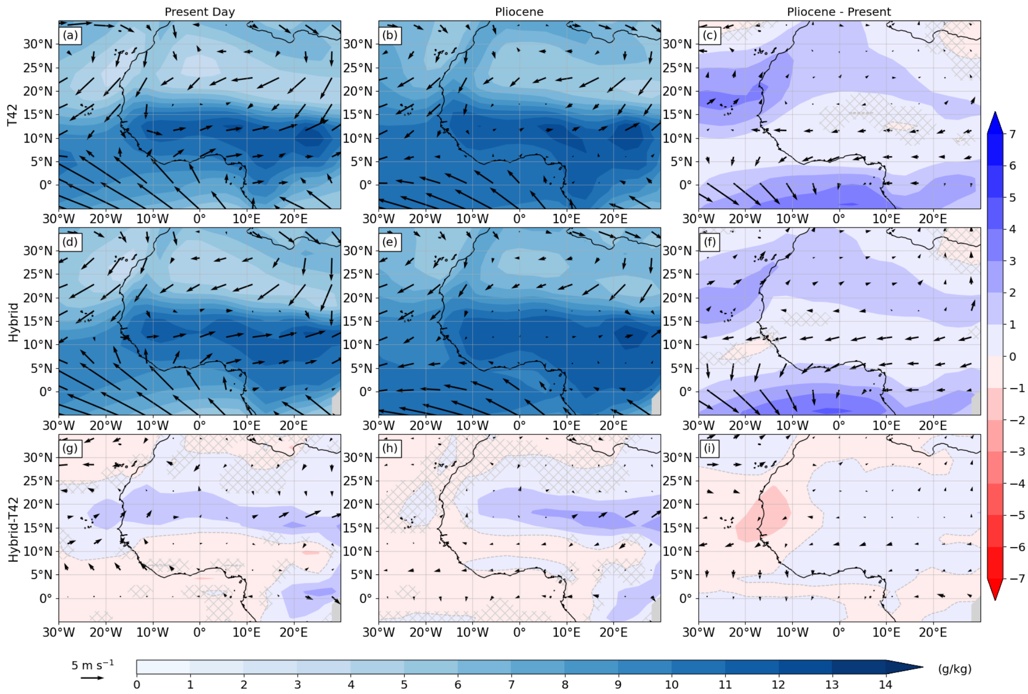

Figure 5.12: JJAS averaged specific humidity under low and hybrid resolutions for the WAM region at 880mb. Panels a,b,d,e show full fields for present (left) and Pliocene (middle) with contour intervals of 1 g kg^{-1} (bottom). Differences between fields are shown on the last row and right column with same contour intervals. Grey hatching indicates areas below the 95% significance threshold using a student's T-test.

increases specific humidity off the West African coast (panels g,i). All of the aforementioned humidity differences occur in areas of increased (reduced) moist (dry) air flow, as seen by changes to the wind fields (panels g,h). The moist monsoon flow strengthens slightly while the dry Saharan flow weakens to the north.

Precipitation differences (Figure 5.13) between present day and Pliocene are mostly insignificant inland for low resolution (panel c), as the main rain band across 10°N is very similar in both scenarios (panels a,b). On the western coast, peak rainfall is more spread out in the Pliocene and extends north by a few degrees of latitude just off the shore, with lower rainfall amounts compared with peak rainfall in the present day in the same area. A large area of excess precipitation over the ocean at the equator exists in the Pliocene, in an area corresponding to higher SSTs. Hybrid resolution sees more significant differences between the two scenarios (panel f), with a reduction in peak rainfall amounts in the Pliocene compared with low resolution (panel h), while the present day sees an increase in rainfall in the peak area (panel g). This combined effect leads to a large drying of the Pliocene compared with present day under hybrid resolution, with a change to the rainfall band which sees the area of peak rainfall almost indistinguishable from the main rain band.

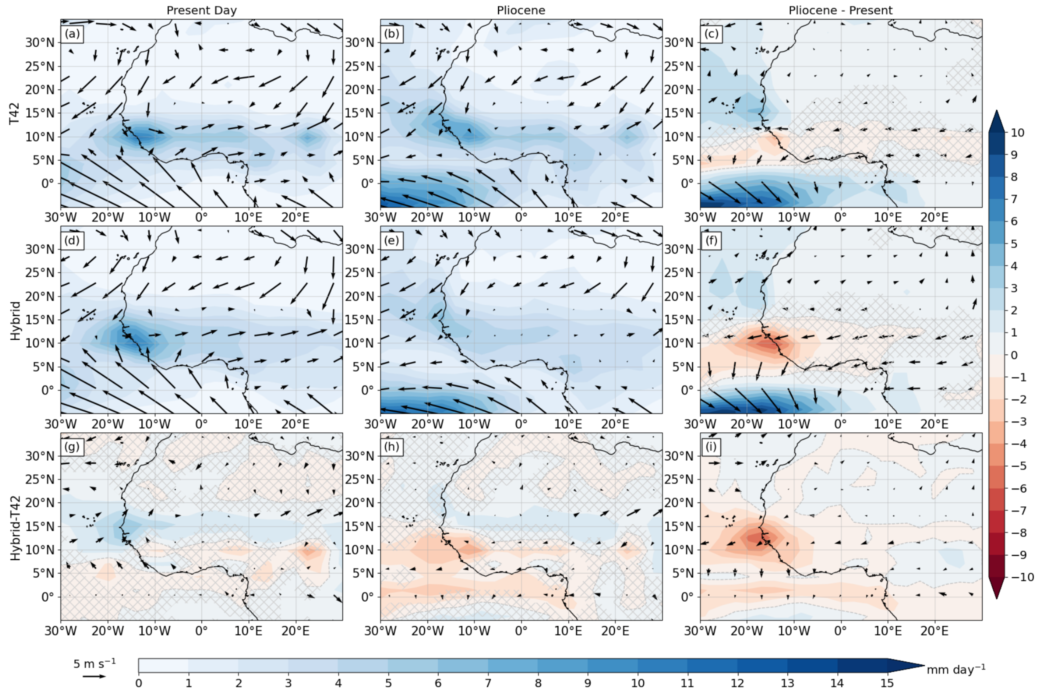

Figure 5.13: JJAS averaged precipitation under low and hybrid resolutions for the WAM region and wind vectors at 880mb. Panels a,b,d,e show full fields for present (left) and Pliocene (middle) with contour intervals of 1 mm day^{-1} (bottom). Differences between fields are shown on the last row and right column with same contour intervals. Grey hatching indicates areas below the 95% significance threshold using a student's T-test.

5.2.3 Topographic Resolution Increase

Increasing the model's topographic resolution in addition to the dynamical resolution (from hybrid to a full, T170 high resolution integration) induces strictly local effects relating directly to the immediate change in topography; there are no differences to speak of to most climatic features. To not overburden this chapter, only a small selection of figures will be shown to demonstrate this.

The soil moisture (Figure 5.14) gradient crucial to the initiation of the AEJ has more detail under high resolution but the gradient itself remains unchanged. The Pliocene sees more(less) moisture north(south) of about 6°N than the present day (panels g,h,i) and Africa remains much more moist than present day (panels c,f).

The AEJ (Figure 5.15) is essentially unchanged between topographic resolutions, with the present day seeing no noticeable changed between hybrid and high resolutions (panel g), while the Pliocene sees a slight decrease in zonal wind speeds to the west, resulting in a more centred jet (panel h). As a result of this decrease to the west, the difference field between Pliocene and present day is slightly more exaggerated to the west, with the Pliocene having slightly slower zonal wind speeds

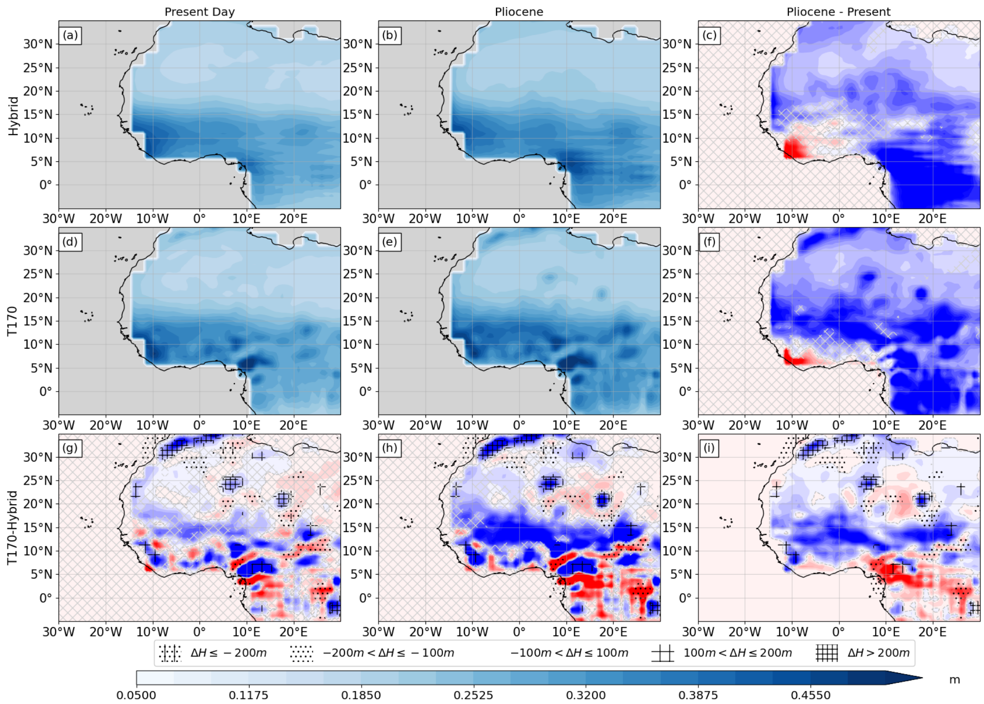

Figure 5.14: JJAS averaged soil moisture under hybrid and high resolutions for the WAM region. Panels a,b,d,e show full fields for present (left) and Pliocene (middle) with contour intervals of 0.0225 m (bottom). Differences between fields are shown on the last row and right column with contour intervals of 0.05 m. Grey hatching indicates areas below the 95% significance threshold using a student's T-test.

on the west coast and over the ocean than the present day in high resolution (panel f) than under hybrid resolution (panel c). There is no change in the meridional extent or position of the jet.

Precipitation (Figure 5.16) only shows significant change around areas of orographic features in western Africa. The increase in rainfall due to increased resolution is the same for both present day (g) and Pliocene (h), and so the effect of resolution on the difference between the two scenarios is essentially cancelled out (panel i). While these changes to local rainfall give a more detailed, realistic view of the precipitation field, the main rain band remains unchanged - as do the differences between Pliocene and present day (panels c,f).

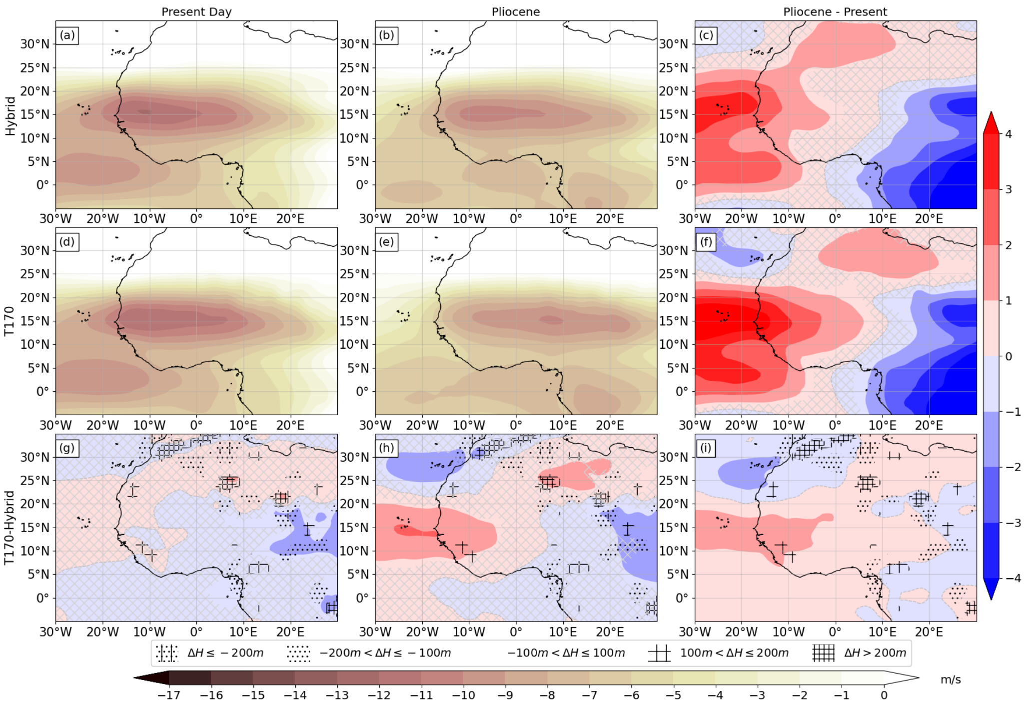

Figure 5.15: JJAS averaged zonal wind at 620mb under hybrid and high resolutions for the WAM region. Panels a,b,d,e show full fields for present (left) and Pliocene (middle) with contour intervals of 1 m s^{-1} (bottom). Differences between fields are shown on the last row and right column with same contour intervals. Grey hatching indicates areas below the 95% significance threshold using a student's T-test. Note that only negative (westward) winds are shown.

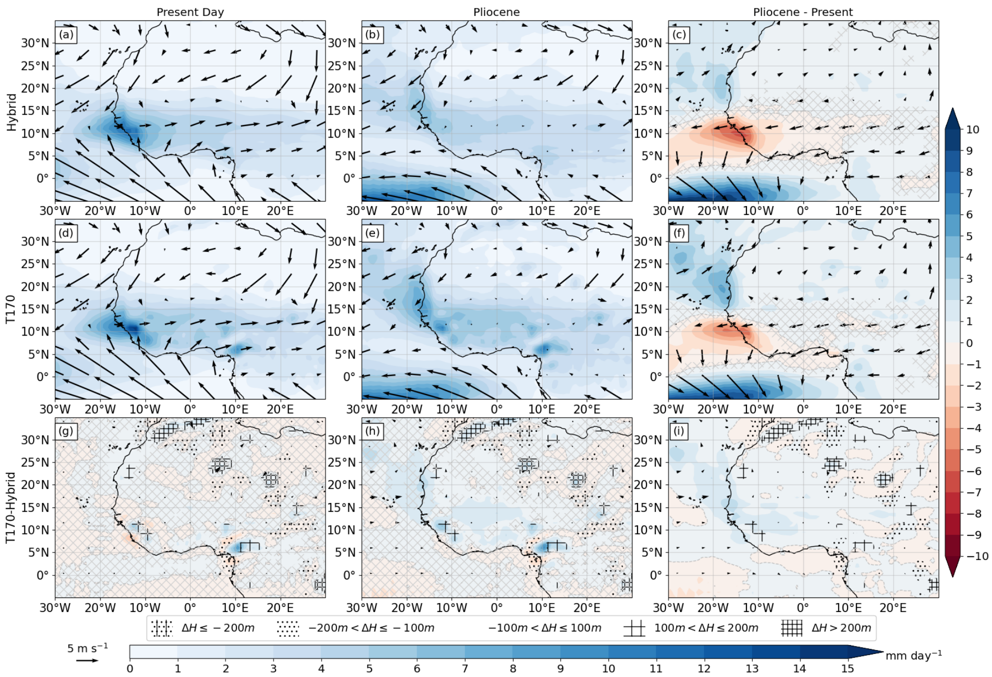

Figure 5.16: JJAS averaged precipitation under hybrid and high resolutions for the WAM region and wind vectors at 880mb. Panels a,b,d,e show full fields for present (left) and Pliocene (middle) with contour intervals of 1 mm day^{-1} (bottom). Differences between fields are shown on the last row and right column with same contour intervals. Grey hatching indicates areas below the 95% significance threshold using a student's T-test.

5.2.4 African Easterly Waves

As mentioned in the introduction (section 5.1), Mesoscale Convective Systems (MCSs) resulting from African Easterly Waves (AEWs) are responsible for a substantial amount of rainfall in the monsoon season. The remaining part of this section will deal with rainfall relating to these waves.

A composite approach was undertaken to identify AEW-related events. A 6 day, high pass filtered meridional wind timeseries at 5°W in the southern flank of the AEJ (5-15°N, see Figure 5.17) was normalised and analysed for peaks which most likely correspond with wave-related events. Selection criteria includes a restriction on event timings - events must be at least 5 days apart (as this is the higher limit of the period of AEWs) and only meridional wind events with a standard deviation of 2 or higher were included to ensure the strongest of AEWs were included and to gain a realistic representation of the AEW season which lasts from May until October (Céron and Guérémy (1999)).

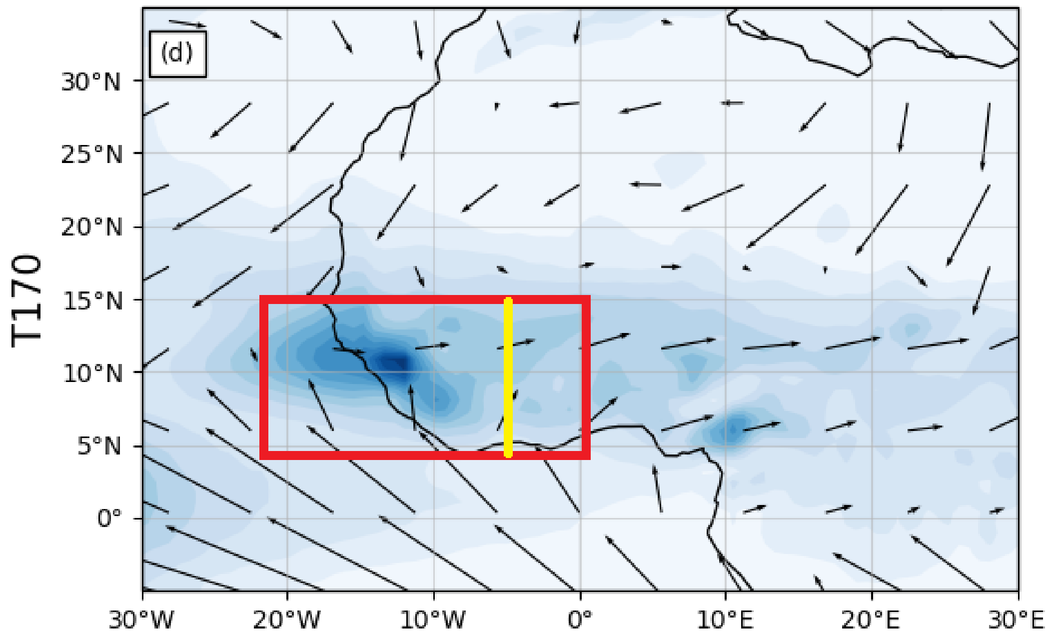

Figure 5.17: A sample JJAS averaged rainfall for T170 present day showing methodology used in this subsection. The yellow line across 5°W, between 5-15°N shows the cross-section chosen for the meridional wind timeseries (Figure 5.18) while the red rectangle shows the area selected for AEW-related rainfall averaging (Figure 5.19 and Figure 5.20)

Figure 5.18 shows a meridional wind timeseries for the present day under low resolution, accompanied by a non-filtered, smoothed rainfall timeseries in an area corresponding to peak rainfall on the western coast. Timeseries for other model runs are not shown here, but are of very similar structure.

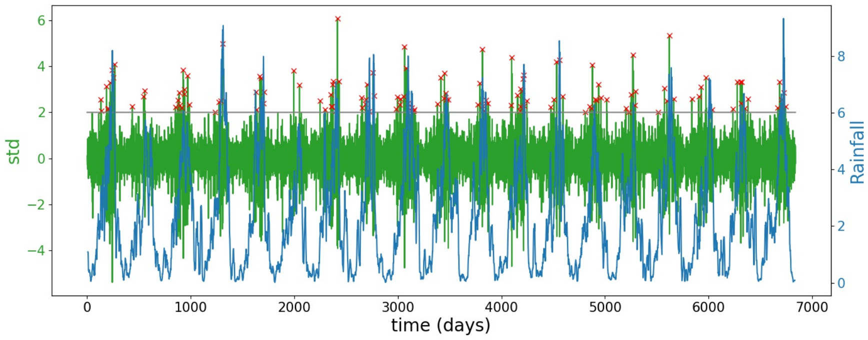

Figure 5.18: Meridional wind timeseries for a full (19 year) model integration, averaged at 5°W over 5-15°N. Data is normalised. Red crosses indicate AEW events, horizontal line at 2 standard deviations indicates threshold for identifying AEW events. 15-day smoothed rainfall average in the 20-0°W, 5-15°N box is overlaid in blue, amounts in mm day^{-1}.

Figure 5.19 and Figure 5.20 show the distribution of selected AEW events across the months of the year and the resulting monthly rainfall percentages caused by these events (rainfall from an AEW event defined as the day of the peak and the day following it). in the peak area (4-15°N, 22-0°W, see Figure 5.17) for all model integrations. The data displayed is for the full, 19-year model run; and so for example for the low, present day model integration (Figure 5.19a) an average July sees just over 1.5 AEW events which cause 12% of monthly rainfall over just 3 days.

The month of peak AEW-related rainfall is July for the present day (Figure 5.19) and August for the Pliocene Figure 5.20, across resolutions. Furthermore, in the present day, the AEW season arrives later than in the Pliocene, with peak rainfall amounts early in the season (July) which then dwindle and largely reduce by October, while for the Pliocene AEW season arrives a month earlier and sees rainfall amounts slowly increase before peaking at the end of the season (August) and falling sharply in September.

Increasing resolution seems to generally increase the total number of AEW events and concentrate these during JJAS (panels a to b to c, both figures). Higher resolution seems to also regulate the percentage of rainfall caused by AEW events, with both the present day and Pliocene (panel c, both figures) seeing just over 2 events in peak months causing 15% of rainfall over 4 days. In low resolution, the Pliocene (Figure 5.20a) sees no relationship between number of events in a month and resulting rainfall with June, July and August seeing 10% of monthly rainfall caused by varying amounts of events. This carries on under hybrid resolution (Figure 5.20b), with peak rainfall occurring in a month without the highest number of events.

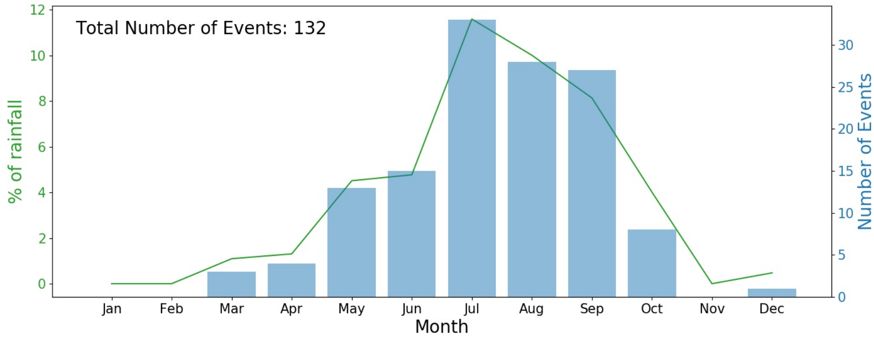

(a) T42

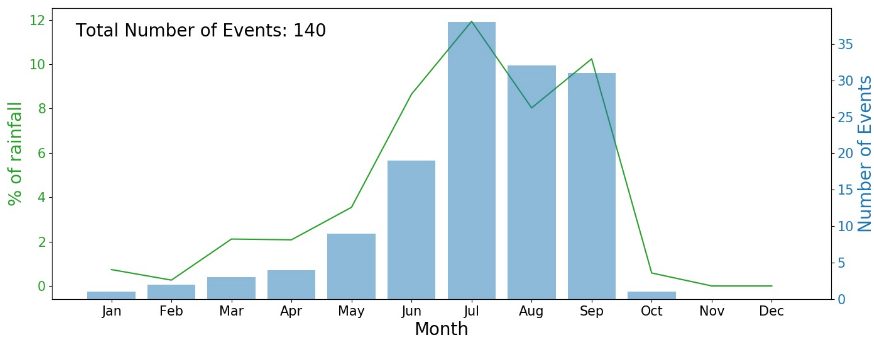

(b) Hybrid

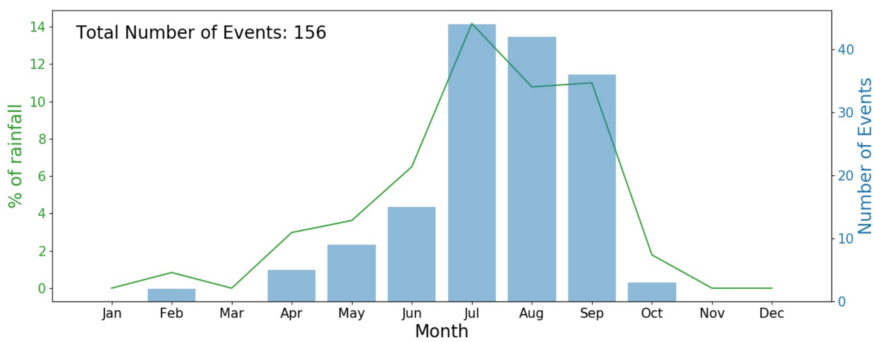

(c) T170

Figure 5.19: Distribution of Annual African Easterly Wave events and associated monthly rainfall percentages for the present day, all resolutions

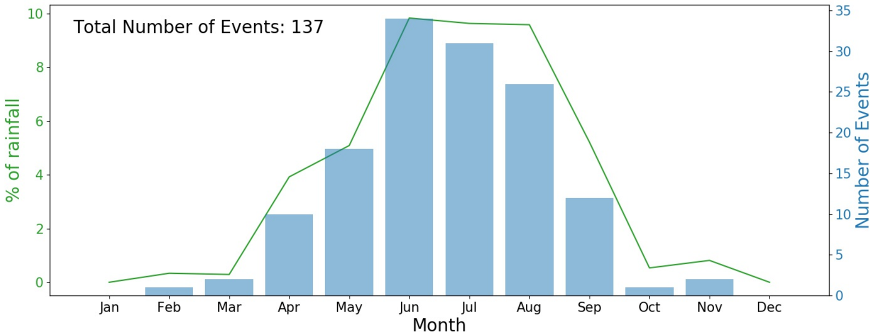

(a) T42

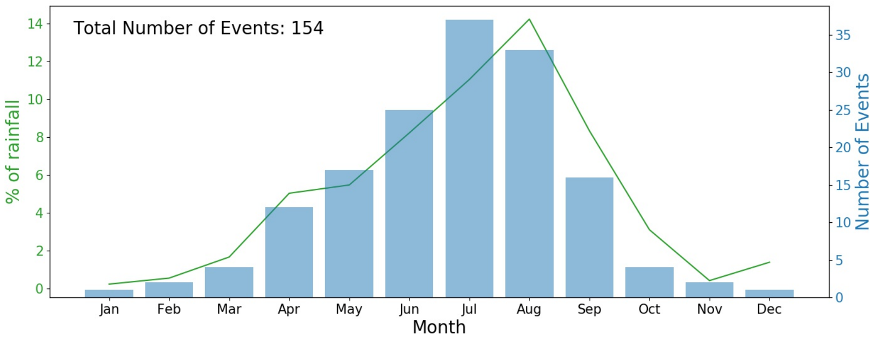

(b) Hybrid

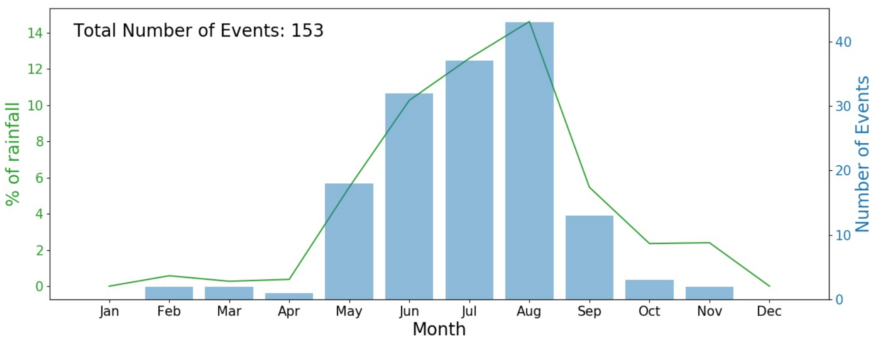

(c) T170

Figure 5.20: Distribution of Annual African Easterly Wave events and associated monthly rainfall percentages for the Pliocene, all resolutions

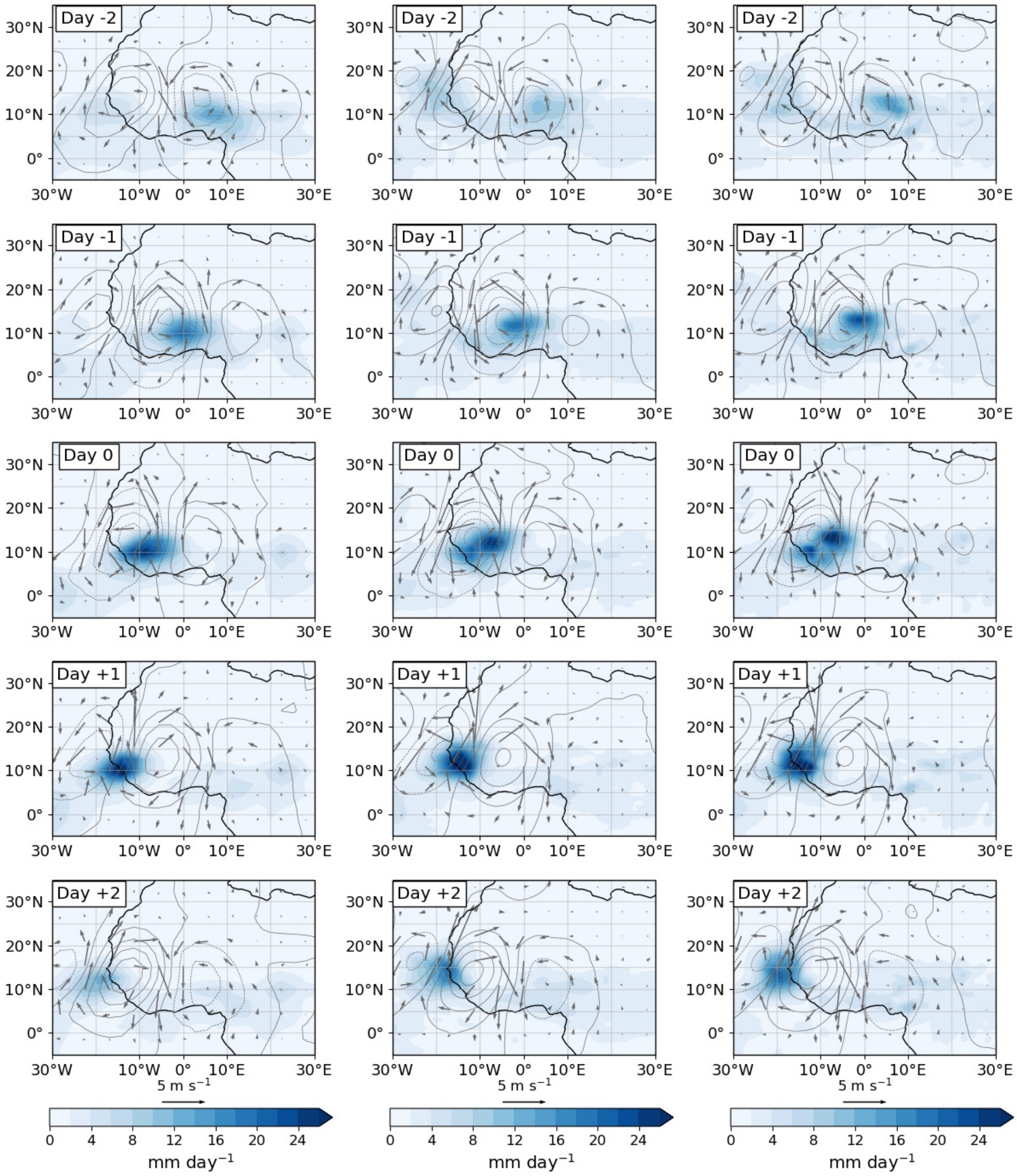

(a) T42 (b) Hybrid (c) T170

Figure 5.21: Lagged precipitation composites (based on meridional wind at 5°W, 4-15°N) for an average AEW event, present day. See text for methodology. Wind and streamline fields are filtered using a 6 day high-pass filter. Precipitation data is unfiltered, contour intervals 2 mm day^{-1}.

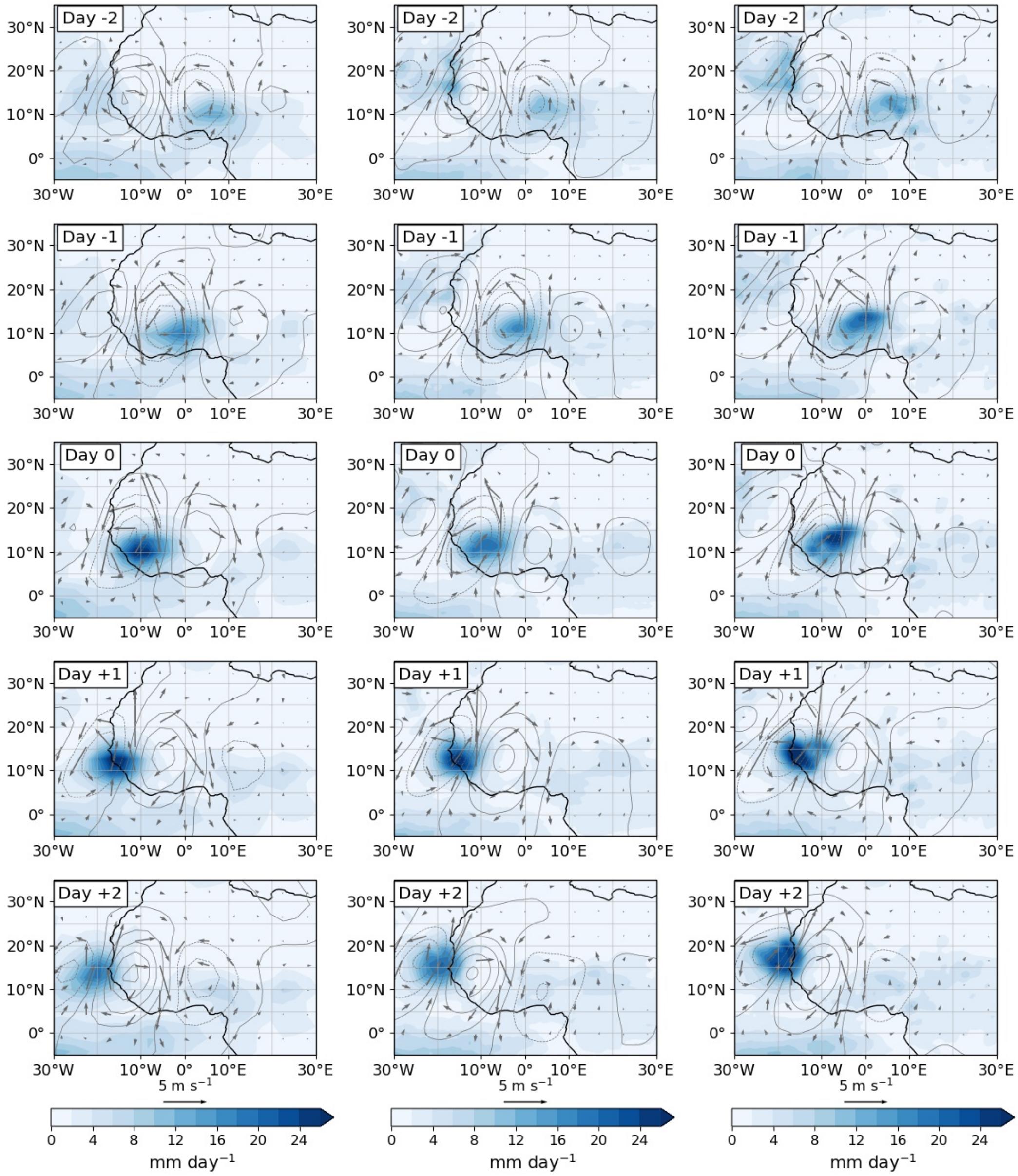

(a) T42 (b) Hybrid (c) T170

Figure 5.22: Lagged precipitation composites (based on meridional wind at 5°W, 4-15°N) for an average AEW event, Pliocene. See text for methodology. Wind and streamline fields are filtered using a 6 day high-pass filter. Precipitation data is unfiltered, contour intervals 2 mm day^{-1}.

Figure 5.21 and Figure 5.22 show lagged rainfall composites for an average AEW event for all resolutions, for the present day and Pliocene respectively. The rainfall is not filtered, while streamlines and wind vectors are 6-day high pass filtered to show wave structure.

A westward-propagating area of rain is seen travelling from central North Africa towards the coast, centred in an area of cyclonic flow. As it progresses, rainfall amounts increase and peak on the western African coast on day 0/1 before reducing significantly as the AEW continues to travel over the ocean. The area of rainfall slowly shifts from the centre of the cyclonic motion to its eastern edge before being wedged out and experiencing mostly southerly flow on day 1. on day 2, anticyclonic motion covers the area of reduced rainfall.

Rainfall amounts slightly increase and the pattern of rainfall becomes more defined as resolution increases but there are no fundamental differences to rainfall across resolutions, for either scenario. The temporal development of rainfall following and preceding AEW events as identified by meridional wind speeds are very similar across resolutions, with rainfall travelling westward with the wave train, increasing in intensity as the cyclonic motion that drives it provides increasingly moist ocean air to feed rainfall. By day 2, rainfall has moved far enough west to barely reach the coastline and rainfall amounts reduce. Peak rainfall amounts during day 0 and day 1 exceed 26 mm day^{-1} which doubles the JJAS rainfall average shown in Figure 5.13 and Figure 5.16.

A further lagged rainfall composite analysis was repeated for meridional wind at 45°W, averaged over 5-25°N, to examine wave activity further west into the Atlantic (Figure 5.23 and Figure 5.24). These show stronger waves with more associated rainfall as resolution increases and more markable wave activity this further west in the Pliocene compared with present day for a given resolution.

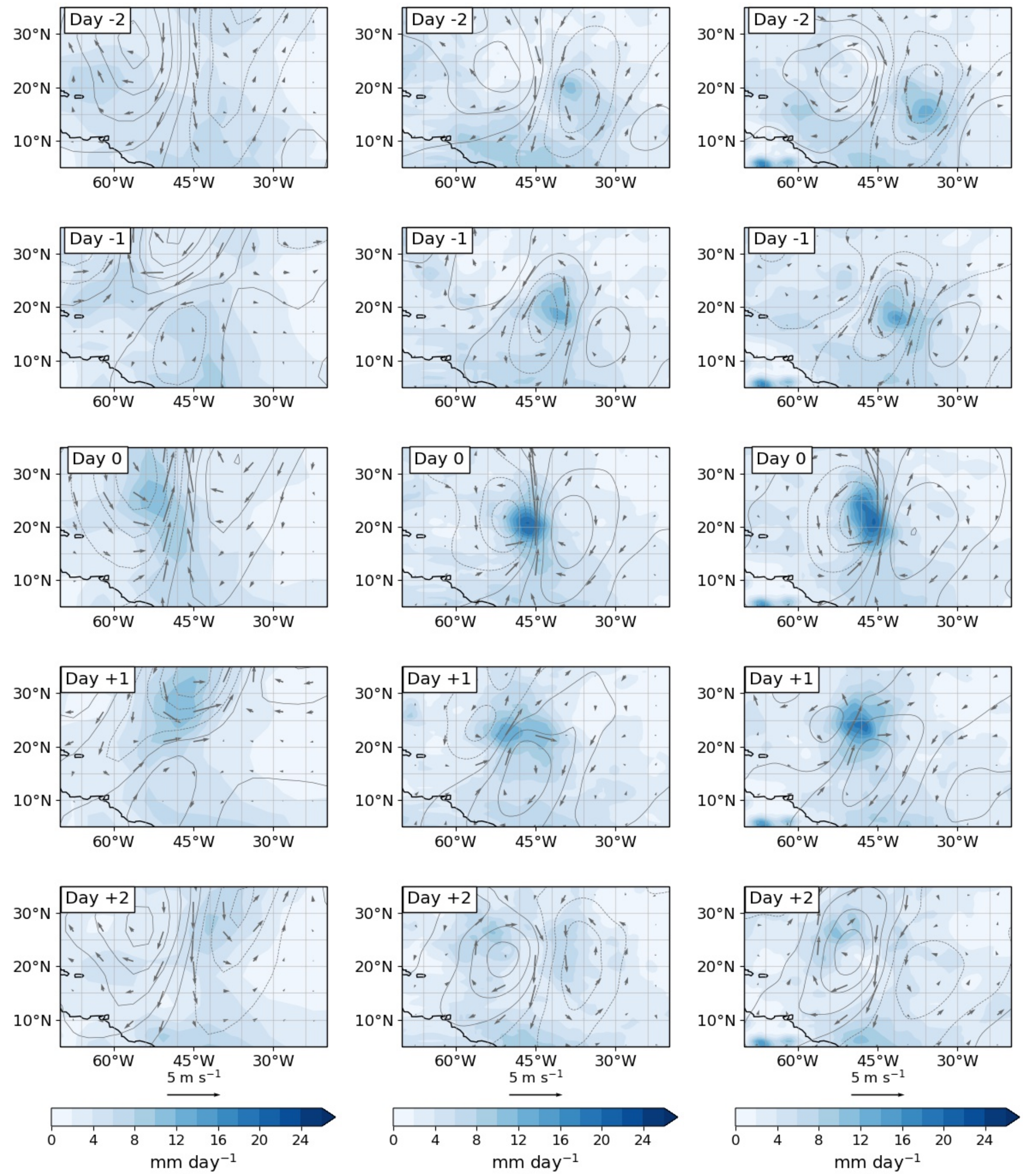

(a) T42 (b) Hybrid (c) T170

Figure 5.23: Lagged precipitation composites (based on meridional wind at 45°W, 4-25°N) for an average AEW event, present day. See text for methodology. Wind and streamline fields are filtered using a 6 day high-pass filter. Precipitation data is unfiltered, contour intervals 2 mm day^{-1}.

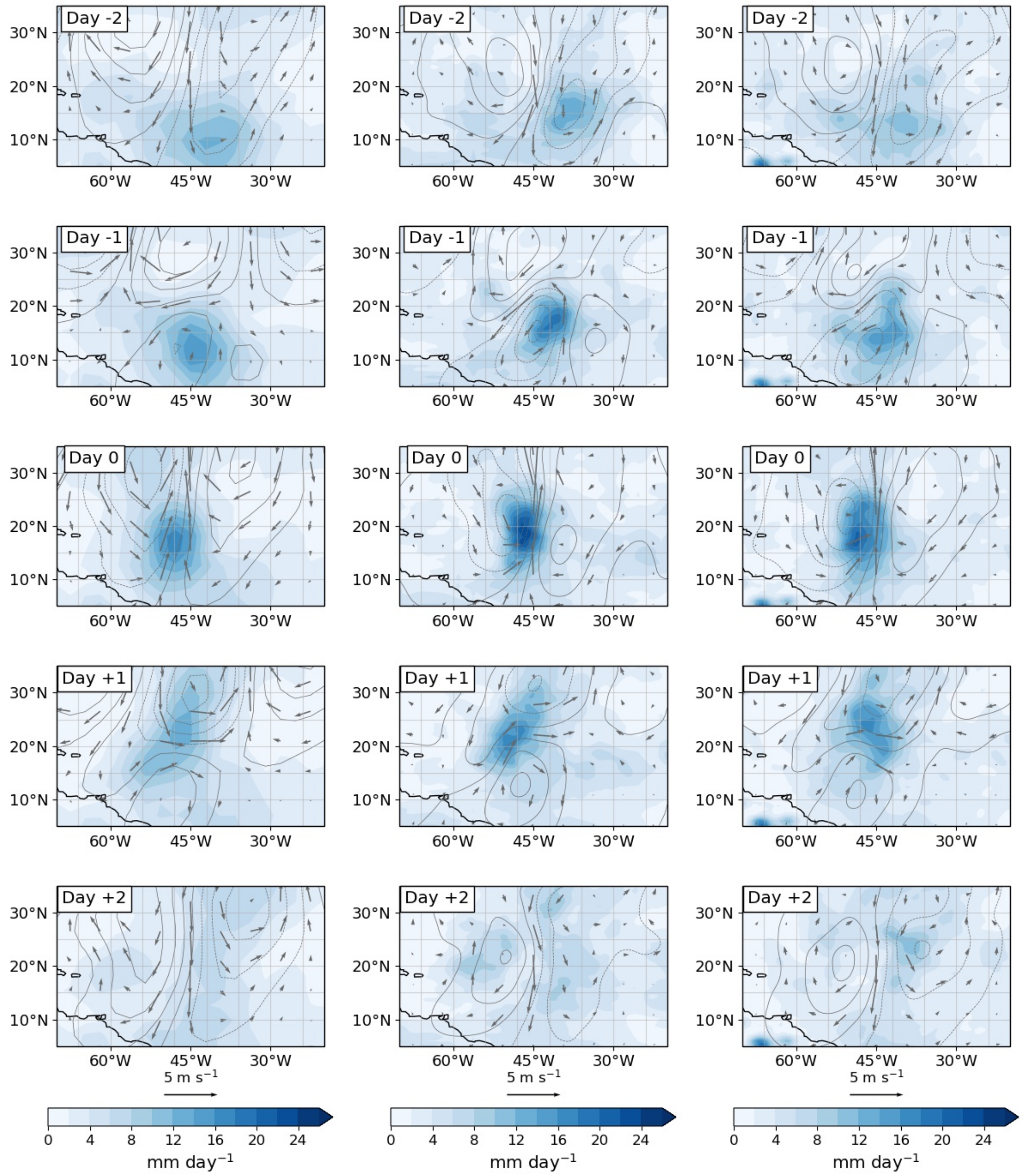

(a) T42 (b) Hybrid (c) T170

Figure 5.24: Lagged precipitation composites (based on meridional wind at 45°W, 4-25°N) for an average AEW event, Pliocene. See text for methodology. Wind and streamline fields are filtered using a 6 day high-pass filter. Precipitation data is unfiltered, contour intervals 2 mm day^{-1}.

5.3 Discussion

5.3.1 Model Bias

As mentioned previously, biases within the IGCM fall within the envelope of the Coupled Model Intercomparison Project (CMIP) phase 5 ensemble (Joshi *et al.* (2015)). Specifically for the West African monsoon, Roehrig *et al.* (2013) find that even the more advanced CMIP5 ensemble, compared with CMIP3, has not yet reached a point of reliability with regards to climate changes and their impacts, as they still do not correctly represent the monsoon in the present day. Cornforth and Hoskins (2009) highlight the difficulty of climate models in simulating the AEJ and AEW that evolve on it, due to the wide range of interacting spatio-temporal scales. Given the overall difficulty and considering the intermediate complexity of the IGCM, the model seems to perform well in capturing the general position of the main monsoon rain band, although rainfall amounts are under-represented. Berntell *et al.* (2018) shows models fail to capture summer rainfall over the Sahel region accurately with some models being in anti-phase of the multidecadal rainfall variation observed in the WAM, possibly related to the Atlantic multidecadal variability (AMV)

The model displays higher wind speeds over the ocean compared with observations; these probably do not allow sufficient time for an air parcel to accumulate moisture over the ocean as well as it should, thus leading to less rainfall in these areas and a reduction in the overall moisture supplied to the monsoon region inland - culminating in the reduced rainfall amounts seen in the IGCM compared with observations.

Hybrid resolution improves peak rainfall slightly and corrects a bias to the east in areas of steeper topography - the Guinea highlands on the coast (around 10°N, 10°W) and the Darfur mountains (10°N, 25°E) to the east. High resolution introduces further localised improvements to rainfall: An additional increase to peak rainfall around the Guinea highlands, a slightly larger increase over Cameroon and Nigeria relating to improvements in the representation of elevation of Mt. Cameroon (5°N, 9°E) and the Jos plateau to the north (around 10°N, 9 °E) and very slight additional improvements to rainfall over the east African topography.

5.3.2 Resolution Effects

While a dynamical resolution increase causes more noticeable changes to different climatic variables in the WAM region, these don't seem to have much of an effect on the local precipitation as the mechanisms which bring about this rainfall - the African Easterly Jet and resulting African Easterly Waves - remain unchanged through resolution for both the present day and the Pliocene. Increasing topographic resolution has very slight, confined, local effects to the immediate area. These help increase the level of detail in rainfall patterns, but do not cause any far-reaching effects in the study area selected. It seems that in the IGCM, the most important factor controlling rainfall in the WAM is the position and relative strength of the AEJ - controlled ultimately by soil moisture gradients which affect atmospheric humidity and cause its creation. Changes to SSTs under Pliocene conditions do not affect this gradient in the IGCM.

Analysis based on dust records of the coast of West Africa indicates a strengthened WAM during the mPWP, as well as wetter conditions over West Africa and the Sahara region (Kuechler *et al.* (2018), Salzmann *et al.* (2008)).

Using 12 PMIP3 models under Holocene conditions, Liu *et al.* (2017) show that a full coupled model may be to properly simulate tropical rainfall as ocean and atmospheric heat transport fluxes are both needed to balance each other - the oceans have increased northward heat transport and the atmosphere shifts the ITCZ northward in order to increase southward heat transport through the Hadley cells. However, in 3 out of 12 PMIP3 models using a slab ocean instead of a fully coupled ocean, the shift in mean ITCZ is southward instead of northward, owing to the lack of upper-ocean gyre circulation changes which exist in the fully coupled ocean simulations.

using zonal model simulations, Zheng and Eltahir (1998) test the role of meridional distribution of vegetative cover in the WAM based on the theory of Eltahir (1998) which implies a positive feedback mechanism between soil moisture and rainfall, with the former representative of a history for the latter, ultimately affecting the energy balance in the boundary layer through surface albedo and Bowen ratio changes. Desertification at the northern edge of the monsoon region, bordering the Sahara, had a minor effect on simulated circulation - these reduced the amount of rainfall at the desert border and slightly increased rainfall along the coast. However, deforestation along the southern coast of Africa excited a significant response which resulted in the collapse of the monsoon circulation for the worst-case scenario. Reducing surface net radiation, total flux of heat from the surface, and hence reducing boundary layer entropy. The role of evapotranspiration in the vegetation–precipitation feedback (Rachmayani *et al.* (2015)) has also been highlighted due to its effect on low-level moist static energy, convective instability, and surface latent heat flux anomalies. These have been shown to strengthen the response of the

WAM to external forcing in the Holocene.

Even though there are substantive changes in SSTs between present day and Pliocene, affecting the meridional land-ocean temperature gradient (which is thought to be central to the development and strength of the WAM through the development of the Saharan Heat Low (Lavaysse *et al.* (2009)), these seem to only affect the extent of the heat low rather than its core temperature (Figure 5.8), with little effect on wind speeds between resolutions. The model simulations utilised in this thesis use same vegetation cover for present day and Pliocene. This highlights the importance of changes in vegetation; even stark changes in the meridional SST gradient alone are not enough to cause substantial changes in the WAM.

Additionally, cycles of orbital parameters through hybrid insolation forcing, may be the driving factor of changes to WAM rainfall in the Pliocene. Using orbitally resolved records of continental hydrology and vegetation changes from West Africa for the mPWP and pre-mPWP, compared with already published records of the last glacial cycle, Kuechler *et al.* (2018) find two modes of insolation forcing: during eccentricity maxima, when precession was strong, the West African monsoon was driven by summer insolation; during eccentricity minima, when precession-driven variations in local insolation were weak, obliquity-driven changes in the summer latitudinal insolation gradient became dominant.

Smyth *et al.* (2018) use Holocene orbital parameters and show that the WAM is sensitive to changes in insolation associated with orbital forcing. Model simulations with fixed SSTs, slab ocean and interactive ocean all showed a northward expansion of the WAM (in accordance with an increase in NH summer insolation) The set of orbital parameter used in this study for the Pliocene are unchanged from present day - any such effect will not be present.

The subtle rainfall differences between present day and Pliocene rainfall, which are not a result of a fundamentally different WAM system, might be a result of the fast, tight flow around the much warmer waters to the south in the Pliocene (Figure 5.12), drawing humidity away from the continent and restricting available moisture slightly just off the western coast.

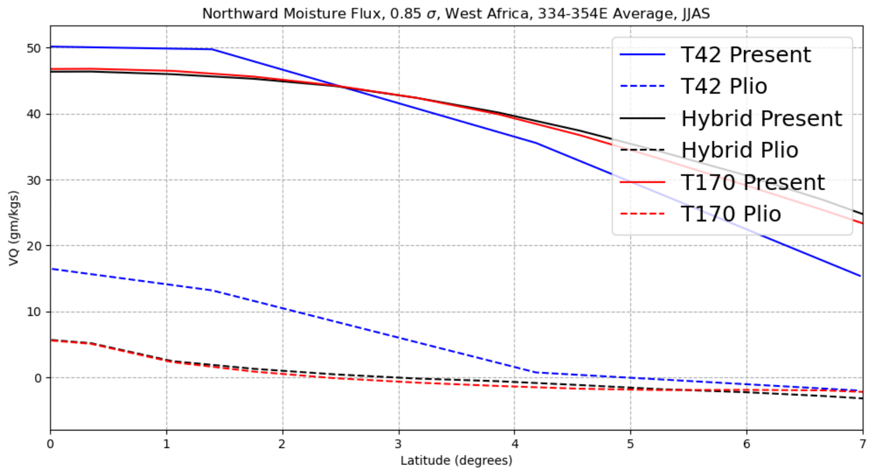

Figure 5.25: Northward moisture flux at the 0.85σ model level (approximately 880mb) during June, July, August and September (JJAS) for the southern cost of West Africa (-25 - -5°W cross-section)

Northward moisture flux in this area (Figure 5.25) is much lower in the Pliocene compared with present day for all resolutions, providing virtually no moisture, with only the low resolution simulation having any northward moisture flux past 2°N. For the present day, northward moisture flux decreases upon reaching the coast (4-5°N) but continues to be positive over land, with high resolution dynamics (Hybrid/T170) having increased northward moisture transport past 2.5°N.

5.4 Conclusions

For the WAM, increased resolution alone does not have far reaching effects and does not seem to be crucial for the description of its properties; inclusion of other aspects (insolation changes, interactive ocean, Pliocene vegetation changes, interactive vegetation) of model complexity/boundary conditions is needed to simulate changes in this region.

It is perhaps somewhat surprising that the IGCM has a good representation of AEWs in the low, T42 resolution set up, considering the minimum retained wavelength is of about 950km and a typical AEW wavelength is 4000km. Céron and Guérémy (1999) provide a detail analysis into AEWs in a similar spectral model under the same resolution. They show that albeit slightly slower, these are well represented under this low resolution and are of adequate energy. However, further in the Atlantic (Figure 5.23 and Figure 5.24) differences between resolutions do occur in the IGCM, in which higher resolution provides better retained (less dispersed) waves away from their genesis location.

This, combined with higher rainfall amounts resulting from these waves under Pliocene conditions, could mean that higher resolution is necessary in order to more accurately describe tropical cyclogenesis in the Pliocene and their plausible role in heat transfer further into the extra tropics, as described in Fedorov *et al.* (2010).

Chapter 6

Summary and Future Work

This thesis presents an in-depth analysis of the South Asian and West African monsoons in the early Pliocene, including seasonal progression of onset and pre-onset fundamental features of each monsoon under varying degrees of resolution, showing the effects of increased dynamical and topographic resolution separately.

Referring back of the research questions presented in section 1.3;

For the South Asian Monsoon:

- Low and high resolution simulations of the present day were found to be qualitatively and quantitatively similar, both adequately capturing observed rainfall. Rain bands were better defined, though still misplaced compared to observations, in the high resolution simulation.
- Dynamical resolution was found to have a much bigger effect than topographic resolution, despite the SAM having many important orographic features.
- Increased resolution has more of an effect on present day conditions than the Pliocene. The differences between Pliocene and present day simulated climates is reduced under increased resolution.
- Increased resolution is beneficial in simulating the SAM in the Pliocene. The Somali jet is less affected by hyperdiffusion under high resolution model dynamics. Topographic resolution increase provides a better defined Himalayan rain band and localised effects.

In addition:

- Monthly monsoon onset in the Pliocene is described in chapter 3, showing the development of a weaker monsoon system in the Pliocene. This weaker monsoon lags behind the present day monsoon in terms of onset and timing of peak monsoon rainfall, as shown in chapter 4.

- Potential vorticity analysis explains how changes in the Somali jet weaken the SAM in the Pliocene. A reduction in transport and lower values of PV around the Mascarene High area in the Pliocene, compared with present day, is evident in both low and high resolution simulations. This results in slower, less curved Somali jet flow which leads to significant rainfall changes in the Pliocene.

- Meridional SST gradient shown to be responsible for most significant SAM features seen; Temperatures in the western Indian Ocean shown to control rainfall in the Arabian sea

- Hyperdiffusion effects on different model resolutions were explored to explain reduction in Somali jet speeds under increased resolution

For the West African Monsoon:

- Increased resolution was found to represent the present day as well as low resolution, with $\sim$5% area-averaged absolute error.

- The difference between increasing dynamical and topographic resolutions for the WAM was not as severe as for the SAM; neither had a substantial effect on the present day or Pliocene simulations.

- Increased resolution induced very similar changes to both scenarios. The strength and position of the African Easterly Jet did not substantially change with increase resolution. Rain bands were better defined under increased Topographical resolution.

- Increased resolution does not seem to be beneficial in simulating the WAM in the Pliocene. The representation of AEWs, and the role they play in the WAM, is very similar under increased resolution for both the Pliocene and the present day.

- Changes to the meridional SST gradient alone seem to be insufficient in order to simulate substantial changes to the WAM in the IGCM. This highlights the importance of soil moisture, vegetation and orbital forcing for the WAM.

Additionally:

- Higher dynamical model resolution was shown to better represent AEWs further into the Atlantic, showing the usefulness of higher resolution in simulating the activity of these waves and their possible effects on climate.

6.1 Implications for the Pliocene

Investigations of the Pliocene using climate models will suffer from the issue of attributing the effects of resolution increase mentioned previously, like any use of climate models under increased resolution.

However, crucially for the Pliocene, the elevation of many topographic features of the epoch are not well known and there is a lot of research into the development of major topographic features, most of which (as mentioned in chapter 1) are in the tropics. The PlioMIP project, for example, includes updates to its topography field with every phase it enters - in an attempt to represent the epoch as accurately as possible. The changes to elevation when increasing the resolution of topography explored in this thesis can reach differences of over 400m in the Himalayan region and over 200m in West Africa. Even though these are significant changes from a geological point of view, the usefulness of increasing dynamical resolution alone has far outweighed that of these changes to elevations in this research, which caused only limited, local effects to climatological features. Thus, seeing as most climate models used to explore the Pliocene are used under low resolutions similar to that used here, consideration should be given to whether or not using higher dynamical resolution with the same, uncertain topography field would be beneficial to more accurately representing the Pliocene climate.

Furthermore, this thesis uses as little change to boundary conditions as possible and tries to focus on attribution of results produced; the only change from present day to Pliocene concerns sea surface temperatures for which a simpler, more zonal field is used in order to highlight just the importance of meridional gradients existing in the Pliocene - a very simplified Pliocene compared with multiple boundary changes in PlioMIP. However, keeping boundary conditions and model configuration as similarly as possible between Pliocene and present day and across resolutions allows for better attribution of features: directly to SST changes, and between dynamical/topographic resolution increases. This assists in understanding dynamical, root causes for differences between the Pliocene and present day climates.

As mentioned in chapter 1, Haywood *et al.* (2013b) suggest large scale changes seen in the Pliocene are most probably attributed to changes in meridional gradients. For the South Asian monsoon, differences in basic states between the present day and Pliocene were found in chapter 3, owing, ultimately, to fundamental differences in potential vorticity and its advection between the two hemispheres - affecting physical properties of monsoon flow. This is probably the result of changes to the SST field in the southern Indian Ocean under Pliocene conditions. For the West African monsoon, however, stark differences in SSTs between Pliocene and present day did not manifest in significant changes to monsoon dynamics, acting to eliminate this boundary condition as a possible factor for a different WAM in the Pliocene using the IGCM.

6.2 Future Work

A variety of additional experiments exploring local features, changing boundary conditions and using more complex GCMs could be used to further enhance our understanding of the SAM, WAM and other monsoons in the Pliocene. Below, suggestions for further research of each of the monsoon regions are presented, starting with the SAM.

Chapters 3 and 4 deal with a climate system which has a strong orographic component in the Himalayan mountains/ Tibetan Plateau and the East African mountains. Even for this monsoon region, simply increasing the model's dynamical resolution around these elements of topography sees the greatest changes compared with a higher, less smoothed topographic resolution. A series of sensitivity experiments relating to the East African Highlands, following Sepulchre *et al.* (2006) for example, could help determine if there is a threshold for the height of topographic features before increased resolution is beneficial.

This thesis has shown the effects of increased resolution to be locally dependent. As such, an individual, step-change analysis could be repeated for other monsoon systems.

The SST reconstruction used here does not include possible changes to Indian Ocean SSTs through the closure of the Indonesian through-flow discussed in chapter 1. Including these could pose an interesting experiment as African rainfall in the Pliocene did not differ from present day in the research presented here and might shed further light on the link between African rainfall and Indian Ocean SSTs in the later Pliocene.

It is important to mention once again that the model used for this research, the IGCM, is an intermediate, atmospheric only climate model. Thus, adding a level of complexity to the South Asian monsoon region explored here could involved using a coupled model, which would include atmopshere-ocean heat exchange and ocean dynamics. This would also provide a better understanding of the mechanism behind PV advection.

Model resolution could be increased further to explicitly resolve convective activity and avoid the need for its parametrisation. Jungandreas *et al.* (2021) investigate the influence of the representation of convection on the WAM during the mid-Holocene and find that the representation of convection (explicitly resolved versus parametrised) had more of an influence on WAM dynamics in the Holocene than an increase in resolution. Rainfall in the higher resolution, convection-permitting simulation is found to peak at a lower latitude than in the lower, parameterised simulation. In contrast, Marsham *et al.* (2013) who explored the effects of explicitly resolved convection on the present day WAM find stronger northward propagation of precipitation in explicit convection simulations compared to the parameterized simulation.

The IGCM operates a bucket model for soil moisture with non interactive vegetation. For the West African monsoon, the use of a Pliocene vegetation fields or fully interactive vegetation and an improved soil scheme might prove more beneficial. Currently, the COSMOS model is the only member of the PlioMIP2 ensemble that is run with dynamic vegetation (Stepanek *et al.* (2020))

In the western Arabian sea during the summer months, a thermal inversion layer develops during the monsoon season as a result of warm, dust-laden winds from the Arabian peninsula (Dwivedi *et al.* (2021)). The IGCM is unable to capture this inversion layer as, even though a relaxation of the vertical temperature gradient is seen in the model due to warmer winds from the peninsula, the lack of aerosol representation in the model means the inversion is not present in the model. A model run using Pliocene SSTs on a higher complexity model with aerosol parameterisation could be utilised. However, since the Pliocene SSTs used here are 2-3 °C higher than the present day in the western Arabian sea, and the inversion includes a decrease of the same or less (depending on measurement/model), it is unlikely that the inversion layer would exist in a Pliocene simulation even with aerosol parameterisation. The representation of aerosols is also important for the WAM - Alamirew *et al.* (2018) finds that dust plays an important part in regulating the Saharan heat low, more so than water vapour outside diurnal time scales.

Modern observations regarding the influence of the Indonesian Throughflow on the Mascarene High (MH) by Vidya *et al.* (2020) indicate that the ITF advects heat originating in the western Pacific Ocean to the Mascarene High region; in a warming world, this causes a reduction in mean sea level pressure and a less intense MH. In turn, this reduces the pressure gradient between the MH and the Indian subcontinent, which suppresses the intensity of the Somali Jet.

A possible experiment arising from the PlioMSST simulation, to further pinpoint the determining factor in the meridional SST gradient crucial to monsoon development, would be to alter only the SSTs in the Arabian sea, while keeping Mascarene high SSTs constant (present day values). This could show the effects of PV advection, without changes to PV values at origin.

The northward shift present in both the South Asian and West African monsoon systems when increasing dynamical resolution seems to be a general, resolution related effect. Features are better defined - with four high resolution grid boxes covering the area of just one grid box in the low resolution equivalent. Better confinement of climatological features is possible and the position of these shifts away from the Equator by roughly 2° in both cases - accounting for the difference in grid box sizes between the two resolutions near the equator (2.7° versus 0.7°). As this research uses a spectral model, this effect is presumed to be less severe in higher latitudes. A possible experiment to compliment those performed here would be to explore this northward shift effect further away from the equator. Further, an investigation into model mechanics to try and determine what precisely happens on the grid box level when dynamical resolution is increased might shed additional light on the effectiveness of increased model resolution.

Appendix A

Convectively Coupled Equatorial Waves

Convectively Coupled Equatorial waves (CCEWs) are important features in tropical climate, dominating a substantial portion of rainfall variability in the region. This family of waves, including Kelvin, Equatorial Rossby (ER), mixed Rossby-gravity (MRG) and inertio-gravity (IG), operate on a wide range of scales while maintaining a similar wave structure. The theory behind these waves was devised by Matsuno (1966), following the discovery of tropical Easterly Waves in the 1940s. Matsuno's solution to the shallow water equations under tropical constrains provided the classical linear wave theory, which instigated the search for these waves in the atmosphere. Dry wave modes were found in the Stratosphere in the early 1970s but it wasn't until well into the satellite era that CCEWs were identified in the tropics and connected with Matsuno's theory. This was partially due to the waves' tilted vertical structure which is a result of complex moist processes and thus does not correspond to linear wave theory.

Wavenumber-frequency diagrams of tropical waves were created for the Pliocene and present day under low resolution, following Wheeler and Kiladis (1999), to asses the model's ability to produce these significant waves and how they change under Pliocene conditions. These are seen in figures Figure A.1 and Figure A.2. Power increases throughout the spectrum for the Pliocene. Kelvin waves are stronger and show highest power around a period of 3 days and zonal number of 7, propagating eastward. Inertio-gravity waves are parametrized in the model and are of too small of a scale to be resolved. Equatorial Rossby (ER) wave activity is similar between the Pliocene and present day, centering around wavenumber -5 (westward propagating) and a period of 30 days. An area of very high power, eastward moving, long waves at around 30 days and 1-2 zonal wavenumber marks the Madden-Julian Oscillation (MJO). The MJO's peak power is confined to the same area on the diagram under both scenarios, but higher power is displayed in shorter wavenumbers in the Pliocene. Another area of high power levels to the top left corner of the diagram, between periods of 2-5 days and between wavenumbers -15 to -6 for the present day and -15 to -4 for the Pliocen, represents wave activity known as tropical depression type (TD-type). This group of waves also includes African Easterly Waves, related to the West African Monsoon. The Pliocene sees increased power in these type of waves, especially around a period of 2-4 days and wavenumbers -10 to -15.

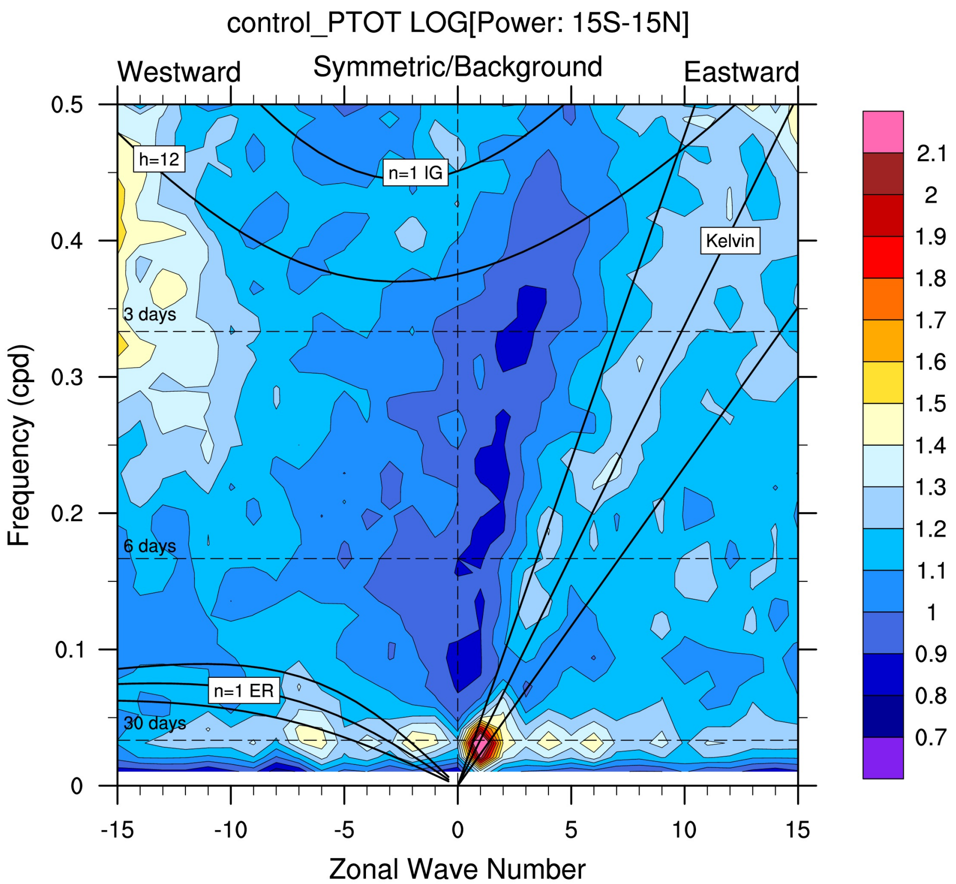

Figure A.1: Wavenumber-frequency power spectrum for the symmetric component of present day precipitation, summed from 15°N-15°N. Contour interval of 0.1, where levels of 1.1 or higher are considered significant. Dispersion curves for equatorial waves as a function of the nondimensional frequency and wavenumber. Westward propagating waves appear to the left and eastward propagating waves appear to the right.

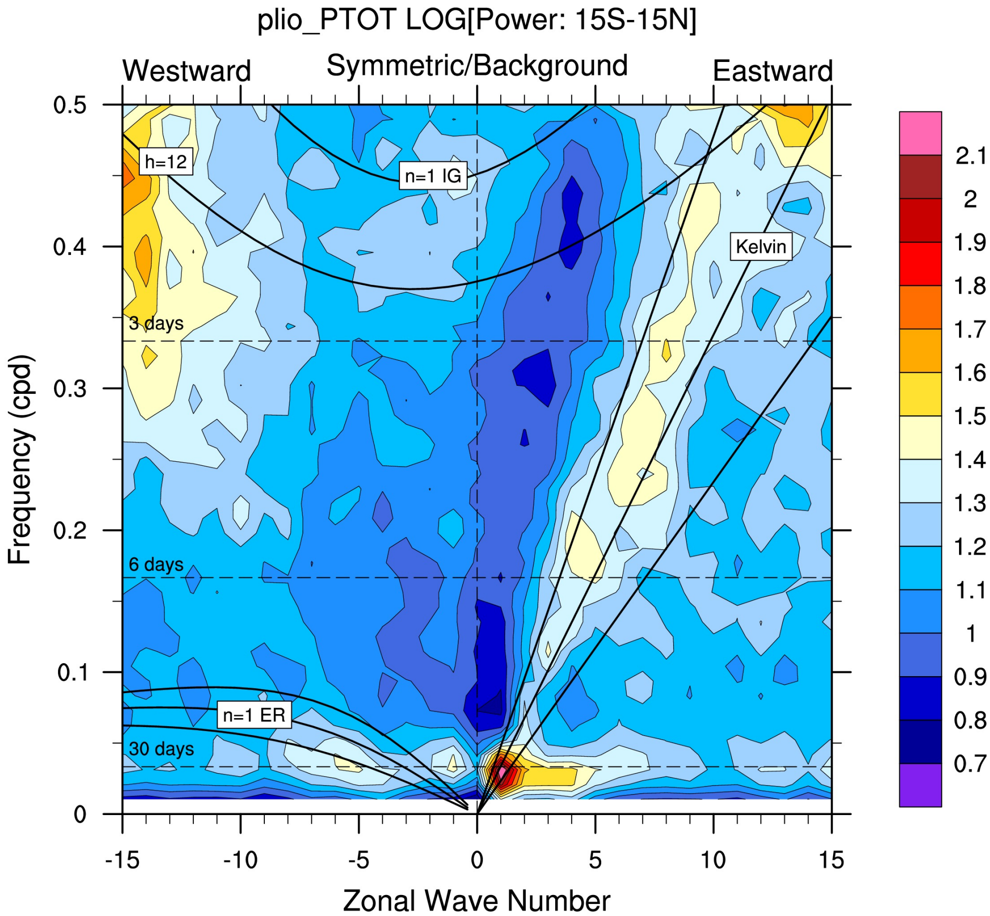

Figure A.2: Wavenumber-frequency power spectrum for the symmetric component of Pliocene precipitation, summed from 15°N-15°N. Contour interval of 0.1, where levels of 1.1 or higher are considered significant. Dispersion curves for equatorial waves as a function of the nondimensional frequency and wavenumber. Westward propagating waves appear to the left and eastward propagating waves appear to the right.

Appendix B

Chapter 3 Supplementary Figures

B.1 Potential Temperature

Figure 3.10 was used for to determine an appropriate potential temperature surface on which to examine Ertel Potential Vorticity (EPV) for comparison between present day and Pliocene in the Arabian Sea area.

The potential temperature surface chosen was 305°K. This surface is fairly consistent between Pliocene and Present day in the western Arabian Sea area (approximately between 60°- 70°E), which ensures the actual pressure levels between Pliocene and Present day don't differ much from each other while allowing the exploration of potential vorticity on a surface of constant potential temperature consistent between the two scenarios.

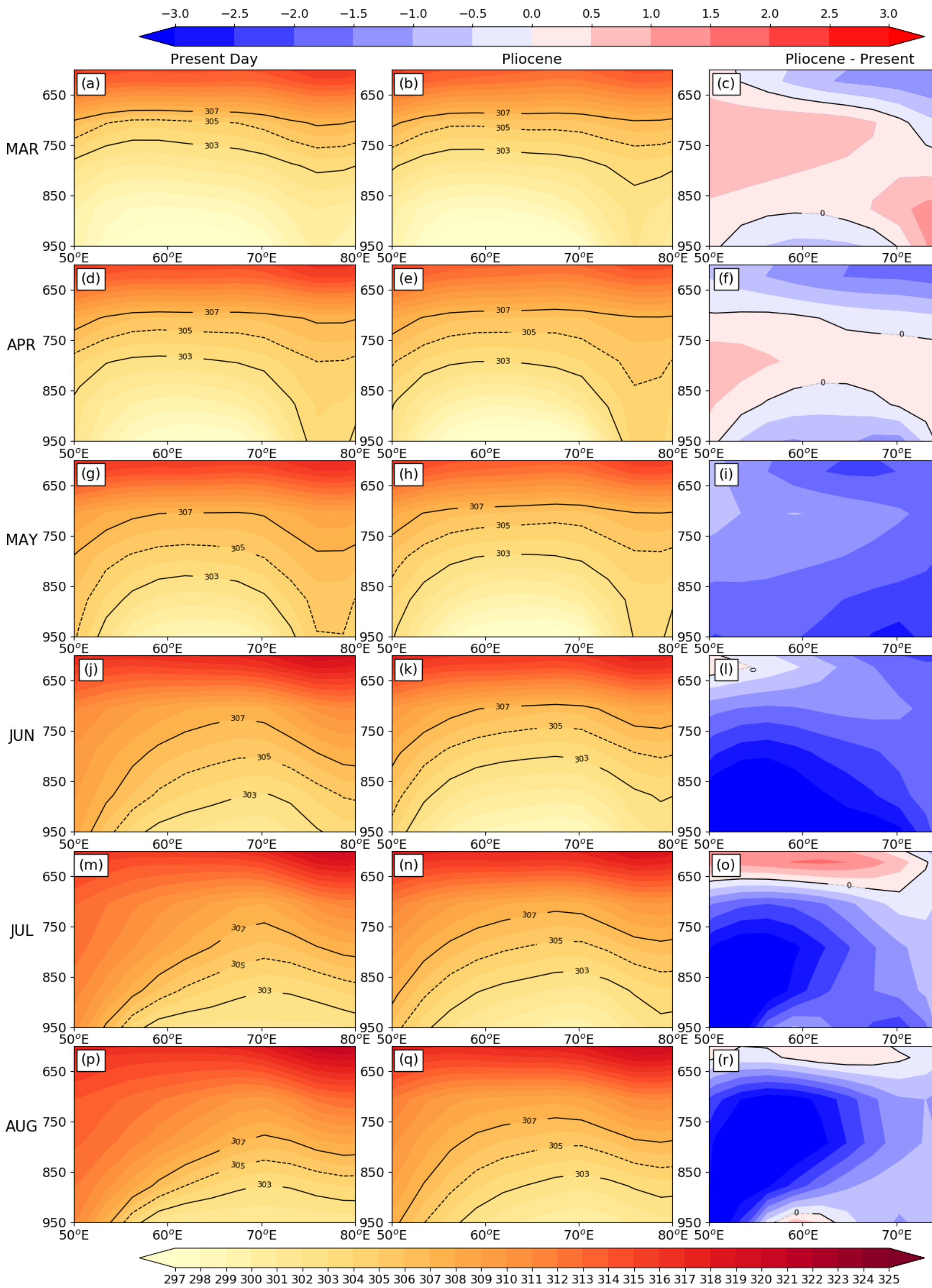

Figure B.1: Monthly potential temperatures averaged over 15°N to 20°N, March to August (rows). Full fields for present (left) and Pliocene (middle) with contour intervals of 1 °K (bottom). 303 and 307 contours in black, 305 dashed. Difference between Pliocene and present day (right) with 0.5 °K contour intervals. Data shown on pressure levels but extracted on model levels.

B.2 Other Cloud Cover

The following plots show low and mid-level cloud amounts for the low resolution model configuration.

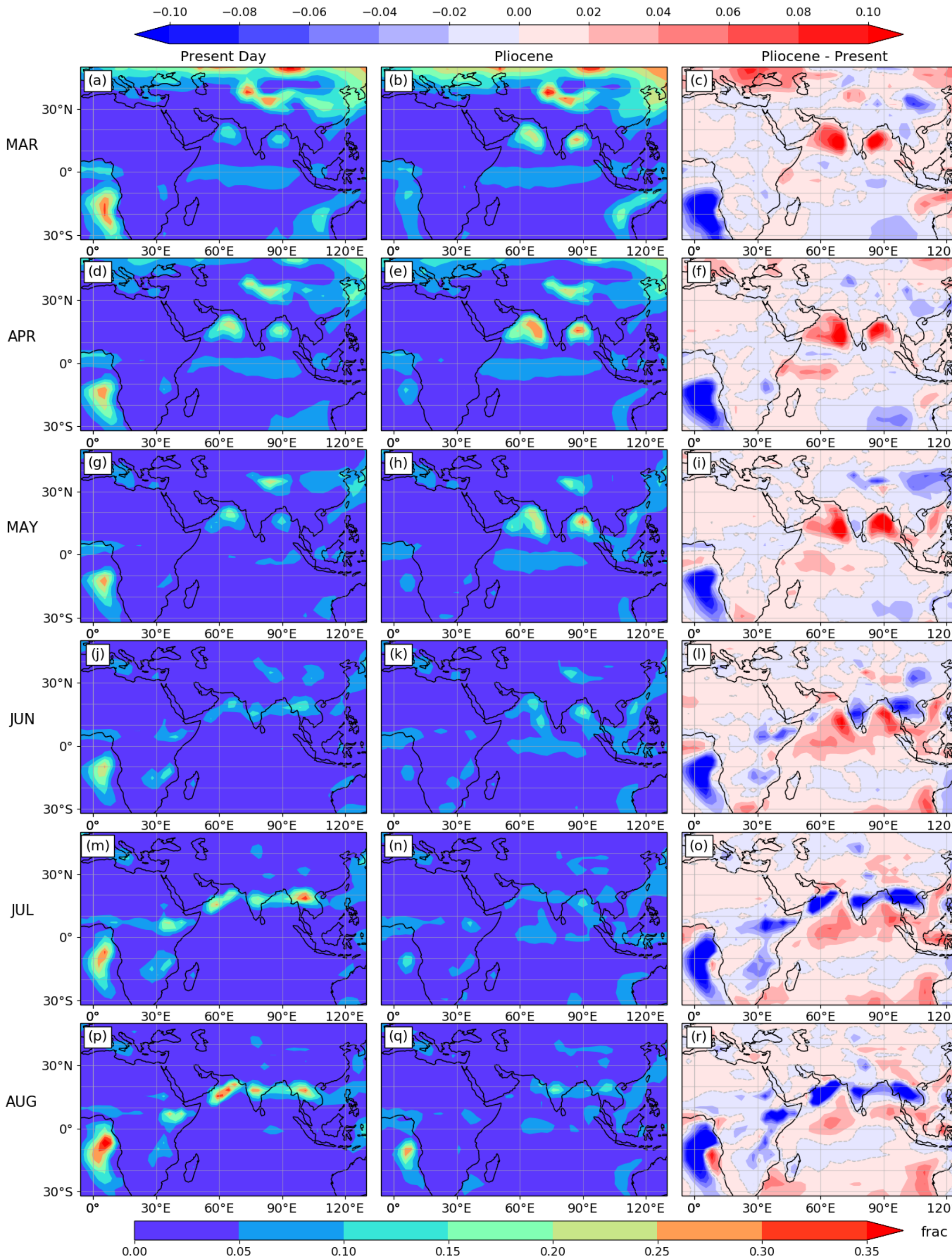

Figure B.2: Monthly low cloud amount for Africa/Asia, March to August (rows). Full fields for present (left) and Pliocene (middle) with contour intervals of 0.05 (bottom). Difference between Pliocene and present day (right) with contour intervals of 0.02. Units are of time fraction.

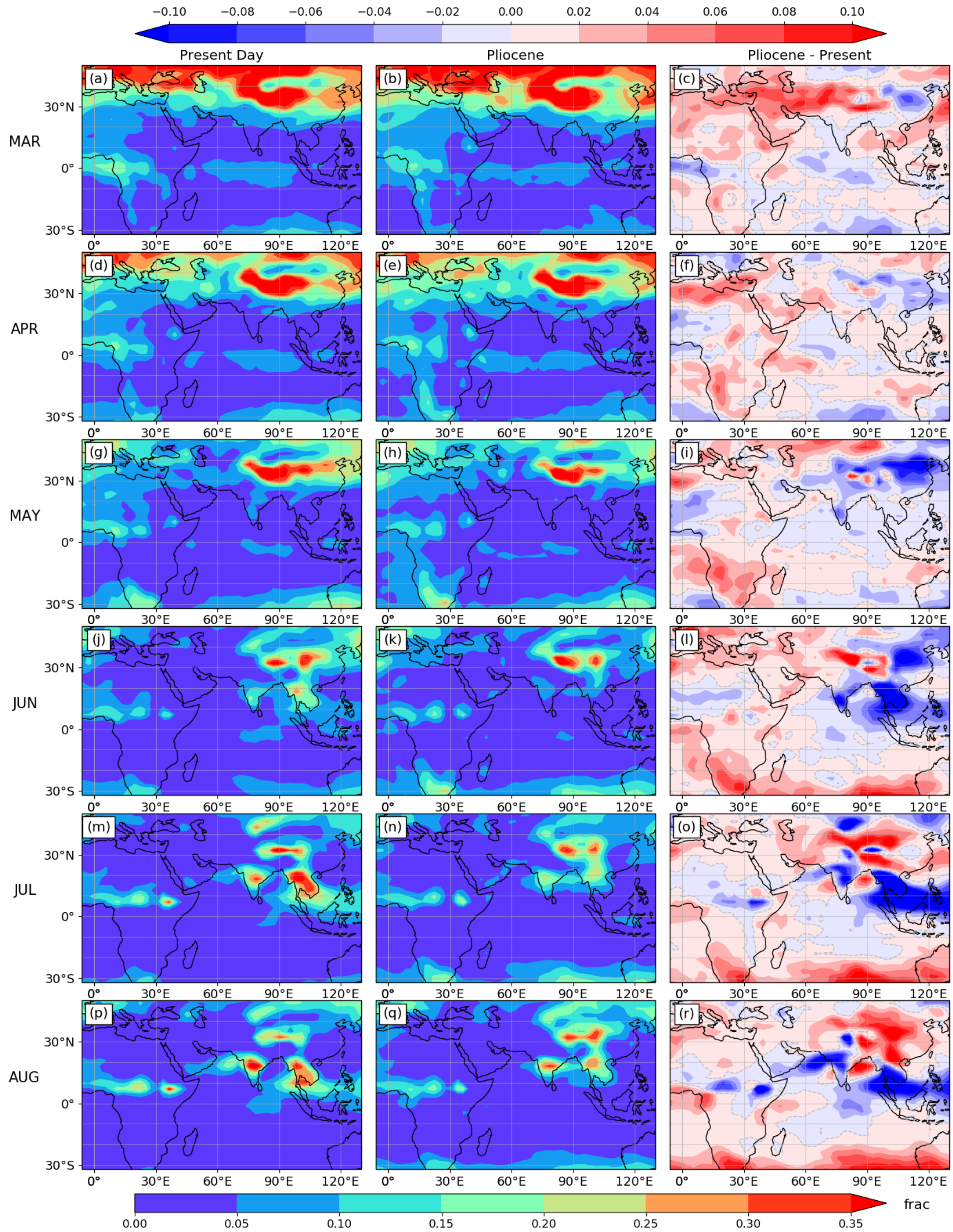

Figure B.3: Monthly mid-level cloud amount for Africa/Asia, March to August (rows). Full fields for present (left) and Pliocene (middle) with contour intervals of 0.05 (bottom). Difference between Pliocene and present day (right) with contour intervals of 0.02. Units are of time fraction.

B.3 Present versus PlioMSST

The following plots are to compliment the Pliocene versus PlioMSST analysis in 3

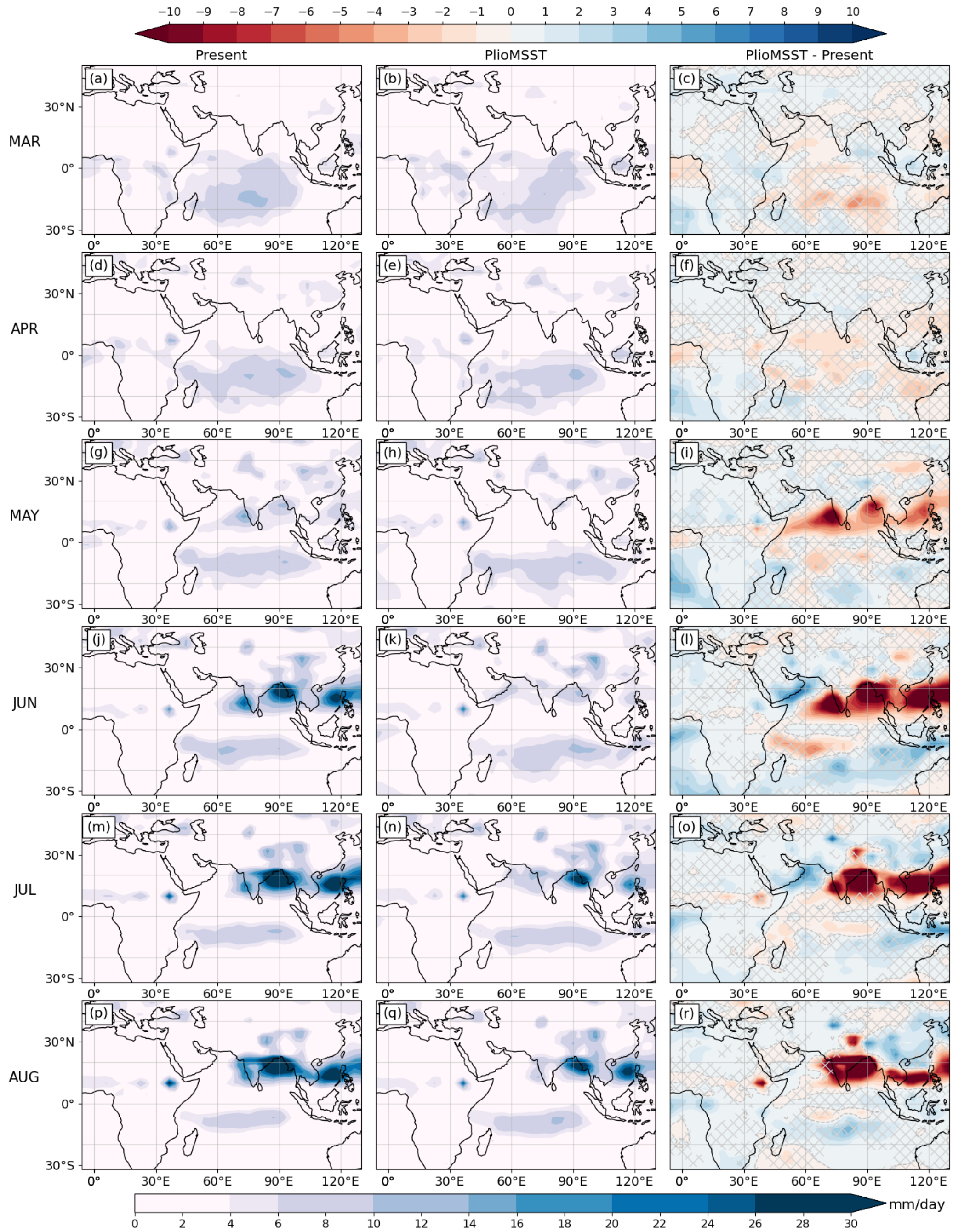

Figure B.4: Monthly precipitation rates for Africa/Asia under low resolution, March to August (rows). Full fields for Present (left) and PlioMSST (middle) with contour intervals of 2 mm day^{-1} (bottom). Difference between PlioMSST and Present day (right) with contour intervals of 1 mm day^{-1} (top).

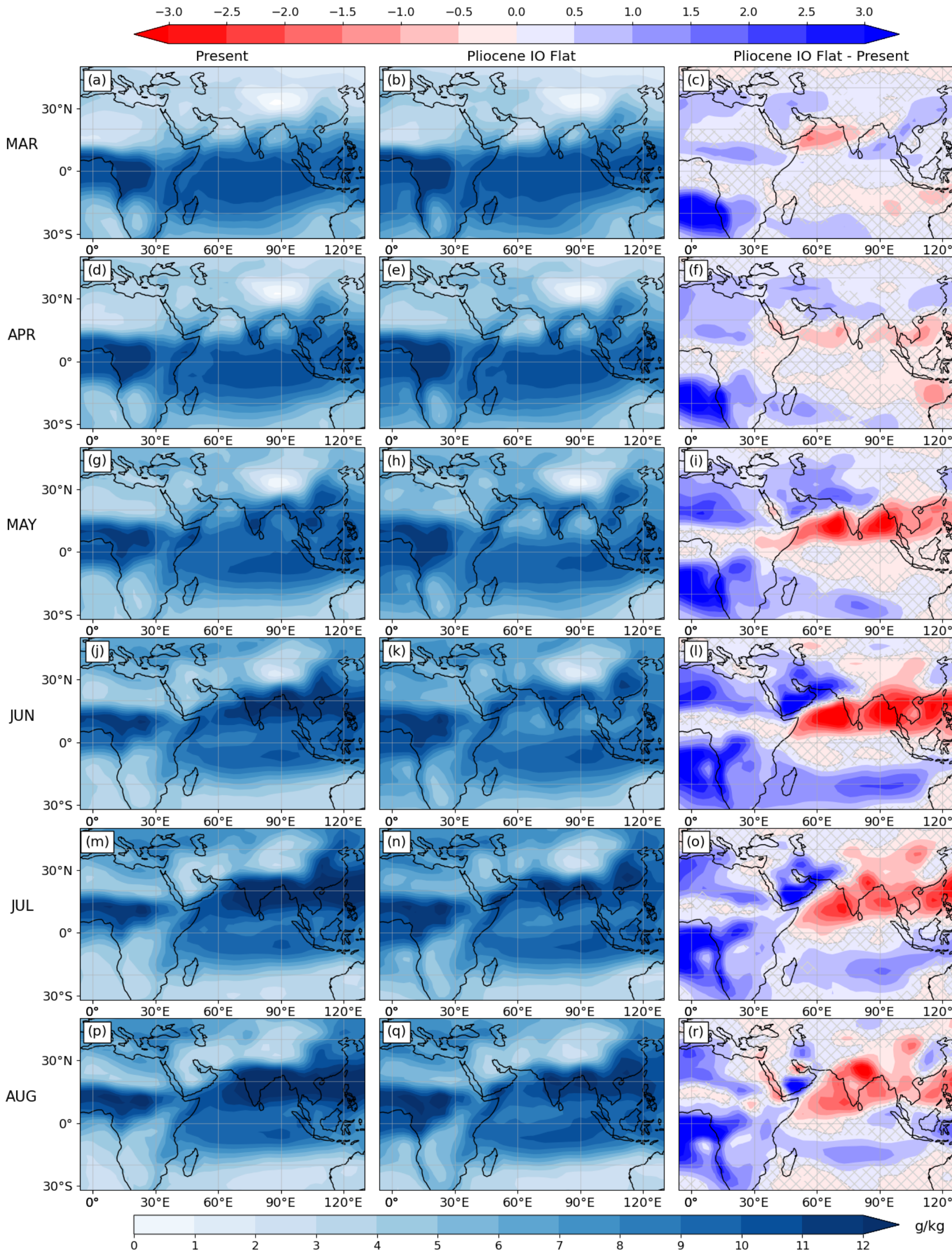

Figure B.5: Monthly Specific Humidity at 880mb for Africa/Asia under low resolution, March to August (rows). Full fields for Present (left) and PlioMSST (middle) with contour intervals of 1 g/kg (bottom). Difference between PlioMSST and Present day (right) with contour intervals of 05 g/kg (top).

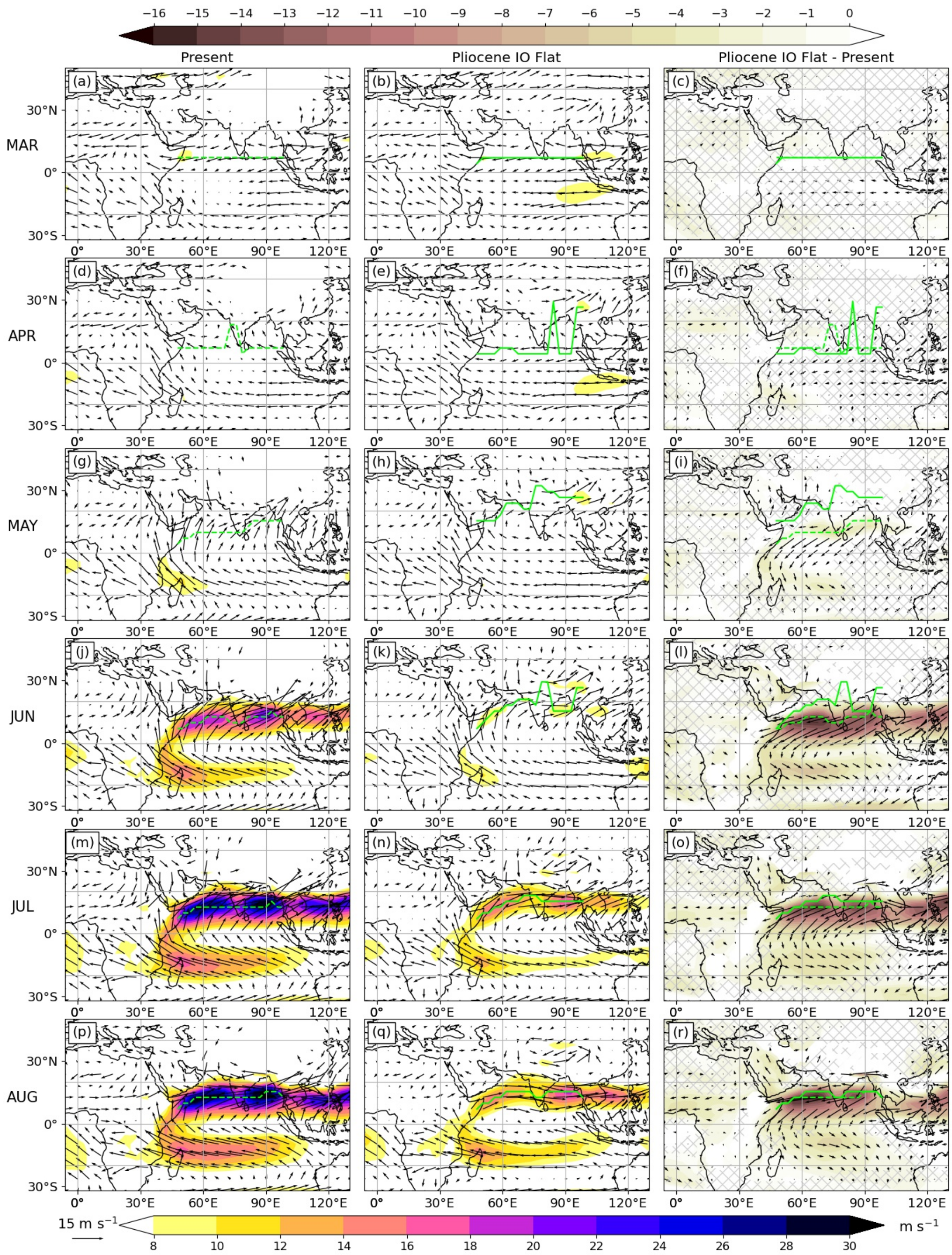

Figure B.6: Monthly wind speed and direction at 880mb for Africa/Asia under low resolution, March to August (rows). Full fields for Present (left) and PlioMSST (middle) with contour intervals of 2 m s^{-1} (bottom). Difference between PlioMSST and present day (right) with 1 m s^{-1} contour intervals (top). Green lines indicate jet axes (dashed - Present, solid - PlioMSST)

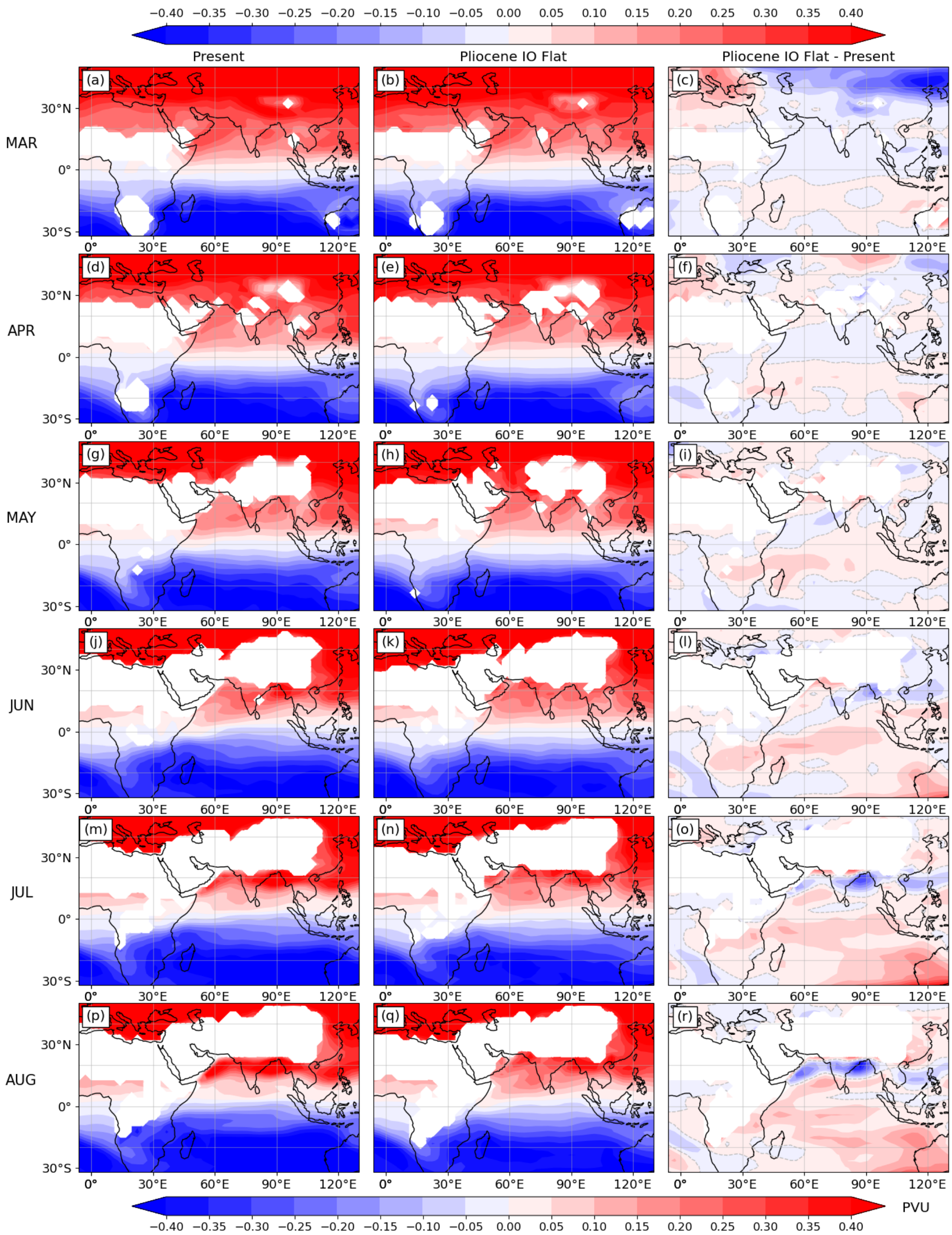

Figure B.7: Monthly Ertel potential vorticity at the 305°θ surface for Africa/Asia under low resolution, March to August (rows). Full fields for present (left) and PlioMSST (middle) with contour intervals of 0.05 PVU (bottom). Days where surface θ exceeded 305°K are discarded. Masked areas indicate 50% of days in the given month had surface θ exceeding 305°K. Difference between PlioMSST and Present day (right) with same intervals (top).

References

Abell, J. T., G. Winckler, R. F. Anderson, and T. D. Herbert (2021), Poleward and weakened westerlies during Pliocene warmth, *Nature*, *589*(7840), 70–75.

Alamirew, N. K., M. C. Todd, C. L. Ryder, J. H. Marsham, and Y. Wang (2018), The early summertime Saharan heat low: Sensitivity of the radiation budget and atmospheric heating to water vapour and dust aerosol, *Atmospheric Chemistry and Physics*, *18*(2), 1241–1262.

Auer, G., D. De Vleeschouwer, R. A. Smith, K. Bogus, J. Groeneveld, P. Grunert, I. S. Castañeda, B. Petrick, B. Christensen, C. Fulthorpe, S. J. Gallagher, and J. Henderiks (2019), Timing and Pacing of Indonesian Throughflow Restriction and Its Connection to Late Pliocene Climate Shifts, *Paleoceanography and Paleoclimatology*, *34*(4), 635–657.

Badger, M. P., T. B. Chalk, G. L. Foster, P. R. Bown, S. J. Gibbs, P. F. Sexton, D. N. Schmidt, H. Pälike, A. Mackensen, and R. D. Pancost (2019), Insensitivity of alkenone carbon isotopes to atmospheric CO2 at low to moderate CO2 levels, *Climate of the Past*, *15*(2), 539–554.

Badger, M. P., D. N. Schmidt, A. Mackensen, and R. D. Pancost (2013), High-resolution alkenone palaeobarometry indicates relatively stable pco2 during the pliocene (3.3-2.8 ma), *Philosophical Transactions of the Royal Society A: Mathematical, Physical and Engineering Sciences*, *371*(2001).

Bamber, J. L., R. L. Layberry, and S. P. Gogineni (2001), A new ice thickness and bed data set for the Greenland ice sheet: 1. Measurement, data reduction, and errors, *Journal of Geophysical Research*, *106*(D24), 33,773–33,780.

Bartoli, G., B. Hönisch, and R. E. Zeebe (2011), Atmospheric CO2 decline during the Pliocene intensification of Northern Hemisphere glaciations, *Paleoceanography*, *26*(4), 1–14.

Bartoli, G., M. Sarnthein, M. Weinelt, H. Erlenkeuser, D. Garbe-Schonberg, and D. W. Lea (2005), Final closure of Panama and the onset of northern hemisphere glaciation, *Earth and Planetary Science Letters*, *237*(1), 33–44.

Berntell, E., Q. Zhang, L. Chafik, and H. Körnich (2018), Representation of Multidecadal Sahel Rainfall Variability in 20th Century Reanalyses, *Scientific Reports*, *8*(1), 6–13.

Berntell, E., Q. Zhang, Q. Li, A. M. Haywood, J. C. Tindall, S. J. Hunter, Z. Zhang, X. Li, C. Guo, K. H. Nisancioglu, C. Stepanek, G. Lohmann, L. E. Sohl, M. A. Chandler, N. Tan, C. Contoux, G. Ramstein, M. L. Baatsen, A. S. Von Der Heydt, D. Chandan, W. R. Peltier, A. Abe-Ouchi, W. L. Chan, Y. Kamae, C. J. Williams, D. J. Lunt, R. Feng, B. L. Otto-Bliesner, and E. C. Brady (2021), Mid-Pliocene West African Monsoon rainfall as simulated in the PlioMIP2 ensemble, *Climate of the Past*, *17*(4), 1777–1794.

Betts, A. K. (1986), A new convective adjustment scheme. Part I: Observational and theoretical basis, *Quarterly Journal of the Royal Meteorological Society*, *112*(473), 677–691.

Blanc, P. L. (2002), The opening of the Plio-Quaternary Gibraltar Strait: Assessing the size of a cataclysm, *Geodinamica Acta*, *15*(5-6), 303–317.

Brierley, C., N. Burls, C. Ravelo, and A. Fedorov (2015), Pliocene warmth and gradients, *Nature Geoscience*, *8*(6), 419–420.

Brierley, C. M. (2015), Interannual climate variability seen in the Pliocene Model Intercomparison Project, *Climate of the Past*, *11*(3), 605–618.

Brierley, C. M., A. V. Fedorov, Z. Liu, T. D. Herbert, K. T. Lawrence, and J. P. Lariviere (2009), Greatly expanded tropical warm pool and weakened Hadley circulation in the early Pliocene., *Science*, *323*(5922), 1714–1718.

Bruce, J., D. Quadfasel, and J. Swallow (1980), Somali Eddy Formation During the Commencement of the Southwest Monsoon, 1978, *Journal of Geophysical Research*, *85*, 6654–6660.

Burls, N. J., and A. V. Fedorov (2014), Simulating Pliocene warmth and a permanent El Niño-like state: The role of cloud albedo, *Paleoceanography*, *29*(10), 893–910.

Burls, N. J., and A. V. Fedorov (2017), Wetter subtropics in a warmer world: Contrasting past and future hydrological cycles, *Proceedings of the National Academy of Sciences of the United States of America*, *114*(49), 12,888–12,893.

Byrne, M. P., and P. A. O'Gorman (2013), Link between land-ocean warming contrast and surface relative humidities in simulations with coupled climate models, *Geophysical Research Letters*, *40*(19), 5223–5227.

Cane, M., and P. Molnar (2001), Closing of the Indonesian seaway as a precursor to east African aridification around 3-4 million years ago, *Nature*, *411*(6834), 157–162.

Céron, J. P., and J. F. Guérémy (1999), Validation of the space-time variability of African easterly waves simulated by the CNRM GCM, *Journal of Climate*, *12*(9), 2831–2855.

Charney, J., A. Arakawa, D. Baker, B. Bolin, R. Dickinson, R. Goody, C. Leith, H. Stommel, and C. Wunsch (1979), *Carbon Dioxide and Climate: A Scientific Assessment*, Tech. rep., Massachusetts Institute of Technology.

Chorowicz, J. (2005), The East African rift system, *Journal of African Earth Sciences*, *43*(1-3), 379–410.

Chung, C. E., and V. Ramanathan (2006), Weakening of north Indian SST gradients and the monsoon rainfall in India and the Sahel, *Journal of Climate*, *19*(10), 2036–2045.

Clemens, S. C., W. Kuhnt, and L. J. LeVay (2015), Indian monsoon rainfall, *International Ocean Discovery Program Expedition Preliminary Report*, p. 353.

Coates, A. G., J. B. C. Jackson, L. S. Collins, T. M. Cronin, J. Dowsett, L. M. Bybell, P. Jung, and J. a. Obando (1992), Closure of the Isthmus of Panama : The near-shore marine record of Costa Rica and western Panama, *Geological Society of America Bulletin*, *104*(July), 814–828.

Cohen, K. M., S. C. Finney, P. L. Gibbard, and J.-X. Fan (2014), The ICS International Chronostratigraphic Chart, *Episodes*, *36*, 199–204.

Collins, M., R. Knutti, J. Arblaster, J.-L. Dufresne, T. Fichefet, P. Friedlingstein, X. Gao, W. J. Gutowski, T. Johns, G. Krinner, M. Shongwe, C. Tebaldi, A. J. Weaver, and M. Wehner (2013), Long-term Climate Change: Projections, Commitments and Irreversibility, *Climate Change 2013: The Physical Science Basis. Contribution of Working Group I to the Fifth Assessment Report of the Intergovernmental Panel on Climate Change*, pp. 1029–1136.

Cook, K. H. (1999), Generation of the African easterly jet and its role in determining West African precipitation, *Journal of Climate*, *12*(5 I), 1165–1184.

Cornforth, r. j., and b. j. Hoskins (2009), Understanding African easterly waves: a moist singular vector approach, *Atmospheric Science Letters*, *10*(3), 249–254.

Dayem, K. E., D. C. Noone, and P. Molnar (2007), Tropical western Pacific warm pool and maritime continent precipitation rates and their contrasting relationships with the Walker Circulation, *Journal of Geophysical Research Atmospheres*, *112*(6), 1–12.

de la Vega, E., T. B. Chalk, P. A. Wilson, R. P. Bysani, and G. L. Foster (2020), Atmospheric CO2 during the Mid-Piacenzian Warm Period and the M2 glaciation, *Scientific Reports*, *10*(1), 14–21.

DeConto, R. M., and D. Pollard (2016), Contribution of Antarctica to past and future sea-level rise, *Nature*, *531*(7596), 591–597.

Dee, D. P., S. M. Uppala, A. J. Simmons, P. Berrisford, P. Poli, S. Kobayashi, U. Andrae, M. A. Balmaseda, G. Balsamo, P. Bauer, P. Bechtold, A. C. M. Beljaars, L. van de Berg, J. Bidlot, N. Bormann, C. Delsol, R. Dragani, M. Fuentes,

A. J. Geer, L. Haimberger, S. B. Healy, H. Hersbach, E. V. Hólm, L. Isaksen, P. Kållberg, M. Köhler, M. Matricardi, A. P. Mcnally, B. M. Monge-Sanz, J. J. Morcrette, B. K. Park, C. Peubey, P. de Rosnay, C. Tavolato, J. N. Thépaut, and F. Vitart (2011), The ERA-Interim reanalysis: Configuration and performance of the data assimilation system, *Quarterly Journal of the Royal Meteorological Society*, *137*(656), 553–597.

Dekens, P. S., A. C. Ravelo, and M. D. McCarthy (2007), Warm upwelling regions in the Pliocene warm period, *Paleoceanography*, *22*(3), 1–12.

Dowsett, H., A. Dolan, D. Rowley, R. Moucha, A. M. Forte, J. X. Mitrovica, M. Pound, U. Salzmann, M. Robinson, M. Chandler, K. Foley, and A. Haywood (2016), The PRISM4 (mid-Piacenzian) paleoenvironmental reconstruction, *Climate of the Past*, *12*(7), 1519–1538.

Dowsett, H., M. Robinson, A. Haywood, U. Salzmann, D. Hill, L. Sohl, M. Chandler, M. Williams, K. Foley, and D. Stoll (2010), The PRISM3D paleoenvironmental reconstruction, *Stratigraphy*, *7*, 123–139.

Dowsett, H. J., K. M. Foley, D. K. Stoll, M. A. Chandler, L. E. Sohl, M. Bentsen, B. L. Otto-Bliesner, F. J. Bragg, W.-L. Chan, C. Contoux, A. M. Dolan, A. M. Haywood, J. A. Jonas, A. Jost, Y. Kamae, G. Lohmann, D. J. Lunt, K. H. Nisancioglu, A. Abe-Ouchi, G. Ramstein, C. R. Riesselman, M. M. Robinson, N. A. Rosenbloom, U. Salzmann, C. Stepanek, S. L. Strother, H. Ueda, Q. Yan, and Z. Zhang (2013), Sea surface temperature of the mid-Piacenzian ocean: a data-model comparison., *Scientific reports*, *3*, 2013.

Dowsett, H. J., and M. M. Robinson (2009), Mid-Pliocene equatorial Pacific sea surface temperature reconstruction: a multi-proxy perspective., *Philosophical transactions. Series A, Mathematical, physical, and engineering sciences*, *367*(1886), 109–125.

Duque-Caro, H. (1990), Neogene stratigraphy, paleoceanography and paleobiology in northwest South America and the evolu- tion of the Panama Seaway., *Palaeogeography, Palaeoclimatology, Palaeoecology*, *77*, 203–234.

Dwivedi, S., V. Yesubabu, M. V. Ratnam, H. P. Dasari, S. Langodan, S. T. Raj, and I. Hoteit (2021), Variability of monsoon inversion over the Arabian Sea and its impact on rainfall, *International Journal of Climatology*, *41*(S1), E2979–E2999.

Edwards, T. L., M. A. Brandon, G. Durand, N. R. Edwards, N. R. Golledge, P. B. Holden, I. J. Nias, A. J. Payne, C. Ritz, and A. Wernecke (2019), Revisiting Antarctic ice loss due to marine ice-cliff instability, *Nature*, *566*(7742), 58–64.

Eltahir, E. A. (1998), A soil moisture-rainfall feedback mechanism 1. Theory and observations, *Water Resources Research*, *34*(4), 765–776.

Fedorov, A., C. Brierley, and K. Emanuel (2010), Tropical cyclones and permanent El Niño in the early Pliocene epoch, *Nature*, *463*(7284), 1066–70.

Fedorov, A., P. Dekens, M. McCarthy, A. Ravelo, P. DeMenocal, M. Barreiro, R. Pacanowski, and S. Philander (2006), The Pliocene Paradox (Mechanisms for a Permanent El Nino), *Science*, *312*(5779), 1485–1489.

Fedorov, A. V., N. J. Burls, K. T. Lawrence, and L. C. Peterson (2015), Tightly linked zonal and meridional sea surface temperature gradients over the past five million years, *Nature Geoscience*, *8*(12), 975–980.

Fielding, E. J. (1996), Tibet uplift and erosion, *Tectonophysics*, *260*(1-3), 55–84.

Forster, P. M. D. F., M. Blackburn, R. Glover, and K. P. Shine (2000), An examination of climate sensitivity for idealised climate change experiments in an intermediate general circulation model, *Climate Dynamics*, *16*(10-11), 833–849.

Foster, G. L., D. L. Royer, and D. J. Lunt (2017), Future climate forcing potentially without precedent in the last 420 million years, *Nature Communications*, *8*, 1–8.

Garcia-Castellanos, D., F. Estrada, I. Jiménez-Munt, C. Gorini, M. Fernàndez, J. Vergés, and R. De Vicente (2009), Catastrophic flood of the Mediterranean after the Messinian salinity crisis., *Nature*, *462*(7274), 778–781.

Gill, A. (1980), Some simple solutions for heat-induced tropical circulation, *Quarterly Journal of the Royal Meteorological Society*, *106*, 447–462.

Gill, E. C., B. Rajagopalan, P. Molnar, and T. M. Marchitto (2016), Reduced-dimension reconstruction of the equatorial Pacific SST and zonal wind fields over the past 10,000 years using Mg/Ca and alkenone records, *Paleoceanography*, *31*(7), 928–952.

Goddard, L., and N. E. Graham (1999), Importance of the Indian Ocean for simulating rainfall anomalies over eastern and southern Africa, *Journal of Geophysical Research*, *104*(D16), 19,099.

Grant, G. R., T. R. Naish, G. B. Dunbar, P. Stocchi, M. A. Kominz, P. J. Kamp, C. A. Tapia, R. M. McKay, R. H. Levy, and M. O. Patterson (2019), The amplitude and origin of sea-level variability during the Pliocene epoch, *Nature*, *574*(7777), 237–241.

Hahn, D. G., and S. Manabe (1975), Role of Mountains in the South Asian Monsoon Circulation., *Journal of the Atmospheric Sciences*, *32*(8), 1515–1541.

Hall, N. M., and P. Peyrille (2006), Dynamics of the West African monsoon, *Journal de Physique IV*, (June), 1–5.

Hameed, S. N., D. Jin, and V. Thilakan (2018), A model for super El Niños, *Nature Communications*, *9*(1), 1–15.

Han, Z., Q. Zhang, Q. Li, R. Feng, A. Haywood, J. Tindall, S. Hunter, B. Otto-Bliesner, E. Brady, N. Rosenbloom, Z. Zhang, X. Li, C. Guo, K. Nisancioglu,

C. Stepanek, G. Lohmann, L. Sohl, M. Chandler, N. Tan, G. Ramstein, M. Baatsen, A. Heydt, D. Chandan, W. R. Peltier, C. Williams, D. Lunt, J. Cheng, Q. Wen, and N. Burls (2021), Evaluating the large-scale hydrological cycle response within the PlioMIP2 ensemble, *Climate of The Past Discussions*, (November), 1–32.

Haug, G. H., and L. Keigwin (2004), How the Isthmus of Panama Put Ice in the Arctic, *Oceanus*, *42*(2).

Haug, G. H., and R. Tiedemann (1998), Effect of the formation of the Isthmus of Panama on Atlantic Ocean thermohaline circulation, *Nature*, *393*(6686), 673–676.

Haug, G. H., R. Tiedemann, R. Zahn, and A. C. Ravelo (2001), Role of Panama uplift on oceanic freshwater balance, *Geology*, *29*(3), 207–210.

Haywood, A. M., A. M. Dolan, S. J. Pickering, H. J. Dowsett, E. L. Mcclymont, C. L. Prescott, U. Salzmann, D. J. Hill, S. J. Hunter, D. J. Lunt, J. O. Pope, and P. J. Valdes (2013a), On the identification of a pliocene time slice for data-model comparison, *Philosophical Transactions of the Royal Society A: Mathematical, Physical and Engineering Sciences*, *371*(2001).

Haywood, A. M., H. J. Dowsett, and A. M. Dolan (2016a), Integrating geological archives and climate models for the mid-Pliocene warm period, *Nature Communications*, *7*(May 2015).

Haywood, A. M., H. J. Dowsett, A. M. Dolan, D. Rowley, A. Abe-Ouchi, B. Otto-Bliesner, M. A. Chandler, S. J. Hunter, D. J. Lunt, M. Pound, and U. Salzmann (2016b), The Pliocene Model Intercomparison Project (PlioMIP) Phase 2: Scientific objectives and experimental design, *Climate of the Past*, *12*(3), 663–675.

Haywood, a. M., H. J. Dowsett, B. Otto-Bliesner, M. a. Chandler, a. M. Dolan, D. J. Hill, D. J. Lunt, M. M. Robinson, N. Rosenbloom, U. Salzmann, and L. E. Sohl (2010), Pliocene model intercomparison project (PlioMIP): Experimental design and boundary conditions (Experiment 1), *Geoscientific Model Development*, *3*(1), 227–242.

Haywood, A. M., D. J. Hill, A. M. Dolan, B. L. Otto-Bliesner, F. Bragg, W. L. Chan, M. A. Chandler, C. Contoux, H. J. Dowsett, A. Jost, Y. Kamae, G. Lohmann, D. J. Lunt, A. Abe-Ouchi, S. J. Pickering, G. Ramstein, N. A. Rosenbloom, U. Salzmann, L. Sohl, C. Stepanek, H. Ueda, Q. Yan, and Z. Zhang (2013b), Large-scale features of Pliocene climate: Results from the Pliocene Model Intercomparison Project, *Climate of the Past*, *9*, 191–209.

Haywood, A. M., P. participants , H.J. Dowsett, J.C. Tindall, and PlioMIP2 (2021), PlioMIP: The Pliocene Model Intercomparison Project, *Past Global Changes Magazine*, *29*(2), 92–93.

Haywood, A. M., J. C. Tindall, H. J. Dowsett, A. M. Dolan, K. M. Foley, S. J. Hunter, D. J. Hill, W. L. Chan, A. Abe-Ouchi, C. Stepanek, G. Lohmann, D. Chandan, W. Richard Peltier, N. Tan, C. Contoux, G. Ramstein, X. Li, Z. Zhang, C. Guo, K. H. Nisancioglu, Q. Zhang, Q. Li, Y. Kamae, M. A. Chandler, L. E. Sohl, B. L. Otto-Bliesner, R. Feng, E. C. Brady, A. S. Von Der Heydt, M. L. Baatsen, and D. J. Lunt (2020), The Pliocene Model Intercomparison Project Phase 2: Large-scale climate features and climate sensitivity, *Climate of the Past*, *16*(6), 2095–2123.

Hoskins, B. J., and M. J. Rodwell (1995), A Model of the Asian Summer Monsoon. Part I: The Global Scale, *Journal of the Atmospheric Sciences*, *52*(9), 1329–1340.

Hoskins, B. J., and A. J. Simmons (1975), A multi-layer spectral model and the semi-implicit method, *Q.J.R. Meteorol. Soc.*, *101*(429), 637–655.

Hsu, K., W. Ryan, and M. Cita (1973), Late Miocene Desiccation of the Mediterranean, *Nature*, *242*(5395), 240–244.

Hsü, K. J., P. Guitang, and a. M. C. Sengör (1995), Tectonic Evolution of the Tibetan Plateau: A Working Hypothesis Based on the Archipelago Model of Orogenesis, *International Geology Review*, *37*(6), 473–508.

Huang, B., P. W. Thorne, V. F. Banzon, T. Boyer, G. Chepurin, J. H. Lawrimore, M. J. Menne, T. M. Smith, R. S. Vose, and H. M. Zhang (2017), Extended reconstructed Sea surface temperature, Version 5 (ERSSTv5): Upgrades, validations, and intercomparisons, *Journal of Climate*, *30*(20), 8179–8205.

Issa Lélé, M., and P. J. Lamb (2010), Variability of the Intertropical Front (ITF) and Rainfall over the West African Sudan–Sahel Zone, *Journal of Climate*, *23*(14), 3984–4004.

Izumo, T., J. Vialard, M. Lengaigne, C. De Boyer Montegut, S. K. Behera, J. J. Luo, S. Cravatte, S. Masson, and T. Yamagata (2010), Influence of the state of the Indian Ocean Dipole on the following years El No, *Nature Geoscience*, *3*(3), 168–172.

Jablonowski, C., and D. L. Williamson (2011), The Pros and Cons of Diffusion, Filters and Fixers in Atmospheric General Circulation Models, in: *Numerical Techniques for Global Atmospheric Models. Lecture notes in computational science and engineering,* (Peter H. Lauritzen, Christiane Jabloniwski, Mark A. Taylor, R. D. N., ed.), vol. 80, pp. 381–482, Springer.

Jain, S., S. K. Mishra, A. Anand, P. Salunke, and J. T. Fasullo (2021), Historical and projected low-frequency variability in the Somali Jet and Indian Summer Monsoon, *Climate Dynamics*, *56*(3-4), 749–765.

Johnson, R. H., and R. A. Houze (1987), Precipitating Cloud Systems of the Asian Monsoon, *Monsoon Meteorology*, pp. 298–353.

Joshi, M., and C. Brierley (2013), Stratospheric modulation of the Boreal response to Pliocene tropical Pacific sea surface temperatures, *Earth and Planetary Science Letters*, *365*, 1–6.

Joshi, M., M. Stringer, K. van der Wiel, a. O'Callaghan, and S. Fueglistaler (2015), IGCM4: a fast, parallel and flexible intermediate climate model, *Geoscientific Model Development*, *8*(4), 1157–1167.

Jungandreas, L., C. Hohenegger, and M. Claussen (2021), Influence of the representation of convection on the mid-Holocene West African Monsoon, *Climate of the Past*, *17*(4), 1665–1684.

Karas, C., D. Nürnberg, A. Bahr, J. Groeneveld, J. O. Herrle, R. Tiedemann, and P. B. Demenocal (2017), Pliocene oceanic seaways and global climate, *Scientific Reports*, *7*(January), 4–11.

Karas, C., D. Nürnberg, A. K. Gupta, R. Tiedemann, K. Mohan, and T. Bickert (2009), Mid-Pliocene climate change amplified by a switch in Indonesian subsurface throughflow, *Nature Geoscience*, *2*(6), 434–438.

Kawai, H., and T. Inoue (2006), A simple parameterization scheme for subtropical marine stratocumulus, *Scientific Online Letters on the Atmosphere*, *2*(1980), 17–20.

Keigwin, L. (1982), Isotopic Paleoceanography of the Caribbean and East Pacific: Role of Panama Uplift in Late Neogene Time, *Science*, *217*(4557), 350–353.

Krishnamurti, T. N., and H. N. Bhalme (1976), Oscillations of a Monsoon System - 1. Observational Aspects., *Journal of the Atmospheric Sciences*, *33*(10), 1937–1954.

Kuechler, R. R., L. M. Dupont, and E. Schefuß (2018), Hybrid insolation forcing of Pliocene monsoon dynamics in West Africa, *Climate of the Past*, *14*(1), 73–84.

Kummerow, C., W. Barnes, T. Kozu, J. Shiue, and J. Simpson (1998), The tropical rainfall measuring mission(TRMM) sensor package, *Journal of Atmospheric and Oceanic Technology*, *15*(3), 809–817.

Kürschner, W. M., J. Van Der Burgh, H. Visscher, and D. L. Dilcher (1996), Oak leaves as biosensors of late Neogene and early Pleistocene paleoatmospheric CO2 concentrations, *Marine Micropaleontology*, *27*(1-4), 299–312.

Lavaysse, C., C. Flamant, S. Janicot, D. J. Parker, J. P. Lafore, B. Sultan, and J. Pelon (2009), Seasonal evolution of the West African heat low: A climatological perspective, *Climate Dynamics*, *33*(2-3), 313–330.

Le Fort, P. (1975), Himalayas: the collided range. present knowledge of the continental arc, *American Journal of Science*, *275*, 1–44.

Li, C., and M. Yanai (1996), The onset and interannual variability of the asian summer monsoon in relation to land-sea thermal contrast, *Journal of Climate*, *9*(2), 358–375.

Li, X., D. Jiang, Z. Tian, and Y. Yang (2018), Mid-Pliocene global land monsoon from PlioMIP1 simulations, *Palaeogeography, Palaeoclimatology, Palaeoecology*, *512*(June), 56–70.

Lisiecki, L. E., and M. E. Raymo (2005), A Pliocene-Pleistocene stack of 57 globally distributed benthic d18O records, *Paleoceanography*, *20*(1), 1–17.

Lisiecki, L. E., and M. E. Raymo (2007), Plio-Pleistocene climate evolution: trends and transitions in glacial cycle dynamics, *Quaternary Science Reviews*, *26*(1-2), 56–69.

Liu, X., D. S. Battisti, and A. Donohoe (2017), Tropical precipitation and cross-equatorial ocean heat transport during the mid-Holocene, *Journal of Climate*, *30*(10), 3529–3547.

Lucas-Picher, P., J. H. Christensen, F. Saeed, P. Kumar, S. Asharaf, B. Ahrens, A. J. Wiltshire, D. Jacob, and S. Hagemann (2011), Can Regional Climate Models Represent the Indian Monsoon?, *Journal of Hydrometeorology*, *12*(5), 849–868.

Lunt, D., A. Haywood, G. Schmidt, U. Salzmann, P. J. Valdes, and H. J. Dowsett (2009), Earth system sensitivity inferred from Pliocene modelling and data, *Nature Geoscience*, *3*(1), 60–64.

Lunt, D. J., A. M. Haywood, G. A. Schmidt, U. Salzmann, P. J. Valdes, H. J. Dowsett, and C. A. Loptson (2012), On the causes of mid-Pliocene warmth and polar amplification, *Earth and Planetary Science Letters*, *321-322*, 128–138.

Lunt, D. J., P. J. Valdes, A. Haywood, and I. C. Rutt (2007), Closure of the Panama Seaway during the Pliocene: implications for climate and Northern Hemisphere glaciation, *Climate Dynamics*, *30*(1), 1–18.

Lythe, M. B., and D. G. Vaughan (2001), BEDMAP: A new ice thickness and subglacial topographic model of Antarctica, *Journal of Geophysical Research*, *106*(B6), 11,335–11,351.

MA, H., Y. ZHU, and W. HUA (2019), Interdecadal change in the South Asian summer monsoon rainfall in 2000 and contributions from regional tropical SST, *Atmospheric and Oceanic Science Letters*, *12*(6), 399–408.

Manucharyan, G. E., and A. V. Fedorov (2014), Robust ENSO across a wide range of climates, *Journal of Climate*, *27*(15), 5836–5850.

Marshall, L. G., D. S. Webb, J. J. Sepkoski, and D. M. Raup (1982), Mammalian Evolution and the Great American Interchange, *Science*, *215*(4538), 1532–1357.

Marsham, J. H., N. S. Dixon, L. Garcia-Carreras, G. M. Lister, D. J. Parker, P. Knippertz, and C. E. Birch (2013), The role of moist convection in the West African monsoon system: Insights from continental-scale convection-permitting simulations, *Geophysical Research Letters*, *40*(9), 1843–1849.

Maslin, M. A., C. M. Brierley, A. M. Milner, S. Shultz, M. H. Trauth, and K. E. Wilson (2014), East african climate pulses and early human evolution, *Quaternary Science Reviews*, *101*, 1–17.

Maslin, M. A., X. S. Li, M. F. Loutre, and A. Berger (1998), The contribution of orbital forcing to the progressive intensification of Northern Hemisphere glaciation, *Quaternary Science Reviews*, *17*(4-5), 411–426.

Masson-Delmotte, V., P. Zhai, A. Pirani, S. Connors, C. Péan, S. Berger, N. Caud, Y. Chen, L. Goldfarb, M. Gomis, M. Huang, K. Leitzell, E. Lonnoy, J. Matthews, T. Maycock, T. Waterfield, O. Yelekçi, R. Yu, and B. Z. (eds.) (2021), Framing, Context, and Methods. Contribution of Working Group I to the Sixth Assessment Report of the Intergovernmental Panel on Climate Change, *Climate Change 2021: The Physical Science Basis.*, p. 3949.

Mathon, V., H. Laurent, and T. Lebel (2002), Mesoscale convective system rainfall in the Sahel, *Journal of Applied Meteorology*, *41*(11), 1081–1092.

Matsuno, T. (1966), Quasi-geostrophic motions in the equatorial area, *Journal of the Meteorological Society of Japan*, *44*(February), 25–43.

Matthews, A. J., G. Pickup, S. C. Peatman, P. Clews, and J. Martin (2013), The effect of the Madden-Julian Oscillation on station rainfall and river level in the Fly River system, Papua New Guinea, *Journal of Geophysical Research Atmospheres*, *118*(19), 10,926–10,935.

McClymont, E. L., H. L. Ford, S. Ling Ho, J. C. Tindall, A. M. Haywood, M. Alonso-Garcia, I. Bailey, M. A. Berke, K. Littler, M. O. Patterson, B. Petrick, F. Peterse, A. Christina Ravelo, B. Risebrobakken, S. De Schepper, G. E. Swann, K. Thirumalai, J. E. Tierney, C. Van Der Weijst, S. White, A. Abe-Ouchi, M. L. Baatsen, E. C. Brady, W. L. Chan, D. Chandan, R. Feng, C. Guo, A. S. Von Der Heydt, S. Hunter, X. Li, G. Lohmann, K. H. Nisancioglu, B. L. Otto-Bliesner, W. Richard Peltier, C. Stepanek, and Z. Zhang (2020), Lessons from a high-CO2 world: An ocean view from sim million years ago, *Climate of the Past*, *16*(4), 1599–1615.

Miller, K. G., M. a. Kominz, J. V. Browning, J. D. Wright, G. S. Mountain, M. E. Katz, P. J. Sugarman, B. S. Cramer, N. Christie-Blick, and S. F. Pekar (2005), The Phanerozoic record of global sea-level change., *Science*, *310*(5752), 1293–1298.

Miller, K. G., J. D. Wright, J. V. Browning, A. Kulpecz, M. Kominz, T. R. Naish, B. S. Cramer, Y. Rosenthal, W. R. Peltier, and S. Sosdian (2012), High tide of the warm pliocene: Implications of global sea level for Antarctic deglaciation, *Geology*, *40*(5), 407–410.

Molnar, P., and T. W. Cronin (2015), Growth of the Maritime Continent and its possible contribution to recurring Ice Ages, *Paleoceanography*, *30*(3), 196–225.

Otto-Bliesner, B., P. Braconnot, S. Harrison, D. Lunt, A. Abe-Ouchi, S. Albani, P. Bartlein, E. Capron, A. Carlson, A. Dutton, H. Fischer, H. Goelzer, A. Govin, A. Haywood, F. Joos, A. Legrande, W. Lipscomb, G. Lohmann, N. Mahowald, C. Nehrbass-Ahles, F. Pausata, J.-Y. Peterschmitt, S. Phipps, and H. Renssen (2016), The PMIP4 contribution to CMIP6 – Part 2: Two Interglacials, Scientific Objective and Experimental Design for Holocene and Last Interglacial Simulations, *Geoscientific Model Development Discussions*, pp. 1–36.

Pagani, M., Z. Liu, J. LaRiviere, and A. C. Ravelo (2010), High Earth-system climate sensitivity determined from Pliocene carbon dioxide concentrations, *Nature Geoscience*, *3*(1), 27–30.

Parker, D. J., C. D. Thorncroft, R. R. Burton, and A. Diongue-Niang (2005), Analysis of the African easterly jet, using aircraft observations from the JET2000 experiment, *Quarterly Journal of the Royal Meteorological Society*, *131*(608), 1461–1482.

Pound, M. J., J. Tindall, S. J. Pickering, A. M. Haywood, H. J. Dowsett, and U. Salzmann (2014), Late Pliocene lakes and soils: A global data set for the analysis of climate feedbacks in a warmer world, *Climate of the Past*, *10*(1), 167–180.

Rachmayani, R., M. Prange, and M. Schulz (2015), North African vegetation-precipitation feedback in early and mid-Holocene climate simulations with CCSM3-DGVM, *Climate of the Past*, *11*(2), 175–185.

Rai, P., M. Joshi, A. P. Dimri, and A. G. Turner (2018), The role of potential vorticity anomalies in the Somali Jet on Indian Summer Monsoon Intraseasonal Variability, *Climate Dynamics*, *50*(11-12), 4149–4169.

Ratna, S. B., A. Cherchi, T. J. Osborn, M. Joshi, and U. Uppara (2021), The Extreme Positive Indian Ocean Dipole of 2019 and Associated Indian Summer Monsoon Rainfall Response, *Geophysical Research Letters*, *48*(2), 1–11.

Raymo, M., B. Grant, M. Horowitz, and G. Rau (1996), Mid-Pliocene warmth: stronger greenhouse and stronger conveyor, *Marine Micropaleontology*, *27*(1-4), 313–326.

Raymo, M. E., J. X. Mitrovica, M. J. O'Leary, R. M. DeConto, and P. J. Hearty (2011), Departures from eustasy in Pliocene sea-levelrecords, *Nature Geoscience*, *4*(5), 328–332.

Raymo, M. E., and W. F. Ruddiman (1992), Tectonic forcing of late Cenozoic climate, *Nature*, *359*(6391), 117–122.

Rodgers, K. B., M. Latif, and S. Legutke (2000), Sensitivity of equatorial Pacific and Indian Ocean watermasses to the position of the Indonesian throughflow, *Geophysical Research Letters*, *27*(18), 2941–2944.

Rodwell, M. J., and B. J. Hoskins (1995), A Model of the Asian Summer Monsoon.Part II: Cross-Equatorial Flow and PV Behavior.

Roehrig, R., D. Bouniol, F. Guichard, F. déric Hourdin, and J. L. Redelsperger (2013), The present and future of the west african monsoon: A process-oriented assessment of CMIP5 simulations along the AMMA transect, *Journal of Climate*, *26*(17), 6471–6505.

Routledge, C. M., D. K. Kulhanek, L. Tauxe, G. Scardia, A. D. Singh, S. Steinke, E. M. Griffith, and R. Saraswat (2020), A revised chronostratigraphic framework for International Ocean Discovery Program Expedition 355 sites in Laxmi Basin, eastern Arabian Sea, *Geological Magazine*.

Rovere, A., M. E. Raymo, J. X. Mitrovica, P. J. Hearty, M. J. O'Leary, and J. D. Inglis (2014), The Mid-Pliocene sea-level conundrum: Glacial isostasy, eustasy and dynamic topography, *Earth and Planetary Science Letters*, *387*, 27–33.

Ruchith, R., P. Ernest raj, M. Kalapureddy, S. M. Deshpande, and K. K. Dani (2014), Time evolution of monsoon low-level jet observed over an Indian tropical station during the peak monsoon period from high-resolution Doppler wind, *Journal of Geophysical Research: Atmospheres*, pp. 1786–1795.

Saji, N., B. Goswami, P. Vinayachandran, and T. Yamagata (1999), A dipole mode in the Tropical Ocean, *Nature*, *401*(6751), 360–363.

Salzmann, U., A. M. Dolan, A. M. Haywood, W. L. Chan, J. Voss, D. J. Hill, A. Abe-Ouchi, B. Otto-Bliesner, F. J. Bragg, M. A. Chandler, C. Contoux, H. J. Dowsett, A. Jost, Y. Kamae, G. Lohmann, D. J. Lunt, S. J. Pickering, M. J. Pound, G. Ramstein, N. A. Rosenbloom, L. Sohl, C. Stepanek, H. Ueda, and Z. Zhang (2013), Challenges in quantifying Pliocene terrestrial warming revealed by data-model discord, *Nature Climate Change*, *3*(11), 969–974.

Salzmann, U., A. M. Haywood, D. J. Lunt, P. J. Valdes, and D. J. Hill (2008), A new global biome reconstruction and data-model comparison for the Middle Pliocene, *Global Ecology and Biogeography*, *17*(3), 432–447.

Sarathchandraprasad, T., M. Tiwari, and P. Behera (2021), South Asian Summer Monsoon precipitation variability during late Pliocene: Role of Indonesian Throughflow, *Palaeogeography, Palaeoclimatology, Palaeoecology*, *574*(October 2020), 110,447.

Schott, F. A., M. Dengler, and R. Schoenefeldt (2002), The shallow overturning circulation of the Indian Ocean, *Progress in Oceanography*, *55*(3-4), 373–384.

Ségalen, L., J. A. Lee-Thorp, and T. Cerling (2007), Timing of C4 grass expansion across sub-Saharan Africa, *Journal of Human Evolution*, *53*(5), 549–559.

Seki, O., G. L. Foster, D. N. Schmidt, A. Mackensen, K. Kawamura, and R. D. Pancost (2010), Alkenone and boron-based Pliocene pCO2 records, *Earth and Planetary Science Letters*, *292*(1-2), 201–211.

Semunegus, H., A. Mekonnen, and C. J. Schreck (2017), Characterization of convective systems and their association with African easterly waves, *International Journal of Climatology*, *37*(12), 4486–4492.

Sepulchre, P., G. Ramstein, F. Fluteau, M. Schuster, J.-J. Tiercelin, and M. Brunet (2006), Tectonic uplift and Eastern Africa aridification., *Science (New York, N.Y.)*, *313*(5792), 1419–23.

Slingo, J. M. (1987), The Development and Verification of A Cloud Prediction Scheme For the Ecmwf Model, *Quarterly Journal of the Royal Meteorological Society*, *113*(477), 899–927.

Smyth, J. E., S. A. Hill, and Y. Ming (2018), Simulated Responses of the West African Monsoon and Zonal-Mean Tropical Precipitation to Early Holocene Orbital Forcing, *Geophysical Research Letters*, *45*(21), 12,049–12,057.

Sommerfeld, A., K. Prömmel, and U. Cubasch (2014), The East African Rift System and the impact of orographic changes on regional climate and the resulting aridification, *International Journal of Earth Sciences*.

Sperber, K. R., H. Annamalai, I. S. Kang, A. Kitoh, A. Moise, A. Turner, B. Wang, and T. Zhou (2013), *The Asian summer monsoon: An intercomparison of CMIP5 vs. CMIP3 simulations of the late 20th century*, vol. 41.

Stepanek, C., E. Samakinwa, G. Knorr, and G. Lohmann (2020), Contribution of the coupled atmosphere-ocean-sea ice-vegetation model COSMOS to the PlioMIP2, *Climate of the Past*, *16*(6), 2275–2323.

Stuecker, M. F., A. Timmermann, F. F. Jin, Y. Chikamoto, W. Zhang, A. T. Wittenberg, E. Widiasih, and S. Zhao (2017), Revisiting ENSO/Indian Ocean Dipole phase relationships, *Geophysical Research Letters*, *44*(5), 2481–2492.

Sun, Y., T. Zhou, G. Ramstein, C. Contoux, and Z. Zhang (2015), Drivers and mechanisms for enhanced summer monsoon precipitation over East Asia during the mid-Pliocene in the IPSL-CM5A, *Climate Dynamics*.

Tierney, J. E., A. M. Haywood, R. Feng, T. Bhattacharya, and B. L. Otto-Bliesner (2019), Pliocene Warmth Consistent With Greenhouse Gas Forcing, *Geophysical Research Letters*, *46*(15), 9136–9144.

Tierney, J. E., and M. P. Tingley (2018), BAYSPLINE: A New Calibration for the Alkenone Paleothermometer, *Paleoceanography and Paleoclimatology*, *33*(3), 281–301.

Turner, A. G., and H. Annamalai (2012), Climate change and the South Asian summer monsoon, *Nature Clim. Change*, *2*(8), 587–595.

van der Wiel, K., A. J. Matthews, M. M. Joshi, and D. P. Stevens (2016), Why the South Pacific Convergence Zone is diagonal, *Climate Dynamics*, *46*(5-6), 1683–1698.

Vidya, P. J., M. Ravichandran, M. P. Subeesh, S. Chatterjee, and N. M. (2020), Global warming hiatus contributed weakening of the Mascarene High in the Southern Indian Ocean, *Scientific Reports*, *10*(1), 5670.

Wang, H., H. Lu, L. Zhao, H. Zhang, F. Lei, and Y. Wang (2019), Asian monsoon rainfall variation during the Pliocene forced by global temperature change, *Nature Communications*, *10*(1), 4–11.

Webster, P. J., A. M. Moore, J. P. Loschnigg, and R. R. Leben (1999), Coupled oceanic-atmoshperic dynamics in the Indian Ocean during 1997-1998, *Nature*, *401*(23), 356–360.

Wheeler, M., and G. N. Kiladis (1999), Convectively Coupled Equatorial Waves: Analysis of Clouds and Temperature in the Wavenumber–Frequency Domain, *Journal of the Atmospheric Sciences*, *56*(3), 374–399.

White, S. M., and A. C. Ravelo (2020), Dampened El Niño in the Early Pliocene Warm Period, *Geophysical Research Letters*, *47*(4), 1–10.

Wycech, J. B., E. Gill, B. Rajagopalan, T. M. Marchitto, and P. H. Molnar (2020), Multiproxy Reduced-Dimension Reconstruction of Pliocene Equatorial Pacific Sea Surface Temperatures, *Paleoceanography and Paleoclimatology*, *35*(1), 1–20.

Xiangyu, L. I., J. Dabang, Z. Zhongshi, Z. Ran, T. Zhiping, and Y. A. N. Qing (2015), Mid-Pliocene Westerlies from PlioMIP Simulations, *Advances in Atmospheric Sciences*, *32*(July), 909–923.

Yin, A., C. S. Dubey, A. A. Webb, T. K. Kelty, M. Grove, G. E. Gehrels, and W. P. Burgess (2010), Geologic correlation of the Himalayan orogen and Indian craton: Part 1. Structural geology, U-Pb zircon geochronology, and tectonic evolution of the Shillong Plateau and its neighboring regions in NE India, *Bulletin of the Geological Society of America*, *122*(3-4), 336–359.

Yu, S. Y., L. Fan, Y. Zhang, X. T. Zheng, and Z. Li (2021), Reexamining the Indian Summer Monsoon Rainfall–ENSO Relationship From Its Recovery in the 21st Century: Role of the Indian Ocean SST Anomaly Associated With Types of ENSO Evolution, *Geophysical Research Letters*, *48*(12).

Zachos, J., M. Pagani, L. Sloan, E. Thomas, and K. Billups (2001), Trends, rhythms, and aberrations in global climate 65 Ma to present, *Science*, *292*(5517), 686–693.

Zhang, R., D. Jiang, Z. Zhang, Q. Yan, and X. Li (2019), Modeling the late Pliocene global monsoon response to individual boundary conditions, *Climate Dynamics*, *53*(7-8), 4871–4886.

Zhang, R., Z. Zhang, D. Jiang, Q. Yan, X. Zhou, and Z. Cheng (2016), Strengthened African summer monsoon in the mid-Piacenzian, *Advances in Atmospheric Sciences*, *33*(9), 1061–1070.

Zhang, Y. G., M. Pagani, Z. Liu, S. M. Bohaty, and R. Deconto (2013), A 40-million-year history of atmospheric CO2, *Philosophical Transactions of the Royal Society A*, *371*(September).

Zheng, H., C. M. Powell, Z. An, J. Zhou, and G. Dong (2000), Pliocene uplift of the northern Tibetan Plateau, *Geology*, *28*(8), 715.

Zheng, H., C. M. Powell, D. K. Rea, J. Wang, and P. Wang (2004), Late Miocene and mid-Pliocene enhancement of the East Asian monsoon as viewed from the land and sea, *Global and Planetary Change*, *41*(3-4), 147–155.

Zheng, X., and E. A. Eltahir (1998), The role of vegetation in the dynamics of West African monsoons, *Journal of Climate*, *11*(8), 2078–2096.

Zhisheng, A., J. E. Kutzbach, W. L. Prell, and S. C. Porter (2001), Evolution of Asian monsoons and phased uplift of the Himalaya-Tibetan plateau since Late Miocene times, *Nature*, *411*(6833), 62–66.

Zhong, W., and J. D. Haigh (1995), Improved broadband emissivity parameterization for water vapor cooling rate calculations, *Journal of the Atmospheric Sciences*, *52*(1), 124–138.